FACULTY OF SCIENCE AND TECHNOLOGY

MASTER THESIS

Study programme / specialisation: MSc in Marine and Offshore Technology/ Marine and Subsea Technology	The spring semester, 2022 Open / ~~Confidential~~
Author: Rajiv Balakrishna	..... *Rajiv Balakrishna*.....
Course coordinator: Professor Yihan Xing Supervisor(s): Professor Yihan Xing	
Thesis title: Characterization and Optimization of Control System and Extreme Value Analysis of a Wind Turbine	
Credits (ECTS): 30	
Keywords: Wind Turbine Control System PID Extreme Values ACER1D ACER2D Univariant Bivariate	Pages: .....111... + appendix: .....57... Stavanger, ...30.06.22..... date/year

Abstract

The global hunger for energy has only been rising every day as we progress more into adopting superior and better technology to make lives better and easier. As more countries tread the path of industrialization, the need for cleaner and greener energy is imperative to reduce damage to an already deteriorating environment. Wind energy accounts for about 15% of renewable energy and is one of the fastest-growing renewable technologies. The energy produced by wind has doubled in the past decade. The wind industry is only expected to grow with an infinite supply of natural wind. Wind turbines in the 1980s had a capacity of 0.1MW, but today they average at around 10MW, with the largest wind turbines having a capacity of 15MW. Due to a surge in demand and potential for growth, it has become more critical than ever to find newer strategies to maximize turbine efficiency. Numerous approaches can be adopted to improve a turbine's efficiency, including design, material, or control system changes. Other options include using novel or better prediction models to estimate extreme values that can be useful in fine-tuning designs of wind turbines. In this thesis, two main strategies are adopted in an attempt to optimize the efficiency of wind turbines. Firstly, in Paper-I, a novel change to the pitch controller is adopted by adding and optimizing the bending moments to reduce the bending moment in the low-speed shaft. A reduction in the bending moment will reduce the internal drive train loads within the gearbox, thus extending its lifespan. A reduction of bending moment with minimal loss in shaft rotational speed was observed through this optimization. While in, Paper-II and -III, the novel ACER1D and 2D (univariate and bivariant analysis) models were used to estimate extreme load values. Paper-II presented the ACER1D results but focused on the ACER2D as it fitted it against other models, such as the optimized Asymmetric and Gumbel logistic models. This paper showed that ACER2D was advantageous since it could produce very accurate results compared to the other models with very little data set. While in Paper-III, extreme values estimate from ACER2D were compared against the Gumbel model, and the results obtained were positive, showing that ACER1D was better at estimating extreme values with a small data set. Optimizing the extreme values is critical when designing wind turbines as proper values enable better and more reliable turbine designs. Thus, both the strategies adopted in this thesis showed that through proper optimization, a reduction of load or a better design could be achieved, resulting in better efficiency in wind turbines.

Acknowledgement

This thesis is a part of the master's programme, Marine and Offshore Technology, at the University of Stavanger under the Department of Mechanical and Structural Engineering and Material Science, Faculty of Science and Technology.

Firstly, I would like to take this opportunity to express my deepest gratitude to my supervisor, Professor Yihan Xing, for his support, motivation, and invaluable guidance throughout this project. I am incredibly grateful, especially since he always made time to guide me through the problems I encountered throughout this project. Furthermore, his dedication drove me to learn more about the wind industry and develop my interest in Wind Technology.

I would also like to thank Dr. Oleg Gaidai and Dr. Shuaishuai Wang for their guidance, knowledge, insight, expertise and unanimous support on this project.

I would also like to thank my fellow co-students and friends for their support, motivation, and shared adventures during the study period.

I want to take this opportunity to thank my friends, Vinnit George, Tan Aditya Dwi Santoso, Anuraj Karuvathil and Karan Sandipkumar Patel. I am thankful for their support and help throughout the process.

Most of all, I would like to thank my family for their support in fulfilling my academic goals, as, without them, I would not be able to fulfil my dreams.

Thank you all!

Stavanger, 30 June 2022

Publications

The following four papers were written during the period of the thesis. These papers are annexed in the same format they were submitted or published to the respective conferences and journals.

I. Balakrishna, R., & Xing, Y. (2021). Compensation scheme applied on wind turbine blade pitch control for the reduction of non-torque main shaft loads. IOP Conference Series: Materials Science and Engineering.

II. Balakrishna, R., Gaidai, O., Wang, F., Xing, Y., & Wang, S. (2022). A novel design approach for estimation of extreme load responses of a 10-MW floating semi-submersible type wind turbine. Under Review.

III. Xing, Y., Wang., Karuvathil., A, Balakrishna., R, & Gaidai, O., (2022). Characterisation of extreme load responses of a 10-1 MW floating semi-submersible type wind turbine. Under Review.

Table of Contents

List of Figures

List of Tables

Abbreviations

ACER	–	Average Conditional Exceedance Rate
DNV	–	Det Norske Veritas
DTU	–	Danmarks Tekniske Universitet
EVD	–	Extreme Value Distribution
FOWT	–	Floating Offshore Wind Turbine
FWT	–	Floating Wind Turbine
HAWT	–	Horizontal Axis Wind Turbine
kN	–	Kilo Newton
kW	–	Kilo Watt
LC	–	Load Case
MBS	–	Multi-Body System
MW	–	Mega Watt
N	–	Newton
NREL	–	National Renewable Energy Laboratory
OWT	–	Offshore Wind Turbine
RWT	–	Reference Wind Turbine
ULS	–	Ultimate Limit State
VAWT	–	Vertical Axis Wind Turbine

Introduction

1.1 Overview of Thesis

Wind energy is a key agent in the “Net Zero Emissions by 2050” agenda set forth by many countries, including Norway (IEA, 2020). Norway has been actively spearheading efforts to develop technologies and capabilities to harness wind energy more efficiently (A1). One key area of focus in this pursuit is the development and fine-tuning of wind turbine technology. According to Betz’s Law, there is a higher cap on how much kinetic energy can be converted to electrical energy. Therefore, any new methods or prediction strategies that can maximize the extraction of useful electrical energy are useful. Research and development of maximizing wind turbine efficiency only encourage reducing the dependence on fossil fuels and facilitate the movement toward wind energy. Wind Turbines (WTs) power or its cost efficacy can be improved through modifications in their mechanical designs, material properties, control system designs, better loads estimation, etc. However, with very little room for any more design improvements, research on WTs today has focused on better materials, control systems and loads estimation. This thesis will focus on optimizing wind turbines’ control systems and extreme loads estimation methods.

The first part of this thesis (Paper I) focuses on optimizing the present control system through a novel and effective modification and then analyzing this modified control system. Wind turbine (WT) control concepts have been evolving since their conceptualization. From its early days of controlling the stall-controlled-constant-speed WTs to the present pitch-controlled-variable-speed WTs, these concepts have been evolving according to their requirements. Control algorithms are principally implemented to control the pitch and torque of turbines to maximize their effectiveness. It enables the control system to maximize or optimize the wind's kinetic energy within the WT operational limits. Within such operating limits, it targets maximizing electrical power produced by the generator or maximizing the shaft-designed rotating speed. While as a secondary function, the control system is designed to minimize excessive mechanical loading in the WTs, thus extending the turbine lifespan. With much research on control algorithms focusing on improving the efficiency of the wind turbine (Pao, 2009; Laks, 2011), this thesis hopes to look at the control algorithm which can reduce bending moment in the low-speed shaft. Better control systems lead to reduced loads and life expectancy of the wind turbines. An example of fine-tuning control systems includes varying shaft speed or blade pitch to reduce the loads on the turbines. Unfortunately, such variations are problematic since whenever the rotational speed increases, the loads acting on the WTs increase equally, decreasing the turbine's lifespan. This dilemma of finding a delicate balance between the two has inspired more focused and detailed studies on control concepts. Like the control systems, a more accurate extreme statistical

loads estimation can improve the wind turbine cost efficiency. Modelling a wind turbine according to these values is critical as it can minimize damage or predict faults in the design in a better way. In the past decades, more research and investments have been used on wind turbines allowing wind turbines to become bigger and more cost-effective. Furthermore, as more and more turbines are being built, it has become even more vital to minimize their developmental and servicing cost. An important chokepoint in smooth economic viability is the increased expenditure from wind turbine failure. Thus, ensuring such failures are minimized will reduce extended downtime (which can last from months to years) or the reliance on the availability of the materials or manpower (IEA,2020; IRENA, 2012; Sheng, 2012), thereby reducing cost overruns.

This thesis's second and third parts (Paper II and III) focus on characterizing extreme load estimation using the ACER1D and ACER2D methods and then comparing them with the Gumbel method. According to International Electrotechnical Commission (IEC) standards, wind turbines must be designed to operate in the highly stochastic wind and wave environments for at least 20 years (Veers, 2001). Since larger wind turbines (both in numbers and size) are constructed, especially offshore, it has become essential to minimize construction, maintenance, and operational costs. Turbines and their components are vulnerable to various cyclic loads such as axial and transverse loading, bending moments and torque. Furthermore, the loads acting on the wind turbines are also influenced by the wind's stochastic behaviours in speed, direction, shear, and vorticity, making extreme load analysis imperative for wind turbine design and operation. Any failure in the turbine system can result in unnecessary downtime, which can be extremely expensive (Igba, 2015; Irena, 2012; Sheng, 2012). Despite this, engineers in the 1970s believed that it was unnecessary to conduct detailed modelling, resulting in the design of wind turbines with huge safety margins. However, this changed with the further development of larger wind turbines as it became more expensive to maintain similar safety margins. On top of that, inaccurate estimation of design loads led to unnecessary failures. These led to an industry revamp, where a better accurate prediction technique was developed by the 1990s using dynamic structural models, turbulence models, aerodynamic models, and control algorithms (Veers, 1998). Thus, a better and more accurate estimation of these extreme responses will help designers better understand the outcome of these loads on the components, thus developing better design and control systems for future wind turbines (Xu, 2019). The ACER1D and ACER2D analysis done in the second and third parts of the thesis offers a more reliable description of the extreme load distribution's tail behaviour and have been used reliably in numerous marine structures (Zhang,2019; Gaidai, 2018; Gaidai, 2016), and (Naess, 2008; Naess, 2009; Naess, 2010; Naess, 2013).

1.2 Background

The global population is expected to grow to 9.7 billion by the end of 2010 and 11 billion by 2100 (United Nations, PPP2015), see Figure 1. With such a significant change in the population, energy consumption is expected to grow exponentially. In addition, industrial development in developing countries which is part of economic growth, will also drive up the need for energy demand. Even as fossil fuels can keep up with such growth, it is noteworthy to acknowledge that it also comes with an expiry date. Furthermore, burning fossil fuels also increases greenhouse gases in the atmosphere while contributing to hazardous effects such as global warming and climate change. Even as new projects such as carbon reinjection promises to mitigate the problems in the future, it is premature to conclude that it will be able to eradicate the problem associated with fossil fuels. Global investment in the energy sector has doubled in the past decade to over 1600 billion and is expected to be around 2000 billion in the 2030s (IEA, 2014).

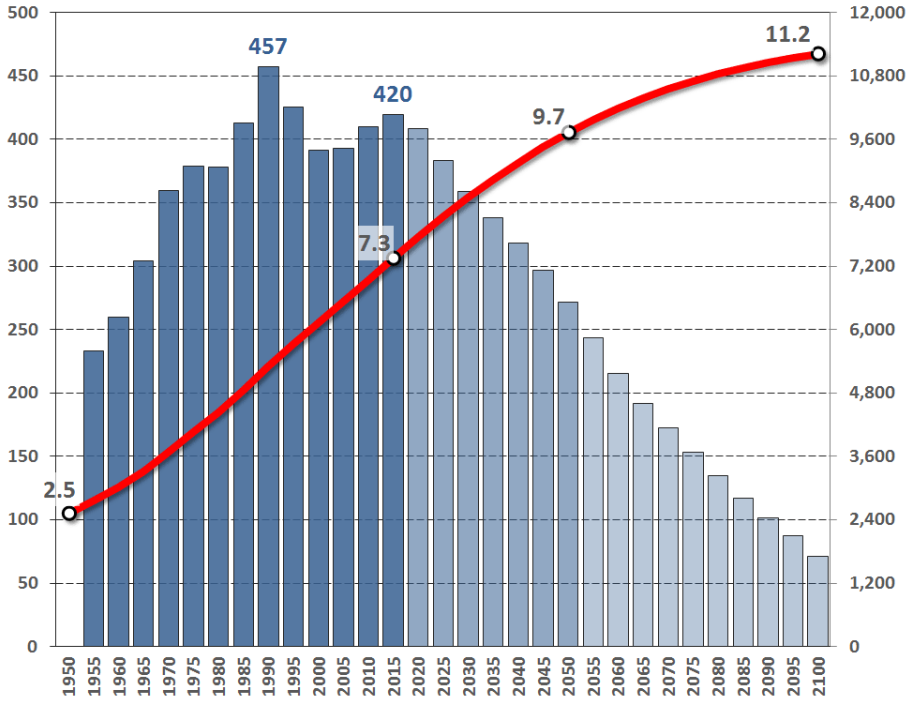

Figure 1 Global Population growth (Demographics 2018)

Socially responsible ideas such as the Paris Climate Change Agreement (PCCA) and The Green New Deal have successfully caught traction over the years. Even as over 187 countries sign the PCCA helps mitigates greenhouse-gas emissions rates, further research and development in technology will also play a critical role in lowering carbon footprint and eventually achieving a target of net-zero carbon emissions in the near future. However, a more practical method to reduce our dependence on fossil rules in the future would be to adopt renewable energy such as nuclear, hydro, solar, wind, etc. With numerous alternatives for fossil fuels, renewable energy is a viable and realistic option. Especially as shallower oil and gas fields are starting to dry up, exploration has started moving further offshore, and

prices associated with deeper oil fields are expected to rise again. However, a transition towards a more renewable energy-friendly market is an ambitious challenge faced by most counties globally (IEA, 2014).

1.3 Wind Turbine

As of 2018, Denmark tops the EU-28's annual electricity demand covered by wind by about 41%, with about only about 25% of them produced offshore, While Ireland uses about 28% of its energy generated from wind (all onshore), see Figure 2. In Europe, Germany is the highest wind energy producer by the sheer size and produces about 60GW of energy from its onshore and offshore wind turbine installations (Wind 2018). While globally, in 2014, China produced the most wind energy accounting for 145GW (World Wind 2015). The European Union has also set a target to increase the percentage of energy produced by renewable to 20% (14% in 2018), while counties like the Netherlands have targeted to achieve over 15% energy generation from renewable by 2025 (Wind, 2014). Within renewable energy, wind energy dominates the Netherlands and is only second to biomass (Netherlands, 2019).

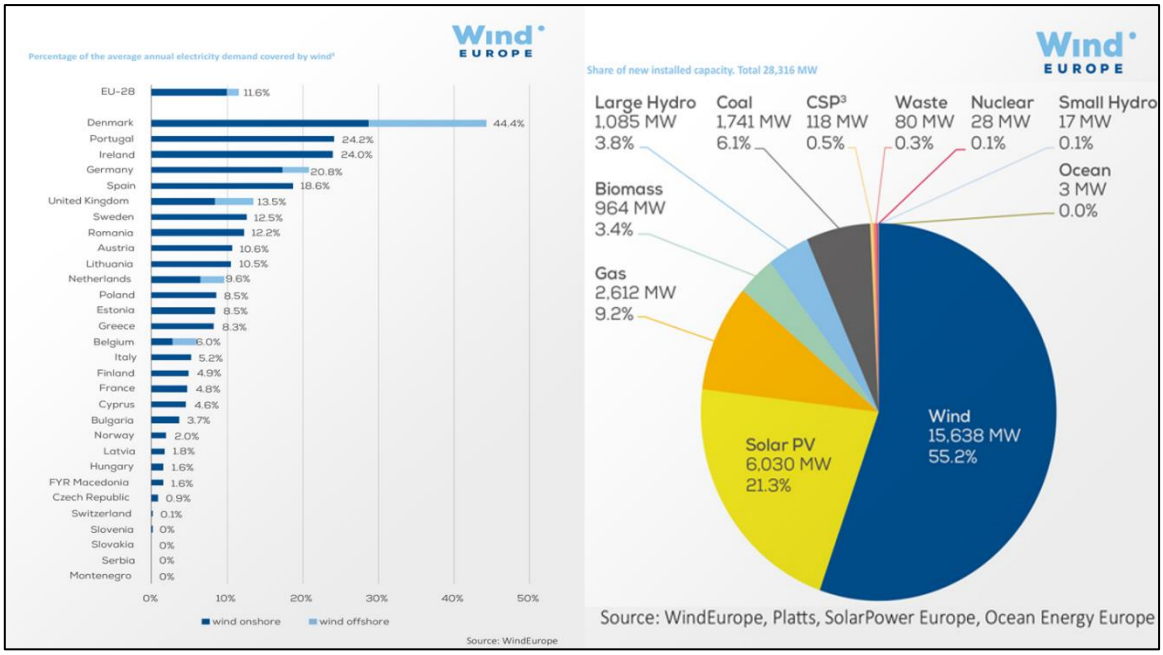

Figure 2 Highest wind energy produce in Europe (Wind Energy)

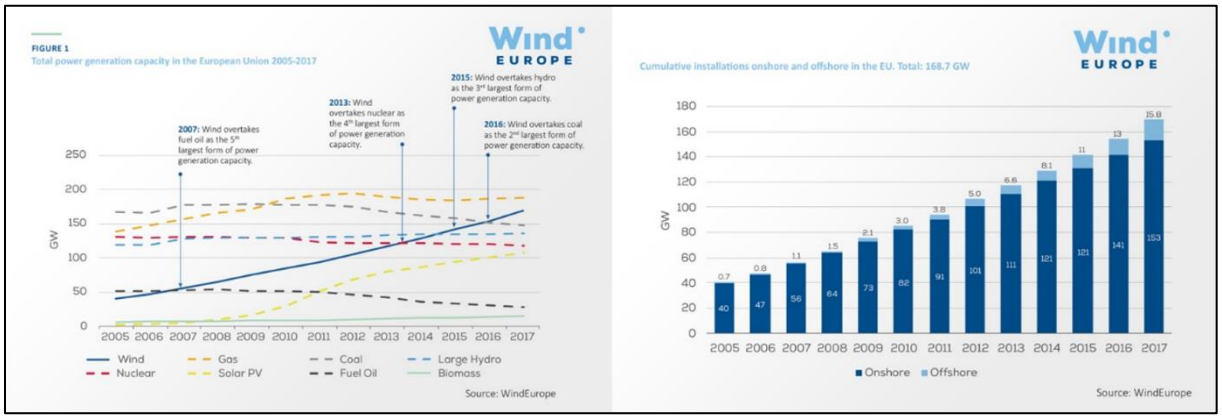

Figure 3 Growing wind energy in Europe (Wind Energy)

Wind energy is the fastest-growing energy source, only second to gas in the EU as of 2017 (Wind, 2018). With faster progress expected in the next decade, wind energy is touted to overtake gas and become number one. Wind energy primarily is generated from either a horizontal axis wind turbine (HAWT) or a vertical axis wind turbine (VAWT). A HAWT rotates on a horizontal axis, while a VAWT rotates on a vertical axis.

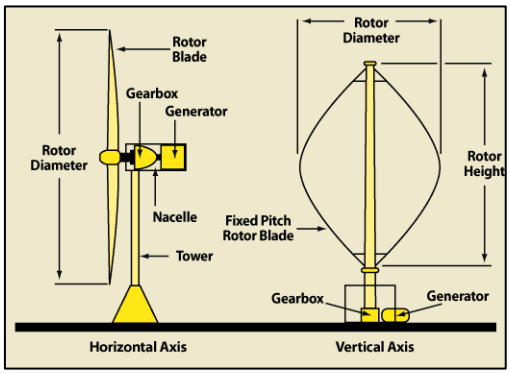

Figure 4 Horizontal Axis and Vertical Axis for Wind Energy (American Wind Energy Association)

The HAWT is the most common type of wind turbine and is further subcategorized as an onshore or offshore wind turbine. A simple diagram of a HAWT and VAWT is illustrated in Figure 4 above. The onshore wind turbine is a common sight throughout Western Europe. Most HAWT are onshore and have dominated the sector since they are usually more affordable and easily built. More than 75% of Denmark wind energy is generated using onshore turbines (Wind, 2019). Infrastructure transport of electricity is also more accessible and affordable onshore than offshore. However, lately, more offshore wind turbines are being built in Europe and around the world (Wind, 2019). Over the past decade, there has been a steady increase in the total number of offshore wind turbines. Figure 3, in 2017, about 15% of the energy produced by wind turbines have been produced offshore, as opposed to in 2007, where less than 1% were generated offshore (Wind 2018).

1.4 Onshore Wind Turbine

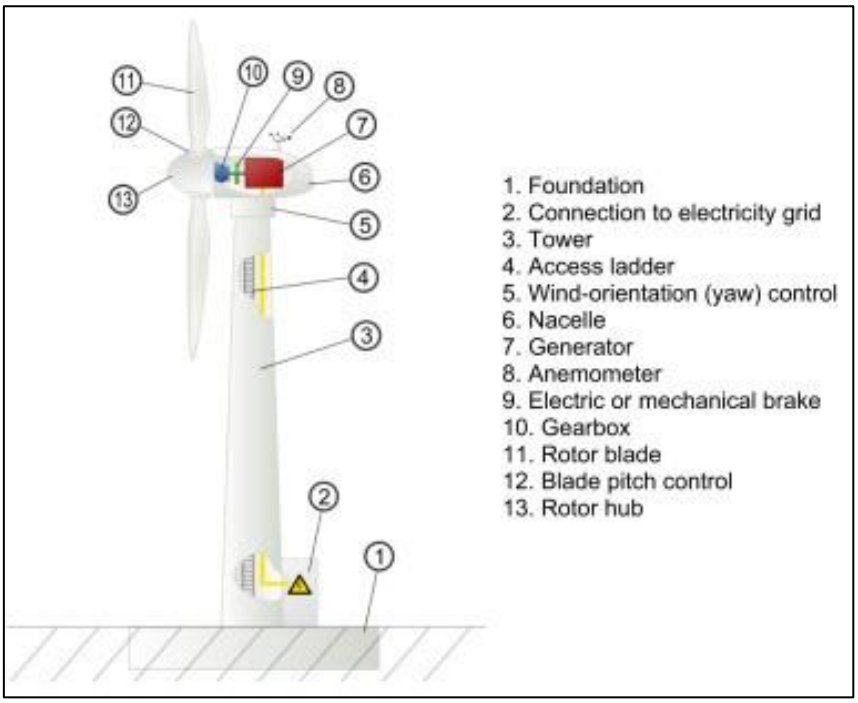

Figure 5 Standard turbine with description of the components (McKenna, 2016)

Over the past few decades economic growth throughout the globe has led to an Increase in the need of electricity, and within the wind industry such an upsurge has led to the production of larger turbines specially focused on increasing the rotor span and the hubs height. In the start of the 1990s, onshore wind turbines were built to support a turbine capacity of about 1 MW but now is built to support 5 to 10 MW with this expected to increase in the new future, see Figure 5. The driving force behind increasing the turbine capacity is accounted for by the decrease in levelized costs for electricity generation, which has been aided by various optimization criteria (Chehouri, 2015). This has been commonly achieved by building at higher hub heights (wind speeds are lager, and power is related to the wind speed with a cubic relationship) or increasing the rotor diameters (power is related to the rotor diameter with a squared relationship), see Figure 6. However, there is a limitation to the size in which we can build onshore as they are limited by different local regulations. Therefore, various new ideas such as wind turbine optimization and modelling have been suggested over the years to bring down the levelized costs for electricity generation (McKenna, 2016). In an ideal situation, WTs' aerodynamic performance must be optimized at rated speed and be made to endure extreme loads for wind speeds higher than it (Capuzzi, 2014). To achieve this objective, it is vital to adopt a two-frontier approach, with the first being the development of control systems that are better able to integrate and give feedback about the system, which enables the reduction of load acting on the system. At the same time, a second viable option could be to develop a new method to better predict

the extreme load values acting on the turbines that will enable us to build better and more efficient WTs (McKenna, 2016). Therefore, with precise control system modification or better extreme values predictions, WT can achieve an increase in the annual energy production or a decrease in the total turbine cost, decreasing the levelized costs for electricity generation (McKenna, 2016).

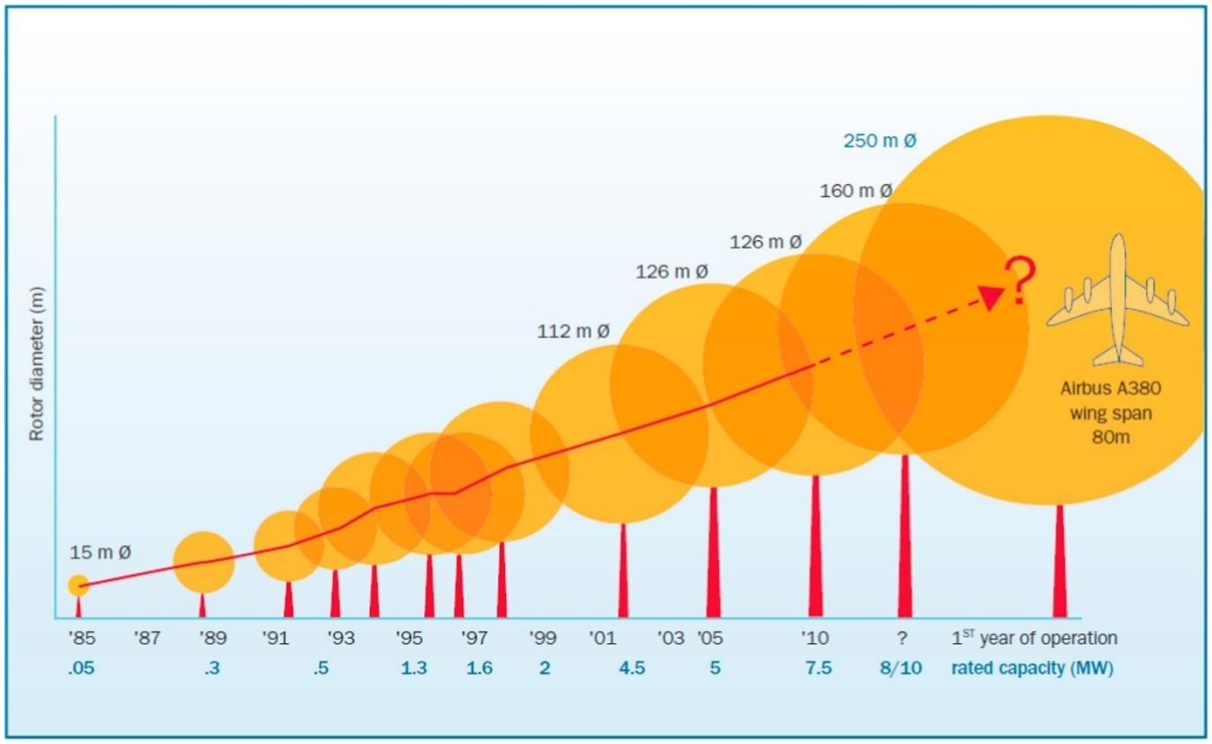

Figure 6 Development of upper end size turbines over the years (McKenna, 2016)

1.5 Offshore Wind Turbine

Offshore wind turbines do not have the same regulation or size limitations as their onshore counterparts. Instead, offshore wind turbines are built with a greater liability, and their primary limitation with the size is mostly due to engineering or the environment (Tande, 2014). Thus, offshore wind turbines can fully exploit the rich wind speeds and availability in deep-sea areas. Like the onshore wind turbines, their offshore counterparts have increased their sizes even more rapidly (Tande, 2014), see Figure 7. In shallow water lesser than 50 meters, a bottom-fixed base is usually selected as a preferred choice. While at deep waters above 100 meters, wind turbines are built with floating bases. While, at the intermediate depths ranging from 50.-100 meters, both the bottom-fixed and floating bases are chosen based on various factors, e.g., technical feasibility, environmental factors, and cost. Bottom-fixed bases are usually the preferred choice if possible, as it cheap and is well established. However, further away from the shore, as the water gets deeper, building a bottom-fixed base no longer is viable due to the technical feasibility, environmental factor, and cost. Offshore wind technologies are commonly considered a game changer as they are seen as a key in achieving environmentally target set globally due to the large wind energy availability and the turbine conversion potential (Breton, 2009; Hong, 2011; Ackermann, 2001).

Many bottom-fixed offshore wind farms have been scheduled to be completed mostly in Northern Europe and with new farm plans being planned out for the future (Arapogianni, 2011). Nevertheless, there are only a few places with good wind conditions and low shallow water, with most of them located in deeper waters, e.g., the Northern Americas, Pacific Coast, Portugal, and Japan Coast. In the past, such deep water coast would have been considered impossible to be financially viable. Still, with the recent development and commercialization of such wind farms, such projects are becoming viable with concepts made by HyWind, WindFloat and DeepWind (Tande, 2014). With the development of these concepts, there has been a focus on design, control, and operation. Therefore, the two-frontier approach, as described in the previous section, can similarly increase the annual energy production or decrease the total turbine cost, reducing the levelized costs for electricity generation.

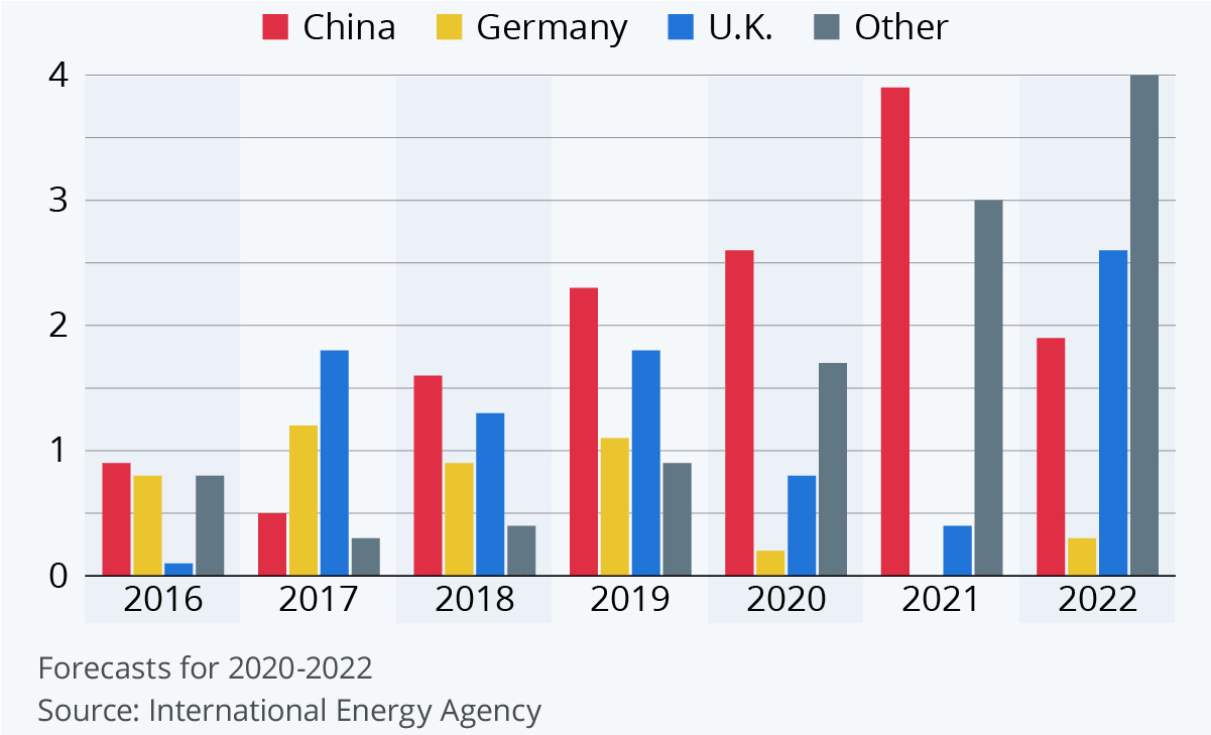

Figure 7 Offshore wind turbine installation (International Energy Agency)

1.6 Basics of a Control System

The control regime of variable speed wind turbines is divided into the above-rated and below-rated regions. In the above-rated region, the control system changes the blade pitch angle, which changes the blade's angle of attack, allowing the generator speed regulation to sustain the rated power output. While in the below-rated region, the control system aims to control the generator (by regulating in between its maximum and minimum value) speed maximizing its power output.

In this thesis, as in Paper I, the primary multivariable control will be done with the speed in the above-rated region. Typical control systems use the generator torque and blade pitch angle to control the generator power/torque or generator speed, respectively (Leith, 1997; Leithea, 2000). With the construction of bigger and more powerful turbines, the importance of minimizing loads acting on the tower and gearboxes using the pitch control system has become more important than ever and has been illustrated in previous studies (Leithead, 2003). While previously, as mentioned (Leithead, 2006), the pitch control only used the generator speed as a feedback mechanism to control the generator speed. Paper-I has suggested that the shaft moment can also be used in the feedback loop to enable better pitch control and thus speed control. It has been previously established that for the tower loads, only the fore-aft motion needs to be studied as it is the main driving factor that acts on the tower (Leithead, 2006). Similarly, minimizing the low-speed shaft moment is a determining factor when

analyzing the loads in the gearbox (Leithead, 2006). The study area is focused in the above-rated regions with the under-rated and rated regions used as illustrations, since most of the loads occur in the above-rated regions. After considering the low-speed shaft moment control, a more efficient controller model is feasible since the control is designed to maximize the collaboration between low-speed shaft moment and generator pitch control. A moment reduction is in this manner possible. The control analysis and design are performed later in this thesis for the NREL 5 MW wind turbine.

1.7 Basics of Extreme Values

Extreme value analysis (EVA) is a division within statistics that predicts the extreme deviations of probability/ statistical distributions. The statistical distribution is often used to estimate these extreme values are usually from the Weibull, Gumbel or Fréchet extreme value distributions. Such analysis aims to predict the probability of events at the ends and those that are more extreme than usual. EVA looks to answer the probabilistic questions relating to extreme tail-end values (high or low) in sequences of random variables and in stochastic processes (Saeb 2014). EVA is used in various fields, including structural engineering, mechanical engineering, finance and traffic prediction. Examples include a design engineer who wants to predict a 50-year wind allowing a better design of a wind turbine. There are primarily two different ways for EVA. The first method involves deriving block maxima (minima) series and then extracting an annual maximum (minima), which produces an "Annual Maxima Series" (AMS). In comparison, the second method involves obtaining the peak values when it exceeds a certain threshold during the selected period range, known as the "Peak Over Threshold" (POT) method. The AMS analysis results in a generalized extreme value distribution being used for fitting, while the POT analysis attempts to fit two different distributions (Agarwal, 2009; Fogle, 2008; Ragan, 2008).

Statistical extrapolation is often used when approximating stimulated long-term extreme loads acting on wind turbines. Even though many statistical extrapolation methods are well established, the values derived from simulations can be inaccurate if there are uncertainties in estimated extreme loads and the usability of the chosen extrapolation method is not addressed. Furthermore, the 3rd edition of the International Electrotechnical Commission (IEC) Standard: 61400-1 requires developers to use statistical extrapolation approaches to investigate loads on the turbines. These load case requirements state that characteristic loads need a return period of 50 years to be determined. The initial response indicates the turbines' stochastic response to randomized environmental conditions and is completed using the aeroelastic simulations (Agarwal, 2009; Fogle, 2008; Ragan, 2008).

To ensure that proper estimation and robust predictions is done for such infrequent loads, an adequate quantity and quality extreme loads data are required. However, the reliability of such extrapolation has always been a heated debate among scholars. For example, scholars have debated the necessary number of ten-minute responses, if a single maximum load is saved or if a few time-separated (block) maxima are preferred. Furthermore, even though every speed in between the cut-in or -out speed affects the turbine load types differently, often only a region which experiences the largest variation is considered (Agarwal, 2009; Fogle, 2008; Ragan, 2008).

1.8 Objective

The main objective of this thesis is centered on characterizing and optimizing the parameters that will help better predict the structural loads acting on the wind turbines with greater accuracy by simulating different conditions that give different moments/loads acting on the turbines. It is achieved by modifying the conditions such as speed and the turbulence acting on the turbine. To characterize, optimize and better predict the load acting on the wind turbine, we have presented the thesis based on two strategies applied over three papers:

1. Paper-I: Characterizing and optimizing the moments acting on the low-speed wind shaft by developing a compensation scheme for the pitch controller in the NERL 5MW RWT. It has been shown to impact the loads acting on the gearbox directly.
2. Paper-II: Characterizing and optimizing the extreme load prediction through the ACER1D/ ACER2D methods from results obtained from the DTU 10MW RWT. Verifying the credibility of values obtained from the ACER2D method by fitting and comparing It against the Asymmetric and Gumbel logistic model.
3. Paper-III: Characterizing and optimizing the extreme load prediction through the ACER1D methods from results obtained from the DTU 10MW RWT. Verifying the credibility of values obtained from the ACER2D method and comparing It against the Gumbel model.

Different RWTs (NREL 5MW RWT and DTU 10MW RWT) have been used in this thesis to create three papers. The NREL 5MW RWT used in Paper-I has a better-established control system and is more reliable when attempting to optimize a modified control system. Furthermore, it allows the controller is better tested before being imported into other turbine models. While characterizing and optimizing extreme values, the DTU 10MW RWT was used as it is a larger, contemporary and pertinent wind turbine and will thus give suitable loads values, which can be used to develop and build future wind turbines.

The current thesis is performed in the following steps:

Paper-I:

1. Developing a new compensation scheme on Simulink-MATLAB that can be used as a control system in the NERL 5MW RWT.
2. Generation of multiple inflow linear wind and turbulent wind fields (speed) with the NERL 5MW baseline model in MATLAB and TURBSIM, respectively.
3. Characterizing how the loads and motions (low-speed shaft RPM, bending moment and generator power) on the NERL 5MW RWT are affected by the generated linear and turbulent wind spectra when using the new compensation scheme.
4. Investigate how different compensation weight factor (K_{BM}) used in the compensation scheme affects the system and optimizing it to attain the appropriate K_{BM} values.
5. The results are then computed to find the best K_{BM} values with the maximum reduction in shaft bending moments, which also minimizes the rotational speed and power losses.

Paper-II:

1. Characterizing the approach to better estimate the extreme load responses of a DTU 10-MW floating semi-submersible wind turbine focusing on the ACER1D and ACER2D methods. The ACER2D results were then compared against the Asymmetric and Gumbel logistic model.
2. Generation of environmental data (wind and wave data) based on hindcast data from an offshore site in the Northern North Sea from 2001 to 2010. Three representative load cases with a high probability of occurrence in the normal operating conditions are used.
3. The Kaimal turbulence model generates the three-dimensional turbulent wind fields, simulated using TurbSim. Time-varying irregular waves are generated using the JONSWAP (Joint North Sea Wave Project) spectrum according to the specified Hs and Tp.
4. Generate two-bending moments (blade one root flap wise bending moment - RootMyb1 and tower bottom fore-aft bending moment - TwrBsMyt) on the DTU 10MW FWT using the generated wind and wave spectra.
5. Generate and investigate how the extreme responses (MATLAB) is affected by the univariate and bivariate analysis to predict accurate responses.
6. Characterize the univariate ACER1D extreme response, phase space response; M1 vs M3, ACER2D fitted and compared against the Asymmetric and Gumbel logistic model, the design safe zone (dashed) due to bivariate analysis and the 50- and 100-year return period ACER1D response predictions.
7. Optimize the ACER model by investigating and optimizing to the relevant k values.

Paper III:

1. Characterizing the approach to better estimate the extreme load responses of a DTU 10-MW floating semi-submersible type wind turbine focusing for the ACER1D. The ACER1D results were then compared against the Gumbel model.
2. The generation of environmental data and wind field model similar to Paper II.
3. Generate the three-bending moment (blade one root flap wise bending moment - RootMyb1, main shaft tip up-down bending moment (LSSTipMys) and tower bottom fore-aft bending moment - TwrBsMyt) on the DTU 10MW FWT using the generated wind and wave spectra.
4. Generate and investigate how the extreme responses (MATLAB) is affected by the univariate analysis to predict accurate responses.
5. Characterize the univariate ACER1D extreme response, compared against the Gumbel distribution and optimizing the k-values for this ACER1D model.

1.9 Report Methodology

To better understand the various concepts in this thesis,

1. Literature reviews on other publications, thesis and projects were undertaken. The theories, concepts and equations related to the Turbines Model, Control Systems, FAST, ACER1D method and ACER2D method were understood. In addition, background studies on wind and turbine engineering were undertaken to understand better the TurbSim wind model and the mechanism behind the modelling codes in FAST.
2. Paper-I: The respective model parameter and simulation were prepared to stimulate each linear and turbulent wind profile according to each K_{BM} parameter. These simulations yielded results such as shaft bending moments, shaft rotational speed, and generator power, which were then used to evaluate the best K_{BM} value and the net reduction of bending moments when the rotational speed and generator power are minimized.
3. Paper-II: The respective model parameter and simulations were prepared to stimulate each linear and turbulent wind profile. These simulations yielded results such as blade one root flap wise bending moment and tower bottom fore-aft bending moment, which were then used to characterize the system's univariant and bivariant extreme value and then discussed.
4. Paper-III: The same steps were undertaken as Paper-II, but the moment for the main shaft tip up-down bending moment (LSSTipMys) was also evaluated. Eventually, the univariant extreme value prediction of ACER1D and Gumbel was characterized and discussed.

1.10 Report Organization

This report is organized in the following structure:

Chapter 1: - Introduction

- A brief introduction and synopsis of the background of the topic
- The organization of the report

Chapter 2: - Theory (Fundamentals Theory for Wind Energy Operations)

- Description of pertinent theories for wind energy operation like wind power, wind profiles, atmospheric stabilities, turbulence and turbulent models, wind coherence, is used to generate linear field or turbulent flow via Turbsim,

Chapter 3: - Wind Turbine Model

- Description of turbine engineering: the main turbine parts, blades properties and turbine power curve
- Description of the wind turbine models: NREL 5MW turbine and DTU 10MW turbine,
- Background information on the FAST framework

Chapter 4: - Paper-I: A novel compensation scheme for wind turbine controllers

- Methodology discussing selected wind turbines properties, wind model, cases studies selection, Simulink and the compensation scheme
- Results and discussion of the effect of the compensation scheme on the bending moment. rotational speed and generator power
- Conclusion of the paper

Chapter 5: - Paper-II: Extreme values analysis using ACER1D and ACER2D

- Methodology discussing selected wind turbines properties, load cases and environmental conditions, ACER1D and ACER2D studies
- Results and discussion of the ACER1D and ACER2D extreme values analysis and the reliability of ACER2D results against other models
- Conclusion of the paper

Chapter 5: - Paper-III: Extreme values analysis of Gumbel against ACER1D

- Methodology discussing selected wind turbines properties, load cases and environmental conditions, Gumbel and ACER1D studies

- Results and discussion of the Gumbel and ACER1D extreme values analysis and the reliability of ACER1D results
- Conclusion of the paper

Chapter 6: - Conclusion

- Overall conclusions from the analysis of this study
- Recommendations on further future investigations

Chapter 7: - Reference

Chapter 7: - Appendices

- Publications

2 Fundamentals Theory of Wind Energy

The following section of this thesis discusses the concept behind wind energy. Wind fields generated in this thesis were either laminar inflow wind or normal turbulent models, which are generated from MATLAB or TurbSim. The underlying concept of wind will be discussed in Sections 2.1 to 2.11. Sections 2.1 to 2.11 are the theocratical backgrounds used to generate the turbulent wind profile with TurbSim and are used in all three papers in this thesis.

2.1 Wind Power

The wind is converted into usable energy when it moves the blades linked to the turbines in the form of mechanical energy. The turbines then spin the electric generator to generate electricity. Wind power is environmentally friendly with a minimal carbon footprint with good sustainability. i.e.,25% of Denmark runs on the wind. The power generated is related to the wind characteristics (shear and turbulence), turbine properties (size, rotor, transmission system and generator), and the blade's sweep area. E.g., A larger rotor area can generate more energy. However, these properties are also limited since increasing this value will simultaneously increase the load excreted on the wind turbine system. The maximum power that can be generated by a wind turbine follows the equation (Manwell, 2010):

$$P = \frac{1}{2}\rho A U^3 \quad (1)$$

Where, ρ: density in air, A: rotor swept area, U: wind speed

In reality, it is not possible for all power from the wind to be converted into usable energy. Thus, the maximum power that can be converted is limited by a power coefficient:

$$P = C_p * \frac{1}{2}\rho A U^3 \quad (2)$$

Where, C_p: power coefficient

While it is also important to note the maximum theoretical power that can be extracted by a wind turbine is limited by the fraction 16/27. This fraction is commonly known as the Betz limit (Betz, 1926). The Betz limit differentiates the maximum power available in the wind and the amount of this power that is converted to usable power. As the formula above implies, the Betz limit indicates the maximum power that can be converted into usable energy from the wind in the atmosphere given 100% turbine efficiency. However, as 100% turbine efficiency is impossible, the real usable energy is further

dependent on the turbine efficiency after the Betz limit is applied. The efficiency of the wind turbine is influenced by wind shear, turbulence, and yaw misalignment (Micallef, 2016).

2.2 Atmosphere Layers

The atmosphere is a set of different layers made up of gases. It is held in place near the body surface by gravity. An atmosphere only forms if gravity is present and if its temperature is low. The atmosphere on Earth is surrounded by different layers known as Troposphere, Stratosphere, Mesosphere, and Thermosphere, with the Troposphere closest to the surface and the Thermosphere the furthest from the surface. The troposphere is the heaviest and the warmest of all layers due to its proximity to the surface. Its composition consists primarily of nitrogen (78%), oxygen (21%), carbon dioxide, and other gases. All wind turbines are located within this layer, and in greater relevance, extensive research and computer simulation are conducted with values from this layer.

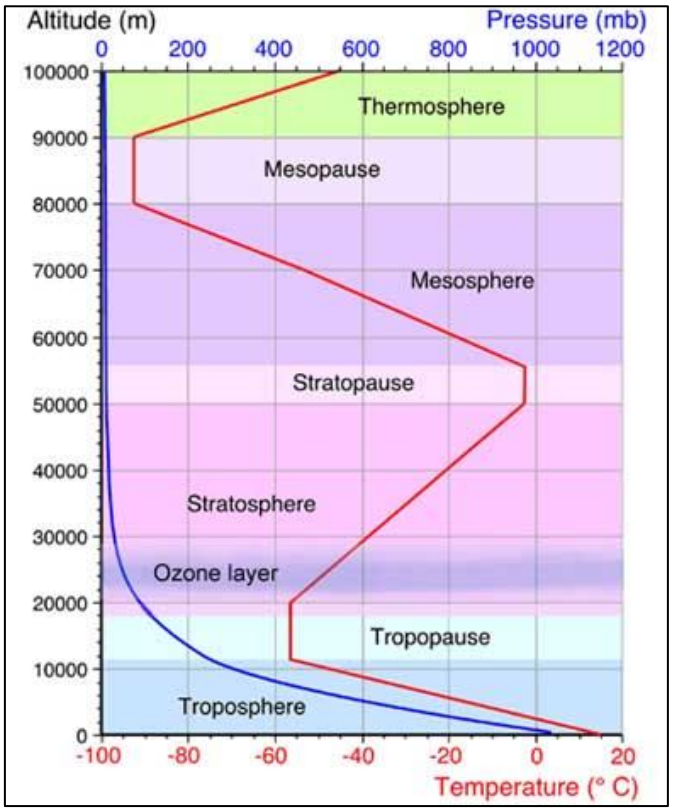

Figure 8 Atmosphere Layer and temperature gradient line (Pidwirny, 2006)

The troposphere can be further divided into the free atmosphere layer and a planetary boundary layer. The planetary boundary layer is then further subdivided into the Ekman Layer and the Surface Layer. The surface layer ranges between 50 to 200 meters depending on surface roughness values (Z_0) and the atmospheric stabilities. Z_0 is the height above the ground where the wind profile has a zero value

(Dyrbye, 1997). This elucidates that a higher Z_0 would indicate higher surface roughness and thus a longer boundary layer.

2.3 Wind Turbulence

In fluid dynamics, turbulence is the disturbance in fluid motion due to chaotic changes in the flow velocity or pressure (Burton, 2011). It is an uneven movement of air- particles that occur due to the presence of eddies and vertical currents. It is characterized by disordered variations in pressure and flow velocity. In the case of a wind turbine, wind turbulences affect wind energy in various ways, including the fatigue and wake effects, noise proliferation and the turbines' performances. Eddies develop because of the instabilities present in wind flow consisting mainly of kinetic energy (Kaimal, 1994).

Often insignificant at lower or laminar winds, it can be considerably different offshore, contributing to significant damage. Turbulence causes major fatigue damage on wind turbines because of the dissipation of kinetic energy into thermal energy due to eddies (Kaimal, 1994). Turbulence is concomitant with wind shear and thunderstorms, etc. Especially concerning wind, turbulences within the boundary layer emerge by shear friction or temperature. Apart from the commonly understood turbulence due to friction (mechanically generated), differences in air temperatures can contribute substantially to wind turbulence and is commonly called atmospheric stability. Turbulence is often denoted as the summation of mechanical-generated turbulence and buoyancy-generated turbulence.

2.4 Atmospheric Stability

The temperature of the air in the boundary layer affects atmospheric stability. A positive heat flux also results in a deeper boundary layer than a zero/negative heat flux (North, 2014). Atmospheric stability is categorized into three classes: stable, neutral, and unstable. These classes are labelled based on the propensity for the air particles to move on the vertical axis resulting in turbulence, often also known as “buoyancy-generated” turbulence. (Atmospheric Stability, 2019).

When the air particles are cooler than the atmospheric air, they remain in the same position or sink and are rendered stable. This results in lesser mixing and friction velocity; thus, there exists a steeper difference in the velocity gradient and a more significant velocity shear. A lower boundary later height is expected under this condition. The stable conditions’ turbulence is often known as “mechanically-generated” or “shear-produced” turbulence.

While when the air particles are warmer than the atmospheric air, they rise and are rendered unstable. This results in more mixing and friction velocity; thus, there exists a small difference in the velocity gradient and smaller velocity shear. Therefore, a lower boundary later height is expected under this condition. The stable conditions' turbulence is often known as "buoyancy-generated" turbulence. As the air particles are usually mixed vertically under unstable conditions, higher turbulent fluctuations and fatigue loads are prevalent, especially at offshore locations (Sathe, 2013). However, the stability conditions can vary largely according to the locations (Jonkman, 2019).

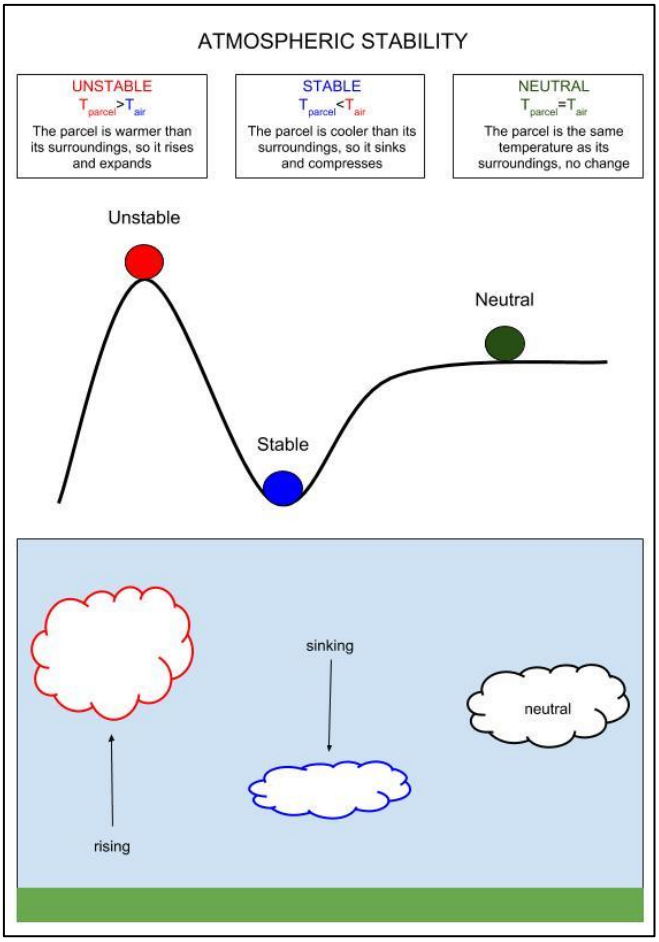

Figure 9 Atmospheric stability (University of Hawai)

The length scale of energy that characterizes the influence of shear friction to buoyancy ratio in relation to the vertical movement of air is known as Monin-Obukhov length (L) (Gasch, 2011) (Chougule, 2017). It describes atmospheric stabilities. The (L), is known as the height when the buoyancy begins to surpass the shear values in the turbulent energy (Monin & Obukhov, 1954):

$$L = -\frac{v_*^3}{k\frac{g}{T_o}\frac{q}{c_p\rho}} \qquad (3)$$

Where, $v*$: characteristic velocity scale, κ: von Karman constant = 0.40 ± 0.01, g: gravity, T_o: surface layer temperature, g/T_o: dimensional constant, $q/c_p\rho$: temperature flux, q is the heat flux

The sign that L takes varies with the heat flux (q) direction. Whenever q < 0 is negative in a stable condition, the L > 0 takes a positive value. The opposite is true when q > 0 is positive in an unstable condition, and the L< 0 takes a negative value (Monin & Obukhov, 1954).

The absolute value of the Monin-Obukhov length gives lesser information when studied alone, but when compared to the height above ground (z) becomes a good stability parameter. The z/L stability parameter, which is dimensionless, can reveal the importance of the different turbulence when there is a variation in height and stability conditions (Kaimal, 1994). Its ratios display the relationship between the mechanical/shear turbulence and the buoyancy turbulence.

As given in in (Kaimal, 1994), when solving L using the dimensionless stability:

$$\frac{Z}{L} = \frac{(g/\overline{\theta})(\overline{w'\theta'})_o}{(u_*^3/kz)} \quad (4)$$

Where, $\overline{\theta}$: mean potential temperature, $g/\overline{\theta}$: buoyancy parameter $(\overline{w'\theta'})_o$: temperature flux at the surface, u_*: Friction velocity, and k: constant of proportionality

The bulk Richardson number (R_b) can be used to estimate the atmospheric stability. The R_b value is determined according to L value, where R_b < 0 for an unstable condition.

The R_b is derived from the following equation:

$$R_b = \frac{(g/\overline{\theta})(\overline{\theta_z} - \overline{\theta_o})/2}{(\overline{u}_z/z)^2} \quad (5)$$

Where, $\overline{\theta_z}$; $\overline{\theta_o}$: mean potential temperatures at height z, $\overline{u}_z$: mean wind speed at height z

The Monin-Obukhov length can used to classify atmospheric stability. The atmospheric stability varies from very unstable to very stable according to the Monin-Obukhov length. It is per the atmospheric stability classes that are frequently used (Gryning et al., 2007).

Monin-Obukhov length(m)	Atmospheric Stability
$-100 \leq L \leq -50$	Very unstable
$-200 \leq L \leq -100$	Unstable
$-500 \leq L \leq -200$	Near unstable
$\lvert L \rvert \geq 500$	Neutral
$200 \leq L \leq 500$	Near stable
$50 \leq L \leq 200$	Stable
$10 \leq L \leq 50$	Very stable

Table 1 Stability Class for Atmospheric Layer (Gryning, Batchvarova et al. 2007)

2.5 Wind Profile

A wind profile is a relationship between wind speeds at a particular height and other heights. A vertical wind profile's gradient varies at different locations depending on the surface layer thickness. The surface layer thickness fluctuates with respect to the roughness length z_o. The two most functional approaches to predicting a wind speed profile are the power or logarithmic law approaches. The possible value of roughness length z_o, which greatly influences wind speed profile on different surfaces, is displayed in the table below (Knight, 2019 and Dyrbye, 1997).

Roughness Length, z_o (m)	Terrain Type
10^{-5}	Plane ice
10^{-4}	Open sea, no waves
10^{-3}	Coastal area, onshore wind
0,01	Open land with little vegetation and few houses
0,05	Agricultural area with few houses and wind-breaks
0,3	Village and agricultural areas with lots of wind breaks
1 to 10	Urban areas

Table 2 Surface layer thickness with respect to the roughness length

Wind profile can vary differently offshore as compared to onshore. Wind speed significantly affects the power output as it is proportional to the cube of the wind speed. The marine atmospheric boundary layer (MABL) is in direct contact with the water surface of the ocean. Therefore, it is impacted by and transfer of mass, momentum and energy from the water to itself (Kaimal, 1994).

The planetary boundary layer (varies from 50 to 200 m) has constant vertical shearing stress. Thus, the wind profile at this layer is usually influenced by surface friction and atmospheric stability (vertical temperature gradients) (Kaimal , 1994). Above this layer, the Ekman layer, wind profiles are influenced more heavily by the variable shear stress resulting from the earth's rotation. In addition, the surface friction and atmospheric stability (vertical temperature gradients) also contribute to these layers' wind profile.

The Monin-Obukhov similarity theory has been able to successfully predict many wind speed profiles in the boundary layer (Monin and Obukhov, 1954). However, discrepancies identified offshore at levels as low as about 30m above sea levels indicated its unreliability in using this wind profile offshore (Peña et al., 2008). This is a significant problem when designing wind turbines offshore, as most offshore turbines are intended to be at a height ranging above 30. However, to mitigate the problems better newer technologies has aided the collection of more reliable data from offshore, and it has shortened this gap and helped identify a more reliable wind profiles (Peña, 2008; Cheynet, 2018a).

2.6 Power Law Wind Profile

The power law is comparing the wind speeds at one height against another. This law is mainly used under neutral atmospheric conditions. The power coefficient (α) determines the vertical shear gradient and the eventual shape of the wind profile. However, the power coefficient cannot fully compensate for the different atmospheric stability effects and thus is usually not used in the other cases. Instead, different power coefficient is used in different terrain. The formula associated with this wind profile is as follows:

$$U(Z) = U_{ref}\left(\frac{Z}{Z_{ref}}\right)^{\alpha} \quad (6)$$

Z_{ref}: reference height, U_{ref}: mean wind velocity at z_{ref}, z: height considered, α: power-law or empirical wind shear exponent,

2.7 Logarithmic Wind Speed Profile

The logarithmic wind speed profile is a semi-empirical equation often used to define the vertical distribution of horizontal wind speeds. It is also widely used because it is able to better compensate for the

differences in atmospheric stability by inputting a correlation factor. The logarithmic wind speed profile is also recommended in the (DNV-RP-C205, 2010) handbook. The neutral atmospheric version of the equation with mean speed at height z is as follows:

$$U(Z) = \left(\frac{u_*}{k}\right) ln\left(\frac{z}{z_0}\right) \quad (7)$$

u_*: friction velocity, κ: von Kármán constant = 0.4, z: height considered, z_o: roughness length

Using a reference wind speed and height, the equation can be simplified to:

$$U(Z) = U_{ref} \frac{\ln\left(z \,/\, z_o\right)}{\ln\left(z_{ref} \,/\, z_o\right)} \quad (8)$$

Where, $zref$: reference height, U_{ref}: mean wind velocity at z_{ref}, z: height considered, z_o: roughness length

2.8 Turbulence Spectra Models

Wind turbulence can be described in terms of turbulence intensity (TI). TI measures the fluctuation of wind speed about its mean value. Wind turbulence can come in all three directions and is named in respect to their respective wind directions. Even though the longitudinal wind contributes is the most significant, the lateral (cross-wind) and vertical wind should also be computed to ensure that the wind turbine response and movement are fully understood (Eliassen and Obhrai, 2016; Knight, 2019). The TI at a particular height (z) is the ratio of the standard deviation (σ) and mean of the wind velocity (U), which is represented in the longitudinal, lateral, and vertical directions, respectively:

$$I_u(z) = \frac{\sigma_u(z)}{U(z)} \; (Eq.9)$$

$$I_v(z) = \frac{\sigma_v(z)}{U(z)} \; (Eq.10) \quad (9)$$

$$I_w(z) = \frac{\sigma_w(z)}{U(z)} \; (Eq.11)$$

2.9 Kaimal Spectra Model

Kaimal Horizontal Spectra Model can be sub-divided into three parts. It is made up of a low-frequency boundary layer height, a high-frequency distance above the ground, and an intermediate range that is an interpolation of both the high and low-frequency ranges. The Kaimal Spectra Model has been

identified to correctly define the surface layer's energy content for turbulent wind for neutral stability conditions (ranging between 0.01 Hz - 4 Hz) (Knight, 2019).

The Kaimal Spectra used in most engineering applications are (Kaimal, 1972):

$$\frac{nS_u}{u_*^2} = \frac{105f}{(1+33f)^{5/3}}$$
$$\frac{nS_v}{u_*^2} = \frac{105f}{(1+33f)^{5/3}} \quad (10)$$
$$\frac{nS_w}{u_*^2} = \frac{105f}{(1+33f)^{5/3}}$$

Where, n: frequency in Hertz, S_u, S_v, S_w: velocity spectra in the along, cross, and vertical wind respectively, u_*: friction velocity

2.10 Coherence

The wind particles on a different horizontal or vertical plane are not totally independent from one another. They influence each other naturally or reasonably. There are correlated with one another through a frequency domain. This coherence between them is determined by the separation distance between the particles, the mean wind speed, and the frequency. Particles influence each other with more intensity as their distance between one another decreases, while their coherence decreases exponentially with frequency. Numerous projects have been undertaken to study and understand the correlation between the wind speed and the temperature of the particles (Panofsky, 1965; Knight, 2019).

The coherence between two different air particles is the normalized cross-spectrum of the particles' turbulent velocities. These values are made up of real and imaginary numbers, where the real number is officially known as co-coherence, and the imaginary number is known as quad-coherence. Different literature defines these differently, but in many works, the real number (co-coherence) is referred to as coherence. For example, the magnitude square of the cross-spectrum is defined in (Højstrup, 1999):

$$\gamma(n) = \sqrt{\frac{Co^2(n)+Q^2(n)}{s_1(n)s_2(n)}} \quad (11)$$

Where, n: frequency in Hz Co: co-spectrum density of the cross-spectrum. Q: quadrature spectrum density of the cross-spectrum, $s_1(n) and\ s_2(n)$: spectral densities of the velocity components

3 Fundamentals Theory of Wind Turbine Model

In Section 3.1.1, the wind turbine's primary components and its model are discussed. These include the turbines' basic structures and the energy generation method. Then, in Sections 3.2 and 3.3, the primary models (NREL 5MW and DTU 10MW) used in this thesis will be introduced in detail. Furthermore, the floating structure (LIFES50+ OO-Star Wind Floater semi-submersible floating structure) used in Paper-II and III will also be discussed in Section 3.3.2.

In Paper-I, the NREL 5MW wind turbine is used as it has been more reliable and tested over a more extended period, thus making it more suited for control system testing. While in Paper-II and -III, the DTU 10MW wind turbine is used as it produces more relevant results and is applicable for future larger turbine designs.

3.1 Wind Turbine Engineering

A wind turbine is an apparatus that converts the kinetic energy into the wind into mechanical energy and electric energy. The wind that passes over the blade forces the blades to move due to differences in pressure in accordance with aerodynamics (Figure 13). As a result, the shaft connected to the blades rotates, resulting in the eventual rotation of the generator. The generator produces the electricity which is then converted into an appropriate voltage to be transmitted via an electric grid (Figure 10).

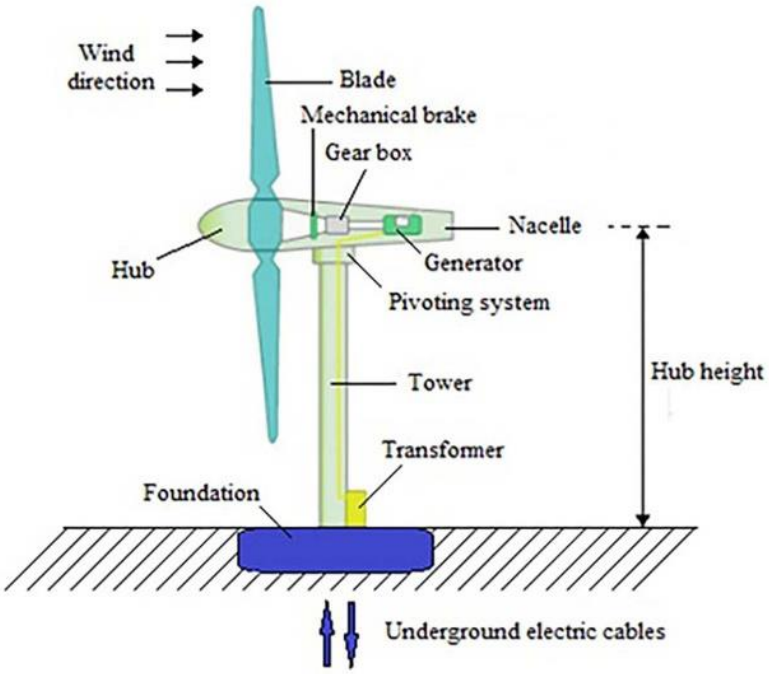

Figure 10 Wind Turbine Components Diagram (Creative Commons)

Wind turbines are usually optimized to function best at a particular speed as they usually lose their efficacy when the speed is too fast or slow. The wind turbines are built with the ability to shut off at

high speed, ranging above 25 km/h, (cut-out speed) as they can be easily damaged at higher speeds. Also, the modern wind turbine is installed with a small motor that allows it to pivot itself in the direction to maximize its ability to generate energy at all times.

The function of wind turbines can vary according to their needs. The smaller turbines can be used to charge batteries or power traffic signs on highways. In comparison, bigger turbines can be used to generate energy for household consumption as the electric energy is directly injected into the power grid lines. Wind turbines lined up together are commonly known as wind farms and are becoming an important source of energy in several counties. Many countries today attempt to reduce their dependence on fossil fuels by shifting their focus to renewable sources.

3.1.1 Wind Turbine Components

A wind turbine diagram with its primary parts can be seen in Figure 11, IEC 61400-3. The figure includes the foundation attached with the substructure, the tower, and the rotor-nacelle assembly. The rotor-nacelle assembly is made up of numerous sub structure such as the nacelle, hub and blade forming the powerhouse of the wind turbine. An onshore wind turbine will have its own support structure attached to the tower (e.g., Lattice or tubular tower foundation), and an offshore wind turbine will have its tower supported by various substructure (e.g., gravity-based, monopile, jacket, etc.) possibly attached to a mooring line (Putri, 2016).

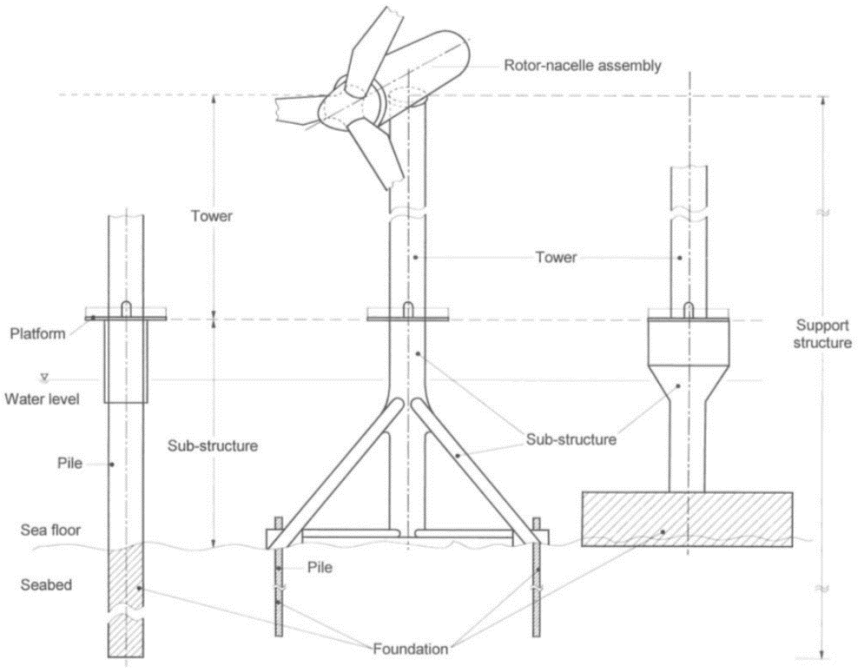

Figure 11 Definition of an offshore wind turbine (IEC, 2009)

The nacelle is made up of the drivetrain, control system, generator, and blade-pitch regulator. The kinetic energy generated through the blade movement is converted into electrical energy in the

generator. Kinetic energy is transferred from the blade, shaft, drivetrain and eventually to the generators. Blade-pitch regulator helps control the speed of the rotation at above-rated speeds, while the yaw bearing ensures the nacelle always faces the incoming wind (Putri, 2016).

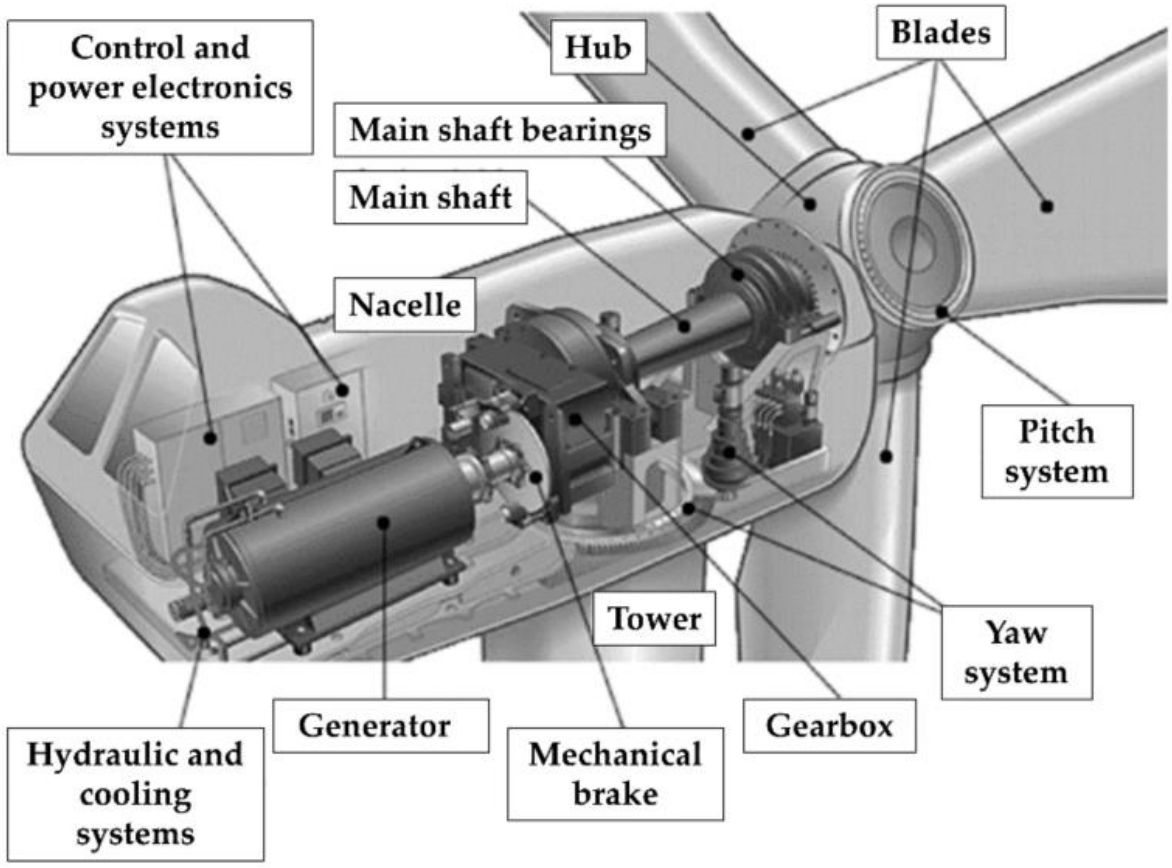

Figure 12 Rotor-nacelle assembly anatomy of a wind turbine (Ayee et al., 2009)

3.1.2 Blade Properties and Operation

Blades' structure is the fundamental structure that captures wind energy and converts it into kinetic energy. The blade is made up of the leading edge (thickest part) and the trailing edge (thinnest part), and the line connecting the leading edge to the trailing edge is called the chord line (Putri, 2016).

The wind speed that reaches the head of the hub/ turbine (V_2) is not the same as the free undisturbed wind speed (V_1). It gets reduced by the factor of ($1-a$). a is the induction factor, which is the factor due to the change of wind speed with the presence of the blades, and it acts relative to incoming wind speed. However, the blade/ aero foil experiences V_{rel} instead of V_2. V_{rel} is defined by the following formula and is illustrated in Figure 13,

$$\mathrm{V_{rel}} = \sqrt{{V_2}^2 + {V_r}^2} \quad (12)$$

Where $V2$ is the reduced wind speed and Vr is the rotor speed, V_{rel} create four different forces (lift, drag, thrust and moment force) due to the impact on the blades. The angle of attack (α) determines the results of maximum lift (F_L), and this maximum lift affects and results in the output power. (F_L: lift force, FD: drag force, FT: thrust force and FM: moment force).

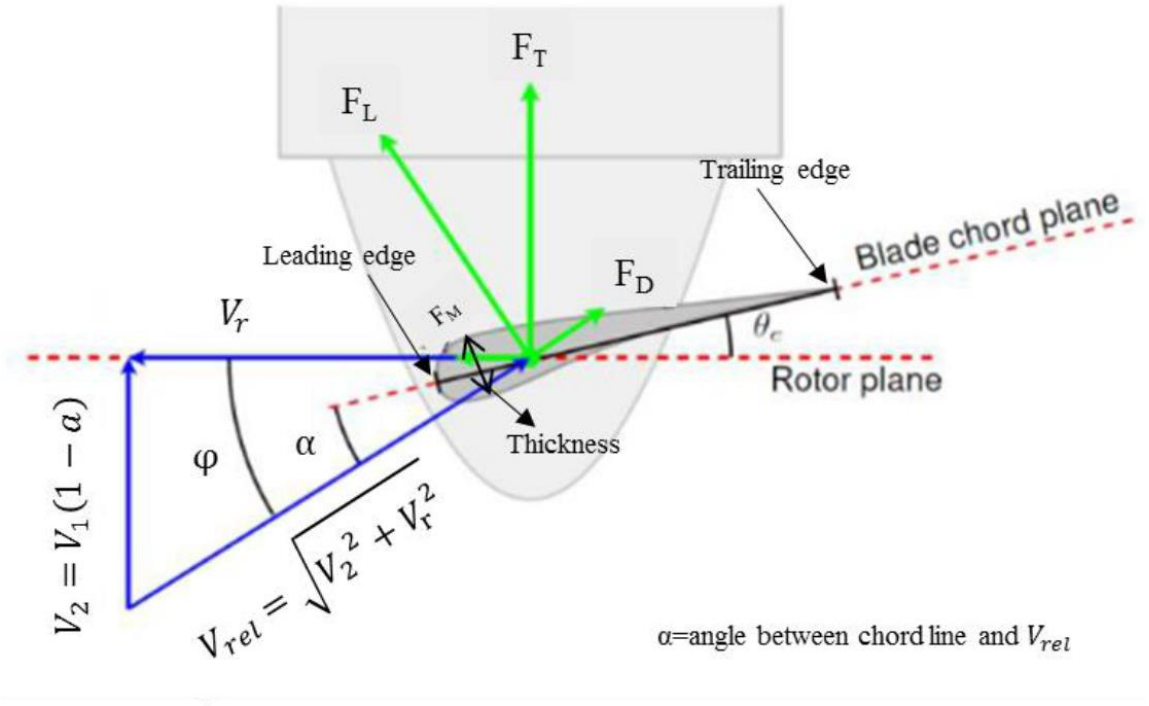

Figure 13 Aerofoil 2D Diagram (DTU, 2016)

The tip speed ratio (TSR) is a critical parameter when determining the power generated by a turbine and is the ratio of the V_{tip} (rotational speed of the blade tip) and V_2. THE TSR is governed by the following equation:

$$\mathrm{TSR} = \frac{V_{tip}}{V_2} = \frac{V_r}{V_1(1-a)} \quad (13)$$

The blade rotational speed and the angle of attack must be maintained to ensure that power generation is optimized, and this can be done by maintaining the TSR. According to previous studies, the optimal value of TSR is between 6 and 8 (Wilson, 1974).

3.1.3 Wind Turbine Power Curve

A wind turbine power curve can be divided into four main operating regions (with three cut-off regions: cut-in, rated and cut-out wind speed). Each of these four regions requires different control strategies. Before the cut-in region, the wind turbine is non-operational, and the wind is helping the blades or the system to start up. After the cut in speed starts to produce power and rises until it reaches rated power at the rated wind speed. After this point, the turbines continue to function at the rated wind speed until it reaches the cut-off wind speed, leading to a turbine shutdown. The visual description of each region is shown in Figure 14. While in, Table 3 (DTU, 2016) has further subdivided the regions to explain the processes and the procedure of the turbines and control system in a descriptive manner.

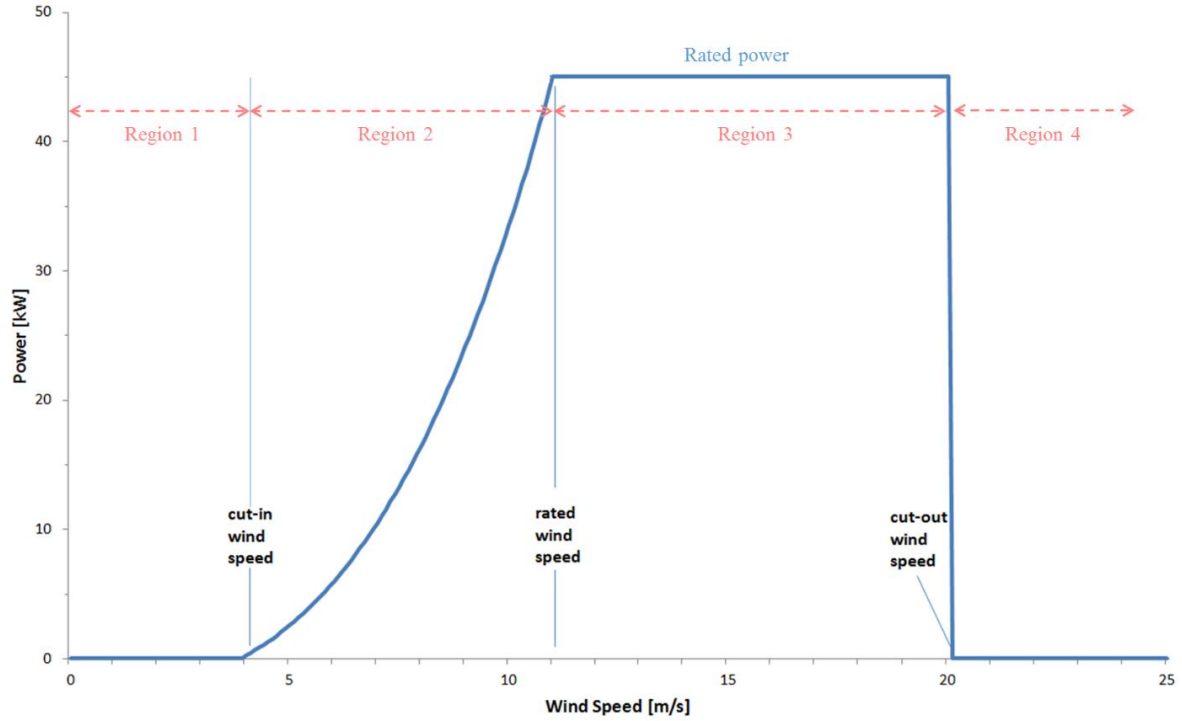

Figure 14 Classical Power Generation Curve (STFC, 2016)

Region	Description
Region 1	In this region, there is no power extraction due to the low wind speed
Region 2	At below-rated wind, generator torque optimizes its function for power generation. Pitch angel is fixed to capture a maximum lift
Region 2A	Constant rotor speed, changing generator torque with constant pitch angle
Region 2B	Increasing rotor speed to maximize power capture, changing generator torque to optimize TSR with constant pitch angle
Region 2C	Constant rotor speed, as wind speed approaches rated speed, changing torque as wind speed increases until power production reaches rated power as constant pitch angle is maintained
Region 3	Wind speed crosses the above rated speed, and the generator torque remains unaffected and constant and now pitch angel is adjusted to reduce the load on the rotor
Region 4	Turbines switch off as there is no power generated. Turbines and blades switch off and set to feather conditions to prevent any damages
Region 4	Turbines switch off as there is no power generated. Turbines and blades switch off and set to feather conditions to prevent any damages

Table 3 Power Region Definition

3.2 NREL 5-MW Reference Turbine

NREL 5-MW RWT used in Paper I, focused on modifying the control systems. The NREL 5-MW RWT was used with changes made to the control system model.

The NREL 5-MW Reference Turbine is one of the most well-established RWTs that was established in 2015 using data from industrial turbines and RWTs (Jonkman, 2009). Research institutes and universities have commonly used the open-source designs of NREL 5-MW to understand better and develop the RWTs. The DTU 10-MW RWTs is another commonly used open-source design RWT used for research and was designed using NREL 5-MW as a reference (Muggiasca, 2021).

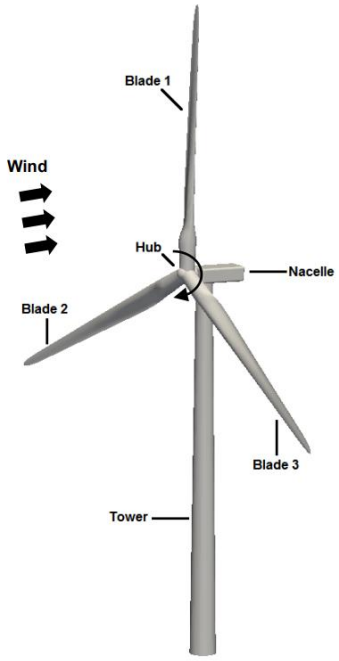

Figure 15 NREL 5-MW Reference Turbine Diagram (Liu, 2017)

Similarly, this thesis uses the NREL 5 MW reference turbine (Jonkman, 2019) as the study object. It is a three-bladed, variable pitch-to-feather bladed, upwind, and variable-speed controlled megawatt wind turbine developed to study wind technology concepts. The method used in this thesis aims to reduce the non-torque bending moment in the turbine's low-speed shaft. Reduction in the non-torque bending moment is also expected to reduce the loads acting on the gearboxes. The algorithm used in the control systems is performed using the Simulink/FAST framework (Jonkman, 2005) and is presented in Paper-I in this thesis.

Parameter	Value
Rating	5 MW
Rotor Orientation, Configuration	Upwind, 3 Blades
Control	Variable Speed, Collective Pitch
Drivetrain	High Speed, Multiple-Stage Gearbox
Rotor, Hub Diameter	126 m, 3 m
Hub Height	90 m
Cut-In, Rated, Cut-Out Wind Speed	3 m/s, 11.4 m/s, 25 m/s
Cut-In, Rated Rotor Speed	6.9 rpm, 12.1 rpm
Rated Tip Speed	80 m/s
Rotor Mass	110,000 kg

Nacelle Mass	240,000 kg
Tower Mass	347,460 kg

Table 4 Main Properties Chosen for the NREL 5-MW Wind Turbine

This project uses the Wind-Plant Integrated System Design and Engineering Model (WISDEM) (IEA Wind: 16) codeveloped by NREL and DTU (Bortolotti, 2019). The WISDEM toolkit is an open-source toolkit used for the multidisciplinary design, analysis and optimization (MDAO), aerodynamics, aeroelastic analysis, loads analysis, controls system analysis, etc (Bortolotti, 2019;).

This project also uses the Multidisciplinary Horizontal Axis Wind Turbine Optimization Tool (HAWTOpt2) which was developed by DTU (Zahle, 2017). This tool is used to analyse codes which predict the wind turbine's structural properties and aeroelastic response. When predicating the turbine's structural properties BECAS (Blasques, 2012; Bortolotti, 2019) works together with HAWTOpt2. While for the aeroelastic analysis, both the HAWC2 (Larsen, 2014) and HAWCStab2 (Hansen, 2004) are needed, and it works together with HAWTOpt2.

NREL used the WISDEM framework when designing the drivetrain. DriveSE was used to size the load-bearing components in the drivetrain (Guo, 2015), while GeneratorSE was used to design the generators (Bortolotti, 2019; Sethuraman, 2017).

3.2.1 NREL 5-MW Drivetrain

Wind turbines' drivetrain comprises the gearbox and the generator, see Figure 16 NREL 5-MW Drive Train (NREL) . It is primarily the main component of a wind turbine that converts kinetic energy into electrical energy. The gearbox aids in the initial process by connecting the low-speed shaft (via blades and the hub) to the high-speed shaft connected to the generator. The high-speed shaft then rotates the coil/magnet to produce electricity in the generator. The main properties of the drivetrain used in the NREL 5MW RWT are described in *Table 5*.

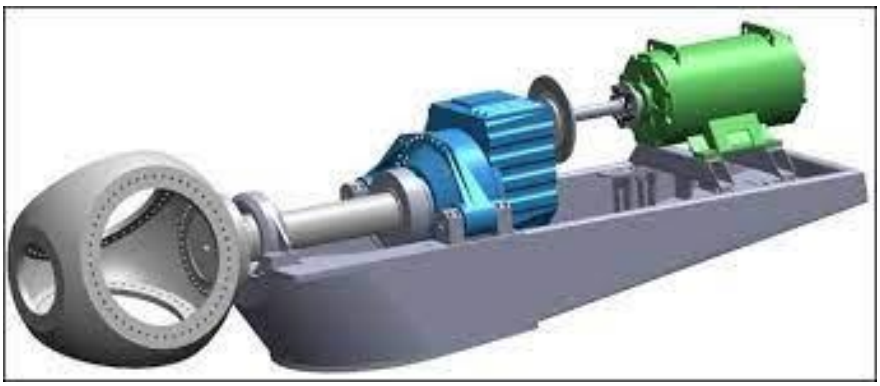

Figure 16 NREL 5-MW Drive Train (NREL)

Parameter	Value
Rated Rotor Speed	12.1 rpm
Rated Generator Speed	1173.7 rpm
Gearbox Ratio	97:1
Electrical Generator Efficiency	94.4 %
Generator Inertia about High-Speed Shaft	534.116 kgm^2
Equivalent Drive-Shaft Torsional-Spring Constant	867,637,000 Nm/rad
Equivalent Drive-Shaft Torsional-Damping Constant	6,215,000 Nm/(rad/s)
Fully Deployed High-Speed Shaft Brake Torque	28,116.2 Nm
High-Speed Shaft Brake Time Constant	0.6 s

Table 5 Drivetrain properties - NREL 5MW Wind Turbine (Jonkman, 2009)

3.2.2 NREL 5-MW Control Systems

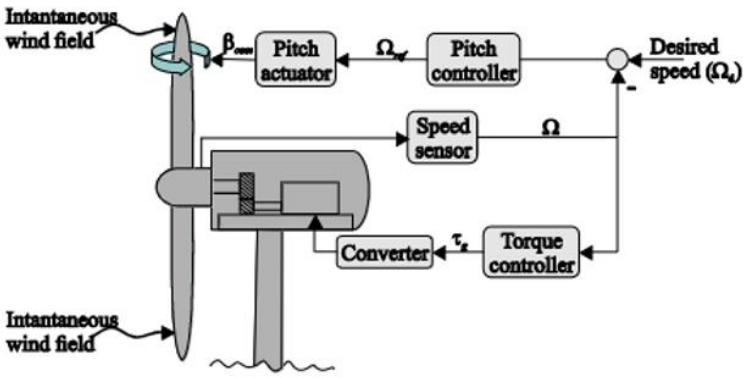

Figure 17 Overview of Control Systems (Njiri, 2016)

Modern controllers (Figure 17) in a wind turbine can simultaneously handle multiple operations, e.g., the rotational speed, the generator speed, its voltage, current and how it responds to the wind turbine components. In modern times, improved and advanced control systems have been a primary reason for the increase in turbine efficiency. Such systems have increased energy production & reliability and reduced platform movement & structural loads. The baseline controller in the NREL 5 MW reference turbine entails both a generator-torque controller and a rotor-collective blade-pitch controller. The

baseline controller, as in Figure 18 is meant to control the rotational speed by receiving feedback from the system and adjusting the pitch angle of the blade according, thus allowing the system to optimize its efficiency (Jonkman, 2009). The NREL 5MW Baseline Control System Properties are described in *Table 6*.

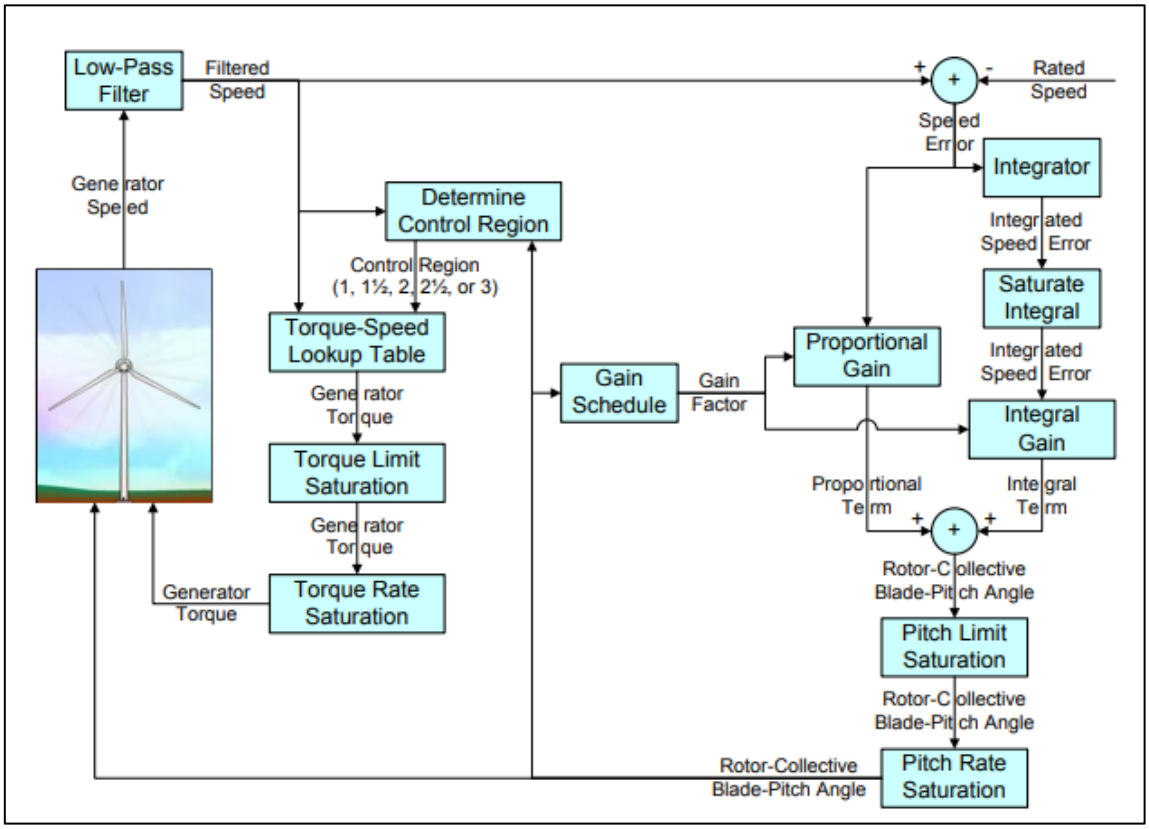

Figure 18 NREL 5MW Control System Flowchart (Jonkman. 2009)

Parameter	Value
Corner Frequency of Generator-Speed Low-Pass Filter	0.25 Hz
Peak Power Coefficient	0.482
Tip-Speed Ratio at Peak Power Coefficient	7.55
Rotor-Collective Blade-Pitch Angle at Peak Power Coefficient	0.0 º
Generator-Torque Constant in Region 2	0.0255764 Nm/rpm^2
Rated Mechanical Power	5.296610 MW
Rated Generator Torque	43,093.55 Nm
Transitional Generator Speed between Regions 2½ and 3	1,161.963 rpm
Generator Slip Percentage in Region 2½	10 %
Minimum Blade Pitch for Ensuring Region 3 Torque	1 º
Maximum Generator Torque	47,402.91 Nm
Maximum Generator Torque Rate	15,000 Nm/s

Proportional Gain at Minimum Blade-Pitch Setting	0.01882681 s
Integral Gain at Minimum Blade-Pitch Setting	0.008068634
Minimum Blade-Pitch Setting	0 º
Maximum Blade-Pitch Setting	90 º
Maximum Absolute Blade Pitch Rate	8 º/s

Table 6 NREL 5MW Baseline Control System Properties (Jonkman, 2009)

The generator torque controller functions in five different regions (1, 1½, 2, 2½ and 3), as seen in Figure 19. The NREL generator torque controller functioning principles are like the explanation given in Table 3. Furthermore, Region 1½ ensure a smooth linear transformation or shift between regions 1 and 2 and is known as the start-up region for the rotor. Similarly, region 2½ ensures a smooth linear transformation or shift between regions 2 and 3 at the rated power to minimize the tip speed and noise emissions (Slot, 2018; Jonkman 2007).

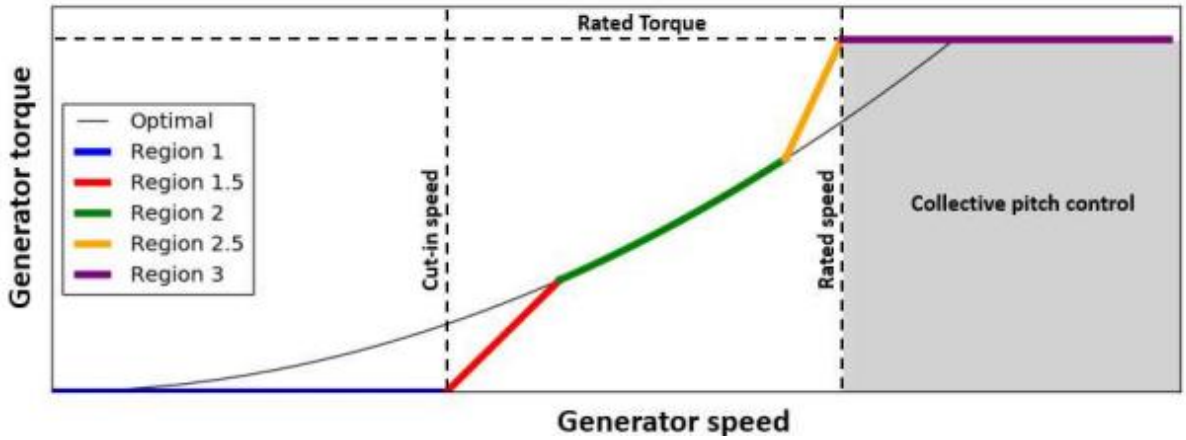

Figure 19 NREL 5ME Power Generation Graph (Slot, 2018)

3.2.3 Baseline Generator-Torque Controller

At speeds larger than the cut-in speed but smaller than the rated speed, the generator torque controller is activated to ensure that the generator power is maximized. Such an operation is accomplished by ensuring that the turbine is operated close to the optimal power efficiency by accelerating or decelerating the turbine's rotor to ensure that the tip-speed ratio remains constant. Whenever this ratio is optimized, the turbine can achieve maximum power. The blades' pitch angle is also fixed to generate maximum lift. The following equation governs the general controller.

$$\tau_g = K_T \Omega^2 \qquad (14)$$

where K_T is,

$$K_T = \frac{1}{2}\rho\pi R^5 \frac{C_{Pmax}(\beta_{opt}, \lambda)}{\lambda^3} \quad (15)$$

Where the λ is the optimum tip-speed-ratio at the C_{Pmax}.

$$J_R\dot{\Omega} = \tau_{aero} - \tau_g \quad (16)$$

Where: τ_g: Demanded generated torque, ρ: Air density, R: Rotor radius, λ is the optimum tip-speed ratio at the C_{Pmax}, C_{Pmax}: Maximum power coefficient ,Ω: Rotor speed ,β_{opt}: Optimum pitch angle ,τ_{aero}: Aerodynamic torque

Thus, when the τ_g is equal the τ_{aero} the generator remains constant, otherwise it will either accelerate or decelerates to achieve a steady state condition (constant tip-speed-ratio).

3.2.4 Baseline collective pitch control

While in region III, the primary aim is to ensure that the generated power and loads are controlled to prevent mechanical and electrical damage to the turbine. In a conventional setting, this is achieved by maintaining generator torque and activating collective pitch control to control the generator's speed. Collective pitch control is achieved through a proportional–integral- derivative (PID) controller, which controls the speed in region III (above-rated speed).

$$\beta_c(t) = K_p\Omega_e(t) + K_i\int_0^t \Omega_e(\tau)d\tau \quad (17)$$

Where: $\Omega_e = \Omega_d - \Omega$: Rotor speed error, Ω_d: Desired rotor speed, K_p: proportional gain, K_i: integral gain

The major downside of such a control method is that all the blades in the wind turbines are expected to be alike with similar properties. It is assumed that they all experience the same load during operation. In reality they experience unequal loading which results in unbalanced controls which results in induced stressing acting on the rotor disc.

3.3 DTU 10-MW FWT and LIFES50+ OO-Star Wind Floater

The DTU 10-MW reference wind turbine (RWT) (Bak, 2013) used in this thesis is designed from the NREL 5-MW RWT (Muggiasca, 2021). The operation ideology is similar to the NREL 5-MW RWT and thus will not be repeated in this section. Furthermore, the DTU 10-MW RWT used in Paper II and Paper III focused on finding the extreme value for the loads using a statistical model. The regular DTU 10-MW RWT was used with minimal changes to the actual model.

Instead, this section will expound on both the design of the DTU 10-MW RWT system and the OO-Star Semi-submersible Wind Floater. An overview of the figure used in this thesis is shown in Figure 1. In

the first part, the DTU 10-MW RWT system will be explained, which then will be followed by the description of the properties of the semi-submersible floater and the mooring system. Combined, these two systems become the DTU 10-MW Floating Wind Turbine (FWT) system.

3.3.1 DTU 10-MW RWT

Figure 20 The LIFES50+ OO-Star Wind Floater Semi 10MW structure 10-MW OO-Star floating wind turbine (Yu, 2017)

The DTU 10-MW RWT system was made according to the standards established by the International Electrotechnical Commission (IEC) Class 1A wind regime and consists of a traditional three-bladed, clockwise rotation-upwind turbine equipped with a variable speed and collective pitch control system. The DTU 10-MW RWT numerical model has been successfully developed and studied in many academic works e.g. (Muggiasca, 2021; Yu, 2022; Wang, 2022; Hu, 2021). The summary of the DTU 10-MW RWT is shown in Table 1.

Parameter	Value
Rating	10-MW
Type	Upwind/3 blades
Control	Variable speed, collective pitch

Drivetrain	Medium-speed, multiple stage gearbox
Cut-in, rated and cut-out wind speed (m/s)	4, 11.4, 25
Minimum and maximum rotor speed (rpm)	6.0, 9.6
Maximum generator speed (rpm)	480
Rotor diameter (m)	178.3
Hub height (m)	119.0
Rotor mass (kg)	227962
Nacelle mass (kg)	446036
Tower mass (kg)	1.257×10^6

Table 7 Main parameters of the DTU 10-MW RWT (Bak, 2013)

3.3.2 LIFES50+ OO-Star Wind Floater semi-submersible floating structure system

The DTU 10-MW RWT is supported using a semi-submersible floating structure announced in the LIFES 50+ project (Yu, 2017). The floater consists of a central column and three outer columns (post-tensioned concrete) attached to a star-shaped pontoon with the slab attached at the bottom. Three mooring lines (each line had a clumped mass close to the middle that separates the line into two different sections) help hold the floater in position. Detailed properties and images of the OO-Star Wind Floater attached to the mooring system can be seen in Figure 21, Figure 22, Table 8 and Table 9, respectively.

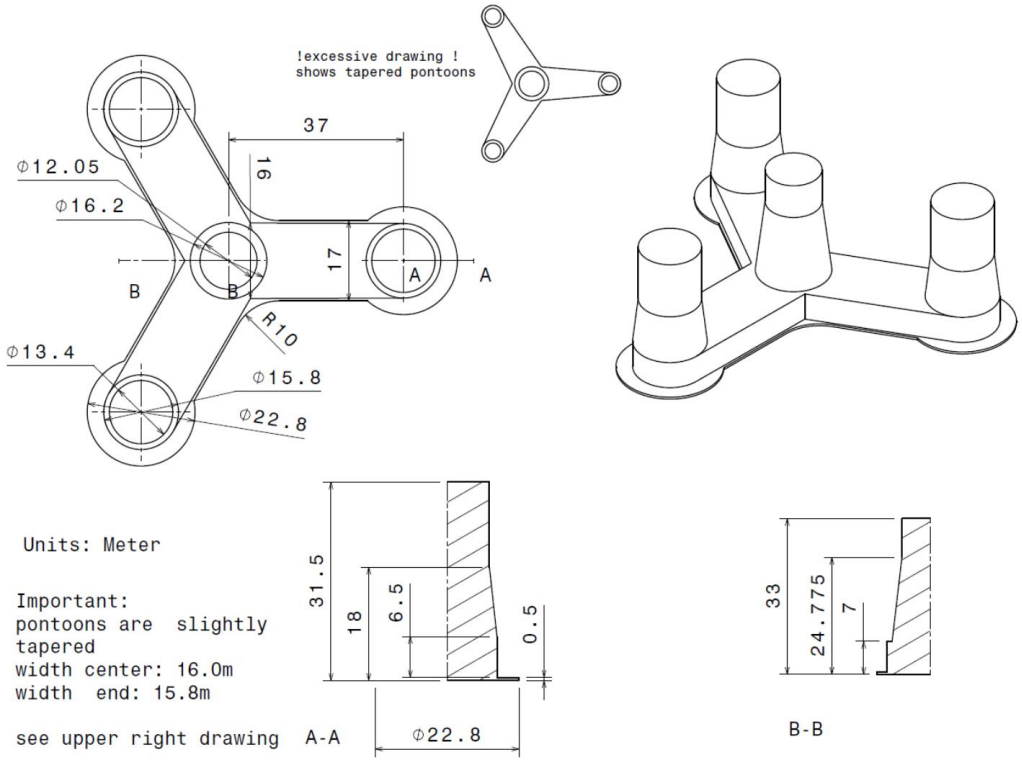

Figure 21 Main dimensions of the OO-Star floater of the LIFES50+ OO-Star Wind Floater Semi 10MW structure (Yu, 2017)

Parameter	Value
Water depth (m)	130
Draft (m)	22
Tower-base interface above mean sea level (m)	11
Displacement (kg)	24158
Overall gravity, including ballast (kg)	21709
Roll and pitch inertia about center of gravity (kg·m^2)	1.4462 x 10^{10}
Yaw inertia about centre of gravity (kg·m^2)	1.63 x 10^{10}
Centre of gravity height below mean sea level (m)	15.23
Centre of buoyancy height below mean sea level (m)	14.236

Table 8 Main properties for the LIFES50+ OO-Star Wind Floater Semi 10MW structure wind floater (Yu, 2017)

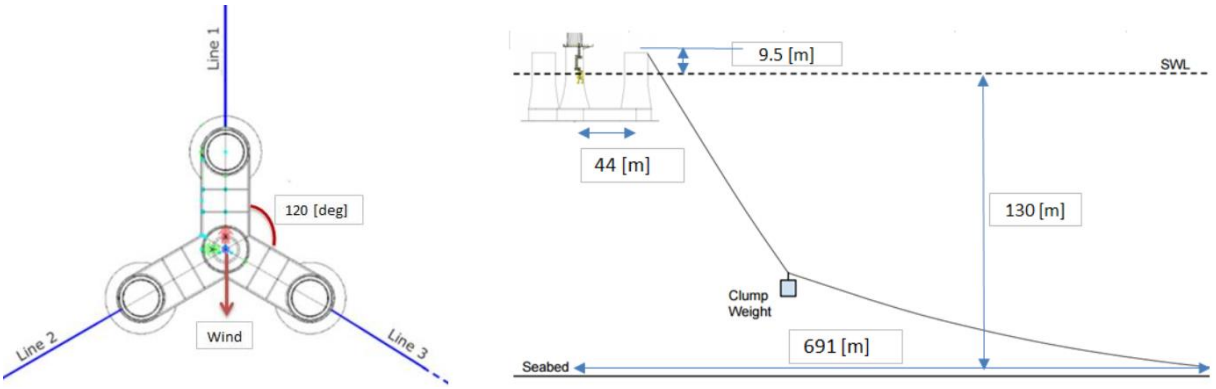

Figure 22 Sketch of the mooring system in the LIFES50+ OO-Star Wind Floater Semi 10MW structure (left: top view; right: side view) (Yu, 2017)

Parameter	Value
Radius to anchors from platform centreline (m)	691
Anchor position below MSL (m)	130
Initial vertical position of clump mass below MSL (m)	90.45
Initial radius to clump mass from centerline (m)	148.6
Length of clump mass upper segment (kg)	118
Length of clump mass lower segment (kg)	585
Equivalent weight per length in water (N/m)	3200.6
Extensional stiffness (N/m)	1.506×10^9

Table 9 Main properties for the mooring system of the LIFES50+ OO-Star Wind Floater Semi 10MW structure (Yu, 2017)

3.3.3 FAST (Fatigue, Aerodynamics, Structures and Turbulence) Framework

In this thesis, the control system algorithm is executed in the FAST framework in a structure that uses previously implemented models to improve and enhance its control capability (Jonkman, 2009; Sarkar, 2021; Vlase, 2020). The FAST software is tied in with the NREL's software-based for the 5-MW Reference Onshore Wind Turbine Development (Sarkar, 2021; Vlase, 2020). Similarly, it is applied in this thesis to obtain the load results for the coupled aero-hydro-elastic-servo dynamic analysis for the DTU 10-MW FWT. FAST is an open-source engineering toolbox that allows us to explore the load study of an onshore wind turbine. It is a computer-aided engineering (CAE) tool that is a comprehensive aeroelastic simulator which can be run within MATLAB. FAST prognosticates the extreme and fatigue

loads acting on the horizontal-axis (2-3 bladed) turbine. The code mimics a turbine as a fusion of rigid and flexible bodies with the hydrodynamic loads considered as a point on the bodies. Thus, the CAE estimates the response on the substructures. For example, a teetering-hub turbine is modelled as a rigid, four-by-four, flexible body. The blades, tower, and drive shaft make up the flexible bodies, while the earth, nacelle, hub, and tip brakes form the rigid bodies. The model connects themselves with varying amounts and degrees of freedom, which can be activated within the input data files (Jonkman, 2007; Sarkar, 2021; Vlase, 2020).

Different computational codes AeroDyn, HydroDyn, ServoDyn, and MoorDyn are used in FAST to generate results (Moriarty, 2005; Hall, 2015; Jonkman, 2014b), see Figure 23. For example, the aerodynamic loads on rotor blades, structural dynamics, control dynamics, hydrodynamic loads on floaters and mooring system dynamics. Furthermore, FAST enables the analysis of time-varying stochastic wind for time-domain simulations. The FAST simulation tool has been successfully used in other well-known projects such as OC3: Offshore Code Comparison Collaboration (Jonkman, 2010) and OC4: IEA Task Wind 30 (Robertson, 2014), and its modelling capability has been authenticated using multiple floating structures in the Netherlands (Coulling, 2013).

For example, for the aerodynamics forces, FAST uses numerical integration to solve the equation of motion (Kane's method of the dynamic equation) and the AeroDyn subroutine package (Windward Engineering) to solve each blade's aerodynamic forces (Jonkman, 2007; Jonkman, 2014 Sarkar, 2021; Vlase, 2020).

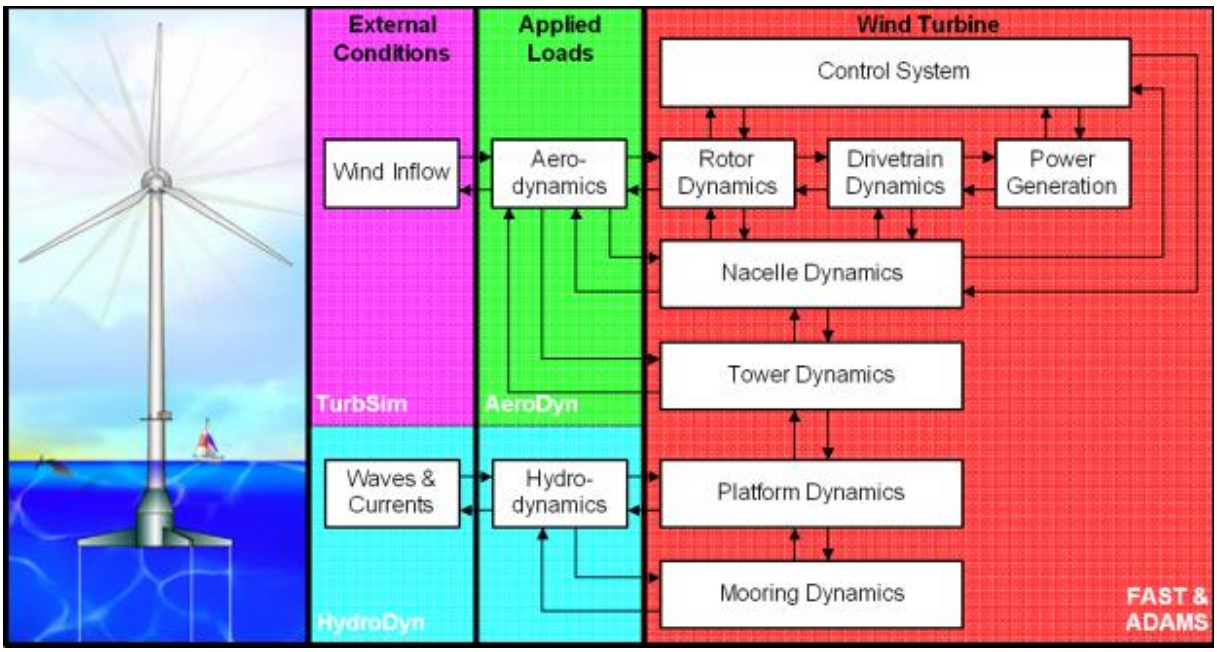

Figure 23 Diagram Illustration of the FAST Model (Jonkman, 2007)

Aerodynamics

The blades' aerodynamic loads are calculated based on the quasi-steady Blade Element Momentum (BEM) theory. BEM theory combines momentum theory and blade element theory. Various advanced corrections, including tip loss, hub loss, skewed inflow and dynamic stall corrections, are included in the BEM method. The Prandtl corrections are implemented to account for the hub and blade tip losses due to a finite number of blades. The Glauert correction is applied to account for the induction factors, while the Pitt and Peters' model accounts for the skewed inflow correction. Finally, the dynamic stall correction is employed in the Beddoes-Leishman model. More details about the aerodynamic load calculation in the FAST code can be seen in the AeroDyn theory manual, see (Moriarty, 2005; Jonkman, 2014).

Hydrodynamics

Hydrodynamic loads acting on the semi-submersible floater are calculated based on potential flow theory with Morison's drag term considered. It accounts for the wave pressures and viscous loads, respectively. Hydrodynamic coefficients, such as added mass and potential damping coefficients, and first-order wave excitation load transfer function are firstly estimated in the frequency domain by a panel code, WAMIT, according to the potential flow theory. These hydrodynamic coefficients are then transformed into the time domain using the convolution technique (Jonkman, 2014b).

Structural dynamics

A combined multi-body and modal structural approach is considered in the FAST code to account for the structural dynamics of the FWT. The blades, tower and driveshaft, are considered flexible bodies, while the nacelle, hub and floater are rigid bodies. The inherent structural damping in the blades and tower are represented using the Rayleigh damping model. The structural dynamic responses in the time domain are calculated by solving the equations of motion of the rigid-flexible coupled system derived from Kane's approach, see (Kane, 1983).

Control system dynamics

The control system used in the 5MW (and later 10-MW RWT) is implemented in two operational modes: the below-rated and full-rated regions. The generator torque-speed curve regulates the rotor rotational speed with an optimal tip speed ratio in the below-rated region, achieving maximum power generation. A proportional-integral (PI) algorithm regulates the blade pitch angle to reduce the structural loading while keeping the rated power generation in the full-rated region. The PI parameters are modified from the land-based RWT to avoid the negative damping effects, which are essential in affecting the platform motions for FWTs (Jonkman, 2014b).

4 Paper I – Characterization of a Compensation Scheme

An increasing number of turbines are being built yearly worldwide to achieve the Net-Zero Emissions target by 2050, and thus it has become increasingly essential to keep the cost of developing and servicing these turbines to a minimum. An essential aspect in keeping the cost low is ensuring wind turbine failure rates are minimized. Failures can cause heavy cost overruns by having downtime, which can extend from months to years, depending on the availability of skilled manpower and or materials such as spares. As such, failure can easily have extended downtime (varying from months to years), and heavily depends on the availability of the materials or manpower (Igba, 2015; Irena, 2012; Sheng, 2012). Furthermore, since some parts within the wind turbines are more susceptible to damage or are expensive to replace, it can significantly affect their base cost due to warranties. One such important example is the gearbox which makes up about 15% of the cost involved in manufacturing a wind turbine, making it one of the more expensive components to service and replace during failure (Irena, 2012). Even with better design and manufacturing processes, many gearboxes are still only commonly achieving lifespans of lesser than 20 years (Sheng, 2012; Korber, 2014). An estimate of about one gearbox failure occurs for every 145 wind turbines per year. Additionally, excessive loading also drives up the operational and maintenance costs for the manufacturers (Irena, 2012; Sheng, 2012). Therefore, uncertainty in failure rates within the gearbox naturally drives up the total cost of the turbines and the insurance cost involved in protecting them against damages (Sheng, 2012). The National Renewable Energy Laboratory (NREL) estimates that about 75 % and 15 % of gearbox failures can be accredited to the bearing (abrasion and adhesion) or gear parts (bending fatigue and corrosion), respectively. In addition, gearboxes experience different loads such as twisting moment or torque, transverse load, and axial load. Therefore, minimizing any of these loads will also vastly help reduce the total load acting on the gearbox. However, with very little room for better design improvements, today's gearbox research focuses on better materials or reducing loads acting on the gearbox by modifying the control systems. Innovations in the control systems focus on improving their controls. Examples include varying shaft speed or individual blade pitch to reduce the loads on the turbine shaft connected to the gearbox.

It has been well established that non-torque main shaft loads influence the internal drive train loads. In (Xing, 2013), the authors showed that changes in floating wind turbine support led to a reduction in the non-torque main shaft loads, gear-teeth loads and bearing loads. While in three different papers (Guo, 2014; Guo,2012; Guo, 2014), the authors confirmed that non-torque loads induced by overhang weight significantly influence the drive train loads and their response. As a result, the authors

attempted to change the drive train design to reduce the effect of the load caused by the shaft. The authors also identified that both gravity and non-torque loads cause excitations within the carrier frame, leading to gearbox loading. In (Link, 2011), the authors confirmed that bending moment (BM) in the main shaft resulted in the planet-ring gear misalignment, which led to an increase in edge loading. Edge loading eventually led to an increase in contact stress which reduced the gear lifespan.

Wind turbines have long used active control to mitigate loads and increase power production under a wide variety of wind conditions. In (Bossanyi, 2000; Bossanyi, 2003a; Bossanyi, 2003b; Bossanyi, 2005), the author suggested that it is possible to further metamorphose controllers (limit pitch controllers), limiting certain types of mechanical loads.

The author further discussed the possibility of using a control system and actuators to adjust the different pitch angles of each individual blade to reduce the loads on the systems. The authors illustrated a straightforward addition to the pitch control algorithm of each individual blade to reduce the peak load on some of the fixed components, which in turn led to a substantial amount of load reduction in the whole structure. At the same time, Henriksen (Henriksen, 2010) investigated the possibility of creating a model predictive controller (MPC) through gain scheduling or re-linearization. In this paper, the author only verified the ability of the MPC to control the turbines subjected to both physical and artificial constraints. However, the author did not focus on the controllers' effect on the loads. While in the doctoral thesis written by (Korber, 2014), the author found that a preview MPCs performed better in reducing both the mechanical extreme and fatigue loads than a non-preview MPCs and classical baseline controllers. Much of this existing research did not focus on reducing non-torque main shaft loads.

The first part of this thesis, as done in Paper I, aims to focus on improving an existing control algorithm on the NREL 5 MW reference turbine, which will reduce the bending moment in the low-speed shaft, which will eventually lead to the reduction of the gearbox or drivetrain loads. This is performed via a simple but highly effective scheme that directly compensates the non-torque main shaft loads in the blade pitch control system.

4.1 Methodology

4.1.1 Wind Turbine Properties

The simulations done on MATLAB/ Simulink on this project used the NREL 5 MW wind turbine, which follows the original project by (Jonkman, 2009). A 5MW offshore wind turbine from the National Renewable Energy Laboratory was used as a standard and was connected to three blades at a hub height towering of 90m. It has a 126m rotor diameter and an operational speed between 3 to 25 m/s (cut-in and cut-out, respectively). The rated speed for this model was 11.4 m/s. Apart from the rated

speed, the thesis will also focus on two other speeds, 8 and 20 m/s (below and above the rated scenario, respectively). The table with a figure below particularizes the specifications for the offshore wind turbine that has been used for the simulation.

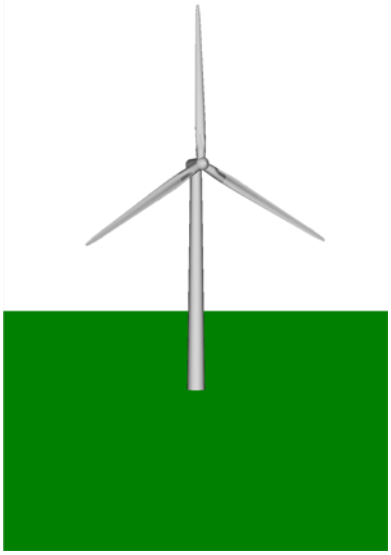

Figure 24 Design of 5 MW NREL wind turbine

But before investigating possible changes in the control algorithm, this section will also look at the main two control algorithm and what is control. Firstly, the WTs electrical system allows the torque demand of the generator to be met even as the shaft rotates independently at different speeds using a frequency converter. This allows the decoupling of the system as the rotational speeds and the grid's frequency become independent of one another. This is accomplished either by converting the generated power in DC setup and then again to match the grid AC power or by using a slip-ring generator (doubly-fed electric machine), allowing the generator torque to be independent of its rotational speed. Secondly, at higher speeds WTs blades pitches (rotates) along its longitudinal axis allowing the WTs shaft to reduce its rotational speed, thus shedding its power. Pitching the blades changes the angle of attack on the blade, which changes the lift and drag forces associated with the blade. Blades designed to pitch to feather decreases the lift as the pitch angle increase with an increasing wind speed. With increasing speeds, the blade progressively moves to the feather position where the pitch angle is the highest, ensuring that insignificant or zero lift is generated. The actuators that control the pitching of the blades are either electric or hydraulic motors. With the improvement in control designs, actuators can pitch each of the three blades independently.

The basic setup was created with the controllers as suggested in (Jonkman, 2010) to ensure that the system was functional and running according to the results given in the manual.

Parameter	NREL 5 MW Wind Turbine
Power Production Rating	5 MW
Number of Blades	3
Rotor Orientation	Upwind
Rotor Diameter	126 m
Hub Height	90 m
Cut in, Rated, Cut out Wind speed	3 m/s, 11,4 m/s ,15 m/s
Cut in, Rated Rotor Speed	6.9 rpm, 12.1 rpm

Table 10 Properties of NREL 5MW Turbine (Jonkman, 2009).

4.1.2 TurbSim

TurbSim, developed by Jonkman & Kelley from NREL, is a computational simulator that allows the generation of stochastic, full-field turbulence flow used mainly in wind models. It differs from the IEC Normal Turbulence Model as it can give additional details, such as spatiotemporal turbulent velocity field relationships as seen with nocturnal boundary layer flows. The turbulent model developed by TurbSim can better depict the dynamic wind features which affect wind turbines' aeroelastic loading and responses unfavourably (Jonkman, 2014b). TurbSim applies the power-law wind and coherent profiles to generate the Normal Turbulence Model wind flow. The simulator integrates the different formulas discussed in Section 2.1 to Section 2.10.

4.1.3 Wind Simulation Model (MATLAB)

The steady-state wind and normal turbulent models were generated using the MATLAB and Turbsim respectively in the three different directions (u, v, and w). The functions used differing input variables such as parameters, frequency, coefficients, Y-Z grid, and spectra. The simulation also was repeated based on the same conditions and different wind speeds for all the different cases

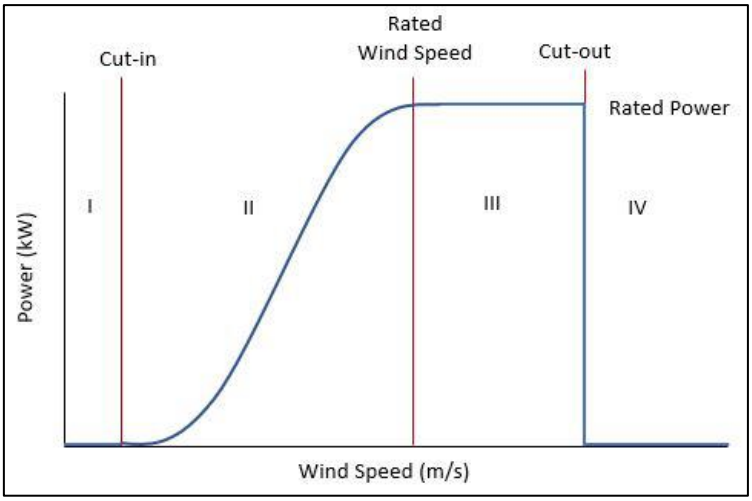

Figure 25 Typical wind turbine power output with wind speed (Knight, 2019)

Three different speed was selected to run this stimulation: the below-rated, rated and above-rated speeds. The three speeds were determined by the functionality of the turbine at these speed. Turbines are designed to aim maximize power extraction. Thus, the focus is centered on cut-in to the rated wind speeds (Region II). Region I is known as the cut-in speed, while Region IV is known as the cut-out speed, Figure 25. Within these two regions (Region I and IV) the turbine does not operate as the wind is too weak to move the blades efficiently or the wind is too fast and would damage the blade and the turbine if switched on (Lackner, 2013). In Region III, the wind turbine ensures that the rated power is maintained for power efficiency. The power efficiency of the turbine during lower or higher speed can be maintained by pitching the blade to optimize the angle of attack (Figure 26).

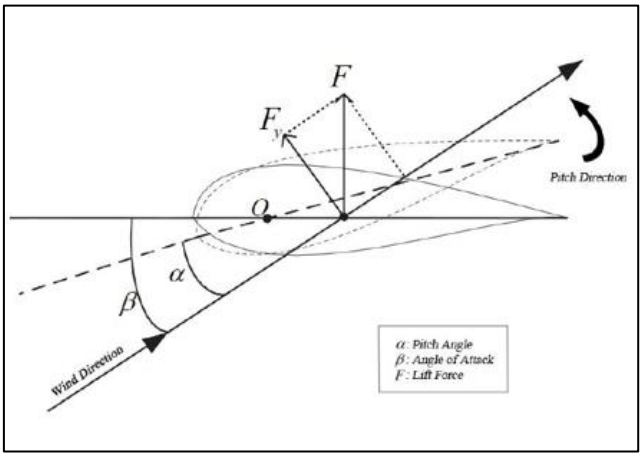

Figure 26 Typical wind turbine blades and its aerodynamics (Bahraminejad, 2014)

4.1.4 Wind Field Grids

The synthetic turbulent wind field input is represented in a 3-dimensional vector box (3D box) consisting of grid points. Each of these grid points is a spatial location in the 3D box that carries the wind speed along with all the 3 directions (v, v, w) locally. The 3D box only covers the rotor swept area, and the forces accounted for in this calculation are derived from this area. The other parts of the turbine are considered to have no significant impact on the results. This assumption is considered sound as it is safe to ignore the force acting on other parts of the turbine-like the tower, as the force excreted by the wind fields on the other parts is insignificant compared to the force excreted by the wind on the rotor area. The speed approaching the vector box is similar as the mean speed as the turbine's hub (DTU, 2016). However, an acceptable number of grid points and spacing must be used to represent a good turbulent wind field.

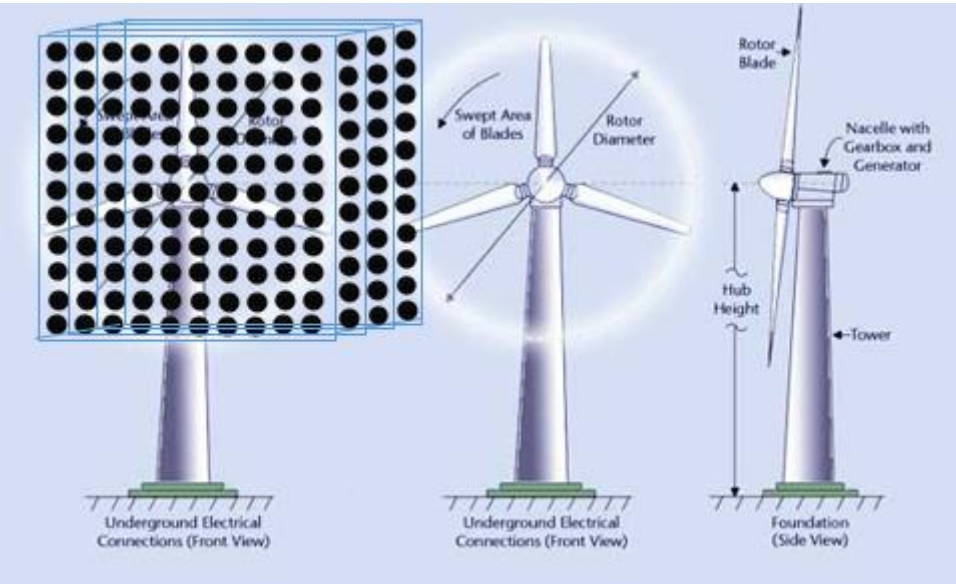

Figure 27 : Y-Z Grid Diagram (Whirlopedia)

The turbulence box used will have - $2n$ grid points (DTU, 2016), making N_x=2^{nx}, N_y=2^{ny}, and N_z=2^{nz}, real and positive float numbers. Values needed for this simulation are as follows (DTU, 2016):

4.1.5 Simulink

In this thesis, the control system for both the torque controller and pitch controller was developed on the SIMULINK graphical programming environment inbuilt within the Matrix Laboratory (MATLAB) system. It was after that, coupled with the FAST program with the goal to integrate it with the aerodynamic and mechanical models within FAST. The generator controller was made using a low pass filter, generator speed-torque curve, and saturation and rate limiters. Values for the generator speed-torque were extracted from the graph (Jonkman, 2019). While, the pitch controllers were made using a proportional–integral–derivative controller (PID controller) together with saturation and rate limiters. The values used for the proportional and integral gains were obtained from the (Jonkman, 2019). Sub-sections 4.1.5.1 to 4.1.5.4 will discuss the basic controller design used in this system, and sections 4.1.6 and 4.1.7 discuss the newly developed controllers.

4.1.5.1 Control Design - Overview

A wind turbine controller's primary function is to control generator torque or blade pitch. The generator controllers used in Paper-I are modelled after the (Jonkman, 2019) to ensure consistency, see Section 0 and Section 4.1.5.4.

The pitch controller is later modified to include the bending moments' errors into the control loop feedback mechanism. By varying only one of the two controller's setups, we can study any improvement in bending moment changes more accurately. The error of the bending moments is added to the PID controller's error because it is expected that the controller would be able to correct

the bending moment better due to the increase in sensitivity. Even if this method is primitive, we will still need it to observe and establish the relationship between the inputs and the outputs. The setup of the newly developed controllers is described below in Section 4.1.6 and Section 4.1.7.

4.1.5.2 PID Controller

This thesis reviewed the well-developed and newly developed control algorithms for both the torque and pitch demands. First, we tested the classical PID algorithms for a single input signal to generate a pitching change on the blades. At the same time, the torque demand was implemented independently using the output turbine speed. After that, the following idea was developed:

- Controlling the blade pitch and torque response using the shaft speed, moments and generator speed which attempts to minimize both the load and energy differences.

PID controllers are commonly used in various industries, including WT applications, to regulate speed, pressure or other process variables. It acts as a control loop feedback mechanism that can regulate the process variable and has been used in many applications due to its stability and accuracy. A PID controller is described using a Laplace variable as:

$$\text{Time Domain: } u(t) = K_P e(t) + K_I \int_0^t e(t)dt + K_D \frac{de(t)}{dt}$$
$$\text{Frequency Domain: } u(s) = (K_P + \frac{K_I}{s} + K_D s)e(s) \quad (18)$$

Where e: tracking error, K_P: proportional gain, K_I: integral gain, K_D: derivative gain

In a pitch-regulated turbine: In an above-rated condition, x is an error, or a combination of errors, evaluated as a summation of differences between the measured input and the demanded or rated input (e.g., shaft speed), while the output value (y) is the demanded pitch angle. The equation mentioned above's integral value restricts the mean value of x to zero, thus ensuring that y would not become indefinitely high or low. While in a below-rated condition, the demanded pitch is limited to the fine position since x becomes a negative value.

It is crucial to study and access the effectiveness of a new controller as it enables further optimization of the controller's algorithm. However, it can often be challenging due to the unpredictability of the wind. It is therefore essential to ensure that field trails supplement the simulation trails.

4.1.5.3 Controller Design – Original Generator Controller

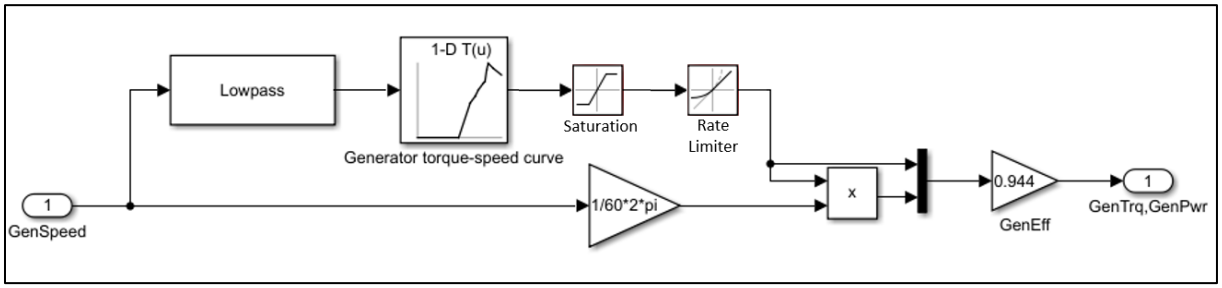

Figure 28 Original Generator Controller

As recommended by (Jonkman, 2019), in the generator controller (Figure 28), the generator speed is taken as an input, and its values are sent through a low pass filter. A single-pole low-pass filters the input by removing the high-frequency excitation with exponential smoothing. Afterwards, the signal is sent to a generator torque-speed lookup table before being saturated and limited. The signal is multiplied according to the generator efficiency and is reported as an output both for generator torque and power. Table 11 shows the values used in this controller.

Low-pass filter	
Passband edge frequency (Hz):	0.25
Stopband edge frequency (Hz):	5
Maximum passband ripple (dB):	0.1
Minimum stopband attenuation (dB):	80
Input sample rate (Hz):	200
Saturation	
Upper/Lower Limit	(+/-) 47402.91
Rate Limiter	
Rising/Falling Slew Rate	(+/-) 15000
Generator	
Efficiency	0.944

Table 11 Original Generator Controller Variables

4.1.5.4 Controller Design – Original Pitch Controller

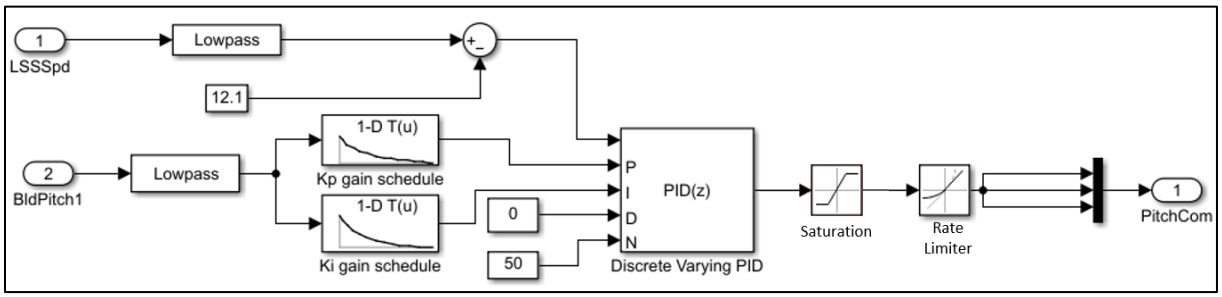

Figure 29 Original Pitch Controller

As recommended by (Jonkman, 2019), the original pitch controllers (Figure 29) receive the filtered low-speed-shaft speed error as an input (x, as described above in the PID section) into the PID controller. The error is the summation of differences between the measured input speed and the rated speed. The proportional and integral gain is inputted into the PID controller using a blade pitch-gain scheduling lookup table as reported in (Jonkman, 2019). The input blade pitch is also filtered before using the lookup table. The output signal (y, as described above in the PID section) is saturated and limited before it becomes the final pitch output which is then sent back to the FAST simulation.

The original pitch controller design will be modified and becomes the novel change introduced that helps reduce the bending moment of the shaft. The details of this novel change will be described in the following sections.

4.1.6 Compensation scheme

The compensation scheme is presented in Figure 30 together with the original blade pitch controller. The original blade pitch controller corrects only for shaft speed error. In contrast, the compensation scheme adds the correction of the main shaft bending moment error. The scheme only modifies the blade pitch control, i.e., the generator control is not modified.

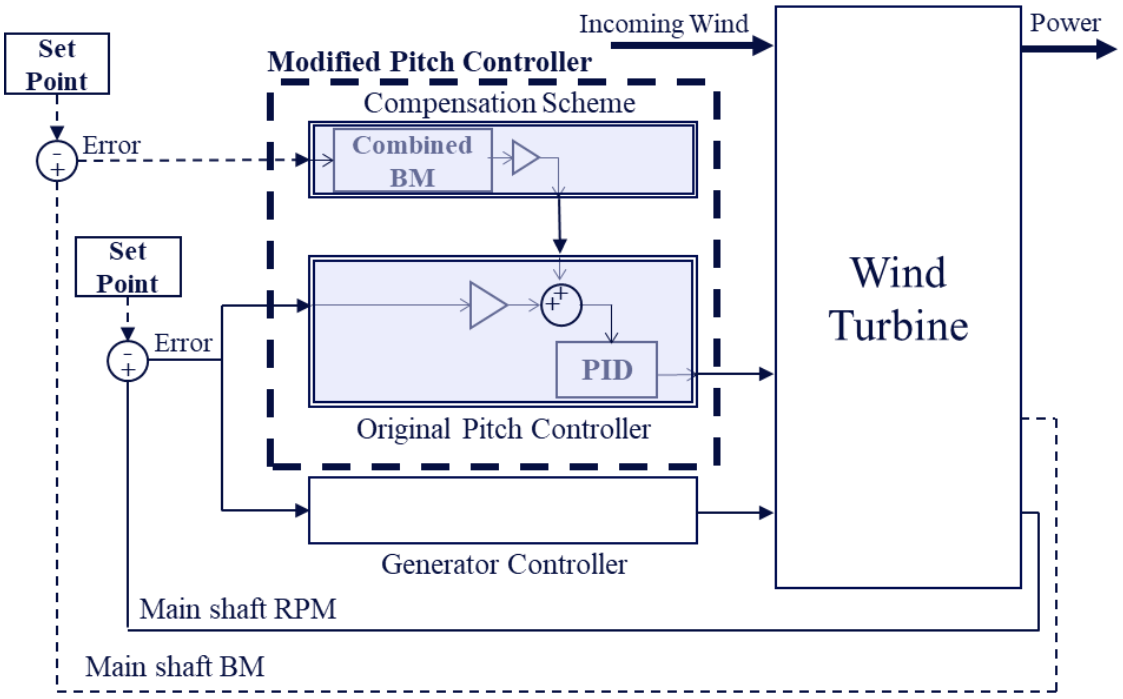

Figure 30 Modified pitch controller (Original controller with compensation scheme)

The collective blade pitch command, ϑ_{com} is calculated as:

$$\theta_{com} = k_p \cdot e_{tot} + k_p \cdot \int e_{tot}\, dt \qquad (19)$$

where e_{tot} is the total error, k_p is the proportional gain coefficient, and k_i is the integral gain coefficient. The derivative gain is zero. There are saturation and rate limiters placed on the commanded pitch.

The total error, e_{tot} is calculated as:

$$e_{tot} = e_{RPM} + k_{BM} \cdot e_{BM} \qquad (20)$$

where e_{RPM} is the shaft speed error, e_{BM} is the bending moment error, and k_{BM} is the compensation weight factor applied on e_{BM}. The values of k_{BM} studied are presented in Table 13. When k_{BM} is set to 0, the errors of the moment are not added to the PID controller. While when k_{BM} is set to 1, it hypothetically means that all the bending moment errors are sent into the PID controller.

The main shaft bending moment is the combined bending moment, M and is calculated as:

$$M = \sqrt{M_y^2 + M_z^2} \qquad (21)$$

where M is the combined bending moment, M_y and M_z are the non-rotating bending moments.

4.1.7 Simulink implementation

The compensation scheme is implemented in Simulink/FAST (Jonkman, 2005) and is presented in Figure 31. The original blade pitch controller is modified to include the compensation scheme (shaded in Figure 31).

In the implementation, the y and z directional low-speed-shaft bending moments are squared and added together. Next, the root of this summation vector is calculated using the equation (21), before passing the signal through a low pass filter. The error of the moment is then calculated as a summation of the differences between the measured input moment and the ideal moment of 0. The signal is then multiplied by the compensation weight factor (K_{BM}). Finally, these two errors are added and then used as inputs into the PID controller. Table 12 shows the Simulink implementation variables.

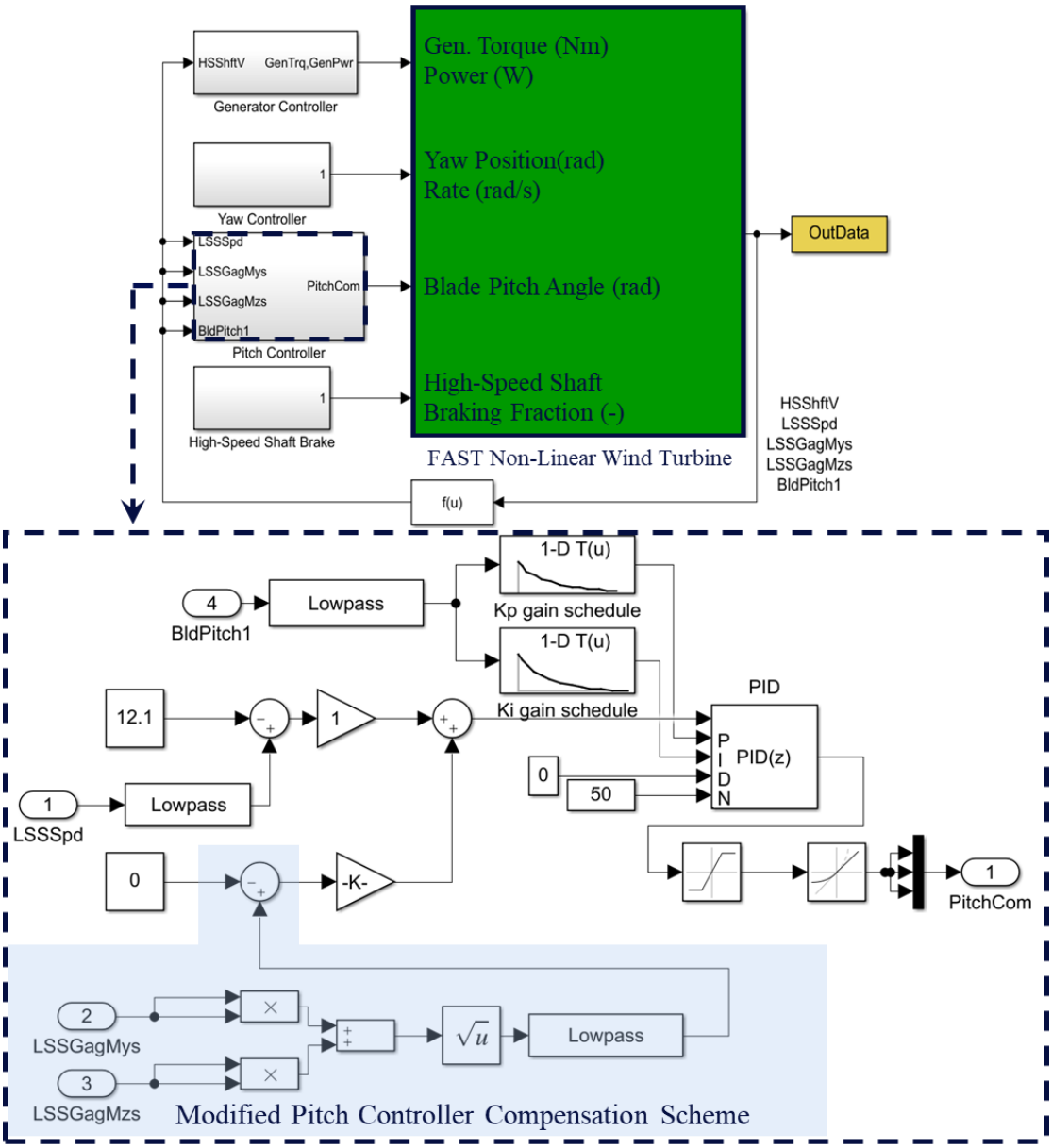

Figure 31 Simulink implementation

Saturation	
Upper Limit	90/180*pi
Lower Limit	0
Rate Limiter	
Maximum Absolute Blade Pitch Rate	8 º/s
Rising/Falling Slew Rate	(+/-) 8/180*pi
K_{BM}	0, 0.0001, 0.0002, 0.00032, 0.0004, 0.00072

Table 12 Simulink implementation Variables

4.2 Results and Discussion

Case studies:

The cases studied in this paper are presented in Table 13. Three wind speeds corresponding to below-rated, rated and above-rated regions are studied for both steady wind and normal turbulent wind (NTM) conditions for a wide range of K_{BM} values. This gives a total of 72 simulation cases. The simulation times for each case are 300 s for both steady and NTM wind conditions.

Case no.	Values
Wind speed (m/s)	8, 11.4, 20
Wind condition	Steady, NTM
K_{BM}	0, 0.0001, 0.0002, 0.00032, 0.00064, 0.00072, 0.0001, 0.0002, 0.00032, 0.00064, 0.00072, 0.001

Table 13 Case studies

The variables studied are the non-torque bending moment (BM) equation **(21)** , the low-speed shaft speed (RPM) and the generator power (Power). Percentage differences, i.e., %BM, %RPM and %Power are also calculated and investigated. As an example, the % difference in BM is calculated as:

$$\%BM = \frac{BM_{comp} - BM_{org}}{BM_{org}} \times 100\% \qquad (22)$$

where BM_{comp} is the bending moment obtained when the compensation scheme is applied and BM_{org} is the bending moment obtained with the original controller scheme with no modifications applied.

4.2.1 Steady Wind

The steady wind cases' results are presented in Figure 32 and Figure 33. When calculating the shaft RPM, generator power and torque, their average values of the last 100 seconds were computed.

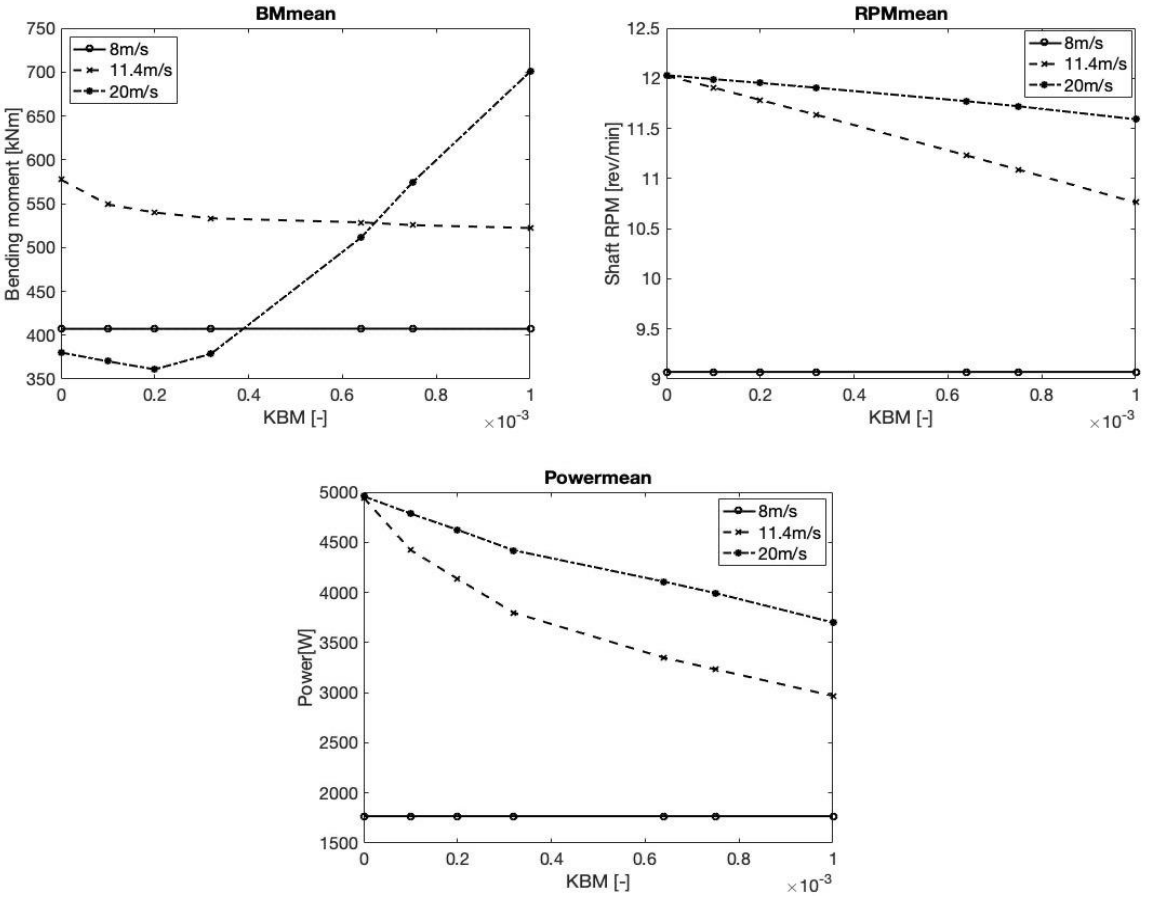

Figure 32 Steady state wind results at 3 different speeds with varying KBM; a. BM (top-left), b. RPM (top-right) and c. Power (bottom)

At the underrated wind speed (8 m/s), the pitch controller is not activated, therefore there are no changes to the results for all values of K_{BM}. At the rated wind speed (11.4 m/s), the bending moment drops with increasing K_{BM} but plateaus after it reaches 0.001. While at the above-rated speed (20 m/s), an interesting phenomenon is observed as the BM drops for the lower K_{BM} values and increases for the higher values. This phenomenon can be explained by the fact that as K_{BM} increases, the error is added to the PID from the bending moments that become significantly larger than the shaft RPM. This causes the system to start behaving erratically as errors are corrected incorrectly. Similar erratic behaviour can similarly be expected at other speeds in the above the rated speed ranges (e.g., 15 or 18 m/s) as the K_{BM} approaches 1). The bending moment drops with a negative gradient from 0 to 0.0002. This is as expected since the bending moments that is added at these K_{BM} suits their shaft error proportionally. Thus, a good proportionality allows the errors to be corrected more accurately. Further detailed analysis is conducted for K_{BM} values (between 0 and 0.0001) in the above-rated speed to garner improved efficiency of the bending moment values in that region. This detailed analysis is shown in Figure 33.

The shaft RPM values drop steadily for an increasing K_{BM} value for the rated and above-rated wind speeds. As these two lines decrease, in both cases, the shaft RPM error corrects the system to achieve

its optimal shaft speed, which is the primary controller objective. The result shows a significant drop in power at the higher K_{BM} at both the rated and above-rated wind speeds. However, at the lower K_{BM} the power loss can be potentially better controlled and minimized.

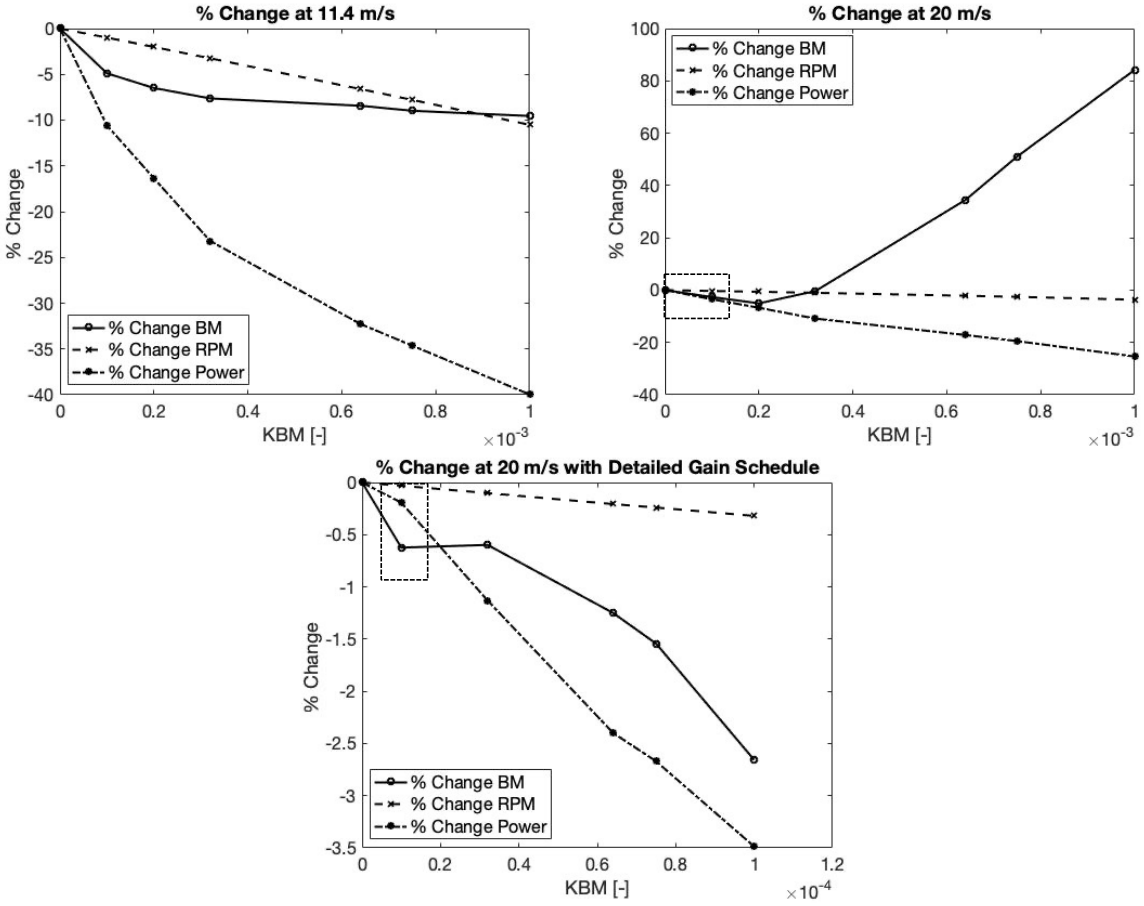

Figure 33 Steady state wind results (percentage (%) change for BM, RPM and Power) with varying KBM; a. Rated (top), b. Above-rated (bottom-left) and c. Above-rated with KBM scheduling(bottom-right)

The results from Figure 33 show that at rated speed (11.4 m/s) and above rated speed (20 m/s), all the percentage changes of bending moments, shaft RPM and generator power are dropping with an increasing K_{BM}, except for the above-rated speed (20 m/s) bending moment which reasoning was explained in the previous section. For the rated speed (11.4 m/s), Figure 33 (a) indicates that 0.0001 gives the minimal proportion of losses between the percentage change of bending moments, shaft RPM and generator power. While for the above-rated speed (20 m/s), a more detailed analysis was done in the ranges of 0.00001 to 0.00015 (boxed-up region: Figure 33 (b)) to identify the best K_{BM} values. Figure 33 (c) shows the results of the detailed gain scheduling. Figure 33 (c) indicates that 0.00001 gives the minimal proportion of losses between the percentage change of bending moments, shaft RPM and generator power. More importantly, in Figure 33 (c) at 0.00001, the bending moment loss is more significant than the power loss. Therefore, even though the percentage change might be small, it gives an ideal situation since the turbine reduction in bending moments is more than the loss in power.

4.2.2 NTM Wind

The results of the steady wind cases are presented in Figure 34 and Figure 35. Like the steady wind cases presented in Section 4.2.1, when calculating the shaft RPM, generator power and generator torque, their average values of the last 100 seconds were computed.

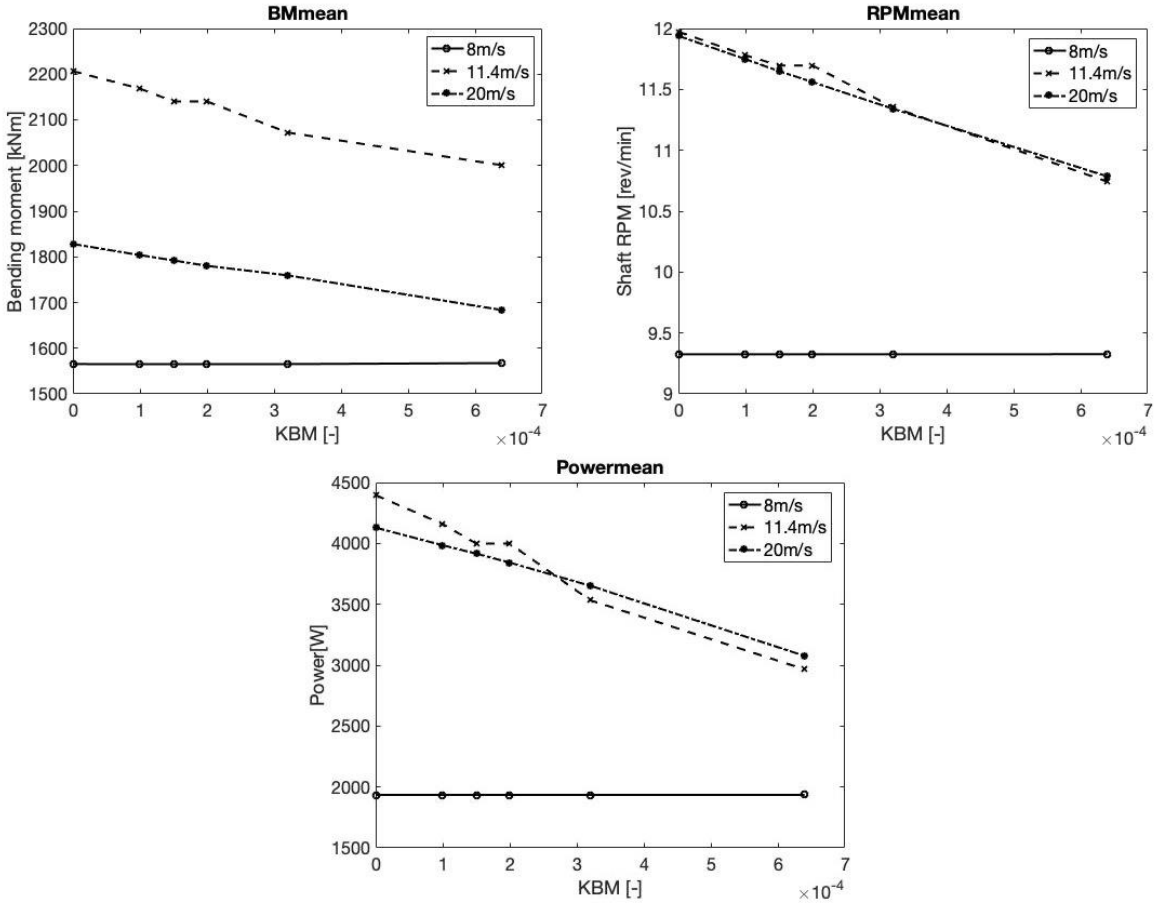

Figure 34 NTM wind results at 3 different speeds with varying KBM; a. BM (top-left), b. RPM (top-right) and c. Power (bottom)

Similarly, for the NTM wind cases, at the under-rated wind speed (8 m/s), the bending moment, shaft RPM and generator power change are assumed to be zero due to the inactivation of the pitch controller. However, in the normal turbulent wind model the drop in the bending moments, shaft RPM and power seem to be relatively linear for both the rated and above-rated wind speeds. This is expected since, with the turbulent wind model, the wind's speed varies differently and averages out at the selected wind speed. The wind's net effect on the bending moment in this model clearly shows the steady dropped experienced with increasing K_{BM}.

The turbulent models rated or above-rated speeds produce very similar shapes for the shaft RPM and power in all measured K_{BM} values. The bending moment values of the above-rated speed are also lesser than the rated speed (using K_{BM} = 0 as reference). This is accounted for correctly because as the blade pitches at above the rated speed, the bending moment acting on the turbine body and shaft is reduced.

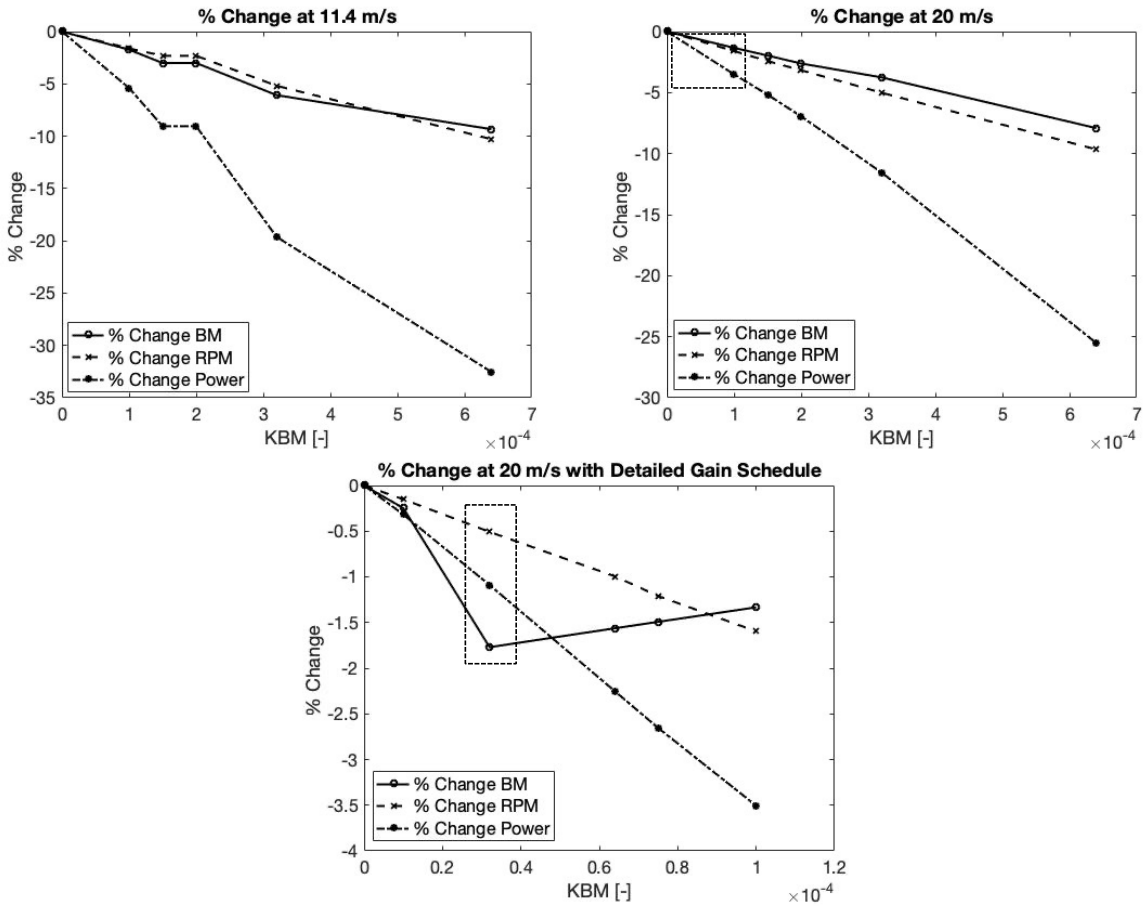

Figure 35 NTM wind results (percentage (%) change for BM, RPM and Power) with varying KBM; a. Rated (top), b. Above-rated (bottom-left) and c. Above-rated with KBM scheduling(bottom-right)

For the rated speed (11.4 m/s), in Figure 35 (a), it can be seen clearly that the percentage change in bending moment and power decreases at the same rate while the power is more significantly affected with increasing K_{BM}. While for the above-rated speed (20 m/s), in Figure 35(b), further investigation was done in the boxed-up region to find an appropriate K_{BM} value that can minimize the losses between the bending moments, RPM and power. These results are shown in Figure 35(c). In Figure 35(c), the best K_{BM} values are identified when there is more percentage loss of bending moment than power. A similar pattern was observed in the steady-state model. However, the *turbulent model's KBM value (0.000032)* is different from the steady-state model.

4.2.3 Best KBM values

To estimate the best K_{BM} values for each wind speed, the best ratio for the percentage bending moment and percentage RPM is calculated. The higher the ratio, the maximum decrease in bending moment has been achieved with minimal change in RPM or power (P). The change is 0 at under-rated wind speed (8 m/s) is insignificant and assumed to be zero. The results are presented in Table 14.

Wind speed (m/s)	8	11.4	20
% difference, BM mean	0	-3.0041	-1.7701
% difference, RPM mean	0	-2.3144	-0.5079
Best ratio (%BM/%RPM)	0	1.29	3.48
Best ratio (%BM/%P)	0	0.33	1.62
K_{BM}	0	0.00015	0.000032

Table 14 Best KBM values

The percentage BM / percentage P ratio is less than 1 at the rated speed (11.4 m/s) and more than 1 at the above-rated speed (11.4 m/s). Even though it might be questionable if the benefits are worthwhile at the rated speed, it is unquestionably beneficial at the above-rated speed. The ability to minimize the bending moments acting on the shaft and eventually the gearbox will significantly increase the gearbox's life span as described by the S-N curve. Furthermore, the K_{BM} value can be scheduled to 0 at the rated speed if cost analysis research shows that it gives the most positive results.

Finally, it can be summarized that varying K_{BM} values and adding the BM errors positively affect the reduction of the structural load oscillations. Furthermore, changing the K_{BM} values and thus the BM errors magnitudes seem to have a linear relationship within the examined ranges of 0.00001 to 0.001. However, it is essential to acknowledge that it does not necessarily mean that this relationship holds to different wind speeds or different ranges of K_{BM} values. Furthermore, it must be emphasized that the control algorithms used only considered the pitch angle controller for one blade and cumulated the results used for all three blades.

4.3 Conclusion

Control algorithms that can reduce the bending moment in the low-speed shaft will eventually reduce the internal drive train loads within the gearbox, thus extending its lifespan. This paper has shown that adding a bending moment error into the pitch controller can positively affect the bending moment acting on the low-speed shaft. The bending moment can be reduced by about 3 % for the rated wind speed (11.4 m/s) and 1.8 % for the above-rated wind speed (20 m/s) while only losing 2.3 % and 0.5 % of the shaft's rotational speed, respectively. Furthermore, a linear relationship was observed between the gain scheduled bending moment errors and the reduction of total bending moments if the K_{BM} values are scheduled/optimized in an appropriate range. However, further studies need to be done to ensure consistency of such reduction at different wind speeds. It is also vital to ensure that lifespan extension does not substantially reduce the turbine's power, torque, or rotational speed.

5 Paper-II - Characterization of Extreme Load Responses using ACER1D and ACER2D

Two different methods can be applied to evaluate extreme wind turbine loads. The first method involves running a simulation for rare occurrences that leads to a high structural load. In contrast, the second method simulates the wind turbine operating under normal conditions. The results are then extrapolated with a probability distribution, and the extreme tail is analyzed (Dimitrov, 2016). The second method is more commonly used as it uses a full statistical distribution instead of an individual event.

Even as researchers can now estimate extreme loads more accurately than ever, they had to develop a better statistical distribution to help them extrapolate the extreme load (Veers, 1998). Thus, many researchers worked on numerous probabilistic methods to increase the precision of the estimated loads. In (Madsen, 1999), the author developed a non-linear parametric model to extrapolate and estimate long-term fatigue loading. In (Ronold, 1999; Ronold, 2000), the authors developed techniques to calibrate partial safety factors which could predict extreme loads through extrapolation and showed that these extreme loads follow the Gumbel distribution. While in the study (Manuel, 2001), the author continued fine-tuning probabilistic methods and parametric models and executed a detailed uncertainty analysis. While to achieve a more accurate estimation for the moment, (Fitzwater 2002; Moriarty 2002) attempted to compile and simplify the different techniques mentioned above. In (Agarwal, 2008), the authors attempted to estimate extreme loads through statistical extrapolation of limited field data. Many studies have recently focused on estimating the wind turbine's extreme loads more precisely. Examples include (Barreto, 2022), where the author used statistics and modelling to estimate long-term extreme responses on an offshore wind turbine. While in (McCluskey, 2021), the author used extreme value statistics to estimate flow-induced responses from a small sample size, (Fogle, 2009) estimated loads using the global and block maxima extrapolation. And in (Ernst, 2012), the authors used the threshold extrapolation method to estimate the extreme loads and turbulent intensity. In (Graf, 2016), the authors used the Monte Carlo method to estimate the long-term fatigue loads. In contrast, many authors such as (Fitzwater, 2001; Moriarty, 2004; Freudenreich 2007; Ragan, 2008; Peeringa, 2009; Abdallah, 2015) have attempted to match different statistical distribution models with extreme load patterns. However, the methods mentioned above fit an assumed extreme value distribution to the empirical data and do not precisely represent the actual characteristics of the data. It can lead to less reliable results, which is even more critical in extreme value prediction. The results are derived at the tail of the probability distribution and are sensitive to uncertainties and errors.

This paper proposes a novel averaged conditional exceedance rate approach based on two-dimensional design points (ACER2D) instead of traditional one-dimensional characteristic design values. ACER2D is a non-trivial approach compared to the classic method, given that there is a non-linear correlation between different response components. The proposed method can predict extreme loads in a 10 MW large floating wind turbine (FWT) more efficiently and reliably. The ACER method combines the structural load statistics with appropriate parametric functions that provide a reliable description of the extreme load distribution's tail behaviour. ACER has been applied in earlier studies on various marine structures (Zhang, 2019; Gaidai, 2018; Gaidai, 2016) and (Naess, 2008; Naess, 2009; Naess, 2010; Naess, 2013). This method provides a statistical depiction and its error bounds of the extreme value distribution inherent in the data, offering a unique approach to estimating the extreme values (Karpa, 2013). The ACER method sets itself apart from other commonly known methods, e.g., the Gumbel and Weibull distribution. ACER method is not purely based on the asymptotic distribution, thus avoiding incorporating generalized extreme value distribution (GEV). The latter allows the values obtained from the ACER method to be more versatile as it represents real-life values that are typically not genuinely asymptotic. Furthermore, the margin of errors for irregularity is reduced as it avoids superposing asymptotic behaviour onto actual non-asymptotic data. The ACER method has been described as having more accurate and reliable results than the peaks-over-threshold or annual maxima methods. The effectiveness of the ACER method has fueled further research to develop a modified ACER method with the adaptive Markov Chain Monte Carlo simulations to estimate the short-term extreme mooring tension.

More efficient and reliable estimations of extreme responses will better help predict the effects these loads have on the components allowing the development and implementation of a better design or control system for the FWT. Optimal wind turbine parameters would minimize potential FWT mechanical damage due to excessive environmental loadings (Xu, 2019). Accurately predicted extreme loads will also make the components more optimally sized. It contributes to more refined designs and lower failure rates, which is particularly important for the offshore wind industry as it advances the design, manufacturing, and deployment of large FWTs (>10 MW) in the coming decade.

In this part of this thesis, Paper-II, the aim is to characterize the reliability of the ACER2D approach as it is fitted and compared against other classic methods (Asymmetric logistic and Gumbel logistic models) and to predict the 50- and 100-year return period ACER1D responses. The ACER methods would need to be optimized by investigating an appropriate k value.

5.1 Methodology

5.1.1 Wind Turbine Properties

This paper presents the methodology for estimating the DTU 10-MW RWT-OO-Star's extreme loads during operating conditions. The simulations done on MATLAB/ Simulink on this project used the DTU 10 MW wind turbine, which follows the original project. A DTU 10MW FWT is used as a standard and connected to three blades at a hub height towering 119m on a floater. The turbine has a 178.3m rotor diameter and an operational speed between 4 to 25 m/s (cut-in and cut-out, respectively). The rated speed for this model was 11.4 m/s. This thesis will focus on three wind speeds, 8, 12 and 16 m/s (below, rated and above the rated scenario, respectively). The figure below represents the wind turbine used for this simulation.

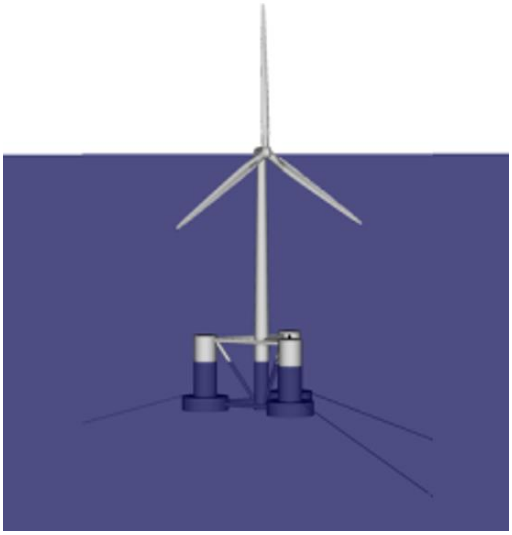

Figure 36 Design of DTU 10MW wind turbine

5.1.2 Load cases and environmental conditions

The environmental data (wind and wave data) used in this paper are established based on hindcast data from an offshore site in the Northern North Sea from 2001 to 2010. The long-term joint wind and wave distribution were developed in (Li, 2013), which considers a one-hour mean wind speed at the position that is 10 meters above the sea level (U_{10}), wave spectral peak period (T_p) and the significant wave height (H_s). The joint distribution of $U_{10,}$ H_s and T_p is expressed as below:

$$f_{U_{10},H_s,T_p}(u,h,t) = f_{U_{10}}(u) \cdot f_{H_s|U_{10}}(h|u) \cdot f_{T_p|U_{10},H_s}(t|u,h) \quad (23)$$

where $f_{U_{10}}(u)$, $f_{H_s|U_{10}}(h|u)$ *and* $f_{T_p|U_{10},H_s}(t|u,h)$ represents the marginal distribution of U_{10}, the conditional distribution of H_s for given U_{10} and the conditional distribution of T_p for given U_{10} and H_s.

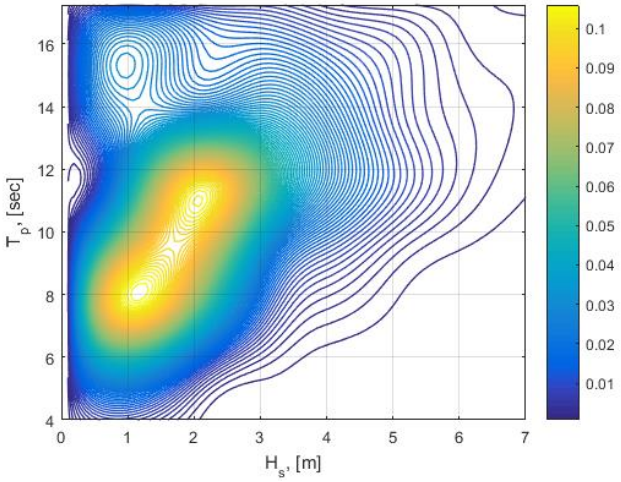

Figure 37 An example of in situ Hs, Tp scattered diagram, used to assign probabilities to individual sea states

Load cases	U_w (m/s)	T_I	H_s (m)	T_p (s)	Samples	Simulation length (s)
LC1	8	0.1740	1.9	9.7	20	4000
LC2	12	0.1460	2.5	10.1	20	4000
LC3	16	0.1320	3.2	10.7	20	4000

Table 15 Three representative load cases

Three representative load cases with a high probability of occurrence in the normal operating conditions are used in the present work and listed in Table 15. The mean wind speed selected for this paper is based on the turbine operating ranges (wind speeds ranging within the cut-in, rated and cut-out zones) with an increment size of 4 m/s. The most probable wave height and spectra peak period in each wind speed condition is selected based on the joint distribution expressed in Eq. (23).

The turbulent wind and irregular waves are modelled and considered to be directionally aligned in all the load cases. The normal turbulence and normal wind profile models are employed, and wind turbine Class C is applied. The wind power-law formulation is used to model the wind speed profile, as represented below:

$$U_w(z) = U_{hub}\left(\frac{Z}{Z_{hub}}\right)^{\alpha} \quad (24)$$

where $U_w(z)$ is the mean wind speed at the height z above the still water level, u_{hub} represents the mean wind speed at the hub height, z_{hub} denotes the hub height above the still water level and is 119 m for the 10-MW FWT. α is the power-law exponent, and it is taken as 0.14 for offshore locations based on the recommendation in IEC 61400-3-2, see (IEC, 2019)

The Kaimal turbulence model generates the three-dimensional turbulent wind fields, simulated using a stochastic turbulent-wind simulator, Turbsim (Jonkman, 2014b). In addition, time-varying irregular waves are generated using the JONSWAP (Joint North Sea Wave Project) spectrum according to the

specified H_s and T_p. Detailed descriptions for the models of turbulent wind and irregular waves can be found in IEC 61400-3-2 (IEC, 2019).

For the three environmental conditions, 20 different random samples of wind and wave are applied for each sea state. Each simulation lasts 4000s, where the first 400s is removed to reduce the transient effect induced by the wind turbine start-up. Therefore, 1-h data in each simulation is formed and is used for extreme value analysis in this work. The results shown in this work are based on the average of 20 1-h simulations to reduce the stochastic variability.

5.1.3 Extreme Value Distribution

Extreme values distributions are distributions of random stochastic process X(t) that focuses on the smallest extreme or the largest extreme variables. For example, it can be either the smallest minimum or the largest maximum from a sequence of individual minima/ maxima.

$$\mathrm{Z}_e = \max\{\mathrm{Z}_{m1}, \ldots, \mathrm{Z}_{mn}\} \quad (25)$$

where Z_e is the largest maximum value and Z_{m1}, Z_{m2},… Z_{mn} are all the individual maxima similar to that shown in Figure 38.

Know if it is identically distributed and independent with a common distribution function $F_{Xm}(x)$, the X_e distribution becomes:

$$\mathrm{F}_{\mathrm{Xe}}(\mathrm{x}) = \mathrm{Prob}\{\mathrm{X}_e \leq \mathrm{x}\} = (\mathrm{F}_{Xm}(\mathrm{x}))^n \quad (26)$$

Numerous methods can be used to predict extreme value distribution, e.g., Gumbel, Fréchet or Weibull distribution and the newly developed ACER (average conditional exceedance rate) method. In this thesis, we will be using the Gumbel fitting method and ACER (average conditional exceedance rate) method.

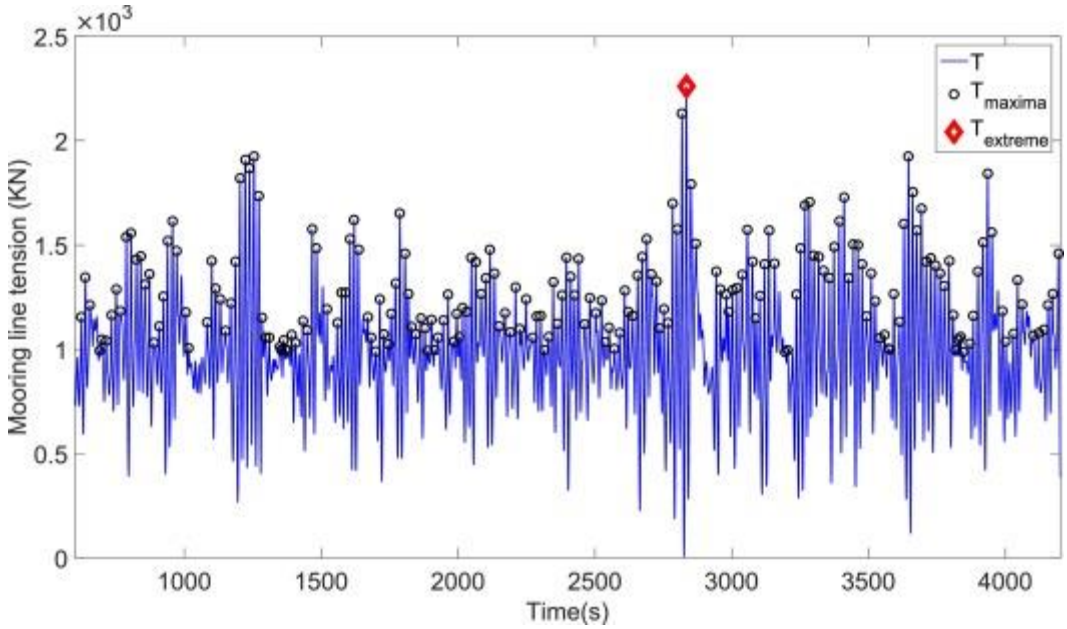

Figure 38 Global maxima (Xu, 2019)

5.1.3.1 Gumbel Distribution

Extreme value distribution. Eq. (25), has been proven on numerous occasions to converge to the Gumbel, Fréchet or Weibull distribution if the sample size (n) is large enough. These distributions, as mentioned previously, are also recognized as the type I, II and III extreme value distributions, respectively and are a family of cumulative distribution probability that combines for the generalized extreme value (GEV) distribution (Xu, 2019).

$$\mathrm{FX}_e(\mathrm{x}) \;=\; \exp\left[-1 \;+\; \gamma\left(\frac{\mathrm{x} \;-\; \mu}{\sigma}\right)^{\frac{-1}{\gamma}}\right] \qquad (27)$$

Where σ describes the scale parameter, γ describes the shape parameter, and μ describes the location parameter. The limiting of γ→0 allows the approximation to fit the Gumbel distribution, which has been commonly used as a recommendation when modelling marine structures (Næss, 2013).

$$\mathrm{FX}_e(\mathrm{x}) \;=\; \exp\left[-\exp\left[-\alpha(\mathrm{x} \;-\; \mu)\right]\right] \qquad (28)$$

Where α describes the scale parameter and μ is the location parameter established using a Gumbel probability paper. Eq. (28) can be rewritten by using a logarithm on the equation to becoming a linear function.

$$-\ln(-\ln(\mathrm{FXe}(\mathrm{x}))) \;=\; \alpha(\mathrm{x} \;-\; \mu) \qquad (29)$$

The parameters α and μ can be approximated from the original data using the least-square fitting method from the cumulative distribution probability, which is characterized as a straight line on a probability paper (Fu, 2017). Figure 39 shows an example of a Gumbel paper as described in (Xu, 2019).

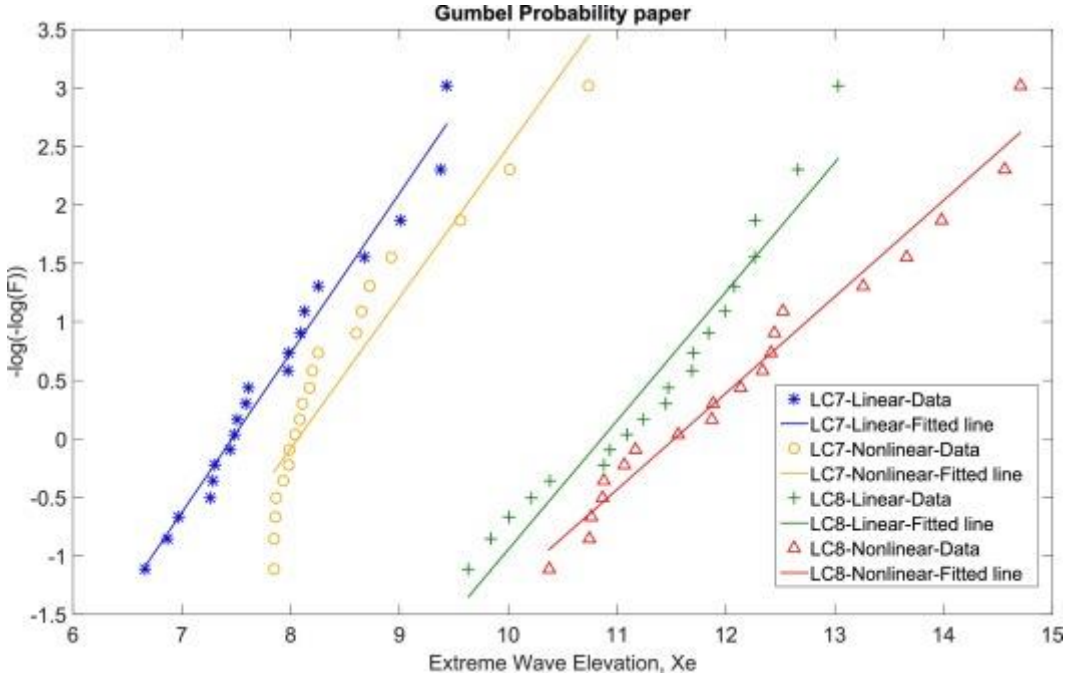

Figure 39 Gumbel Comparison (Xu, 2019)

5.1.4 Extreme value prediction - ACER1D method

Various statistical methods have been used to approximate the extreme value distribution of a recorded time series in its tail. Examples of the extreme value methods used in the study of wind turbines include an estimation of extreme structural responses in floating vertical axis wind turbines, see (Cheng, 2017) and extreme responses due to wave nonlinearity on a semi-submersible floating wind turbine, see (Xu, 2019).

The ACER method used in this paper as in (Naess, 2010; Naess, 2008; Xu, 2021; Zhao, 2021; Galambos, 1999; Naess, 2013; Naess, 2009), and in (Gaidai, 2017; Xu, 2021; Xu, 2020; Naess, 2015; Karpa, 2015; Gaidai, 2016) has numerous advantages when estimating extreme values from a recorded time series. One of these includes the ability to identify the effect of dependency between the time series data on the extreme value distribution. Also, the whole time series can be used as input data without de-clustering (i.e., no requirement to use independent data). However, the most prominent feature of the ACER method is its ability to provide a non-parametric depiction of the extreme value distribution inherent in the data. Therefore, this circumvents the need for explicit modelling due to seasonal effects as this method automatically accounts for it. Also, using the ACER method and an appropriate

parametric function for tail modelling allows for an explicit description of the extreme value distribution suitable for deep tail extrapolation. Furthermore, this method also seeks to approximate the extreme value distribution in the non-asymptotic regime, which differs from the most commonly known extrapolation methods, i.e., Gumbel, POT (peaks over threshold) or Weibull distribution. Recent studies using the ACER method include the study of vessels extreme roll assessment (Xu, 2021) and extreme response in a mooring system, see (Zhao, 2021).

When extrapolating extreme values distributions, the most commonly used distributions are faced with obstacles as they require an asymptotic behaviour. This behaviour cannot be entirely substantiated; thus, its choice is based on convenience. Wrongly selected asymptotic distributions can result in errors when extrapolating to long return period design values. For example, in (Galambos, 1999), the authors explained that a Gumbel distribution might be wrongly interpreted as a Weibull distribution since the data used partially fits the upper bound of the Weibull distribution. The result is a wrongly fitted asymptotically inconsistent distribution, resulting in wrongly approximated values (i.e., wind speed or extreme values).

X(t) is the long-term global response of a floating wind turbine measured between the time interval *(0,T)*. The discrete-time interval in *(0,T)* is defined as $t_1, \dots, t_N$, while process measurement *X(t)* at this discrete-time interval is defined as $X_1, \dots, X_N$ to approximate the distribution function of the extreme value $M_N = \max\{X_j; j = 1, \dots, N\}$, especially to estimate cumulative density function (CDF) $P(\eta) = \mathrm{Prob}(M_N \leq \eta)$ for large values of the response η.

Therefore, the below mentioned random functions are presented:

$$A_{kj}(\eta) = \mathbf{1}\{X_j > \eta, X_{j-1} \leq \eta, \dots, X_{j-k+1} \leq \eta\}, \qquad j = k, \dots, N, k = 2, 3, \dots$$
$$A_{kj}(\eta) = \mathbf{1}\{X_j > \eta, X_{j-1} \leq \eta, \dots, X_{j-k+1} \leq \eta\}, \qquad j = k, \dots, N, k = 2, 3, \dots \quad (30)$$
$$B_{kj}(\eta) = \mathbf{1}\{X_{j-1} \leq \eta, \dots, X_{j-k+1} \leq \eta\}, \qquad j = k, \dots, N, k = 2, 3, \dots$$

Where, when $\mathcal{A}$ is true, $\mathbf{1}\{\mathcal{A}\} = 1$; if not it is 0. As mentioned in (Naess, 2010; Naess, 2008; Xu, 2021; Zhao, 2021; Galambos, 1999; Naess, 2013; Naess, 2009):

$$P_k(\eta) \approx \exp\left(-\sum_{j=k}^{N} \frac{\mathbb{E}(A_{kj}(\eta))}{\mathbb{E}(B_{kj}(\eta))}\right) \approx \exp\left(-\sum_{j=k}^{N} \mathbb{E}\left(A_{kj}(\eta)\right)\right), \qquad \eta \to \infty \quad (31)$$

The recorded time series can be further divided into short-term *K* subsequent blocks where $\mathbb{E}(A_{kj}(\eta))$ remains almost constant for each block. Such that $\sum_{j\in C_i} \mathbb{E}\left(A_{kj}(\eta)\right) \approx \sum_{j\in C_i} a_{kj}(\eta)$ for a large enough range of η-values. Hence, $\sum_{j=k}^{N} \mathbb{E}\left(A_{kj}(\eta)\right) \approx \sum_{j=k}^{N} a_{kj}(\eta)$, where C_i indicates the set of indices for block numbered as i; from $i = 1, \dots, K$, and where $a_{kj}(\eta)$ are the realised values of $A_{kj}(\eta)$ for the

calculated time series. Therefore, for a given stationary process (short-term sea current state), the following is:

$$P_k(\eta) \approx \exp\left(-(N-k+1)\hat{\varepsilon}_k(\eta)\right) \quad (32)$$

where,

$$\hat{\varepsilon}_k(\eta) = \frac{1}{N-k+1}\sum_{j=k}^{N} a_{kj}(\eta) \quad (33)$$

In the above equations, to make an approximation of the short-term expected values, the observed values of the $a_{kj}(\eta)$ functions were used together with the assumption of ergodicity for each short-term section of the recorded time series. Another way of describing the long-term extreme value distribution in Eq. (32) can be realised since the empirical probability distribution of, $m = 1,..,M$, of sea current states has probabilities p_m, and $\sum_{m=1}^{M} p_m = 1$.

Thus, the long-term ACER function of order *k* is:

$$\mathrm{ACER_k}(\eta) \equiv \sum_{m=1}^{M} \hat{\varepsilon}_k(\eta, m)\, p_m \quad (34)$$

where $\hat{\varepsilon}_k(\eta, m)$, which is restricted to a specific sea state with number m, is the same type of function as in Eq. (33), but the averaging is restricted to the short-term block of data with number m.

As mentioned in (Naess, 2010; Naess, 2008; Xu, 2021; Zhao, 2021; Galambos, 1999; Naess, 2013; Naess, 2009), the long-term extreme value distribution of $M(T)$, can then be described according to the ACER function of order *k*:

$$P(\eta) \approx \exp\left(-N \cdot \mathrm{ACER_k}(\eta)\right) \quad (35)$$

where $ACER_k(\eta)$ is defined as the long-term empirical function for ACER in the order of *k*, where *k* "N; N is the number of all the data points from the recorded time series included to approximate the ACER functions. Stereotypically, these are local peaks from the measured time series.

The accuracy of Eq. (35) improves as the order *k* increases; it is observed that the $\mathrm{ACER_k}(\eta)$ functions converge rapidly with an increasing *k,* also mentioned in (Naess, 2010; Naess, 2008; Xu, 2021; Zhao, 2021; Galambos, 1999; Naess, 2013; Naess, 2009). The advantage of the ACER method can be observed when increasing the conditioning level *k*. The probable data clustering effects can be accounted for,

thus improving and refining the accuracy of the estimates of the extreme values, and this also circumvents an otherwise over-conservative design value.

In high response values of η, $ACER_k$ as functions of the level, η are usually in the tail end. Especially for $\eta \geq \eta_0$, when the tail behaves like $\exp\{-a(\eta + b)^c + d\}$ with a, b, c, d becomes suitable constants.

It is possible to do optimisation for the log-level when the mean square error function *F* is minimised with respect to the four arguments: a_k, b_k, c_k, d_k.

$$F(a_k, b_k, c_k, d_k) = \int_{\eta_0}^{\eta_1} \omega(\eta) \left\{ \ln\left(ACER_k(\eta)\right) - d_k + a_k(\eta + b_k)^{c_k} \right\}^2 d\eta, \qquad \eta \geq \eta_0 \qquad (36)$$

where η_1 is a suitable data cut-off value, i.e., the largest η response value, which allows calculation of the confidence interval. The weight function (ω) is defined as $\omega(\eta) = \{\ln C^+(\eta) - \ln C^-(\eta)\}^{-2}$ with $\left(C^-(\eta),\ C^+(\eta)\right)$ with a 95% CI, empirically approximated from the measured data. The comprehensive procedure for additional parameters optimisation a_k, b_k, c_k, d_k has been described in (Zhang,2019; Gaidai, 2018; Gaidai, 2016; Naess, 2008; Naess, 2009; Naess, 2010; Naess, 2013; Karpa, 2013) and, (Naess, 2010; Naess, 2008; Xu, 2021; Zhao, 2021; Galambos, 1999; Naess, 2013; Naess, 2009).

5.1.5 Extreme value prediction – ACER2D method

Now, the 2D (bivariate) Average Conditional Exceedance Rate, or briefly ACER2D method, has been applied to analyse FWT blade root and tower bottom bending moment due to environmental wind and wave loads. A brief introduction of the bivariate ACER2D method is outlined below; see (Naess, 2013; Karpa, 2015; Gaidai, 2016; Jian, 2018) for more details. Note that both of the stochastic response processes (blade root and tower bottom bending moments) are time-synchronous. The latter is undoubtedly beneficial for coupling effects and bivariate statistics study.

This paper studies a bivariate stochastic process $Z(t) = (X(t), Y(t))$, having two scalar processes $X(t), Y(t)$, simulated synchronously, over a time span $(0, T)$. The bivariate data points $(X_1, Y_1), \ldots, (X_N, Y_N)$ correspond to equidistant time instants $t_1, \ldots, t_N$.

The joint CDF (cumulative distribution function) $P(\xi, \eta) := \text{Prob}\left(\hat{X}_N \leq \xi, \hat{Y}_N \leq \eta\right)$ of the maxima vector $\left(\hat{X}_N, \hat{Y}_N\right)$, with $\hat{X}_N = \max\{X_j\,; j = 1, \ldots, N\}$, and $\hat{Y}_N = \max\{Y_j\,; j = 1, \ldots, N\}$ is introduced. In this paper, ξ and η are blade root and tower bottom mooring bending moments, M_1 and M_3 in Figure 40) respectively.

Next, the non-exceedance event is introduced: $\mathcal{C}_{kj}(\xi, \eta) := \{X_{j-1} \leq \xi, Y_{j-1} \leq \eta, \ldots, X_{j-k+1} \leq \xi, Y_{j-k+1} \leq \eta\}$ for $1 \leq k \leq j \leq N + 1$. Based on the definition of the joint CDF $P(\xi, \eta)$

$$
\begin{aligned}
P(\xi,\eta) = \ & \text{Prob}\left(\mathcal{C}_{N+1,N+1}(\xi,\eta)\right) \\
= \ & \text{Prob}\left(X_N \le \xi, Y_N \le \eta \mid \mathcal{C}_{NN}(\xi,\eta)\right) \cdot \text{Prob}\left(\mathcal{C}_{NN}(\xi,\eta)\right) \\
= & \prod_{j=2}^{N} \text{Prob}\left(X_j \le \xi, Y_j \le \eta \mid \mathcal{C}_{jj}(\xi,\eta)\right) \cdot \text{Prob}\left(\mathcal{C}_{22}(\xi,\eta)\right)
\end{aligned}
\tag{37}
$$

The CDF $P(\xi,\eta)$ can be expressed as in (Naess, 2013; Karpa, 2015; Gaidai, 2016; Jian, 2018),

$$
P(\xi,\eta) \approx \exp\left\{-\sum_{j=k}^{N}\left(\alpha_{kj}(\xi;\eta) + \beta_{kj}(\eta;\xi) - \gamma_{kj}(\xi,\eta)\right)\right\} \tag{38}
$$

for a suitably large conditioning level parameter k, and large ξ and η with $\alpha_{kj}(\xi;\eta) \coloneqq \text{Prob}\left(X_j > \xi \mid \mathcal{C}_{kj}(\xi,\eta)\right)$, $\beta_{kj}(\eta;\xi) \coloneqq \text{Prob}\left(Y_j > \eta \ \middle| \mathcal{C}_{kj}(\xi,\eta)\right)$, $\gamma_{kj}(\xi,\eta) \coloneqq \text{Prob}\left(X_j > \xi, Y_j > \eta \mid \mathcal{C}_{kj}(\xi,\eta)\right)$.

Next, the k-th order bivariate average conditional exceedance rate (ACER2D) functions can be introduced

$$
\mathcal{E}_k(\xi,\eta) = \frac{1}{N-k+1}\sum_{j=k}^{N}\left(\alpha_{kj}(\xi;\eta) + \beta_{kj}(\eta;\xi) - \gamma_{kj}(\xi,\eta)\right) \tag{39}
$$

for $k = 1, 2, \ldots$; when $N \gg k$

$$
P(\xi,\eta) \approx \exp\{-(N-k+1)\mathcal{E}_k(\xi,\eta)\}; \text{ for large } \xi \text{ and } \eta. \tag{40}
$$

From Eq. (40), it follows that an accurate estimate of the bivariate CDF $P(\xi,\eta) = P(\xi,\eta)$ relies on the equally accurate estimation of ACER2D functions $\mathcal{E}_k$.

5.2 Results and Discussion

The empirical data is based on accurate numerical simulations using a FAST model on the DTU 10MW FWT as presented in Section 3.3.3. The ACER1D and ACER2D (bivariate averaged conditional exceedance rate) methods used for the extreme load prediction are presented in Sections 5.1.4 and 5.1.5, respectively.

The loads at the two measurement points presented in Figure 40 are considered. These are the blade 1 root flapwise bending moment (RootMyb1) and tower bottom fore-aft bending moment (TwrBsMyt).

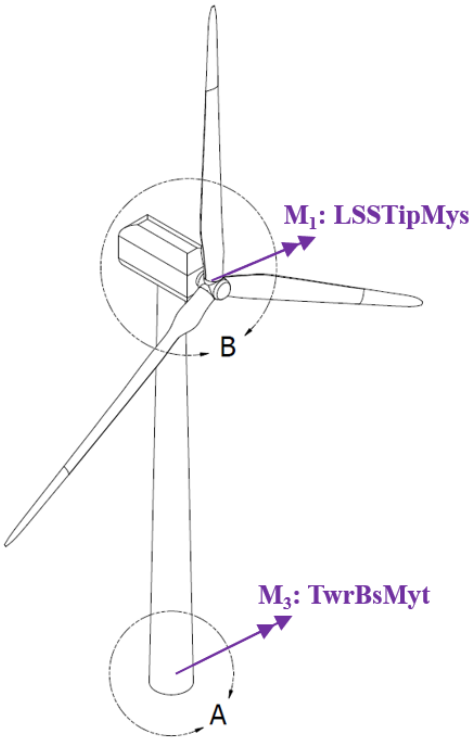

Figure 40 Location of points where bending moments are measured

5.2.1 Power Spectral Density based on time responses

Figure 41 shows the location of M_1, M_3. From Figure 41, it is observed that the PSD (Power Spectral Density) peaks at the frequencies (*f)* at 3P, 6P and 9P. This information is used in the ACER functions' choice of conditioning level k.

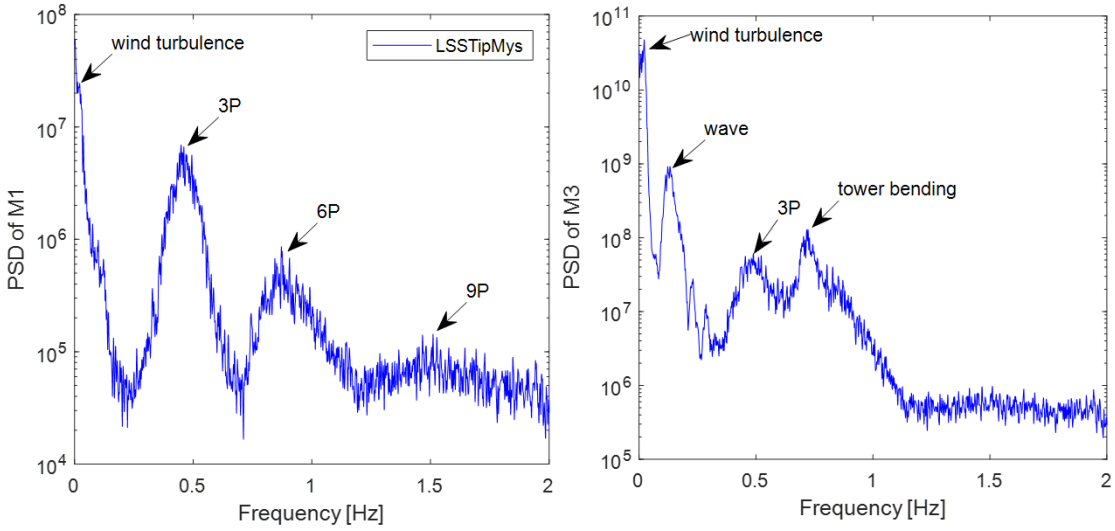

Figure 41 PSD of RootMyb1 – M1 and TwrBsMyt – M3

5.2.2 Extreme responses: univariate and bivariate analysis

This section presents statistical analysis results for M_1 and M_3 bending moments using the univariate and bivariate methods, i.e., ACER1D and ACER2D, respectively. The focus is on accurate predicting extreme responses, which is vital for safety and reliability at the design stage. The conditioning level *k* is set to be 10, as it was observed that ACER functions have converged at that level in the distribution tail.

Figure 42 presents a univariate extreme response 5-year return period prediction with a 95 % confidence interval (CI); the 1-year return period is chosen purely as an example. The predicted extreme probability level corresponds to a 5-year return period.

From Figure 42, the ACER1D method gives a smaller confidence interval and better results as it does not assume any distribution. It shadows the data point as presented Figure 42 for M1 and M3. Paper-II only presents the ACER1D results without comparing them with another extreme value distribution, as this is done with detail in Paper III. Paper-II presents the results and moves on together to do the ACER2D novel investigation. The ACER2D results will be presented in the next sections.

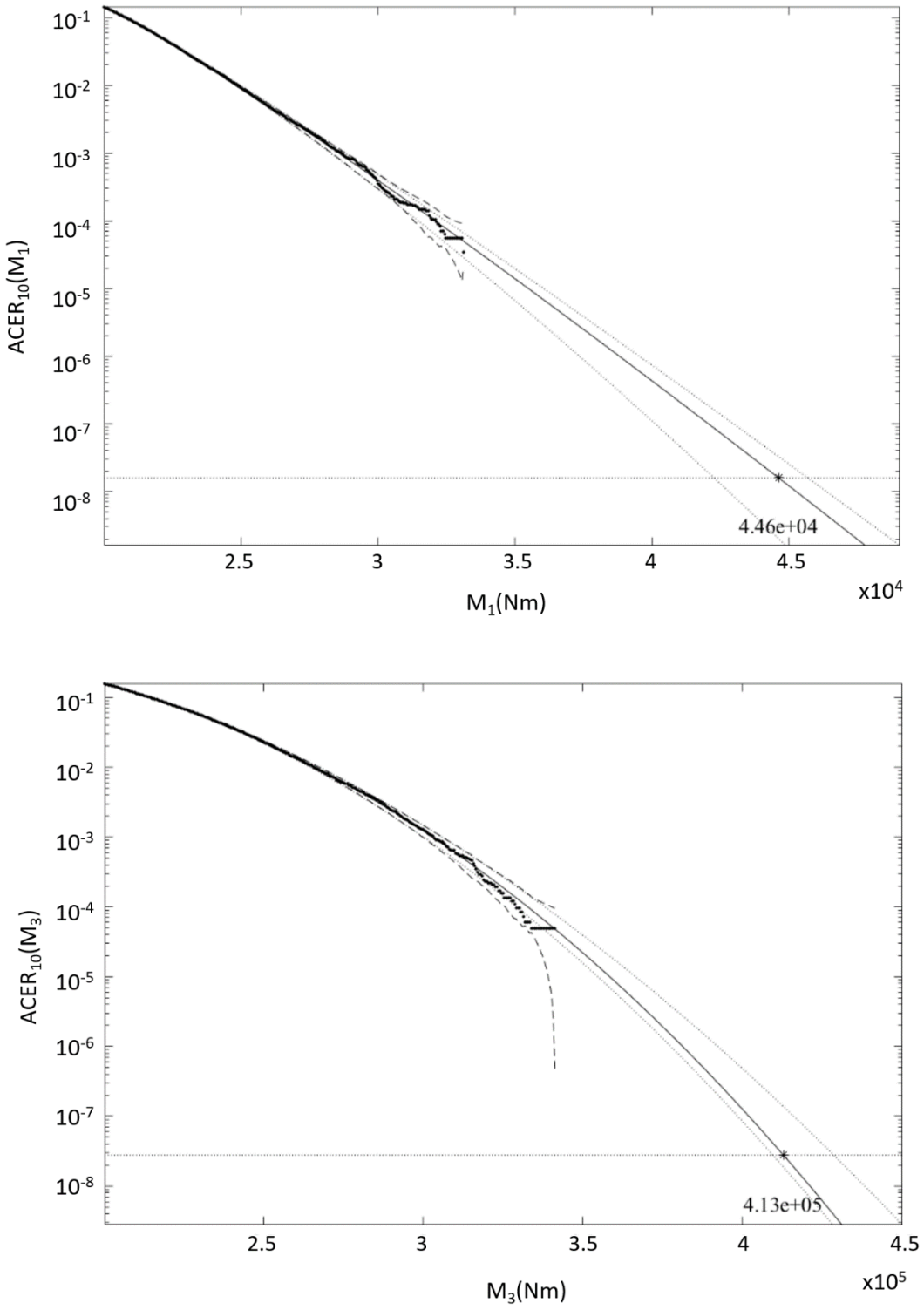

Figure 42 Univariate ACER1D extreme response 5-year prediction with 95% CI (dotted lines). Top: RootMyb1 – M1; Bottom: TwrBsMyt – M3; decimal log scale

Figure 43 presents the phase space of responses M_1 over M_3, along with the bivariate empirical ACER2D function $\hat{\mathcal{E}}_k$. It is clearly seen that there is a non-linear correlation between responses M_1 and M_3. The

bivariate empirical ACER2D surface, $\hat{\mathcal{E}}_k$ obviously marginally corresponds to univariate ACER1D functions presented in Figure.

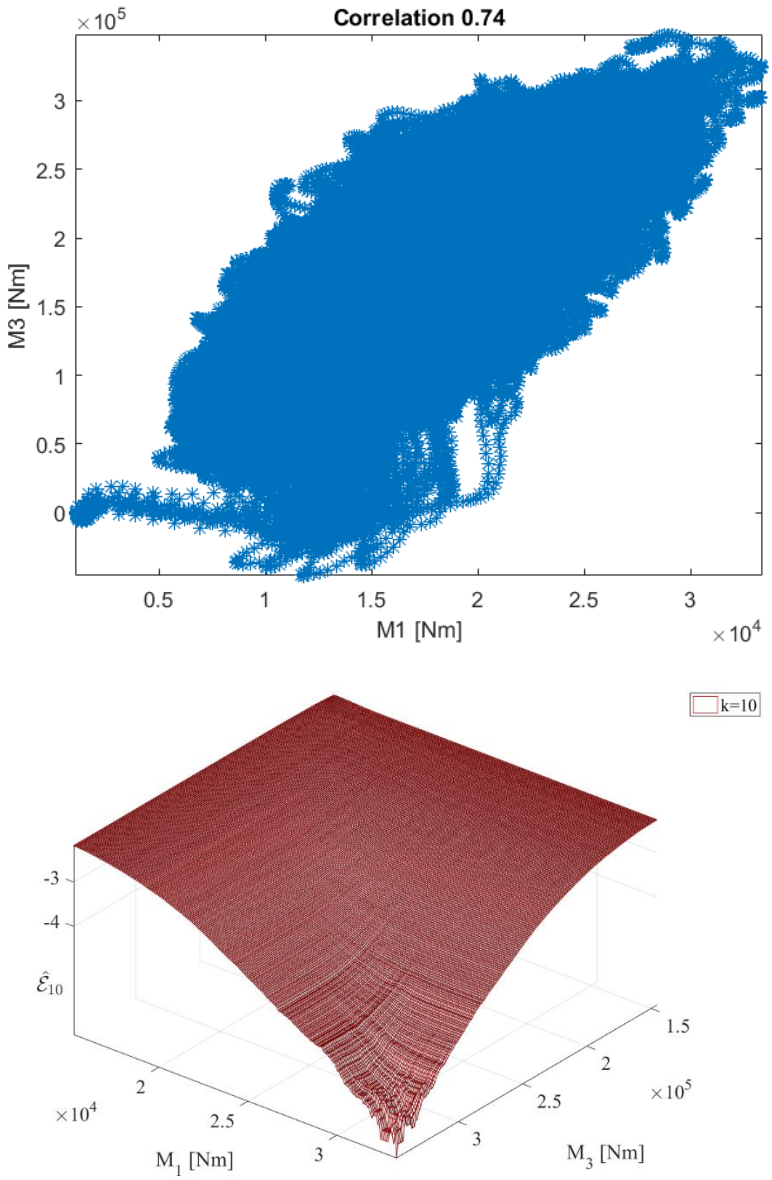

Figure 43 Top: phase space, response M1 vs M3; Bottom: bivariate empirical ACER2D function E^_k, decimal log scale

Figure 44 presents ACER2D fit to the empirical data along with the bivariate predicted contours with return periods in years (lower figure). Figure 44 presents contour lines for the optimized Asymmetric logistic (AL) $\mathcal{A}_k(M_1, M_3)$ and optimized Gumbel logistic (GL) $\mathcal{G}_k(M_1, M_3)$ models, optimally matched to the corresponding empirical bivariate ACER2D function $\hat{\mathcal{E}}_k(M_1, M_3)$, $k = 10$, see (Naess, 2013; Karpa, 2015; Gaidai, 2016; Jian, 2018) for GL and AL definitions. The contour lines' negative labelling numbers in Figure 44 indicate decimal logarithmic scale probability levels of $P(M_1, M_3)$. Figure 44

clearly shows that the empirical bivariate ACER2D surface $\hat{\mathcal{E}}_{10}$ well captures the strong correlation between load/response components. The optimized models $\mathcal{G}_{10}$ and $\mathcal{A}_{10}$ exhibit smooth contours along with matching ACER2D empirical contours. The later models may be better suited for bivariate extreme value distribution response processes. Figure 44 shows good agreement between the estimated optimized AL and GL surfaces and the bivariate ACER2D surface. This means that the correlation between responses M_1 vs M_3 is a crucial non-negligible factor influencing the shape of the bivariate contour lines.

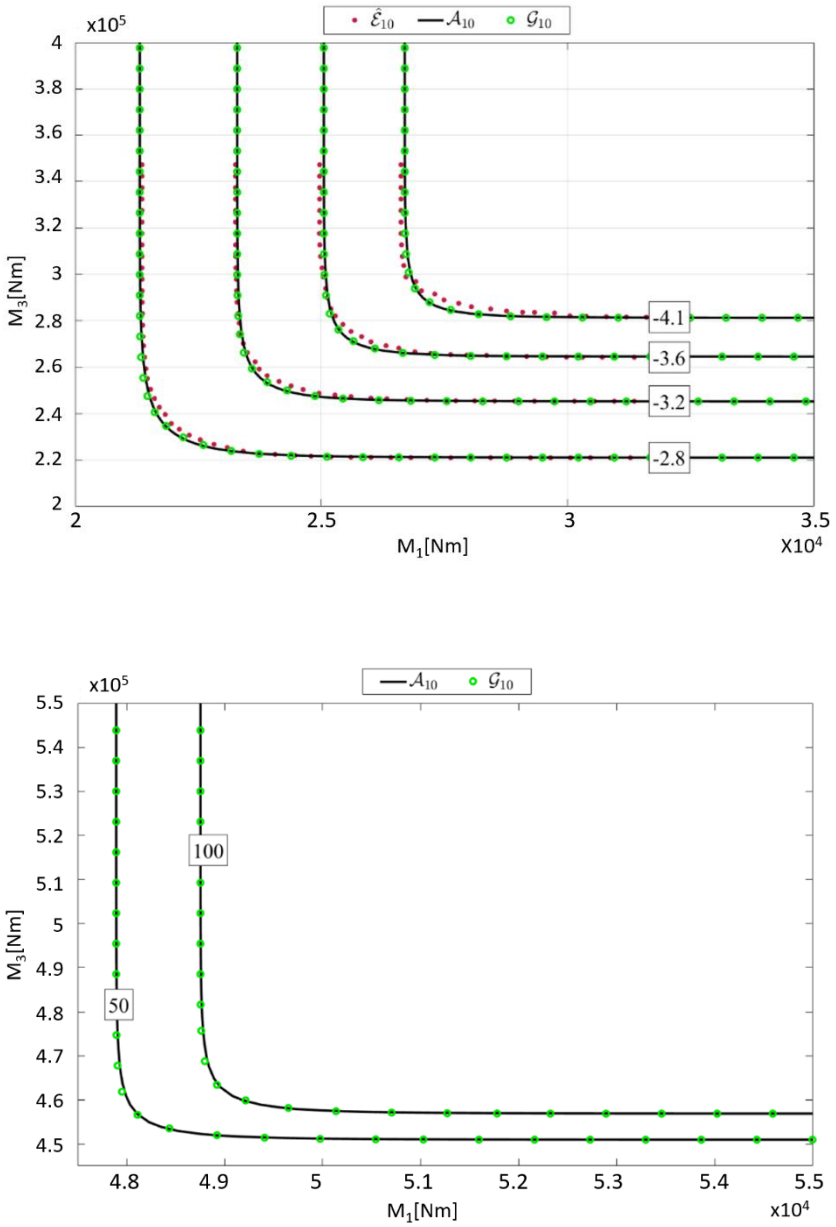

Figure 44 Top: ACER2D fit to empirical data; Bottom: predicted bivariate contours with return periods in years

The lowest probabilities in Figure 43 and Figure 44 correspond to the value N^{-1} where N is the number of equidistant time points in the studied time series, see Eqs. (30) to (37). Figure 43Figure 44 (bottom) presents the predicted bivariate contours with 50- and 100-year corresponding return periods. Note that the return period of a few years is quite long compared to the short duration of the analysed measured record. As seen in Figure 44 (bottom), the fitted lines match well with the empirical data (when seen with the Asymmetric logistic and Gumbel logistic models), highlighting the accuracy of the ACER method. Further, the ACER method is efficient, requiring only 20 1-hour realisations to generate accurate results.

Furthermore, Figure 45 shows that the univariate design point lies outside the safe 50-year zone (dashed area) and is outside the 2D design zone. This means that the 1D method is not conservative.

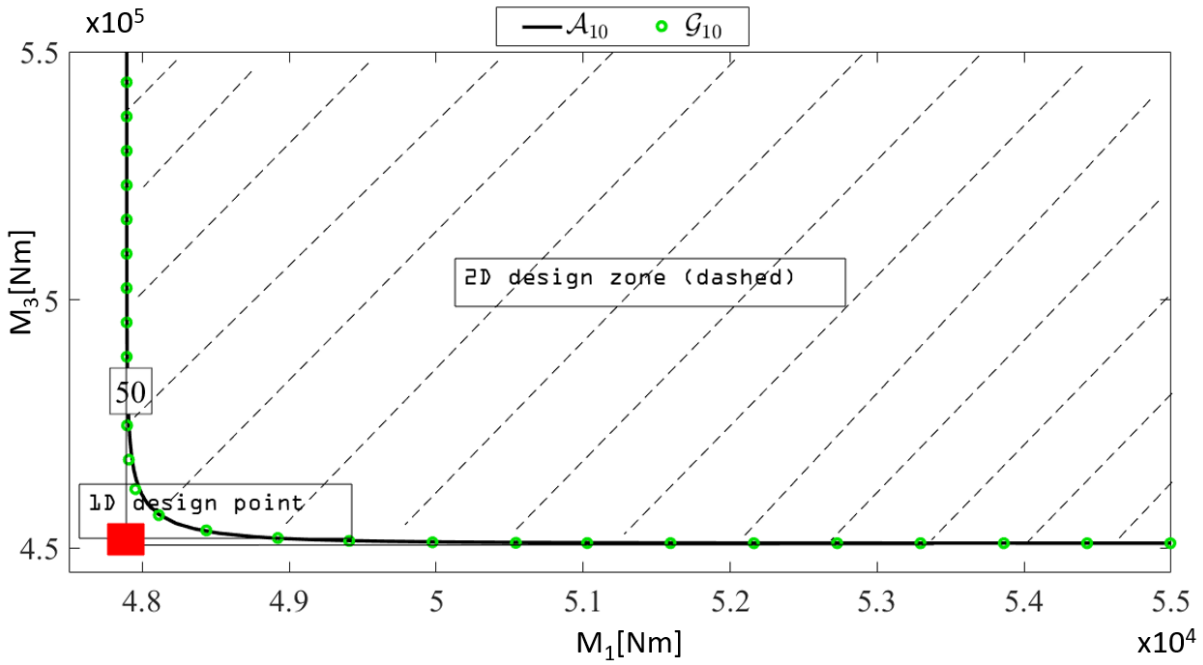

Figure 45 Design safe zone (dashed) due to bivariate analysis, versus univariate design point, based on the previous Figure 44 Asymmetric logistic $\mathcal{A}_k(M_1, M_3)$ 50-year contour line.

	50 yr	**100 yr**
M_1 (Nm)	4.8 x 10^4	4.9 x 10^4
M_3 (Nm)	4.5 x 10^5	4.6 x 10^5

Table 16 50- and 100-year return period response ACER1D predictions

Thus, it is clear from the discussion above that the ACER method gives reliable data, compared with the AL and GL models, with very good ACER2D fitting with minimal data set. It is comparable with the empirical data verifying the accuracy of the ACER method.

5.3 Conclusion

A novel approach that is based on a 2D design point instead of the traditional 1D characteristic design values has been introduced. The proposed methodology provides an accurate bivariate extreme value prediction, utilizing all available data efficiently. Based on the overall performance of the proposed method, it was concluded that the ACER2D method could incorporate environmental input and provide a more robust and accurate bivariate prediction based on proper numerical simulations. The method uses only a relatively small amount of data to provide reasonable predictions with long return periods.

The FWT blade root and tower bottom bending moments due to environmental wind and wave loads were studied for three operating conditions of mean wind speeds of 8, 12 and 16 m/s. The bivariate ACER2D method was briefly described and applied to account for the coupled load effects, namely dynamic moment and force simulated synchronously in time. Bivariate extreme value distribution low probabilities (or equivalently high quantiles) contours were estimated by adopting various bivariate copula models. Potential outliers present in the data set are also well managed by being neglected in the distribution tail through the proposed extrapolation and copula fit technique.

Regarding the safety and reliability of FWT operations, the multivariate analysis is a more proper approach than the classic univariate approach. The presented technique has the following advantages:

- Unlike IFORM/ SORM, the ACER2D method does not simplify model nonlinearities.
- Various kinds of coupled data can be studied: measured or numerically simulated.
- Clustering effects can be accounted for.
- The univariate estimation of design values may not be conservative, as indicated through the comparison to a bivariate analysis as presented in this paper.
- ACER2D method may provide an efficient way of identifying practical design appropriate bivariate copula models.

The described approach may be used at the design stage of a large FWT to provide the opportunity of defining FWT parameters that would minimize extreme loads and potential damages. It is also noted that the study is limited to the quality of the data itself. This limitation applies for any type of statistical method.

6 Paper III - Characterization of Extreme Load Responses using Gumbel and ACER1D

The area of interest in the third part of the thesis is to complete the characterization of extreme load responses of a 10-MW floating semi-submersible type wind turbine. Since sizes of offshore wind turbines have been increasing over the past two decades (1.5MW to 6 MW), it has become more critical than ever to start analyzing the loads acting on the very large offshore wind turbine (10 to 15 MW class). The larger the turbine, the larger structural flexibility, aero-hydrodynamics and the more complex the controller dynamics, which all result in a more complex structural response. Thus, the structural load effects in an FWT become more severe than in the previously used smaller turbines. Thus, more accurate quantification of the extreme load responses becomes important in the Ultimate Limit State (ULS), especially with a fully coupled interaction between the system and environmental conditions.

Accurate quantification of the extreme values is critical when studying dynamic motion in FWT systems. It becomes even more critical when designing a wind turbine based on the Ultimate Limit State (ULS). Furthermore, the responses are expected to be dynamic and nonlinear due to the fully coupled reaction between the wind turbine and the environment. Thus, ensuring that the extreme load effects are all addressed in the requirements is essential. Doing many dynamic simulations to obtain accurate results in an ideal situation might be useful. However, such a process is time-consuming and expensive. Therefore, a statistical extrapolation method is suggested to mitigate such a limitation in IEC 61400-3 when analyzing extreme loads, as it requires a much smaller pool of data to estimate these values accurately. Many studies have been conducted to assess the effectiveness of the ACER1D or ACER2D model, as discussed in the previous chapter. In (Saha, 2014), the author examined the sensitivity of the extreme responses to sample sizes and discovered that the up-crossing rate method outperformed both the Gaussian and non-Gaussian responses. While in (Dimitrov, 2006), the author showed that the statistical load extrapolation method could accurately predict the statistical distribution (under normal operating conditions) of extreme values.

Similar to the second section (Paper-II), the focus of the work was on the DTU 10 MW semi-submersible types floating FWT. However, in Paper III, motivated by previous success from accurate prediction for other statistical methods, the author focused on predicting, characterizing and comparing the extreme responses using the ACER1D and Gumbel methods. The ACER methods would need to be optimized by investigating an appropriate k value. The primary aim of this paper is done with the hope that the results of this paper will steer future research on very large FWTs.

6.1 Methodology

The simulations done on MATLAB/ Simulink on this project used the DTU 10 MW wind turbine, which follows the original project. A 10MW offshore wind turbine from the DTU was used with similar wind turbine properties, load cases and environmental conditions from the methodology section from Paper-II. The characterization of extreme load responses was done with ACER1D and Gumbel prediction and fitting. Additionally, the blade one's root flapwise bending moment (RootMyb1) was added as a third measurement point in this part of the thesis. The Gumbel and ACER1D methods presented in Sections 5.1.3.1 and 5.1.4 respectively, are used in this paper.

Like Paper II, the wind is generated using Turbsim (Jonkman, 2014b), and irregular waves are generated using the JONSWAP (Joint North Sea Wave Project) spectrum. The same load cases (LC1, LC2 and LC3) was also used to maintain consistency. For further information, see Section 5.1.

6.2 Results and Discussion

The empirical data is based on accurate numerical simulations using a FAST model on the DTU 10MW FWT as presented in Section 3.3.3. The extreme load prediction of the Gumbel and ACER1D methods are presented in Sections 5.1.3.1 and 5.1.4 respectively.

The loads at the three measurement points presented in Figure are considered. These are the blade one root flapwise's bending moment (RootMyb1), main shaft tip up-down bending moment (LSSTipMys) and tower bottom fore-aft bending moment (TwrBsMyt).

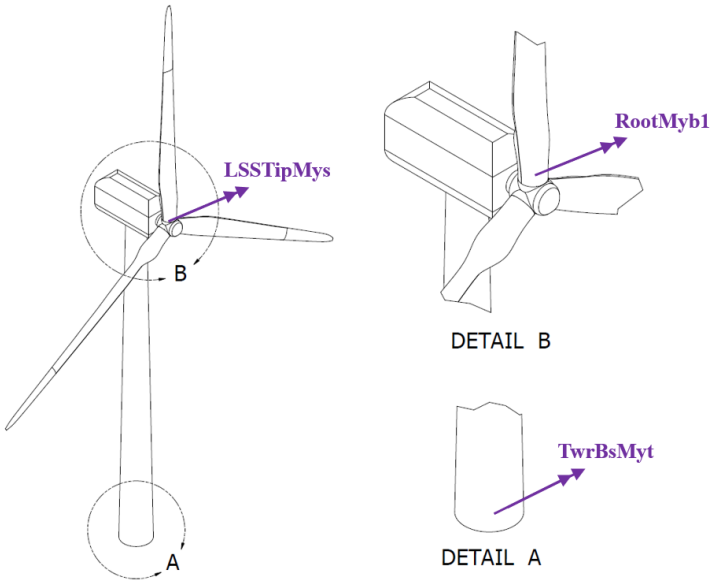

Figure 46 Location of measured bending moments

6.2.1 Time-domain responses, PSD, and maximum values

The time-domain responses for one portion, the power spectral distributions (PSDs) and the maximum values for the different realizations are presented in Figure 47, Figure 48 and Figure 49, Figure, respectively. The results from the different load cases LC1, LC2 and LC3 are generated, and one of each is displayed. In addition, the wind and wave elevation time series and PSDs are plotted in the figure as a reference.

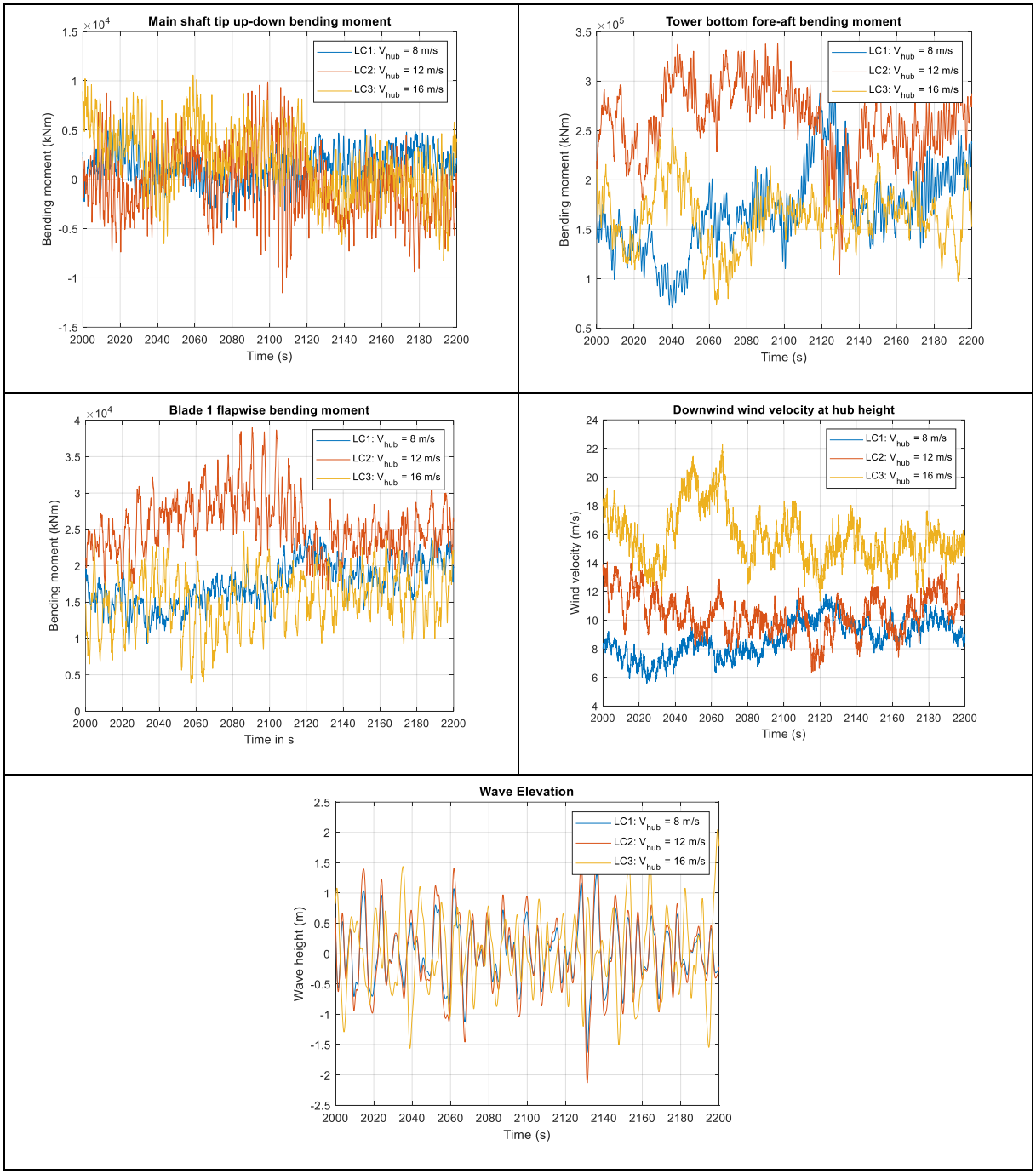

Figure 47 Time domain results. Figures Identity - Top-left: LSSTipMys; Top-right:TwrBsMyt; Centre-left: RootMyb; Centre-right: Wind velocity (Downwind at hub); Bottom: Wave elevation

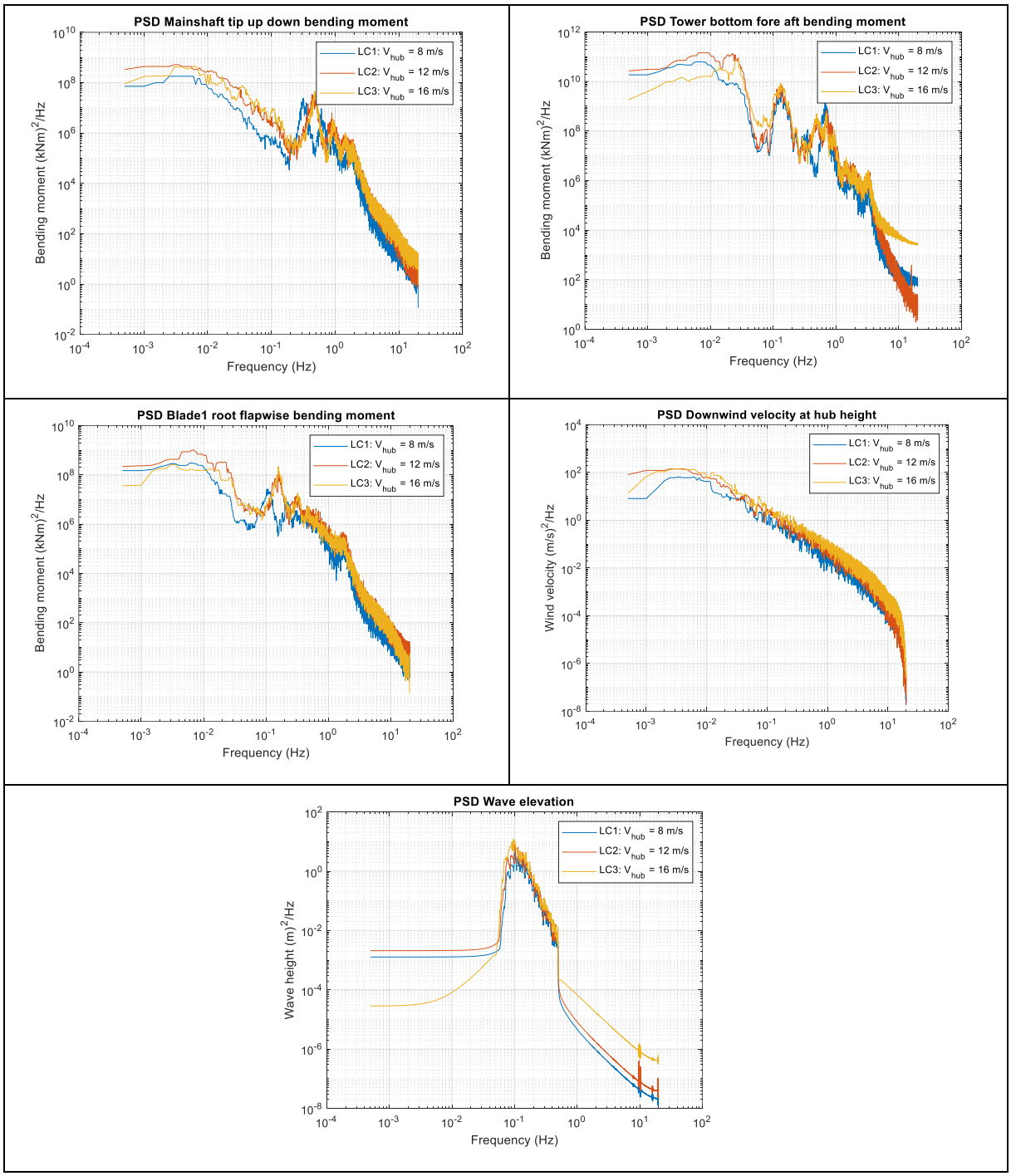

Figure 48 Power-Spectral-Distributions. Figures Identity - Top-left: LSSTipMys; Top-right:TwrBsMyt; Centre-left: RootMyb; Centre-right: Wind velocity (Downwind at hub); Bottom: Wave elevation

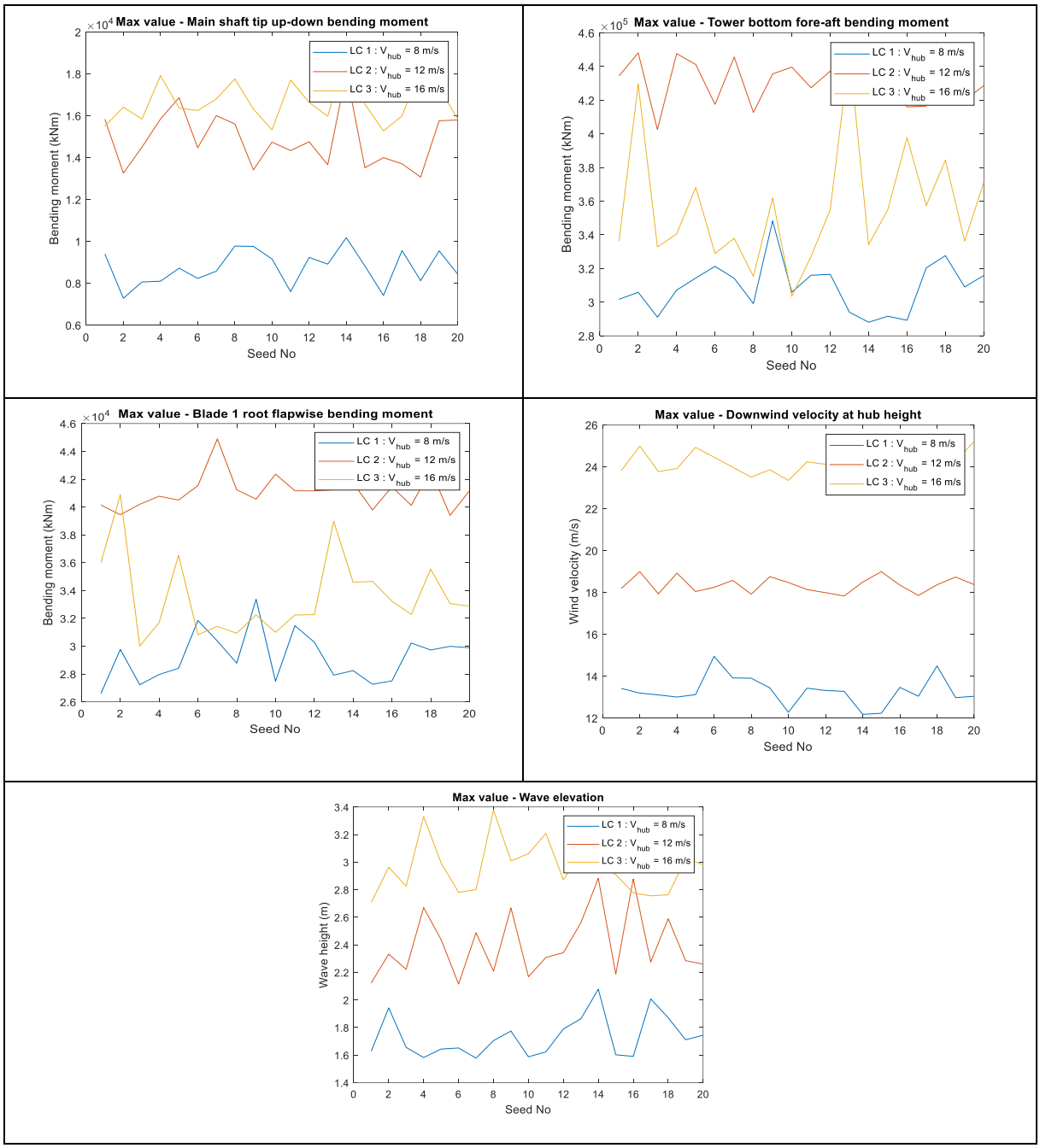

Figure 49 Maximum value in each realization. Figures Identity - Top-left: LSSTipMys; Top-right:TwrBsMyt; Centre-left: RootMyb; Centre-right: Wind velocity (Downwind at hub); Bottom: Wave elevation

6.2.2 Extreme load responses using ACER and Gumbel methods

The figures and table below show the ACER and Gumbel extreme load responses for the different cases (Table 15). shows an example for the ACER extrapolation and Gumbel fitting for TwrBsMyt under LC1. While Figure 50 and Figure 51 show all the three moments with ACER and Gumbel fitting at 95 % CI for all the three cases. K = 6 is used for the ACER method in the stimulations.

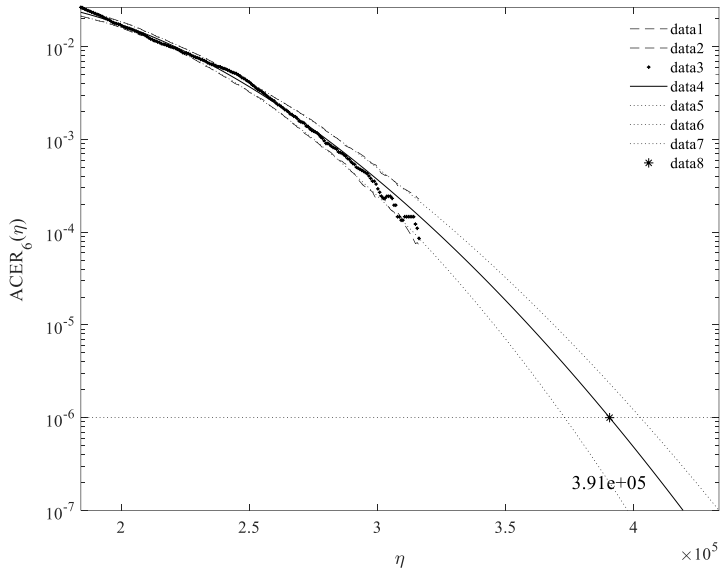

Figure 50 ACER extrapolation plot for TwrBsMyt for LC1

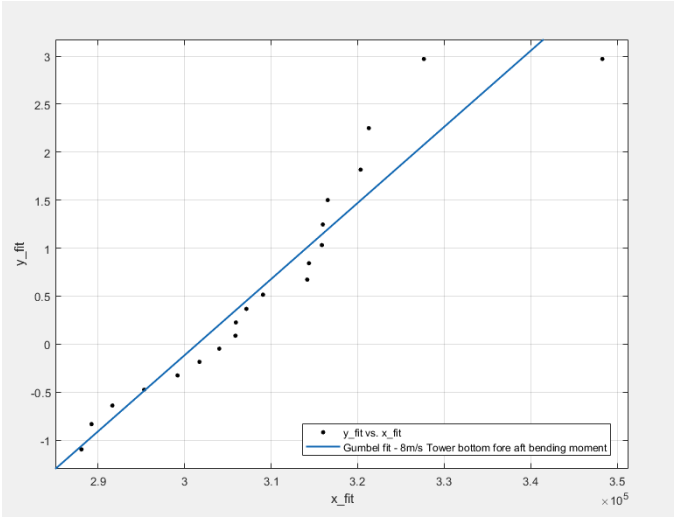

Figure 51 Gumbel fitting, TwrBsMyt, for TwrBsMyt for LC1

It can be seen that with a smaller confidence interval, the ACER1D method gives better results as it does not assume any distribution. Instead, it shadows the data point as presented in Figure 50. While it can be seen from Figure 51 that the Gumbel distribution is deviating away as the data points move towards the left, this result is an overestimation of extreme values in the Gumbel distribution, which clearly illustrates the benefits of the ACER1D method.

The respective extreme load responses and their respective 95% confidence intervals for both the ACER and Gumbel methods are plotted. Figure 52, Figure 53 and Figure 54 represents the RootMyb, LSSTipMys and TwrBsMyt, respectively, and each figure has all three cases (LC1, LC2 and LC3) plotted in them.

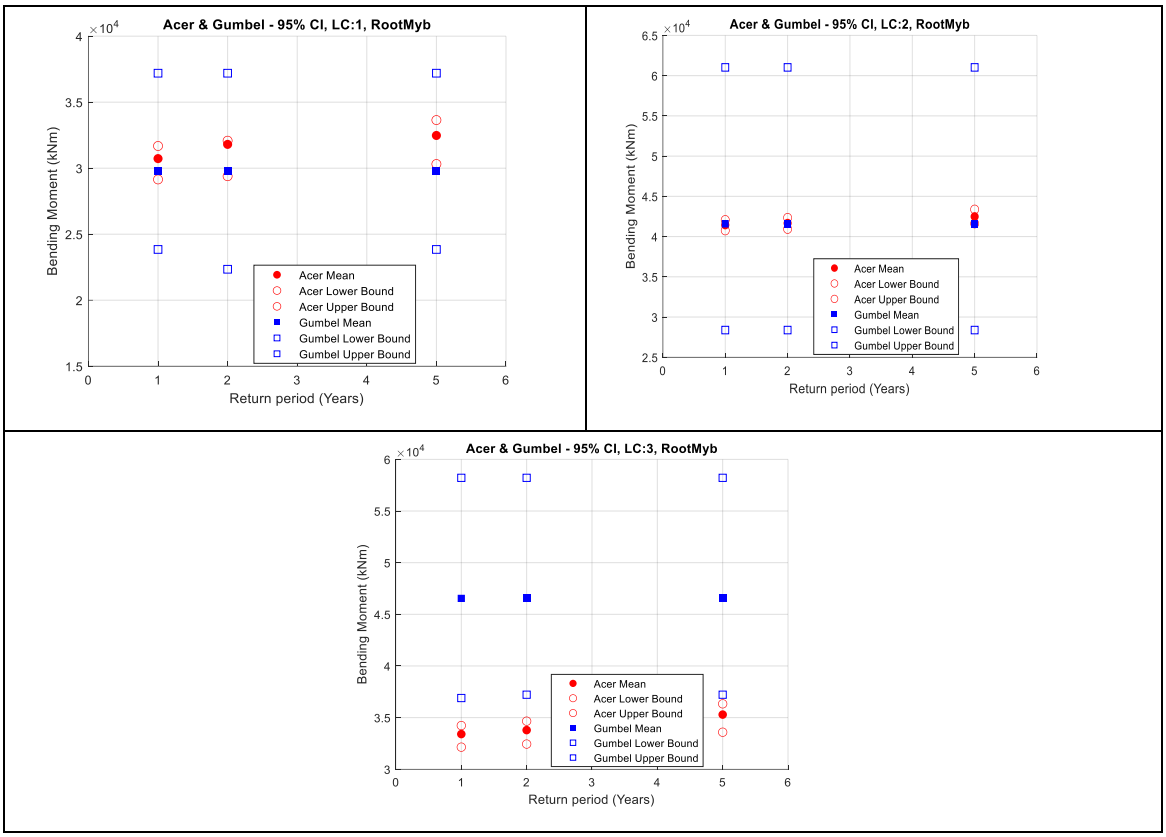

Figure 52 Blade 1 RootMyb. ACER and Gumbel (95 % CI); Top-left: LC1; Top-right: LC2; Bottom: LC3

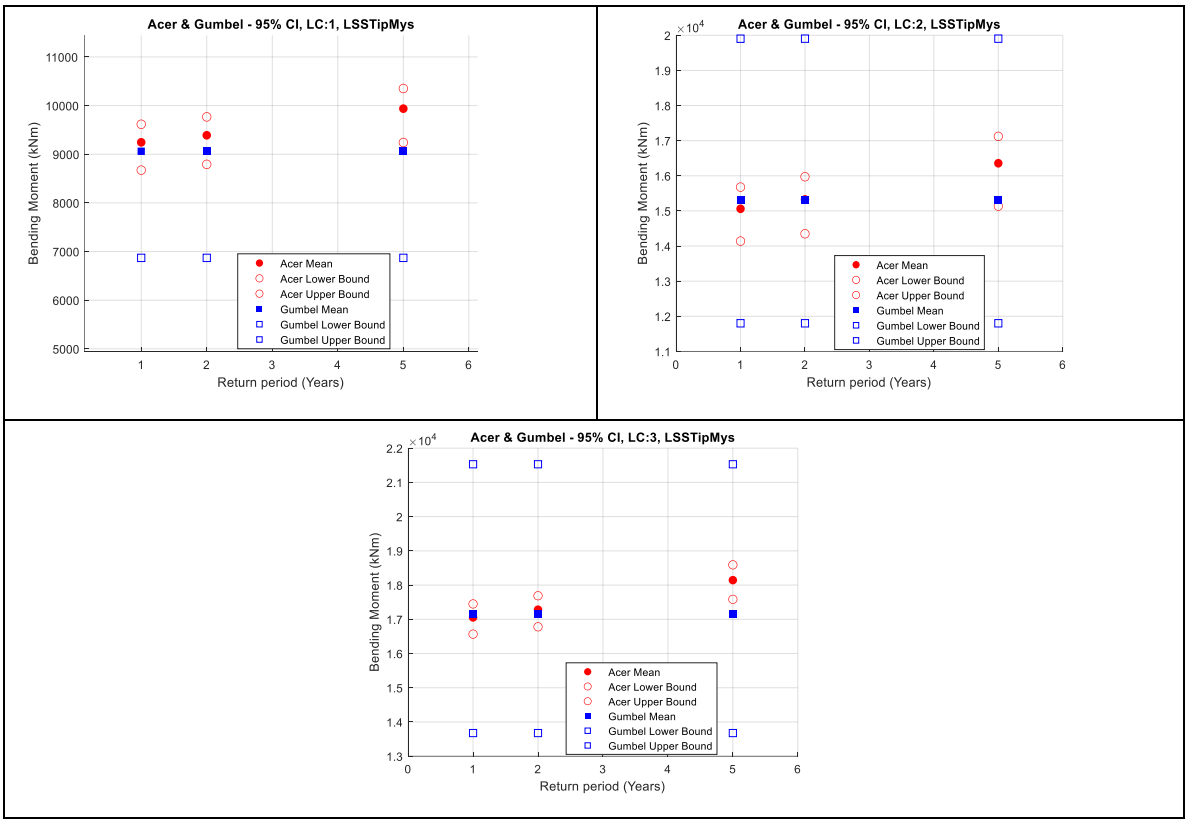

Figure 53 LSSTipMys. ACER and Gumbel (95 % CI); Top-left: LC1; Top-right: LC2; Bottom: LC3

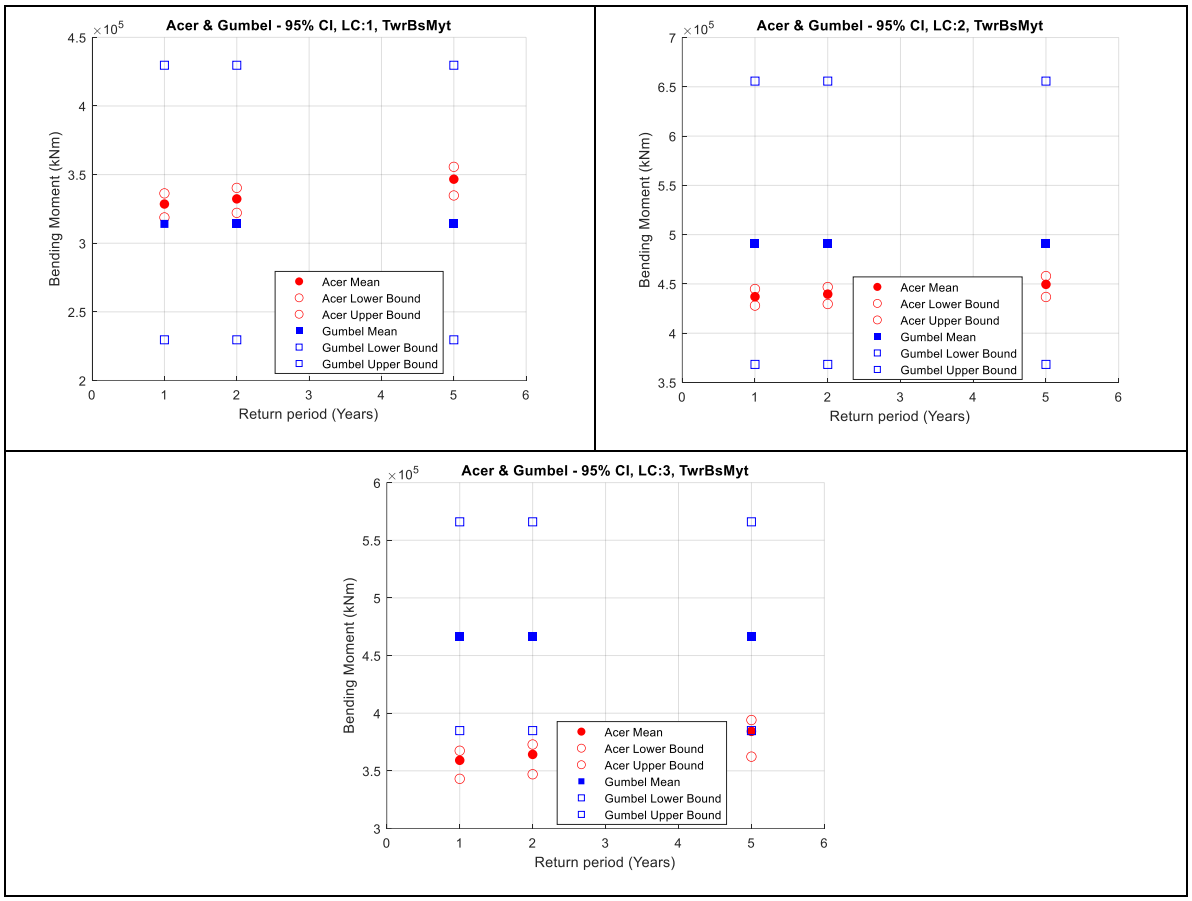

Figure 54 TwrBsMyt. ACER and Gumbel (95 % CI); Top-left: LC1; Top-right: LC2; Bottom: LC3

We can see from the figures that the 1, 2 and 5-year extreme values are about 1.2 x larger than the one-hour stimulation. Therefore, it is crucial to use extrapolation and accurate prediction methods when estimating extreme values with such high variation. This becomes especially important in design engineering. Furthermore, it is clearly observed that the 95 % confidence interval with the ACER1D method is clearly much smaller and thus better than that of the Gumbel distribution. This better ACER1D result can be attributed to the fact that the ACER1D does not impose any distribution on the values. While the Gumbel distribution shows a larger confidence interval indicating that it does not fit with the extreme value responses as well. Additionally, the 1, 2, and 5-year extreme values that the Gumbel method calculated were almost alike because of the inaccurate fitting at the upper tail end of the probability distribution. The slope of the Gumbel distribution is very steep at the upper end which results in a very small change for every minute change in probability.

6.2.3 Choice of k value in ACER method

Sensitivity analyses for the k values are recommended when studying new responses (Næss, 2009b). Thus, different options of k-value are investigated with the q value held at 10^{-6}. The results of the different k values (2,4 ad 6) are present in Table 17. Additionally, ACER1D function plots with k values ranging from1 to 6 is shown in Figure 55 for all three moments and cases.

Load Case	***q* value**	**10^{-6}**		
	***k* value**	**2**	**4**	**6**
LC1, V_{hub} = 8 m/s	RootMyb (kNm)	36103	36441	37018
	LSSTipMys (kNm)	11509	11580	11592
	TwrBsMyt (kNm)	380076	368822	390514
LC2, V_{hub} = 12 m/s	RootMyb (kNm)	44536	44626	44951
	LSSTipMys (kNm)	19511	19228	19607
	TwrBsMyt (kNm)	476606	479938	480159
LC3, V_{hub} = 16 m/s	RootMyb (kNm)	38980	40385	40214
	LSSTipMys (kNm)	20747	20803	20670
	TwrBsMyt (kNm)	450802	447620	450217

Table 17 Extreme values calculated from the ACER1D method considering different values of k.

The Figure 55 show that the extreme values do not vary much with the different k values used. However, a k value of 1 resulted in incorrect answers. Furthermore, the extreme values estimated also increased with an increase in k values. Similarly, it was seen that the responses tend to converge when k > 2. Thus, k = 6 was used for analysis in this paper.

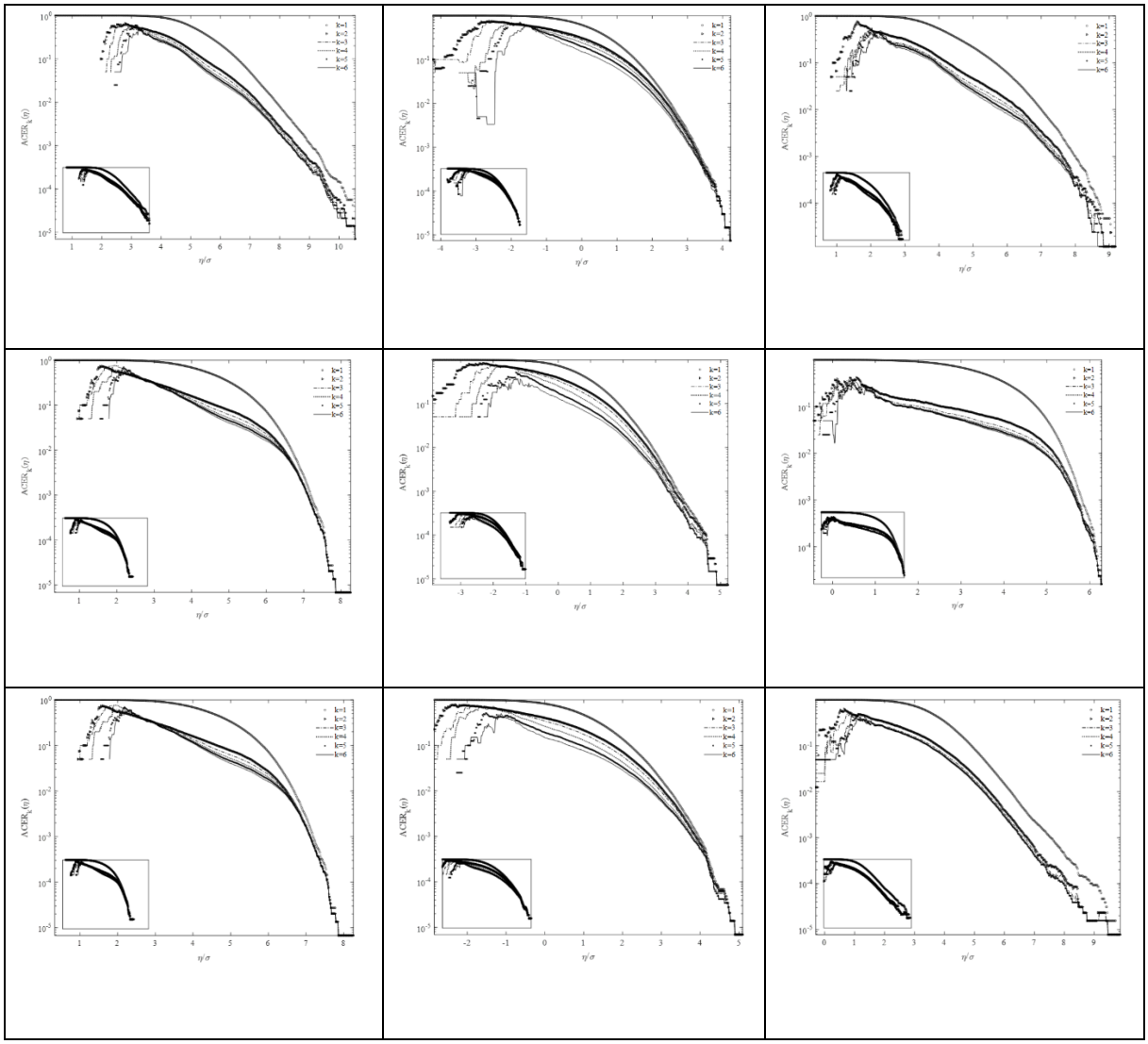

Figure 55 ACER functions for various k values. Top: LC1; Centre: LC2; Bottom: LC3,; Left: RootMyb; Centre: LSSTipMys; Right: TwrBsMyt

6.3 Conclusion

Paper III examined the differences with the extreme responses for a DTU 10 MW semi-submersible type FWT using the ACER1D and Gumbel methods. The results showed the benefits of the ACER1D over Gumbel methods, as the ACER1D method gave better-fitted predictions. The results align with the theory as using the Gumbel distribution led to an overestimation of the extreme values. ACER1D gave better results as the method is not confined to a particular distribution, resulting in better and more accurate results. Furthermore, to reinforce the ACER1D results, its 95% confidence interval was much smaller than the Gumbel results. The studies also verified that the *k* values do not affect the ACER1D results, and any value above 2 gave very similar results. However, *k* = 1 should be avoided as

it gave incorrect results. Furthermore, it is advised that sensitivity studies should be performed on k whenever a new response is being studied.

7 Conclusion

In this study, two main strategies to optimize the efficiency of wind turbines for future design were adopted. In the first strategy, a compensation scheme in the control system was implemented to reduce the bending moment in the low-speed shaft. The novel change implemented in this scheme introduced the errors of the bending moment in the pitch controller and was observed, and the control system's response to the new input was characterized. An in-depth analysis of the PID controllers was performed, and different gains were introduced in the compensation scheme to understand the system better. The analysis showed that optimizing the gain values gave better results and minimized the bending moment. Fine-tuning was also required to ensure that the best K-values varied according to the wind speed. The compensation scheme proved useful and was successful in reducing the bending moment.

In the second part of the thesis, extreme load analysis using ACER1D and ACER2D was performed. The results were then compared with the Gumbel distribution for the ACER1D univariant analysis, and the ACER1D analysis proved superior to a Gumbel distribution even with a small data set. ACER1D also gave a small difference in its confidence interval, which indicates a very effective measure in predicting reliable extreme loads. The K-values in the ACER1D univariant analysis were optimized to ensure that the best possible K-value was selected in this study. As for ACER2D bivariant analysis, the dataset was correlated with the Asymmetric and Gumbel logistic model, and it was found that the former method of analysis provided more robust data points to work with. This is an assertion of the model's reliability, especially when dealing with a minimum dataset.

The characterization and optimization of both the strategies used in this thesis thus proved useful and can be used for further research and recommended for use in designing newer and better wind turbines.

7.1 Future Studies

Further research on developing a more contemporary control system like the Linear–quadratic regulator controller (LQR) or Model predictive control (MPC) to reduce the bending moment in the low-speed shaft should be undertaken as it has a direct impact on the drive train loads. In addition, the load analysis of the drive train and the effect these controllers have on the drive train load can be examined in much more detail.

For the extreme load analysis, new ACER1D and ACER2D analyses can be done on the gearbox to characterize and optimize the effectiveness of the ACER methods. Such studies will be beneficial for optimizing the gearbox as they can facilitate a better and more reliable design of future gearboxes.

Reference

Abdallah, I. (2015). Assessment of extreme design loads for modern wind turbines using the probabilistic approach. DTU Wind Energy. DTU Wind Energy PhD No. 0048(EN).

Ackermann, T., Leutz, R., & Hobohm, J. (2001). World-wide offshore wind potential and European projects. In *2001 Power Engineering Society Summer Meeting. Conference Proceedings (Cat. No. 01CH37262)* (Vol. 1, pp. 4-9). IEEE.

Agarwal, P., & Manuel, L. (2008). Extreme loads for an offshore wind turbine using statistical extrapolation from limited field data. *Wind Energy: An International Journal for Progress and Applications in Wind Power Conversion Technology, 11(6),* 673-684.

Agarwal, P., & Manuel, L. (2009). Simulation of offshore wind turbine response for long-term extreme load prediction. *Engineering structures, 31(10),* 2236-2246.

Bak, C., Zahle, F., Bitsche, R., Kim, T., Yde, A., Henriksen, L., Hansen, M.H., Blasques, J.P.A.A., Gaunaa, M.A., & Natarajan, M. H. (2013). The DTU 10-MW reference wind turbine, Danish wind power Research 2013.

Barreto, D., Karimirad, M., & Ortega, A. (2022). Effects of Simulation Length and Flexible Foundation on Long-Term Response Extrapolation of a Bottom-Fixed Offshore Wind Turbine. *Journal of Offshore Mechanics and Arctic Engineering, 144(3).*

Betz, A. (1926). *Wind Energie und ihre Ausnutzung durch Windmühlen* (Wind Energy and its Extraction through Windmills). Göttingen, Vandenhoeck.

Blasques JP, Stolpe M. (2012). Composite Structures 94 3278 – 3289 ISSN 0263-82

Bortolotti, P., Tarres, H. C., Dykes, K. L., Merz, K., Sethuraman, L., Verelst, D., & Zahle, F. (2019). *IEA Wind TCP Task 37: Systems engineering in wind energy-WP2. 1 Reference wind turbines*. National Renewable Energy Laboratory: Golden, USA.

Bossanyi, E. A. (2000). The design of closed loop controllers for wind turbines, *Wind Energy, 3(3),* 149–163.

Bossanyi, E. A. (2003a). Individual blade pitch control for load reduction, *Wind Energy, 6(2*), 119–128.

Bossanyi, E. A. (2003b). Wind turbine control for load reduction, *Wind Energy, 6(3),* 229–244.

Bossanyi, E. A. (2005). Further load reductions with individual pitch control, *Wind Energy, 8(4)*, 481–485.

Breton, S. P., & Moe, G. (2009). Status, plans and technologies for offshore wind turbines in Europe and North America. *Renewable energy*, *34(3),* 646-654.

Burton, T., Jenkins, N., Sharpe, D., & Bossanyi, E. (2011). *Wind energy handbook*. John Wiley & Sons.

Capuzzi, M., Pirrera, A., & Weaver, P. M. (2014). A novel adaptive blade concept for large-scale wind turbines. Part I: Aeroelastic behaviour. *Energy*, *73*, 15-24.

Chehouri, A., Younes, R., Ilinca, A., & Perron, J. (2015). Review of performance optimization techniques applied to wind turbines. *Applied Energy*, *142*, 361-388.

Cheng, Z., Madsen, H. A., Chai, W., Gao, Z., & Moan, T. (2017). A comparison of extreme structural

responses and fatigue damage of semi-submersible type floating horizontal and vertical axis wind turbines. *Renewable Energy, 108,* 207-219.

Cheynet, E. (2018a). *Wind field simulation (the fast version)*. MathWorks File Exchange. Available online at: https://se.mathworks.com/matlabcentral/fileexchange/68632-wind-field-simulation-the-fast-version (Accessed on 1 December 2019)

Cheynet, E., & Jakobsen, J. (2018b). *Wind Load on Structures Part 1*. Course - OFF580 Marine Technology.

Cheynet, E., Jakobsen, J., & Reuder, J. (2018c). *Velocity Spectra and Coherence Estimates in the Marine Atmospheric Boundary Layer*. Boundary-Layer Meteorology. Springer Nature B.V.

Chougule, A. (2016). In: NORCOWE (Norwegian Centre for Offshore Wind Energy), *Work Projects Meeting.* Grimstad, Norway, 10-11 May 2016.

Coulling, A. J., Goupee, A. J., Robertson, A. N., Jonkman, J. M., & Dagher, H. J. (2013). Validation of a FAST semi-submersible floating wind turbine numerical model with DeepCwind test data. Journal of Renewable and Sustainable Energy, 5(2), 023116.

Davenport, A. G. (1961). The spectrum of horizontal gustiness near the ground in high winds. Quarterly Journal of the Royal Meteorological Society, 87(372), 194-211.

Davenport, A. G. (1977). The prediction of the response of structures to gusty wind. Safety of structures under dynamic loading, 1, 257-284.

Det Norske Veritas AS. (2010). DNV-RP-C205 Environmental conditions and environmental loads. *DNV: Oslo, Norway*.

Dimitrov, N. (2016). Comparative analysis of methods for modelling the short-term probability distribution of extreme wind turbine loads. Wind Energy, 19(4), 717-737.

DTU Wind Energy. (2016). *HAWC2 Online Course.* Danmarks Tekniske Universitet, unpublished. Available online at: https://windenergy.itslearning.com/ContentArea/ContentArea.aspx?LocationID=29&LocationType=1 (Accessed on 1 December 2016).

Dyrbye, C., & Hansen, S.O. (1997). *Wind Loads in Structure*. West Sussex, England: John Wiley & Sons Ltd.

Eliassen, L., & Obhrai, C. (2016). Coherence of turbulent wind under neutral wind conditions at FINO1. *Energy Procedia*, *94*, 388-398.

Energy-WP, W. (2019). IEA Wind TCP Task 37.

Ernst, B., Seume, J. R. (2012). Investigation of site-specific wind field parameters and their effect on loads of offshore wind turbines. Energies, 5(10), 3835-3855.

European Wind Energy Association. (2011). *Wind in our Sails-The coming of Europe's offshore wind energy industry*. EWEA.

Faltinsen, O. (1993). *Sea loads on ships and offshore structures (Vol. 1).* Cambridge university press.

Fitzwater, L., & Cornell A.C. (2002). Predicting the long term distribution of extreme loads from limited duration data: comparing full integration and approximate methods. *J. Sol. Energy Eng., 124(4),* 378-386.

Fitzwater, L. M., & Winterstein, S. R. (2001). Predicting design wind turbine loads from limited data: Comparing random process and random peak models. *J. Sol. Energy Eng., 123(4),* 364-371.

Fogle, J., Agarwal, P., & Manuel, L. (2008a). Towards an improved understanding of statistical extrapolation for wind turbine extreme loads. *Wind Energy: An International Journal for Progress and Applications in Wind Power Conversion Technology*, *11*(6), 613-635.

Fogle, J., Agarwal, P., & Manuel, L. (2008b). Towards an improved understanding of statistical extrapolation for wind turbine extreme loads. *Wind Energy: An International Journal for Progress and Applications in Wind Power Conversion Technology, 11(6),* 613-635.

Freudenreich, K., & Argyriadis, K. (2007). The load level of modern wind turbines according to IEC 61400-1. In Journal of Physics: Conference Series (Vol. 75, No. 1, p. 012075). IOP Publishing.

Fu, P., Leira, B. J., & Myrhaug, D. (2017). Reliability analysis of wake-induced collision of flexible risers. *Applied Ocean Research*, *62*, 49-56.

Gaidai, O., Cheng, Y., Xu, X., & Su, Y. (2018). Long-term offshore Bohai bay Jacket strength assessment based on satellite wave data. *Ships and Offshore Structures, 13(6)*, 657-665.

Gaidai, O., Ji, C., Kalogeri, C., & Gao, J. (2017). SEM-REV energy site extreme wave prediction. *Renewable Energy*, *101*, 894-899.

Gaidai, O., Storhaug, G., & Naess, A. (2016a). Extreme large cargo ship panel stresses by bivariate ACER method. *Ocean Engineering*, *123*, 432-439.

Gaidai, O., Storhaug, G., & Naess, A. (2016b). Extreme value statistics of large container ship roll. *Journal of ship research*, *60*(02), 92-100.

Galambos, J., & Marci, N. (1999). Classical extreme value model and prediction of extreme winds. *Journal of Structural Engineering, 125(7),* 792-794.

Gasch, R., & Twele, J. (2011). *Wind Power Plants: Fundamentals, Design, Construction and Operation*. Springer Science & Business Media.

Graf, P. A., Stewart, G., Lackner, M., Dykes, K., & Veers, P. (2016). High-throughput computation and the applicability of Monte Carlo integration in fatigue load estimation of floating offshore wind turbines. *Wind Energy, 19(5),* 861-872.

Gryning, S., Batchvarova, E., Brümmer, B., Jørgensen, H., & Larsen, S. (2007). On the Extension of the Wind Profile over Homogeneous Terrain beyond the Surface Boundary Layer. *Boundary Layer Meteorology, 124,* 251 – 268

Guo, Y., Bergua, R., Dam, J. V., Jove, J., & Campbell, J. (2015). Improving wind turbine drivetrain designs to minimize the impacts of non-torque loads. *Wind Energy*, *18*(12), 2199-2222.

Guo, Y., Keller, J., & LaCava, W. (2012). *Combined Effects of Input Torque, Non-Torque Load, Gravity, and Bearing Clearance on Planetary Gear Load Share in Wind Turbine Drivetrains*. Technical report, NREL.

Guo, Y., Keller, J., & LaCava, W. (2014). Planetary gear load sharing of wind turbine drivetrains subjected to non-torque loads, *Wind Energy. 18(4),* 757–768.

Hall, M. (2015). *MoorDyn user's guide*. Department of Mechanical Engineering, University of Maine: Orono, USA.

Hansen, M. H. (2004). Wind Energy 7 133–143 ISSN 1099-1824

Henriksen, L. C. (2010). *Model predictive control of wind turbines*. DTU Informatics: Lyngby, Denmark.

Hong, L., & Möller, B. (2011). Offshore wind energy potential in China: Under technical, spatial and

economic constraints. *Energy*, *36*(7), 4482-4491.

Hu, R., Le, C., Gao, Z., Ding, H., & Zhang, P. (2021). Implementation and evaluation of control strategies based on an open controller for a 10 MW floating wind turbine. *Renewable Energy, 179*, 1751-1766.

Højstrup, J. (1999). *Spectral coherence in wind turbine wakes*. Journal of Wind Engineering and Industrial Aerodynamics 80: pp. 137-146.

Igba, J., Alemzadeh, K., Durugbo, C., & Henningsen, K. (2015). Performance assessment of wind turbine gearboxes using in-service data: Current approaches and future trends. *Renewable and Sustainable Energy Reviews*, *50*, 144-159.

IEA. (2020). *World energy outlook 2020*. OECD Publishing.

IEC. (2005*). Wind turbines - Part 1: Design Requirements (IEC 61400-1)*. Geneva: International Electrotechnical Commission, IEC.

IEC. (2009). *Wind Turbines – Part 3 Design Requirements for Offshore Wind Turbines (IEC 61400-3).* Geneva: International Electrotechnical Commission, IEC.

IEC. (2019). Wind energy generation systems - Part 3-2: Design requirements for floating offshore wind turbines (IEC TS 61400-3-2:2019). Geneva: International Electrotechnical Commission, IEC.

IRENA. (2012a). *Renewable Energy Cost Analysis - Wind Power (No. 1).* Technical report, International Renewable Energy Agency.

Irena, I. R. E. A. (2012b). Renewable energy technologies: Cost analysis series. *Concentrating solar power*, *4*(5).

Jian, Z, Gaidai, O, & Gao, J. (2018). Bivariate Extreme Value Statistics of Offshore Jacket Support Stresses in Bohai Bay. *Journal of Offshore Mechanics and Arctic Engineering, Vol 140 (4)*.

Jonkman, J. M. (2007). *Dynamics modeling and loads analysis of an offshore floating wind turbine*. University of Colorado at Boulder.

Jonkman, J. (2010). *Definition of the Floating System for Phase IV of OC3*. National Renewable Energy Laboratory Laboratory: Golden, USA.

Jonkman, J. M., & Buhl Jr, M. L. (2005). *Fast user's guide*. National Renewable Energy Laboratory: Golden, USA.

Jonkman, J. & Veers, P. (2019). DNV GL Joint Industry Project on Validation of Turbulence Models. Cooperative Research and Development Final Report, CRD-17-673.

Jonkman, J., Butterfield, S., Musial, W., & Scott, G. (2009). *Definition of a 5-MW reference wind turbine for offshore system development*. National Renewable Energy Laboratory: Golden, USA.

Jonkman, B. J. (2014a). *TurbSim user's guide: Version 2.00*. National Renewable Energy Laboratory: Golden, USA.

Jonkman, J. M., Robertson, A. N., & Hayman, G. J. (2014b). *HydroDyn user's guide and theory manual*. National Renewable Energy Laboratory.

Jonkman, J., Musial, W. (2010). *Offshore code comparison collaboration (OC3) for IEA Wind Task 23 offshore wind technology and deployment*. National Renewable Energy Laboratory: Golden, USA.

Jonkman, J., et al. (2010). *Offshore code comparison collaboration within IEA Wind Task 23: Phase IV results regarding floating wind turbine modeling*. National Renewable Energy Laboratory: Golden, USA.

Kaimal, J.C. & Finnigan, J.J. (1994). *Atmospheric Boundary Layer Flows. Their Structure and Measurement*. Oxford University Press, Inc.

Kaimal, J. C., Wyngaard, J. C. J., Izumi, Y., & Coté, O. R. (1972). Spectral characteristics of surface-layer turbulence. *Quarterly Journal of the Royal Meteorological Society*, *98*(417), 563-589.

Kaimal, J. C., Wyngaard, J. C., Haugen, D. A., Coté, O. R., Izumi, Y., Caughey, S. J., & Readings, C. J. (1976). Turbulence structure in the convective boundary layer. *Journal of Atmospheric Sciences*, *33*(11), 2152-2169.

Kane, T. R., & Levinson, D. A. (1983). The use of Kane's dynamical equations in robotics. *The International Journal of Robotics Research*, *2*(3), 3-21.

Karpa, O., & Naess, A. (2015). Statistics of extreme wind speeds and wave heights by the bivariate ACER method. *Journal of Offshore Mechanics and Arctic Engineering*, *137*(2).

Karpa, O., & Naess, A. (2013). Extreme value statistics of wind speed data by the ACER method. *Journal of Wind Engineering and Industrial Aerodynamics*, *112*, 1-10.

Knight, J. (2019). *A Study of the Coherences of Turbulent Wind on a Floating Offshore Wind Turbine*. Master Thesis, University of Stavanger.

Korber A 2014 *Extreme and Fatigue Load Reducing Control for Wind Turbines: A Model Predictive Control Approach using Robust State Constraints*. PhD Thesis, University of Berlin.

Lackner, M., & Stewart, G. (2013). Offshore wind turbine load reduction employing optimal passive tuned mass damping systems. *IEEE transactions on control systems technology*, *21*(4), 1090-1104.

Laks, J., Pao, L., Wright, A., Kelley, N., & Jonkman, B. (2011). The use of preview wind measurements for blade pitch control. *Mechatronics*, *21*(4), 668-681.

Lalanne, C. (2009). *Fatigue Damage*. Mechanical Vibration and Shock Analysis (2nd Edition, Vol. 4). John Wiley & Sons.

Larsen, T. J., & Hansen, A. M. (2007). *How 2 HAWC2, the user's manual*. Risø National Laboratory.

Lee, C. H., & Newman, J. N. (2006). Wamit user manual. *WAMIT, Inc*, 42.

Leith, D. J., & Leithead, W. E. (1997). Implementation of wind turbine controllers. *international Journal of Control*, *66*(3), 349-380.

Leithead, W. E., & Connor, B. (2000). Control of variable speed wind turbines: Design task. *International Journal of Control*, *73*(13), 1189-1212.

Leithead, W. E., & Dominguez, S. (2006). Coordinated control design for wind turbine control systems. In *Proceedings of European Wind Energy Conference and Exhibition, Athens, Greece* (Vol. 27).

Leithead, W., & Domınguez, S. (2003). Tower fatigue assesment. *tech. rep*.

Li, L., Gao, Z., & Moan, T. (2013, June). Joint environmental data at five european offshore sites for design of combined wind and wave energy devices. In *International Conference on Offshore Mechanics and Arctic Engineering* (Vol. 55423). American Society of Mechanical Engineers.

Link, H., et al. (2011). *Gearbox reliability collaborative project report: findings from phase 1 and phase 2 testing*. National Renewable Energy Laboratory: Golden, USA.

Madsen, P., Pierce, K., & Buhl, M. (1999). Predicting ultimate loads for wind turbine design. In *37th Aerospace Sciences Meeting and Exhibit* (p. 69).

Manuel, L., Veers, P. S., & Winterstein, S. R. (2001). Parametric models for estimating wind turbine fatigue loads for design. *J. Sol. Energy Eng.*, *123*(4), 346-355.

Manwell, J. F., McGowan, J. G., & Rogers, A. L. (2010). *Wind energy explained: theory, design and application (2nd edition)*. John Wiley & Sons.

McCluskey, C. J., Guers, M. J., & Conlon, S. C. (2021). Minimum sample size for extreme value statistics of flow-induced response. *Marine Structures*, *79*, 103048.

McKenna, R., vd Leye, P. O., & Fichtner, W. (2016). Key challenges and prospects for large wind turbines. *Renewable and Sustainable Energy Reviews*, *53*, 1212-1221.

Micallef, D., & Sant, T. (2016). A review of wind turbine yaw aerodynamics. *Wind Turbines-Design, Control and Applications*. Available online at: http://dx.doi.org/10.5772/63445 (Accessed on 1 June 2022).

Monin, A. S., & Obukhov, A. (1954). Basic Laws of Turbulent Mixing in the Surface Layer of the Atmosphere. *Contrib. Geophys. Inst. Acad. Sci. USSR, 24(151),* 163 –187.

Moriarty, P. J., & Hansen, A. C. (2005). *AeroDyn theory manual*. National Renewable Energy Laboratory: Golden, USA.

Moriarty, P. J., Holley, W. E., & Butterfield, S. (2002). Effect of turbulence variation on extreme loads prediction for wind turbines. *J. Sol. Energy Eng., 124(4),* 387-395.

Moriarty, P. J., Holley, W. E., & Butterfield, S. P. (2004). Extrapolation of extreme and fatigue loads using probabilistic methods. National Renewable Energy Laboratory: Golden, USA.

Muggiasca, S., Taruffi, F., Fontanella, A., Di Carlo, S., Giberti, H., Facchinetti, A., & Belloli, M. (2021). Design of an aeroelastic physical model of the DTU 10MW wind turbine for a floating offshore multipurpose platform prototype. *Ocean Engineering*, *239*, 109837.

Naess, A., & Karpa, O. (2015). Statistics of bivariate extreme wind speeds by the ACER method. *Journal of Wind Engineering and Industrial Aerodynamics*, *139*, 82-88.

Naess, A., & Moan, T. (2013). *Stochastic dynamics of marine structures*. Cambridge University Press.

Naess, A., & Gaidai, O. (2008). Monte Carlo methods for estimating the extreme response of dynamical systems. Journal of Engineering Mechanics, 134(8), 628-636.

Naess, A., Stansberg, C. T., Gaidai, O., & Baarholm, R. J. (2009a). Statistics of extreme events in airgap measurements. *Journal of offshore mechanics and Arctic engineering, 131(4).*

Næss, A., & Gaidai, O. (2009b). Estimation of extreme values from sampled time series. *Structural Safety, 31(4),* 325-334.

Næss A, & Gaidai O. Estimation of extreme values from sampled time series[J]. *Structural safety, 2009, 31(4),* 325-334.

Naess, A., Gaidai, O., & Batsevych, O. (2010). Prediction of extreme response statistics of narrow-band random vibrations. *Journal of Engineering Mechanics, 136(3),* 290-298.

Naess, A., & Moan, T. (2013). *Stochastic dynamics of marine structures*. Cambridge University Press.

Njiri, J. G., & Söffker, D. (2016). State-of-the-art in wind turbine control: Trends and challenges. *Renewable and Sustainable Energy Reviews*, *60*, 377-393.

North, G. R., Pyle, J. A., & Zhang, F. (2014). *Encyclopedia of Atmospheric Sciences 2nd Edition (Volume 1)*. Elsevier.

Obhrai, C. (2018) *Climatology of Offshore Wind*. Course - OFF610 Offshore Wind Turbine Engineering. Lecture 3.

Obhrai, C., & Eliassen, L. (2016). Coherence of Turbulence Wind under Neutral Wind Condition at FINO1. In: EERA (European Energy Research Alliance) DeepWind'2016, *13th Deep Sea Offshore Wind R&D Conference*. Trondheim, Norway, 20-22 January 2016.

Panofsky, H. A. (1962). *Scale Analysis of Atmospheric Turbulence at 2 Meters*. Quarterly Journal of the Royal Meteorological Society 88, pp. 57-69.

Panofsky, H. A., & Singer, I. A. (1965). Vertical structure of turbulence. *Quarterly Journal of the Royal Meteorological Society*, *91*(389), 339-344.

Pao, L. Y., & Johnson, K. E. (2009, June). A tutorial on the dynamics and control of wind turbines and wind farms. In *2009 American Control Conference* (pp. 2076-2089). IEEE.

Peeringa, J. M. (2009). *Comparison of extreme load extrapolations using measured and calculated loads of a MW wind turbine*. Petten: ECN.

Peña, A., Gryning, S. E., & Hasager, C. B. (2008). Measurements and modelling of the wind speed profile in the marine atmospheric boundary layer. *Boundary-layer meteorology*, *129*(3), 479-495.

Pielke, R. A., & Panofsky, H. A. (1970). Turbulence characteristics along several towers. *Boundary-Layer Meteorology*, *1*(2), 115-130.

Platt, A., Jonkman, B., & Jonkman, J. (2016). Inflowwind users guide. *Technical Report*.

Putri, R. (2016). *A Study of the Coherences of Turbulent Wind on a Floating Offshore Wind Turbine*. Master Thesis, University of Stavanger.

Ragan, P., & Manuel, L. (2008). Statistical extrapolation methods for estimating wind turbine extreme loads. *Journal of Solar Energy Engineering, 130(3).*

Robertson, A., Jonkman, J., Musial, W., Popko, W., & Vorpahl, F. (2014). IEA Wind Task 30 Offshore Code Comparison Collaboration Continued.

Robertson, A., Jonkman, J., Masciola, M., Song, H., Goupee, A., Coulling, A., & Luan, C. (2014). *Definition of the semisubmersible floating system for phase II of OC4*. National Renewable Energy Laboratory: Golden, USA.

Robertson, A., et al. (2014). Offshore code comparison collaboration continuation within IEA wind task 30: Phase II results regarding a floating semisubmersible wind system. In *International Conference on Offshore Mechanics and Arctic Engineering* (Vol. 45547). American Society of Mechanical Engineers.

Ronold, K. O., & Larsen, G. C. (2000). Reliability-based design of wind-turbine rotor blades against failure in ultimate loading. *Engineering structures, 22(6),* 565-574.

Ronold, K. O., Wedel-Heinen, J., & Christensen, C. J. (1999). Reliability-based fatigue design of wind-turbine rotor blades. *Engineering structures, 21(12),* 1101-1114.

Ropelewski, C. F., Tennekes, H., & Panofsky, H. A. (1973). Horizontal coherence of wind fluctuations. *Boundary-Layer Meteorology*, *5*(3), 353-363.

Saha, N., Gao, Z., Moan, T., & Naess, A. (2014). Short-term extreme response analysis of a jacket supporting an offshore wind turbine. *Wind Energy, 17(1),* 87-104.

Saeb, A. (2014). General extreme value modeling and application of bootstrap on rainfall data - A case study. *Available online at: https://arxiv.org/pdf/1402.0944.pdf (Accessed on 1 May 2022).*

Sarkar, S., & Fitzgerald, B. (2021). Use of Kane's Method for Multi-Body Dynamic Modelling and Control of Spar-Type Floating Offshore Wind Turbines. Energies 2021, 14, 6635.

Sathe, A., Mann, J., Barlas, T., Bierbooms, W. A. A. M., & Van Bussel, G. J. W. (2013). Influence of atmospheric stability on wind turbine loads. *Wind Energy*, *16*(7), 1013-1032.

Sheng, S. (2012a). *Wind turbine gearbox condition monitoring round robin study-vibration analysis*. National Renewable Energy Laboratory: Golden, USA.

Sheng, S. (2012b). Wind turbine gearbox condition monitoring round robin study-vibration analysis. National Renewable Energy Laboratory: Golden, USA.

SlideServe. (2011). *Atmospheric Stability: Stability of Dry Air*. Available online at: https://www.slideserve.com/Jimmy/atmospheric-stability (Accessed on 1 January 2019)

Slot, R. M. M., Svenningsen, L., Sørensen, J. D., & Thøgersen, M. L. (2018). Consistent direct-drive version of the NREL 5MW turbine. *Proceedings of the WindEurope, Hamburg, Germany*, 25-28.

Stewart, G. M., Lackner, M. A., Arwade, S. R., Hallowell, S., Myers, A. T. (2015). Statistical Estimation of Extreme Loads for the Design of Offshore Wind Turbines During Non-Operational Conditions. *Wind Engineering, 39(6),* 629-640.

Tande, J. O. G., Merz, K., Paulsen, U. S., & Svendsen, H. G. (2015). Floating offshore turbines. *Wiley Interdisciplinary Reviews: Energy and Environment, 4(3),* 213-228.

The Netherlands. (2019). Energy Netherlands - Energy. Available online at: https://www.privacyshield.gov/article?id=Netherlands-Energy (Accessed on 5 December 2019)

Veers, P. S., & Winterstein, S. R. (1998). Application of measured loads to wind turbine fatigue and reliability analysis.

Veers, P., & Butterfield, S. (2001). Extreme load estimation for wind turbines-issues and opportunities for improved practice. In *20th 2001 ASME wind energy symposium* (p. 44).

Vlase, S., Negrean, I., Marin, M., & Năstac, S. (2020). Kane's method-based simulation and modeling robots with elastic elements, using finite element method. *Mathematics*, *8*(5), 805.

Wang, S., Moan, T., Jiang, Z. (2022). Influence of variability and uncertainty of wind and waves on fatigue damage of a floating wind turbine drivetrain. *Renewable Energy, 181,* 870-897.

Wind Energy Industry. (2019). Available online at: https://windeurope.org/ (Accessed on 8 December 2019).

Xu, X. S., Gaidai, O., Karpa, O., Wang, J. L., Ye, R. C., & Cheng, Y. (2021). Wind Farm Support Vessel Extreme Roll Assessment While Docking in the Bohai Sea. *China Ocean Engineering*, *35*(2), 308-316.

Xing, Y., Karimirad, M., & Moan, T. (2014). Modelling and analysis of floating spar-type wind turbine drivetrain. *Wind Energy*, *17*(4), 565-587.

Xu, K., Zhang, M., Shao, Y., Gao, Z., & Moan, T. (2019). Effect of wave nonlinearity on fatigue damage and extreme responses of a semi-submersible floating wind turbine. *Applied Ocean Research*, *91*, 101879.

Xu, S., Ji, C. Y., & Soares, C. G. (2021). Short-term extreme mooring tension and uncertainty analysis by a modified ACER method with adaptive Markov Chain Monte Carlo simulations. *Ocean Engineering*, *236*, 109445.

Xu, X., Gaidai, O., Naess, A., & Sahoo, P. (2020). Extreme loads analysis of a site-specific semi-submersible type wind turbine. *Ships and Offshore Structures*, *15*(sup1), S46-S54.

Yu, W., Müller, K., Lemmer, F., Bredmose, H., Borg, M., Sanchez, G., & Landbo, T. (2017). Public definition of the two LIFES50+ 10MW floater concepts. *LIFES50+ Deliverable*, *4*.

Yu, W., Müller, K., Lemmer, F., Schlipf, D., Bredmose, H., Borg, M., Landbø, T., & Andersen, H. (2018). LIFES50+ D4. 2: Public definition of the two LIFES50+ 10 MW floater concepts. *University of Stuttgart*.

Yu, Z., Amdahl, J., Rypestøl, M., & Cheng, Z. (2022). Numerical modelling and dynamic response analysis of a 10 MW semi-submersible floating offshore wind turbine subjected to ship collision loads. *Renewable Energy, 184*, 677-699.

Zahle F, et al. (2017). HAWTOpt2 Documentation. Available online at: https://gitlab.windenergy.dtu.dk/HAWTOpt2 (Accessed on 1 May 2022).

Zahle, F., Tibaldi, C., Verelst, D. R., Bitche, R., & Bak, C. (2015). Aero-elastic optimization of a 10 MW wind turbine. In *33rd Wind Energy Symposium* (p. 0491).

Zhang, J., Gaidai, O., Wang, K., Xu, J., Ye, R., & Xu, X. (2019). A stochastic method for the prediction of icebreaker bow extreme stresses. *Applied Ocean Research*, *87*, 95-101.

Zhao, Y., Liao, Z., & Dong, S. (2021). Estimation of characteristic extreme response for mooring system in a complex ocean environment. *Ocean Engineering*, *225*, 108809.

Appendix A - Appended Papers

Paper-I

Compensation scheme applied on wind turbine blade pitch control for the reduction of non-torque main shaft loads

Balakrishna, R., & Xing, Y. (2021). Compensation scheme applied on wind turbine blade pitch control for the reduction of non-torque main shaft loads. IOP Conference Series: Materials Science and Engineering.

Paper-II

A novel design approach for estimation of extreme load responses of a 10-MW floating semi-submersible type wind turbine

Balakrishna, R., Gaidai, O., Wang, F., Xing, Y., & Wang, S. (2022). A novel design approach for estimation of extreme load responses of a 10-MW floating semi-submersible type wind turbine. Under Review.

Paper-III

Characterisation of extreme load responses of a 10-1 MW floating semi-submersible type wind turbine

Xing, Y., Wang., Karuvathil., A, Balakrishna., R, & Gaidai, O., (2022). Characterisation of extreme load responses of a 10-1 MW floating semi-submersible type wind turbine. Under Review.

A compensation scheme applied on wind turbine blade pitch control for the reduction of non-torque main shaft loads

R Balakrishna and Y Xing*

Faculty of Science and Technology, University of Stavanger, Norway

* Contact author: yihan.xing@uis.no

Abstract. It has been well established that non-torque main shaft loads influence the internal drive train loads. This paper proposes a scheme that compensates for non-torque loads in the blade pitch controller. The compensation scheme is implemented on a dynamic model developed in FAST/Simulink. Three wind conditions of 8, 11.4 and 20 m/s are examined. The dynamic analysis of the bending moment in the low-speed shaft showed a reduction in bending moment by 3 % for the rated wind speed (11.4 m/s) and 1.8 % for the above-rated wind speed (20 m/s), highlighting the effectiveness of the proposed scheme. However, a reduction in bending moment also slightly decreased the shaft's speed by 2.3 % and 0.5 %, respectively. Similarly, the turbine power was decreased by 9 % and 1 %, respectively. In comparison, further gain scheduling within the compensation scheme reduces the power loss to as low as 0.3 %. The 2 to 3 % reduction in the low-speed shaft bending moment can significantly influence the drive train loads and easily outweigh any loss resulting in the shaft rotational speed and turbine power. Thus, this paper shows that using bending moment error as feedback within the compensation scheme positively affects the low-speed shaft's bending moment with the eventual potential of reducing drivetrain loads.

1. Introduction

Wind energy is a key driving force in achieving the net-zero emissions target 2050 set forth by many countries, including Norway [1]. As more turbines are being built worldwide to achieve this target, it has become ever more equally essential to keep the cost of developing and servicing these turbines to a minimum. An essential aspect in keeping the cost low is ensuring wind turbines failure rates are minimized, as such failure can easily have extended downtime (varying from months to years) and heavily depends on the availability of the materials or manpower [2][3][4]. Furthermore, since some parts within the wind turbines are more susceptible to damages or are expensive to replace, it can significantly affect their base cost due to warranties. One such important example is the gearbox which makes up about 15 % of the cost involved in manufacturing a wind turbine, making it one of the more expensive components to service and replace during failure [3]. Even with better design and manufacturing processes, many gearboxes are still only commonly achieving lifespans of less than 20 years [4][5]. An estimate of about one gearbox failure occurs for every 145 wind turbines per year. Additionally, excessive loading also drives up the operations and maintenance costs for the manufacturers [3][4]. Therefore, uncertainty in failure rates within the gearbox naturally drives up the total cost of the turbines and the insurance cost involved in protecting them against damages [4].

The National Renewable Energy Laboratory (NREL) estimates that about 75 % and 15 % of gearboxes failures can be accredited to the bearing (abrasion and adhesion) or gear parts (bending fatigue

and corrosion), respectively. In addition, gearboxes experience different loads such as twisting moment or torque, transverse load, and axial load. Therefore, minimizing any of these loads will also vastly help reduce the total load acting on the gearbox. However, with very little room for better design improvements, today's research on the gearboxes focuses on better materials or reducing loads acting on the gearbox by modifying the control systems. Innovating the control systems focuses on improving its controls, and example includes varying shaft speed or individual blade pitch to reduce the loads acting on the turbine shaft connected to the gearbox.

It has been well established that non-torque main shaft loads influence the internal drive train loads. In Xing et al. [6], the authors showed that changes in floating wind turbine support led to a reduction in the non-torque main shaft loads, gear-teeth loads and bearing loads. While in three different papers [7][8][9], the authors confirmed that non-torque loads induced by overhang weight significantly influence the drive train loads and their response. The authors attempted to change the drive train design to reduce the effect of the load caused by the shaft. The authors also identified that both gravity and non-torque loads cause excitations within the carrier frame, leading to gearbox loading. In Link et al. [10], the authors confirmed that bending moment (BM) in the main shaft resulted in the planet-ring gear misalignment, which led to an increase in edge loading. Edge loading eventually led to an increase in contact stress which gave a shorter gear lifespan.

Wind turbines have long used active control to mitigate loads and increase power production under a wide variety of wind conditions. In Bossanyi [11][12][13][14], the author suggested that it is possible to further metamorphose controllers (limit pitch controllers), limiting certain types of mechanical loads. The author further discussed the possibility of using a control system and actuators to adjust the different pitch angles of each individual blade to reduce the loads on the systems. The authors illustrated a straightforward addition to the pitch control algorithm of each individual blade to reduce the peak load on some of the fixed components, which in turn led to a substantial amount of load reduction in the whole structure. At the same time, Henriksen [15], investigated the possibility of creating a model predictive controller (MPC) through gain scheduling or re-linearization. In this paper, the author only verified the ability of the MPC to control the turbines subjected to both physical and artificial constraints. However, the author did not focus on the effect the controllers had on the loads. While in the doctoral thesis written by Korber [5], the author found that a preview MPCs performed better in reducing both the mechanical extreme and fatigue loads than a non-preview MPCs and classical baseline controller. Much of this existing research did not focus on reducing non-torque main shaft loads.

This paper aims to focus on improving an existing control algorithm on the NREL 5 MW reference turbine which will reduce the bending moment in the low-speed shaft which will eventually lead to the reduction of the gearbox or drivetrain loads. This is performed via a simple but highly effective scheme that directly compensates the non-torque main shaft loads in the blade pitch control system.

2. NREL 5 MW reference turbine

The NREL 5 MW reference turbine [16] is used as the study object in this paper. It is a three-bladed, variable pitch-to-feather bladed, upwind, and variable-speed controlled megawatt wind turbine developed to study concepts surrounding wind technology. The following method applied on this turbine will help envisage the reduction in non-torque bending moment in the turbine's low-speed shaft. The NREL 5 MW reference turbine's control system algorithm [16] is executed in the Simulink/FAST framework [17] and is presented in Section 3.1.

3. The compensation scheme

The compensation scheme is presented in Figure 1 together with the original blade pitch controller. The original blade pitch controller corrects only for shaft speed error. In contrast, the compensation scheme adds the correction of the main shaft bending moment error. The scheme only modifies the blade pitch control, i.e., the generator control is not modified.

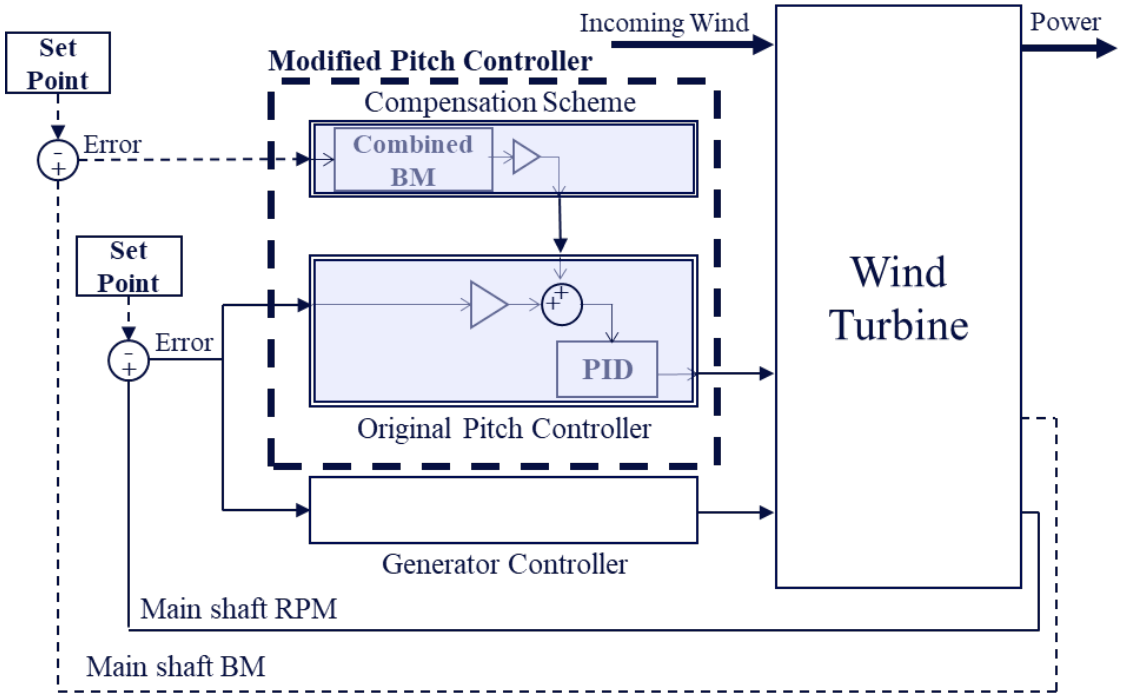

Figure 1. Modified pitch controller (Original controller with compensation scheme).

The collective blade pitch command, θ_{com} is calculated as:

$$\theta_{com} = k_p \cdot e_{tot} + k_p \cdot \int e_{tot}\, dt \quad (1)$$

where e_{tot} is the total error, k_p is the proportional gain coefficient and k_i is the integral gain coefficient. The derivative gain is zero. There are saturation and rate limiter placed on the commanded pitch.

The total error, e_{tot} is calculated as:

$$e_{tot} = e_{RPM} + k_{BM} \cdot e_{BM} \quad (2)$$

where e_{RPM} is the shaft speed error, e_{BM} is the bending moment error and k_{BM} is the compensation weight factor applied on e_{BM}. The values of k_{BM} studied are presented in Table 1. When k_{BM} is set to 0, the errors of the moment are not added to the PID controller. While when k_{BM} is set to 1, it hypothetically means that all the bending moment errors are sent into the PID controller.

The main shaft bending moment is the combined bending moment, M and is calculated as:

$$M = \sqrt{M_y^2 + M_z^2} \quad (3)$$

where M is the combined bending moment, M_y and M_z are the non-rotating bending moments.

3.1. Simulink implementation

The compensation scheme is implemented in Simulink/FAST [17] and is presented in Figure 2. The NREL 5 MW blade pitch controller [16] is modified to include the compensation scheme (shaded in Figure 2).

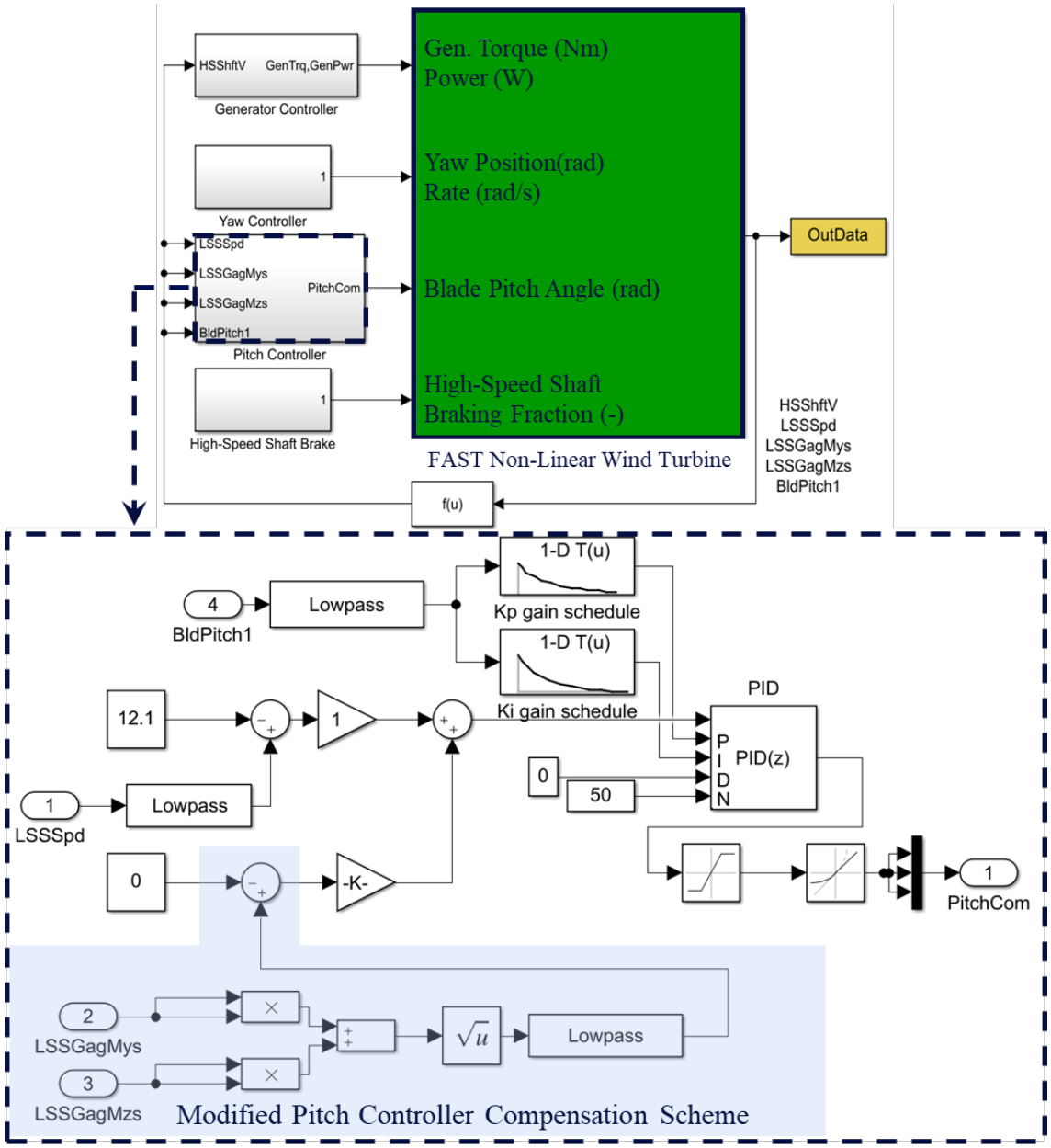

Figure 2. Simulink implementation.

In the implementation, the y and z directional low-speed-shaft bending moments are squared and added together. Next, the root of this summation vector is calculated using equation (3) before passing the signal through a low pass filter. The error of the moment is then calculated as a summation of the differences between the measured input moment and the ideal moment of 0. The signal is then multiplied by the compensation weight factor (K_{BM}). Finally, these two errors are added and then used as inputs into the PID controller.

4. Case studies

The cases studied in this paper are presented in Table 1. Three wind speeds corresponding to below-rated, rated and above-rated regions are studied for both steady wind and normal turbulent wind (NTM) conditions for a wide range of K_{BM} values. This gives a total of 72 simulation cases. The simulation times for each case are 300 s for both steady and NTM wind conditions.

Table 1. Case studies

Case no.	Values
Wind speed (m/s)	8, 11.4, 20
Wind condition	Steady, NTM
K_{BM}	0, 0.0001, 0.0002, 0.00032, 0.00064, 0.00072, 0.0001, 0.0002, 0.00032, 0.00064, 0.00072, 0.001

The variables studied are the non-torque bending moment (BM) (equation (3)), the low-speed shaft speed (RPM) and the generator power (Power). Percentage differences, i.e., %BM, %RPM and %Power are also calculated and investigated. As an example, the % difference in BM is calculated as:

$$\%BM = \frac{BM_{comp} - BM_{org}}{BM_{org}} \times 100\% \quad (4)$$

where BM_{comp} is the bending moment obtained when the compensation scheme is applied and BM_{org} is the bending moment obtained with the original controller scheme with no modifications applied.

5. Results and discussions

5.1. Steady wind

The results of the steady wind cases are presented in Figure 3 and Figure 4. When calculating the shaft RPM, generator power and generator torque, their average values of the last 100 seconds were computed.

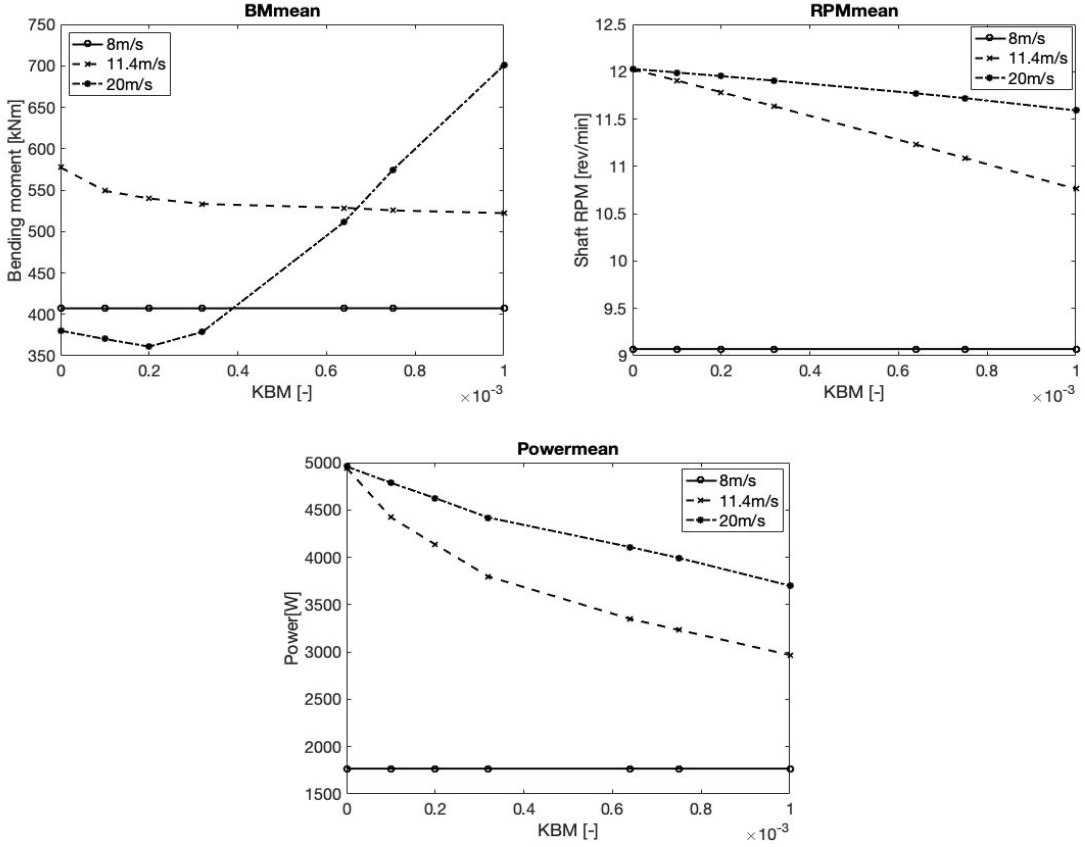

Figure 3. Steady state wind results at 3 different speeds with varying K_{BM}; a. BM (top-left), b. RPM (top-right) and c. Power (bottom).

At the underrated wind speed (8 m/s), the pitch controller is not activated, therefore there are no changes to the results for all values of K_{BM}. At the rated wind speed (11.4 m/s), the bending moment drops with increasing K_{BM} but plateau after it reaches 0.001. While at the above-rated speed (20 m/s), an interesting phenomenon is observed as the BM drops for the lower K_{BM} values and increases for the higher values. This phenomenon can be explained by the fact that as K_{BM} increases, the error is added to the PID from the bending moments that become significantly larger than the shaft RPM. This causes the system to start behaving erratically as errors are corrected incorrectly. Similar erratic behaviour can similarly be expected at other speeds in the above the rated speed ranges (e.g., 15 or 18 m/s) as the K_{BM} approaches 1). The bending moment drops with a negative gradient from 0 to 0.0002. This is as expected since the bending moments that is added at these K_{BM} suits their shaft error proportionally. Thus, a good proportionality allows the errors to be corrected more accurately. Further detailed analysis is conducted for K_{BM} values (between 0 and 0.0001) in the above-rated speed to garner improved efficiency of the bending moment values in that region. This detailed analysis is shown in Figure 4.

The shaft RPM values drop steadily for an increasing K_{BM} value for the rated and above-rated wind speeds. As these two lines decrease, in both cases, the shaft RPM error corrects the system to achieve its optimal shaft speed, which is the primary controller objective. The result shows a significant drop in power at the higher K_{BM} at both the rated and above-rated wind speeds. However, at the lower K_{BM} the power loss can be potentially better controlled and minimized.

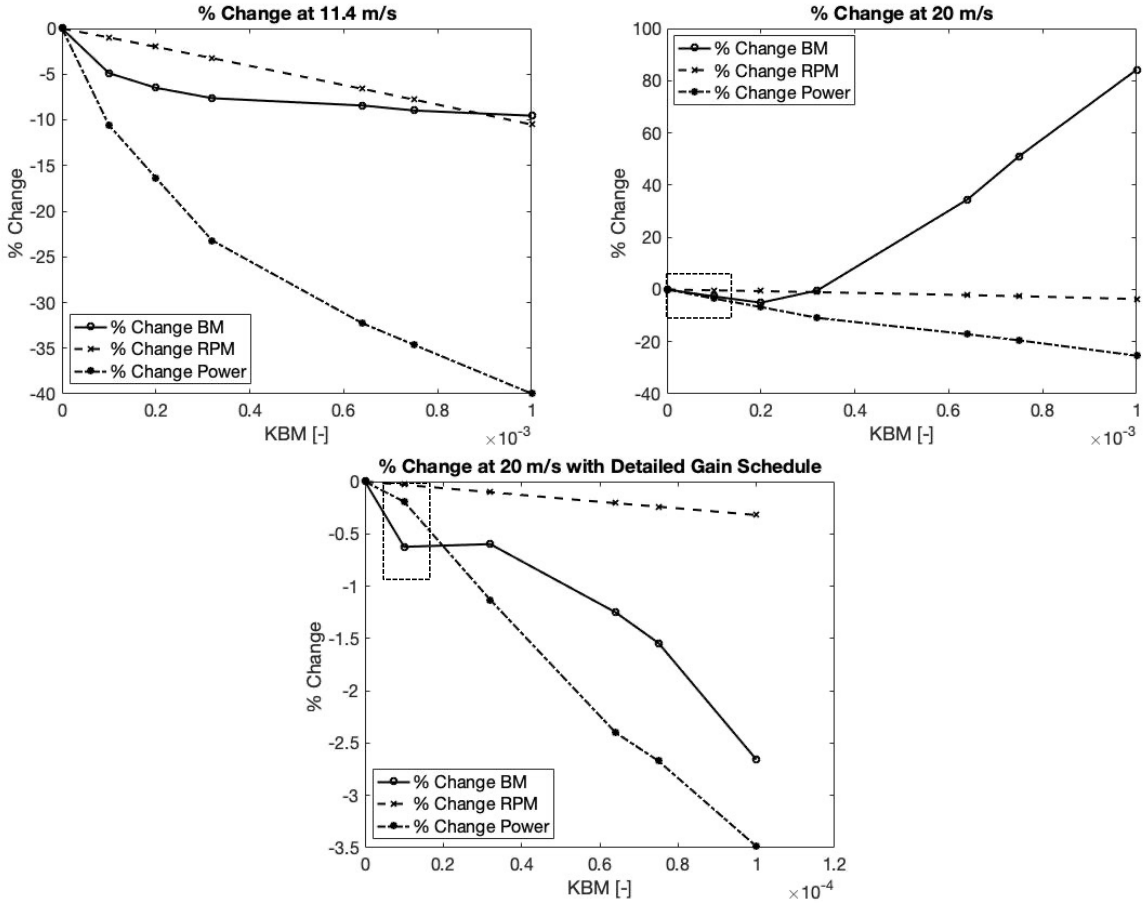

Figure 4. Steady state wind results (percentage (%) change for BM, RPM and Power) with varying K_{BM}; a. Rated (top), b. Above-rated (bottom-left) and c. Above-rated with K_{BM} scheduling(bottom-right).

The results from Figure *4* show that at rated speed (11.4 m/s) and above rated speed (20 m/s), all the percentage change of bending moments, shaft RPM and generator power are dropping with an increasing K_{BM}, except for the above rated speed (20 m/s) bending moment which reasoning was explained in the previous section. For the rated speed (11.4 m/s), Figure 4(a) indicates that 0.0001 gives the minimal proportion of losses between the percentage change of bending moments, shaft RPM and generator power. While for the above rated speed (20 m/s), a more detailed analysis was done in the ranges of 0.00001 to 0.00015 (boxed-up region: Figure 4(b)) to identify the best K_{BM} values. Figure 4(c) shows the results of the detailed gain scheduling of Figure 4(b). Figure 4(c) indicates that 0.00001 gives the minimal proportion of losses between the percentage change of bending moments, shaft RPM and generator power. More importantly, in Figure 4(c) at 0.00001, the bending moment loss is more significant than the power loss. Therefore, even though the percentage change might be small, it gives an ideal situation since the turbine reduction in bending moments is more than the loss in power

5.2. NTM wind

The results of the NTM wind cases are presented in Figure 5 and Figure 6. Like the steady wind cases presented in Section 5.1. , when calculating the shaft RPM, generator power and generator torque, their average values of the last 100 seconds were computed.

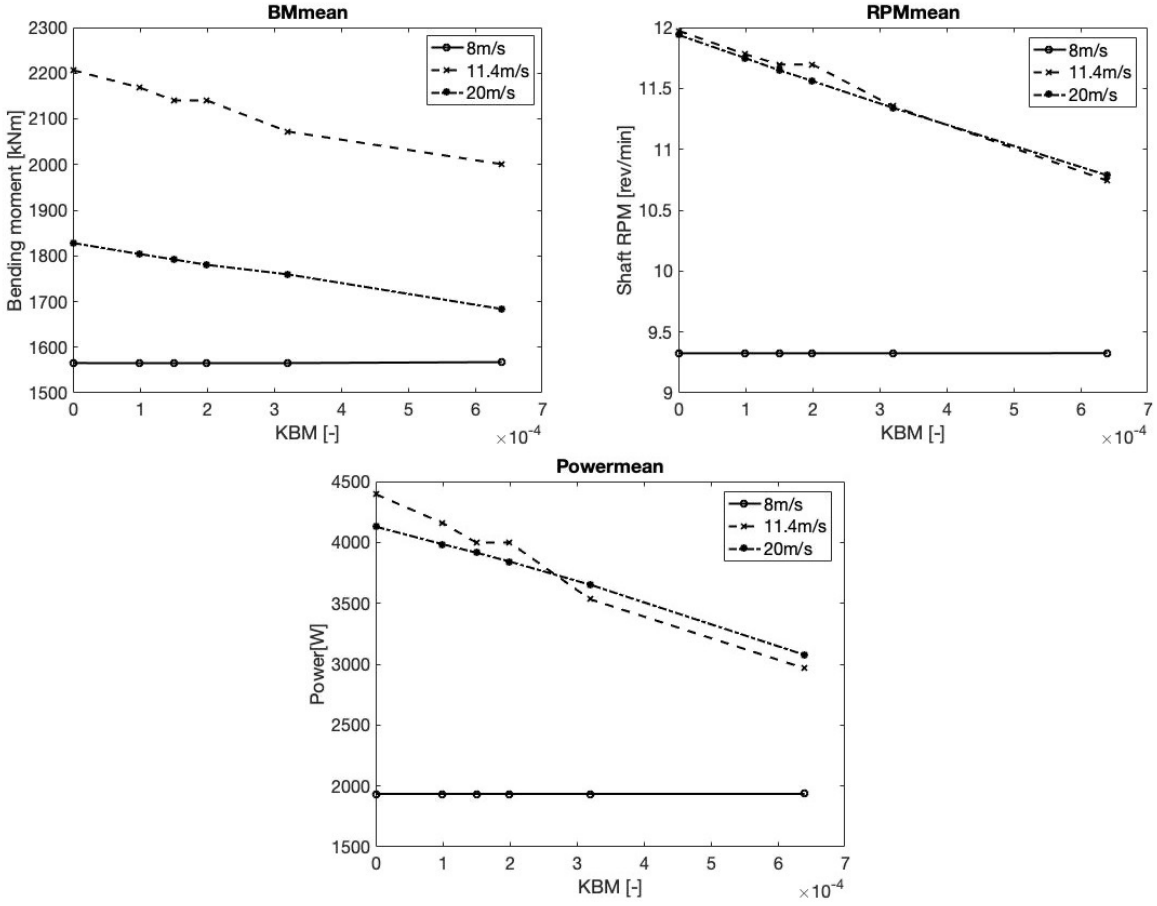

Figure 5. NTM wind results at 3 different speeds with varying K_{BM}; a. BM (top-left), b. RPM (top-right) and c. Power (bottom).

Similarly, for the NTM wind cases, at the under-rated wind speed (8 m/s), the bending moment, shaft RPM and generator power change are assumed to be zero due to the inactivation of the pitch controller. However, in the normal turbulent wind model the drop in the bending moments, shaft RPM and power seem to be relatively linear for both the rated and above-rated wind speeds. This is expected since with

the turbulent wind model the speed of the wind is varying at differently and averages out at the selected wind speed. The wind's net effect on the bending moment in this model clearly shows the steady dropped experienced with increasing K_{BM}.

The turbulent models' rated or above-rated speeds produce very similar shapes for the shaft RPM and power in all measured K_{BM} values. The bending moment values of the above rated speed is also lesser than the rated speed (using $K_{BM} = 0$ as reference). This is accounted for correctly by the fact that as the blades pitches at above the rated speed, the bending moment acting on the turbine body and shaft is reduced.

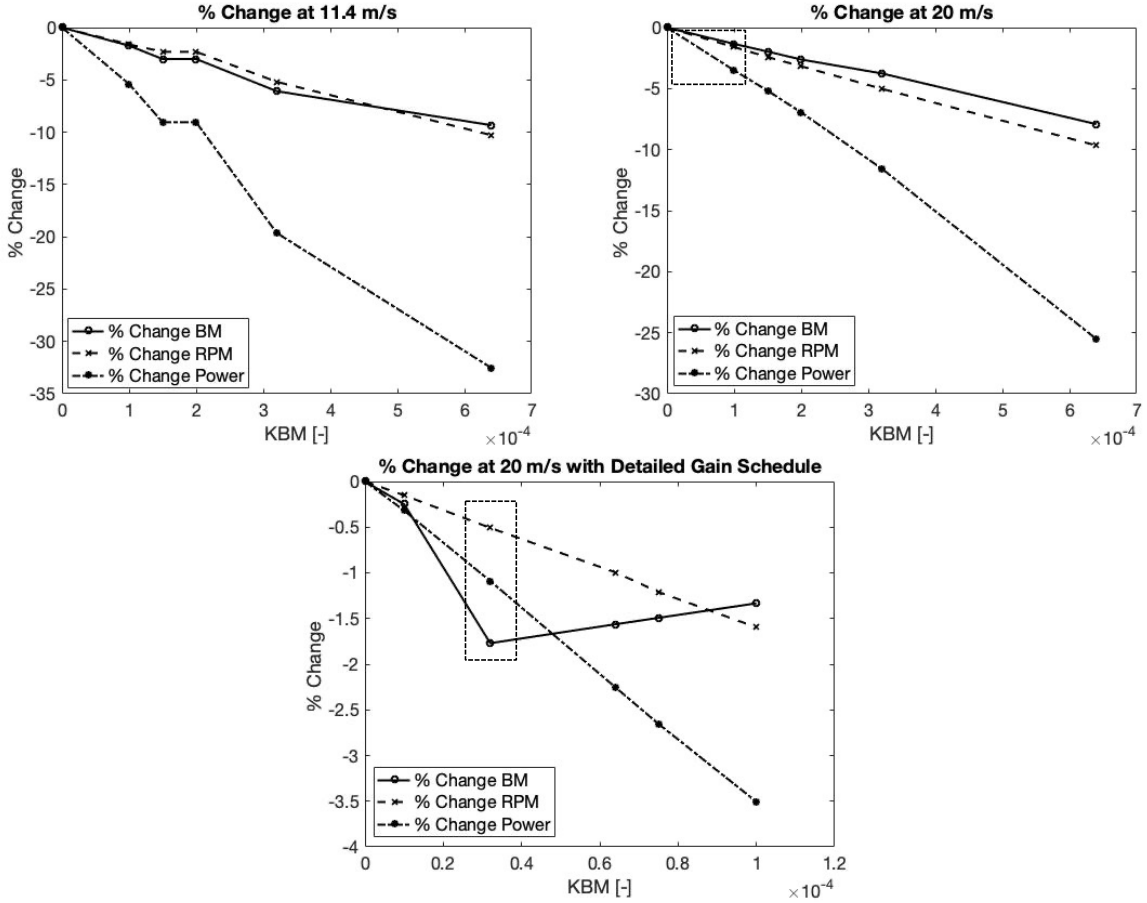

Figure 6. NTM wind results (percentage (%) change for BM, RPM and Power) with varying K_{BM}; a. Rated (top), b. Above-rated (bottom-left) and c. Above-rated with K_{BM} scheduling(bottom-right).

For the rated speed (11.4 m/s), in Figure 6(a), it can be seen clearly that the percentage change in bending moment and power decreases at the same rate while the power is more significantly affected with increasing K_{BM}. While for the above rated speed (20 m/s), in Figure 6(b), further investigation was done in the boxed-up region to find an appropriate K_{BM} value that can minimize the losses between the bending moments, RPM and power. These results are shown in Figure 6(c). In Figure 6(c), the best K_{BM} values are identified when there is more percentage loss of bending moment than power. A similar pattern was observed in the steady-state model. However, the K_{BM} value (0.000032) in the turbulent model is different from the steady-state model.

5.3. Best K_{BM} values

To estimate the best K_{BM} values for each wind speed, the best ratio for the percentage bending moment and percentage RPM is calculated. The higher the ratio would imply that the maximum decrease in

bending moment has been achieved with minimal change in RPM or power (P). The change is 0 at under rated wind speed (8 m/s) is insignificant and assumed to be zero. The results are presented in Table 2.

Table 2. Best K_{BM} values

Wind speed (m/s)	8	11.4	20
% difference, BM mean	0	-3.0041	-1.7701
% difference, RPM mean	0	-2.3144	-0.5079
Best ratio (%BM/%RPM)	0	1.29	3.48
Best ratio (%BM/%P)	0	0.33	1.62
K_{BM}	0	0.00015	0.000032

The percentage BM / percentage P ratio is less than 1 at the rated speed (11.4 m/s) and more than 1 at the above rated speed (11.4 m/s). Even though it might be questionable if the benefits are worthwhile at the rated speed, it is unquestionably beneficial at the above rated speed. The ability to minimize the bending moments acting on the shaft and eventually the gearbox will increase the gearbox's life span significantly as described by the S-N curve. Furthermore, the K_{BM} value can be scheduled to 0 at the rated speed if cost analysis research shows that it gives the most positive results.

Finally, it can be summarized that varying K_{BM} values and then adding the BM errors positively affect the reduction of the structural load oscillations. Furthermore, changing the K_{BM} values and thus the BM errors magnitudes seem to have a linear relationship within the examined ranges of 0.00001 to 0.001. However, it is essential to acknowledge that it does not necessarily mean that this relationship holds to different wind speeds or different ranges of K_{BM} values. Furthermore, it must be emphasized that the control algorithms used only considered the pitch angle controller for one blade and cumulated the results which were used for all three blades.

6. Conclusions

Control algorithms that can reduce the bending moment in the low-speed shaft will eventually reduce the internal drive train loads within the gearbox, thus extending its lifespan. This paper has shown that adding a bending moment error into the pitch controller can positively affect the bending moment acting on the low-speed shaft. The bending moment can be reduced by about 3 % for the rated wind speed (11.4 m/s) and 1.8 % for the above-rated wind speed (20 m/s) while only losing 2.3 % and 0.5 % of the shaft's rotational speed, respectively. Furthermore, a linear relationship was observed between the gain scheduled bending moment errors and the reduction of total bending moments if the K_{BM} values are scheduled in an appropriate range. However, further studies need to be done to ensure consistency of such reduction at different wind speeds. It is also vital to ensure that lifespan extension does not substantially reduce the turbine's power, torque, or rotational speed.

References

[1] IEA 2020 *World Energy Outlook*. (International Energy Agency: Technical report).
[2] Igba J, Alemzadeh K, Durugbo C and Henningsen K 2015 Performance assessment of wind turbine gearboxes using in-service data: Current approaches and future trends. *Renewable and Sustainable Energy Rev.* **50**, 144–159.
[3] IRENA 2012 *Renewable Energy Cost Analysis - Wind Power (No. 1).* (International Renewable Energy Agency: Technical report).
[4] Sheng S 2012 *Wind Turbine Gearbox Condition Monitoring Round Robin Study - Vibration Analysis*. (National Renewable Energy Laboratory: Technical report).
[5] Korber A 2014 *Extreme and Fatigue Load Reducing Control for Wind Turbines: A Model Predictive Control Approach using Robust State Constraints*. (University of Berlin: PhD thesis).

[6] Xing Y, Karimirad M and Moan T 2013 Modelling and analysis of floating spar-type wind turbine drivetrain, *Wind Energy*. **17**(4), 565–587.
[7] Guo Y, Bergua R, van Dam J, Jove J and Campbell J 2014 Improving wind turbine drivetrain designs to minimize the impacts of non-torque loads, *Wind Energy*. **18**(12), 2199–2222.
[8] Guo Y, Keller J and LaCava W 2012 *Combined Effects of Input Torque, Non-Torque Load, Gravity, and Bearing Clearance on Planetary Gear Load Share in Wind Turbine Drivetrains*. (National Renewable Energy Laboratory: Technical report).
[9] Guo Y, Keller J and LaCava W 2014 Planetary gear load sharing of wind turbine drivetrains subjected to non-torque loads, *Wind Energy*. **18**(4), 757–768.
[10] Link H, LaCava W, van Dam J, McNiff B, Sheng S, Wallen R, McDade M, Lambert S, Butterfield S and Oyague F 2011 *Gearbox Reliability Collaborative Project Report: Findings from Phase 1 and Phase 2 Testing*. (National Renewable Energy Laboratory: Technical report).
[11] Bossanyi E A 2000 The design of closed loop controllers for wind turbines, *Wind Energy*. ***3***(3), 149–163.
[12] Bossanyi E A 2003 Individual blade pitch control for load reduction, *Wind Energy*. **6**(2), 119–128.
[13] Bossanyi E A 2003 Wind turbine control for load reduction, *Wind Energy*. **6**(3), 229–244.
[14] Bossanyi E A 2005 Further load reductions with individual pitch control, *Wind Energy*. **8**(4), 481–485.
[15] Henriksen L C 2010 Model Predictive Control of Wind Turbines. (Technical University of Denmark: PhD thesis).
[16] Jonkman J M, Butterfield S, Musial W and Scott G 2009 *Definition of a 5-MW Reference Wind Turbine for Offshore System Development*. (National Renewable Energy Laboratory: Technical report).
[17] Jonkman J M and Buhl Jr M L 2005 *FAST User's Guide*. (National Renewable Energy Laboratory: Technical report).

A novel design approach for estimation of extreme load responses of a 10-MW floating semi-submersible type wind turbine

Rajiv Balakrishna[1], Oleg Gaidai[2], Fang Wang[2*], Yihan Xing[1], Shuaishuai Wang[3]

[1]Department of Mechanical and Structural Engineering and Materials Science, University of Stavanger, Norway

[2]Shanghai Engineering Research Centre of Marine Renewable Energy, College of Engineering Science and Technology, Shanghai Ocean University, Shanghai, China

[3]Norwegian University of Science and Technology, Trondheim, Norway

[*]Corresponding author: wangfang@shou.edu.cn

Abstract

Offshore structures are constructed to withstand extreme wind and wave-induced loads, so studying these extreme loads is vital as it allows offshore structures, e.g., wind turbines, to be designed and operated with minimal disruption. A novel statistical model that is precise and meticulous will facilitate these extreme load values to be estimated accurately. Therefore, the recently developed bivariate average conditional exceedance rate (ACER2D) method is utilized in this paper. This multivariate statistical analysis is more appropriate than a univariate statistical analysis for complete structures, e.g., wind turbines, since it can extrapolate the extreme values with better accuracy. This paper uses this ACER2D method to explore a novel approach to estimating the extreme load responses of a 10-MW semi-submersible type floating wind turbine (FWT). Two cases are considered to understand the feasibility of the ACER2D on the extreme load responses. The first case analyses the blade root flap wise bending moment, while the second one analyses the tower bottom fore-aft bending moment. The numerical bending moments used in this study are obtained from the FAST simulation tool (developed by the National Renewable Energy Laboratory) with the load cases simulated at under-rated, rated and above-rated speeds. Then, the ACER2D method is applied to model an extreme response for both these cases for a 5-year return period prediction with a 95 % confidence interval (CI). The proposed methodology permits accurate estimation of the bivariate extreme value. In conclusion, based on the performance of the proposed novel method, the ACER2D method can offer better robust and precise bivariate predictions of the bending moments of the FWT.

Keywords: Floating wind turbine, FAST, ACER2D method, Extreme responses, Bivariate probability distribution.

1. Introduction

Developing more efficient wind turbines is a driving force enabling engineers to achieve the net-zero emissions target 2050 [1]. According to International Electrotechnical Commission (IEC) standards, wind turbines must be designed to operate in the highly stochastic wind and wave environments for at least 20 years [2]. Since both larger and more wind turbines are constructed, especially offshore, it has become extensional to minimise construction, maintenance, and operational costs. Turbines and their components are vulnerable to various cyclic loads such as axial and transverse loading, bending moments and torque. Furthermore, the loads acting on the wind turbines are also influenced by the wind's stochastic behaviours in speed, direction, shear, and vorticity, making extreme load analysis imperative for wind turbines design and operation. Any failure in the turbine system can result in unnecessary downtime, which can be extremely expensive, see [3]-[5]. Despite this, engineers in the 1970s

believed that it was unnecessary to conduct detailed modelling, resulting in the design of wind turbines with huge safety margins. However, this changed with the further development of larger wind turbines as it became more expensive to maintain similar safety margins. On top of that, inaccurate estimation of design loads led to unnecessary failures. These led to an industry revamp, where a better accurate prediction technique was developed by the 1990s using dynamic structural models, turbulence models, aerodynamic models, and control algorithms, see [6].

Two different methods can be applied to evaluate extreme wind turbines loads. The first method involves running a simulation for rare occurrences that leads to a high structural load. In contrast, the second method simulates the wind turbine operating under normal conditions. The results are then extrapolated with a probability distribution, and the extreme tail is analysed, see [7]. The second method is more commonly used as it uses a full statistical distribution instead of an individual event.

Even as researchers could now estimate extreme loads more accurately than ever before, they still had to develop a better statistical distribution to help them extrapolate the extreme load [6]. Thus, many researchers worked on numerous probabilistic methods to increase the precision of the estimated loads. In [8], the author developed a non-linear parametric model to extrapolate and estimate long term fatigue loading. In [9], [10], the authors developed techniques to calibrate partial safety factors which could predict extreme loads through extrapolation and showed that these extreme loads follow the Gumbel distribution. While in the study [11], the author continued fine-tuning probabilistic methods and parametric models and executed a detailed uncertainty analysis. While to achieve a more accurate estimation for the moment, [12], [13] attempted to compile and simplify the different techniques mentioned above. In [14], the authors attempted to estimate extreme loads through statistical extrapolation of limited field data. Many studies have recently focused on more precise estimation of the wind turbine's extreme loads. Examples include [15], where the author used statistical and modelling to estimate long-term extreme responses on an offshore wind turbine. While in [16], the author used extreme value statistics to estimate flow-induced responses from a small sample size, [17] estimated loads using the global and block maxima extrapolation. While in [18], the authors used the threshold extrapolation method to estimate the extreme loads and turbulent intensity. In [19], the authors used the Monte Carlo method to estimate the long-term fatigue loads. In contrast, many authors such as [20]-[26] have attempted to match different statistical distribution models with extreme load patterns. However, the methods mentioned above fit an assumed extreme value distribution to the empirical data and do not precisely represent the actual characteristics of the data. It can lead to less reliable results, which is even more critical in extreme value prediction. The results are derived at the tail of the probability distribution and are sensitive to uncertainties and errors.

This paper proposes a novel averaged conditional exceedance rate approach based on two-dimensional design points (ACER2D) instead of traditional one-dimensional characteristic design values. ACER2D is a non-trivial approach compared to the classic method given that there is non-linear correlation between different response components. The proposed method can more efficiently and reliably predict extreme loads in a 10 MW large floating wind turbine (FWT). The ACER method combines the structural load statistics with appropriate parametric functions that provide a reliable description of the extreme load distribution's tail behaviour. ACER has been applied in earlier studies on various marine structures, see [27]-[29], and [30]-[33]. This method provides a statistical depiction and its error bounds of the extreme value distribution inherent in the data, offering a unique approach to estimate the extreme values [34]. The ACER method sets itself apart from other commonly known methods like e.g. the Gumbel and Weibull distribution. ACER method is not purely based on the asymptotic distribution, thus

avoiding incorporating generalised extreme value distribution (GEV). The latter allows the values obtained from the ACER method to be more versatile as it represents real-life values that are typically not genuinely asymptotic. The margin of errors for irregularity is reduced as it avoids superposing asymptotic behaviour onto actual non-asymptotic data. The ACER method has been described to give more accurate and reliable results when compared to the peaks-over-threshold or annual maxima methods. The effectiveness of the ACER method has fuelled further research [35] to develop a modified ACER method together with the adaptive Markov Chain Monte Carlo simulations to estimate the short-term extreme mooring tension.

More efficient and reliable estimations of extreme responses will better help predict the effects these loads have on the components allowing the development and implementation of a better design or control system for the FWT. Optimal wind turbine parameters would minimise potential FWT mechanical damage due to excessive environmental loadings [36]. Accurately predicted extreme loads will also allow the components to be more optimally sized. It contributes to more refined designs and lower failure rates, which is particularly important for the offshore wind industry as it advances the design, manufacturing and deployment of large FWTs (>10 MW) in the coming decade.

2. System description

A 10-MW FWT system [37] is used in this work, which is illustrated in **Figure *1***. The FWT system will be expounded in two parts in the following sections. Firstly, the reference wind turbine will be described, then the properties of the semi-submersible floater and the mooring system will be introduced.

Figure 1 The LIFES50+ OO-Star Wind Floater Semi 10MW structure [37].

2.1. DTU 10-MW Reference Wind Turbine

The DTU 10-MW reference wind turbine (RWT) [37] is used in this paper, designed from the NREL 5-MW RWT [37]. The wind turbine was designed per the International Electrotechnical Commission (IEC) Class 1A wind regime and is a traditional three-bladed, clockwise rotation-upwind turbine, equipping with a variable speed and collective pitch control system. The DTU 10-MW RWT numerical model has been successfully developed and studied in many academic works, e.g., [39]-[42]. The summary of the DTU 10-MW RWT is shown in **Table *1***.

Table 1 Key parameters of the DTU 10-MW RWT *[37]*.

Parameter	**Value**
Rating	10-MW
Type	Upwind/3 blades
Control	Variable speed, collective pitch
Drivetrain	Medium-speed, multiple stage gearbox
Cut-in, rated and cut-out wind speed (m/s)	4, 11.4, 25
Minimum and maximum rotor speed (rpm)	6.0, 9.6
Maximum generator speed (rpm)	480
Rotor diameter (m)	178.3
Hub height (m)	119.0
Rotor mass (kg)	227962
Nacelle mass (kg)	446036
Tower mass (kg)	1.257×10^6

2.2. OO-Star Semi-submersible Wind Floater and mooring system

This work uses a semi-submersible floating structure to support the DTU 10-MW RWT . It was introduced by Dr.techn. Olav Olsen AS in the LIFES 50+ project [37]. The floater comprises post-tensioned concrete, hosting a central column with three outer columns. The four columns are mounted on a star-shaped pontoon, where a slab is attached at the bottom. Three catenary mooring lines are used to maintain the floater in position, and in each line, a clumped mass is attached, separating the line into two segments. Greater details of the OO-Star Wind Floater and the mooring system are shown in **Table 2** and **Table 3**, respectively.

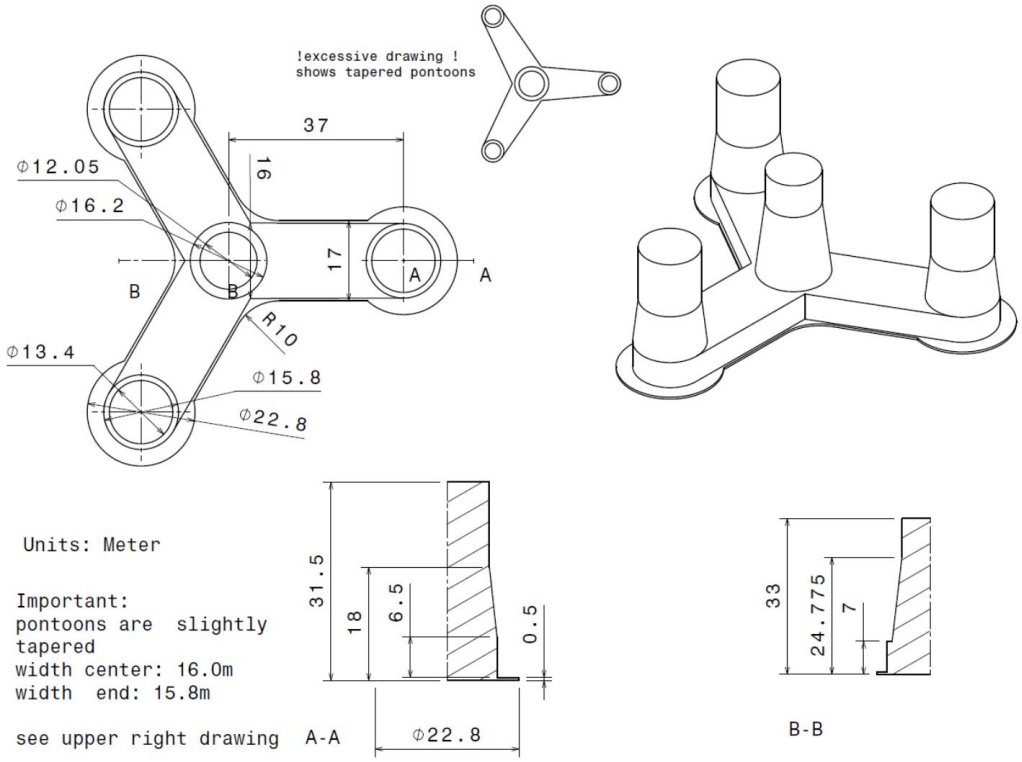

Figure 2 Main dimensions of the OO-Star floater of the LIFES50+ OO-Star Wind Floater Semi 10MW structure [37].

Table 2 The main properties for the LIFES50+ OO-Star Wind Floater Semi 10MW structure wind floater [37].

Parameter	**Value**
Water depth (m)	130
Draft (m)	22
Tower-base interface above mean sea level (m)	11
Displacement (kg)	24158
Overall gravity, including ballast (kg)	21709
Roll and pitch inertia about center of gravity (kg·m^2)	1.4462 x 10^{10}
Yaw inertia about center of gravity (kg·m^2)	1.63 x 10^{10}
Center of gravity height below mean sea level (m)	15.23
Center of buoyancy height below mean sea level (m)	14.236

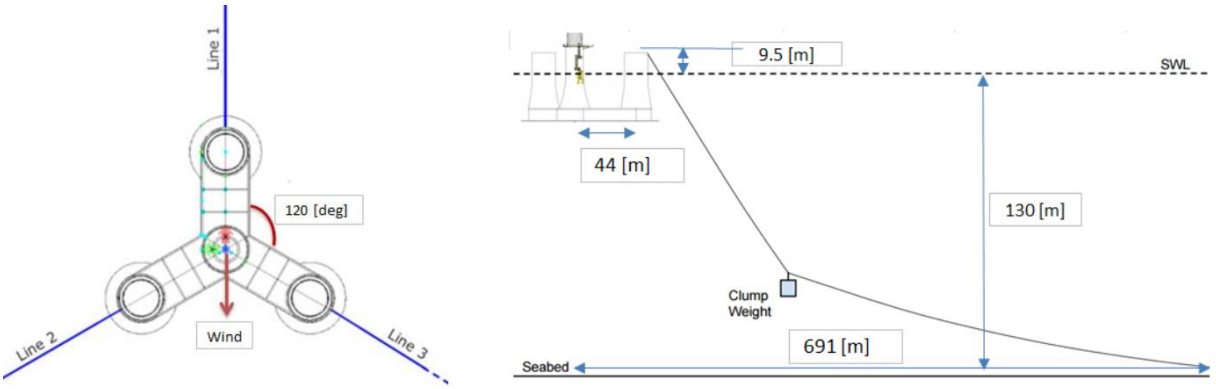

Figure 3 Sketch of the mooring system in the LIFES50+ OO-Star Wind Floater Semi 10MW structure (left: top view; right: side view) [37].

Table 3 The main properties for the mooring system of the LIFES50+ OO-Star Wind Floater Semi 10MW structure [37].

Parameter	**Value**
Radius to anchors from platform centerline (m)	691
Anchor position below MSL (m)	130
Initial vertical position of clump mass below MSL (m)	90.45
Initial radius to clump mass from centerline (m)	148.6
Length of clump mass upper segment (kg)	118
Length of clump mass lower segment (kg)	585
Equivalent weight per length in water (N/m)	3200.6
Extensional stiffness (N/m)	1.506×10^9

3. Methodology

This section describes the methodology adopted by authors to address engineering challenges related to safe and reliable design of FWTs (floating wind turbines). Note that the proposed ACER (Average Conditional Exceedance Rate) method along with the FAST simulation tool [70] was already recently successfully used by the authors, see e.g., [70].

3.1. Aero-hydro-elastic-servo dynamic analysis of the 10-MW FWT

FAST (Fatigue, Aerodynamics, Structures and Turbulence) (version8, v8.16.00a-bjj), an open-source WT simulation tool developed by the National Renewable Energy Laboratory (NREL), is utilized in this work for the fully coupled aero-hydro-elastic-servo dynamic analysis for the 10-MW FWT. The FAST code couples together five computer codes: AeroDyn [44], HydroDyn [45], ServoDyn, and MoorDyn [46], to account for the aerodynamic loads on rotor blades, hydrodynamic loads on floaters, control dynamics, structural dynamics and mooring system dynamics. In addition, FAST provides the interface for reading the time-varying stochastic wind for time-domain simulations. The FAST simulation tool has been successfully used in other well-known projects such as OC3: Offshore Code Comparison Collaboration [47] and OC4: IEA Task Wind 30 [48], and its modelling capability has been authenticated using multiple floating structures in the Netherlands [49].

3.2. Extreme value prediction by ACER1D and ACER2D methods

ACER1D method

Various statistical methods have been used to approximate the extreme value distribution of a recorded time series in its tail. Examples of the extreme value methods used in the study of wind turbines include an estimation of extreme structural responses in floating vertical axis wind turbines, see [53] and extreme responses due to wave nonlinearity on a semi-submersible floating wind turbine, see [36].

The ACER method used in this paper as in [54]-[60], [68]-[1] has numerous advantages when estimating extreme values from a recorded time series. One of these includes the ability to identify the effect of dependency between the data of the time series on the extreme value distribution. Also, the whole time series can be used as input data without de-clustering (i.e., no requirement to use independent data). However, the most prominent feature of the ACER method is its ability to provide a non-parametric depiction of the extreme value distribution inherent in the data. Therefore, this circumvents the need for explicit modelling due to seasonal effects as this method automatically accounts for it. Also, using the ACER method and an appropriate parametric function for tail modelling allows for an explicit description of the extreme value distribution suitable for deep tail extrapolation. Furthermore, this method also seeks to approximate the extreme value distribution in the non-asymptotic regime, which differs from the most commonly known extrapolation methods, i.e., Gumbel, POT (peaks over threshold) or Weibull distribution. Recent studies using the ACER method include the study of vessels extreme roll assessment [56] and extreme response in a mooring system, see [57].

When extrapolating extreme values distributions, the most commonly used distributions are faced with obstacles as they require an asymptotic behaviour. This behaviour cannot be entirely substantiated, and thus, its choice is based on convenience. Wrongly selected asymptotic distributions can result in errors when extrapolating to long return period design values. For example, in [58], the authors explained that a Gumbel distribution might be wrongly interpreted as a Weibull distribution since the data used partially fits the upper bound of the Weibull distribution. The result is a wrongly fitted asymptotically inconsistent distribution, resulting in wrongly approximated values (i.e., wind speed or extreme values).

X(t) is the long-term global response of a floating wind turbine measured between the time interval *(0,T)*. The discrete-time interval in *(0,T)* is defined as $t_1, \ldots, t_N$, while process measurement *X(t)* at this discrete-time interval is defined as $X_1, \ldots, X_N$ to approximate the distribution function of the extreme value $M_N = \max\{X_j; j = 1, \ldots, N\}$, especially to estimate cumulative density function (CDF) $P(\eta) = \text{Prob}(M_N \leq \eta)$ for large values of the response η.

Therefore, the below mentioned random functions are presented:

$$\begin{aligned} A_{kj}(\eta) &= \mathbf{1}\{X_j > \eta, X_{j-1} \leq \eta, \ldots, X_{j-k+1} \leq \eta\}, \quad j = k, \ldots, N, k = 2, 3, \ldots \\ A_{kj}(\eta) &= \mathbf{1}\{X_j > \eta, X_{j-1} \leq \eta, \ldots, X_{j-k+1} \leq \eta\}, \quad j = k, \ldots, N, k = 2, 3, \ldots \\ B_{kj}(\eta) &= \mathbf{1}\{X_{j-1} \leq \eta, \ldots, X_{j-k+1} \leq \eta\}, \quad j = k, \ldots, N, k = 2, 3, \ldots \end{aligned} \tag{1}$$

Where, when $\mathcal{A}$ is true, $\mathbf{1}\{\mathcal{A}\} = 1$; if not it is 0. As mentioned in [54]-[60]:

$$P_k(\eta) \approx \exp\left(-\sum_{j=k}^{N} \frac{\mathbb{E}[A_{kj}(\eta)]}{\mathbb{E}[B_{kj}(\eta)]}\right) \approx \exp\left(-\sum_{j=k}^{N} \mathbb{E}\left[A_{kj}(\eta)\right]\right), \qquad \eta \to \infty \tag{2}$$

The recorded time series can be further divided into short term K subsequent block where $\mathbb{E}[A_{kj}(\eta)]$ remains almost constant for each block. Such that $\sum_{j\in C_i} \mathbb{E}\left[A_{kj}(\eta)\right] \approx \sum_{j\in C_i} a_{kj}\,(\eta)$ for a large enough range of η-values. Hence, $\sum_{j=k}^{N} \mathbb{E}\left[A_{kj}(\eta)\right] \approx \sum_{j=k}^{N} a_{kj}\,(\eta)$, where C_i indicates the set of indices for block numbered as i; from $i = 1, \dots, K$, and where $a_{kj}(\eta)$ are the realised values of $A_{kj}(\eta)$ for the calculated time series. Therefore, for a given stationary process (short term sea current state), the following is:

$$P_k(\eta) \approx \exp\left(-(N-k+1)\hat{\varepsilon}_k(\eta)\right) \tag{3}$$

where

$$\hat{\varepsilon}_k(\eta) = \frac{1}{N-k+1}\sum_{j=k}^{N} a_{kj}\,(\eta) \tag{4}$$

In the above equations, to make an approximation of the short term expected values, the observed values of the $a_{kj}(\eta)$ functions were used together with the assumption of ergodicity for each short-term section of the recorded time series. Another way of describing the long-term extreme value distribution in Eq. (3) can be realised since the empirical probability distribution of, $m = 1, .., M$, of sea current states has probabilities p_m, and $\sum_{m=1}^{M} p_m = 1$.

Thus, the long-term ACER function of order *k* is:

$$\mathrm{ACER_k}(\eta) \equiv \sum_{m=1}^{M} \hat{\varepsilon}_k(\eta, m)\, p_m \tag{5}$$

where $\hat{\varepsilon}_k(\eta, m)$, which is restricted to a specific sea state with number m, is the same type of function as in Eq. (4), but the averaging is restricted to the short-term block of data with number m.

As mentioned in [54]-[60], the long-term extreme value distribution of $M(T)$, can then be described according to the ACER function of order *k*:

$$P(\eta) \approx \exp\left(-N \cdot \mathrm{ACER_k}(\eta)\right) \tag{6}$$

where $ACER_k(\eta)$ is defined as the long-term empirical function for ACER in the order of *k*, where k "N; N is the number of all the data points from the recorded time series included to approximate the ACER functions. Stereotypically, these are local peaks from the measured time series.

The accuracy of Eq. (6) improves as the order *k* increases; it is observed that the $\mathrm{ACER_k}(\eta)$ functions converges rapidly with an increasing *k*, also mentioned in [54]-[60]. The advantage of the ACER method can be observed when increasing the conditioning level *k*. The probable data clustering effects can be accounted for, thus improving and refining the accuracy of the estimates of the extreme values, and this also circumvents an otherwise over-conservative design value.

In high response values of η, $\mathrm{ACER_k}$ as functions of the level, η are usually in the tail end. Especially, for $\eta \geq \eta_0$, when the tail behaves like $\exp\{-\mathrm{a}(\eta + b)^c + d\}$ with a, b, c, d becomes suitable constants.

It is possible to do optimisation for the log-level when the mean square error function *F* is minimised with respect to the four arguments: a_k, b_k, c_k, d_k.

$$F(a_k, b_k, c_k, d_k) = \int_{\eta_0}^{\eta_1} \omega(\eta) \left\{ \ln\left(\mathrm{ACER_k}(\eta)\right) - d_k + a_k(\eta + b_k)^{c_k} \right\}^2 d\eta, \qquad \eta \geq \eta_0 \qquad (7)$$

where η_1 is a suitable data cut-off value, i.e. the largest η response value, which allows calculation of the confidence interval. The weight function (ω) is defined as $\omega(\eta) = \{\ln C^+(\eta) - \ln C^-(\eta)\}^{-2}$ with $\left(C^-(\eta),\ C^+(\eta)\right)$ with a 95% CI, empirically approximated from the measured data. The comprehensive procedure for additional parameters optimisation a_k, b_k, c_k, d_k has been described in [27]-[34], [54]-[60].

ACER2D method

Now, the 2D (bivariate) Average Conditional Exceedance Rate, or briefly ACER2D method, has been applied to analyse FWT blade root and tower bottom bending moment due to environmental wind and wave loads. A brief introduction of the bivariate ACER2D method is outlined below; see [61]-[64] for more details. Note that both of the stochastic response processes (blade root and tower bottom bending moments) mentioned above, are time-synchronous. The latter is undoubtedly beneficial for coupling effects and bivariate statistics study.

This paper studies a bivariate stochastic process $Z(t) = (X(t), Y(t))$, having two scalar processes $X(t), Y(t)$, simulated synchronously, over a time span $(0, T)$. The bivariate data points $(X_1, Y_1), \ldots, (X_N, Y_N)$ correspond to equidistant time instants $t_1, \ldots, t_N$.

The joint CDF (cumulative distribution function) $P(\xi, \eta) := \mathrm{Prob}\left(\hat{X}_N \leq \xi, \hat{Y}_N \leq \eta\right)$ of the maxima vector $\left(\hat{X}_N, \hat{Y}_N\right)$, with $\hat{X}_N = \max\{X_j\,; j = 1, \ldots, N\}$, and $\hat{Y}_N = \max\{Y_j\,; j = 1, \ldots, N\}$ is introduced. In this paper, ξ and η are blade root and tower bottom mooring bending moments, $\mathrm{M_1}$ and $\mathrm{M_3}$ in respectively.

Next, the non-exceedance event is introduced: $\mathcal{C}_{kj}(\xi, \eta) := \{X_{j-1} \leq \xi, Y_{j-1} \leq \eta, \ldots, X_{j-k+1} \leq \xi, Y_{j-k+1} \leq \eta\}$ for $1 \leq k \leq j \leq N + 1$. Based on the definition of the joint CDF $P(\xi, \eta)$

$$
\begin{aligned}
P(\xi,\eta) = \ & \text{Prob}\left(\mathcal{C}_{N+1,N+1}(\xi,\eta)\right) \\
= \ & \text{Prob}\left(X_N \le \xi, Y_N \le \eta \mid \mathcal{C}_{NN}(\xi,\eta)\right) \cdot \text{Prob}\left(\mathcal{C}_{NN}(\xi,\eta)\right) \\
= & \prod_{j=2}^{N} \text{Prob}\left(X_j \le \xi, Y_j \le \eta \mid \mathcal{C}_{jj}(\xi,\eta)\right) \cdot \text{Prob}\left(\mathcal{C}_{22}(\xi,\eta)\right)
\end{aligned}
\tag{8}
$$

The CDF $P(\xi,\eta)$ can be expressed as in [61]-[64]

$$
P(\xi,\eta) \approx \exp\left\{-\sum_{j=k}^{N}\left(\alpha_{kj}(\xi;\eta) + \beta_{kj}(\eta;\xi) - \gamma_{kj}(\xi,\eta)\right)\right\} \tag{9}
$$

for a suitably large conditioning level parameter k, and large ξ and η with $\alpha_{kj}(\xi;\eta) \coloneqq \text{Prob}\left(X_j > \xi \mid \mathcal{C}_{kj}(\xi,\eta)\right)$, $\beta_{kj}(\eta;\xi) \coloneqq \text{Prob}\left(Y_j > \eta \mid \mathcal{C}_{kj}(\xi,\eta)\right)$, $\gamma_{kj}(\xi,\eta) \coloneqq \text{Prob}\left(X_j > \xi, Y_j > \eta \mid \mathcal{C}_{kj}(\xi,\eta)\right)$.

Next, the k-th order bivariate average conditional exceedance rate (ACER2D) functions can be introduced

$$
\mathcal{E}_k(\xi,\eta) = \frac{1}{N-k+1}\sum_{j=k}^{N}\left(\alpha_{kj}(\xi;\eta) + \beta_{kj}(\eta;\xi) - \gamma_{kj}(\xi,\eta)\right) \tag{10}
$$

for $k = 1, 2, \ldots$; when $N \gg k$

$$
P(\xi,\eta) \approx \exp\{-(N-k+1)\mathcal{E}_k(\xi,\eta)\}\text{; for large } \xi \text{ and } \eta. \tag{11}
$$

From Eq. (11), it follows that an accurate estimate of the bivariate CDF $P(\xi,\eta) = P(\xi,\eta)$ relies on the equally accurate estimation of ACER2D functions $\mathcal{E}_k$.

3.3. Load cases and environmental conditions

The environmental data (wind and wave data) used in this paper are established based on hindcast data from an offshore site in the Northern North Sea from 2001 to 2010. The long-term joint wind and wave distribution were developed in [65], which considers a one-hour mean wind speed at the position that is 10 meters above the sea level (U_{10}), wave spectral peak period (T_p) and the significant wave height (H_s). The joint distribution of U_{10}, H_s and T_p is expressed as below:

$$
f_{U_{10},H_s,T_p}(u,h,t) = f_{U_{10}}(u) \cdot f_{H_s|U_{10}}(h|u) \cdot f_{T_p|U_{10},H_s}(t|u,h) \tag{12}
$$

where $f_{U_{10}}(u)$, $f_{H_s|U_{10}}(h|u)$ *and* $f_{T_p|U_{10},H_s}(t|u,h)$ represents the marginal distribution of U_{10}, the conditional distribution of H_s for given U_{10} and the conditional distribution of T_p for given U_{10} and H_s. **Figure 4** illustrates in situ H_s, T_p scattered diagram, used to assign probabilities to individual sea states.

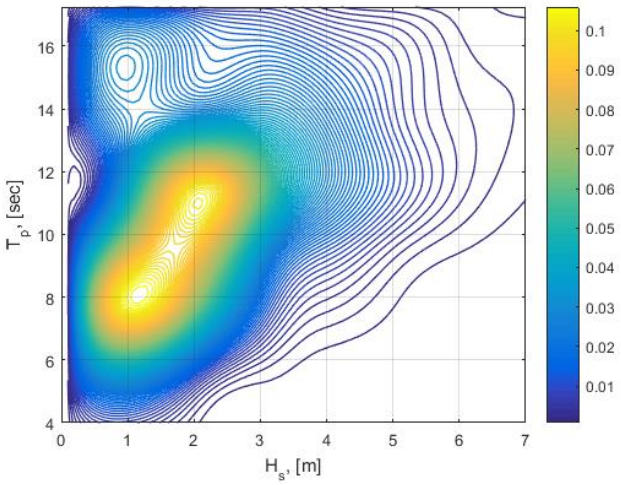

Figure 4 An example of in situ H_s, T_p scattered diagram, used to assign probabilities to individual sea states.

Table 4 Load cases for numerical simulations.

Load cases	U_w **(m/s)**	T_I	H_s **(m)**	T_p **(s)**	**Samples**	**Simulation length (s)**
LC1	8	0.1740	1.9	9.7	20	4000
LC2	12	0.1460	2.5	10.1	20	4000
LC3	16	0.1320	3.2	10.7	20	4000

Three representative load cases with a high probability of occurrence in the normal operating conditions are used in the present work and listed in Table 4. The mean wind speed selected to be used in this paper is based on the turbines operating ranges (wind speeds ranging within the cut-in, rated and cut-out zones) with an increment size of 4 m/s. The most probable wave height and spectra peak period in each wind speed condition is selected based on the joint distribution expressed in Eq. (*12*).

The turbulent wind and irregular waves are modelled, and they are considered to be directionally aligned in all the load cases. The normal turbulence and normal wind profile models are employed, and wind turbine Class C is applied. The wind power-law formulation is used to model the wind speed profile, as represented below:

$$U_w(z) = U_{hub}\left(\frac{Z}{Z_{hub}}\right)^{\alpha} \quad (13)$$

where $U_w(z)$ is the mean wind speed at the height z above the still water level, u_{hub} represents the mean wind speed at the hub height, z_{hub} denotes the hub height above the still water level and is 119 m for the 10-MW FWT. α is the power-law exponent, and it is taken as 0.14 for offshore locations based on the recommendation in IEC 61400-3-2, see [66].

The Kaimal turbulence model is used to generate the three-dimensional turbulent wind fields, simulated using a stochastic turbulent-wind simulator, Turbsim [67]. Time-varying irregular waves are generated using the JONSWAP (Joint North Sea Wave Project) spectrum according to the specified H_s and T_p. Detailed descriptions for the models of turbulent wind and irregular waves can be found in IEC 61400-3-2 [66].

For the three environmental conditions, 20 different random samples of wind and wave are applied for each sea state. Each simulation lasts 4000s, where the first 400s is removed to reduce the transient effect induced by the wind turbine start-up. Therefore, 1-h data in each simulation is formed and is used for extreme value analysis in this work. The results shown in this work are based on the average of 20 1-h simulations to reduce the stochastic variability.

4. Results and discussions

This paper presents the methodology for estimating the DTU 10-MW RWT-OO-Star's extreme loads during operating conditions. The empirical data is based on accurate numerical simulations using a FAST model as presented in Section 3.1. The ACER2D (bivariate averaged conditional exceedance rate) method is presented in Section 3.2.

Response variable:

The loads at the two measurement points presented in are considered. These are the blade 1 root flapwise bending moment (RootMyb1) and tower bottom fore-aft bending moment (TwrBsMyt).

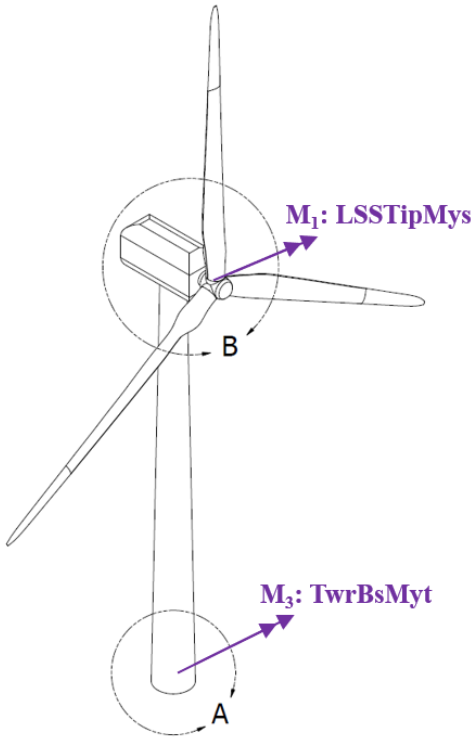

Figure 5 Location of points where bending moments are measured.

4.1. Power Spectral Density based on time responses

Figure 7 of M_1, M_3. It is seen that there are PSD (Power Spectral Density) peaks at the frequencies *f* at 3P, 6P and 9P as observed in Figure **6**. This information should be reflected in the ACER functions' choice of conditioning level k.

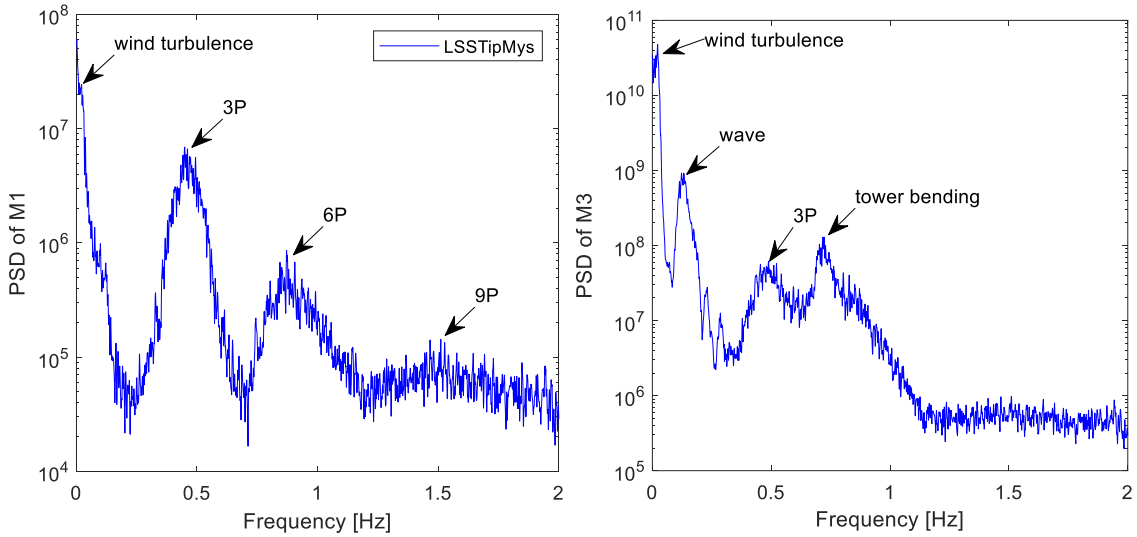

Figure 7 PSD of RootMyb1 – M1 and TwrBsMyt – M3

4.2. Extreme responses: univariate and bivariate analysis

This section presents statistical analysis results for M_1 and M_3 bending moments using the univariate and bivariate methods, i.e., ACER1D and ACER2D, respectively. The focus is on accurate predicting extreme response, which is vital for safety and reliability at the design stage. The conditioning level *k* is set to be 10, as it was observed that ACER functions have converged at that level in the distribution tail.

Figure 8 presents univariate extreme response 5-year return period prediction with 95 % confidence interval (CI); the 1-year return period is chosen purely as an example. The predicted extreme probability level corresponds to 5-year return period.

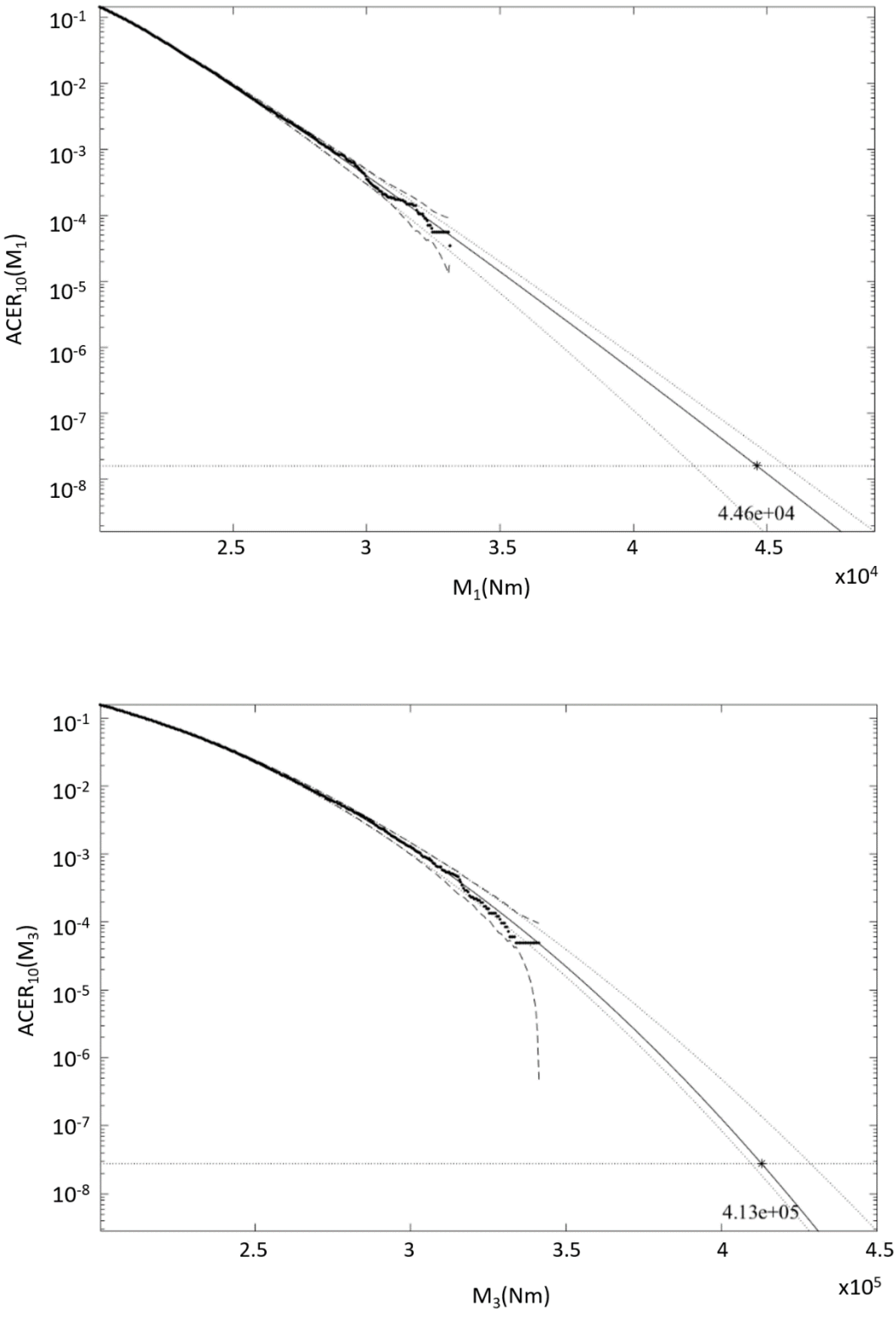

Figure 8 Univariate ACER1D extreme response 5-year prediction with 95% CI (dotted lines). Top: RootMyb1 – M_1; Bottom: TwrBsMyt – M_3; decimal log scale.

Figure 9 presents the phase space of responses M_1 over M_3, along with the bivariate empirical ACER2D function $\hat{\mathcal{E}}_k$. It is clearly seen that there is a non-linear correlation between responses M_1 and M_3. The bivariate empirical ACER2D surface, $\hat{\mathcal{E}}_k$ obviously marginally corresponds to univariate ACER1D functions presented in **Figure 8**.

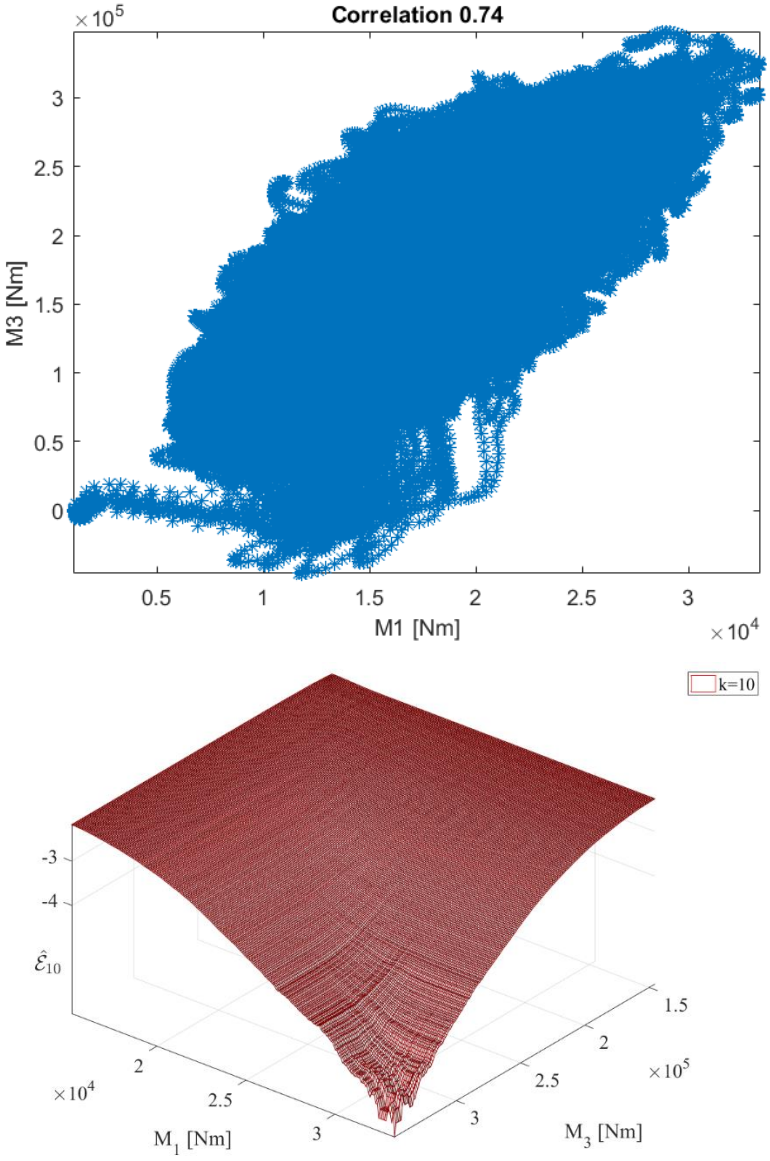

Figure 9 Top: phase space, response M_1 vs M_3; Bottom: bivariate empirical ACER2D function $\hat{\mathcal{E}}_k$, decimal log scale.

Figure 10 presents ACER2D fit to the empirical data along with the bivariate predicted contours with return periods in years (lower figure). **Figure 10** presents contour lines for the optimized Asymmetric logistic (AL) $\mathcal{A}_k(M_1, M_3)$ and optimized Gumbel logistic (GL) $\mathcal{G}_k(M_1, M_3)$ models, optimally matched to the corresponding empirical bivariate ACER2D function $\hat{\mathcal{E}}_k(M_1, M_3)$, $k = 10$, see [61]-[64] for GL and AL definitions. The contour lines negative labelling numbers in **Figure 10** indicate decimal logarithmic scale probability levels of $P(M_1, M_3)$. **Figure 10** clearly shows that the empirical bivariate ACER2D surface $\hat{\mathcal{E}}_{10}$ well captures the strong correlation between load/response components. The optimized models $\mathcal{G}_{10}$ and $\mathcal{A}_{10}$ exhibit smooth contours along with matching ACER2D empirical contours. The later models may be better suited for bivariate extreme value distributions response processes. **Figure 10** shows good agreement between the estimated optimized AL and GL surfaces and

the bivariate ACER2D surface. This means that the correlation between responses M_1 vs M_3 is a crucial non-negligible factor influencing the shape of the bivariate contour lines.

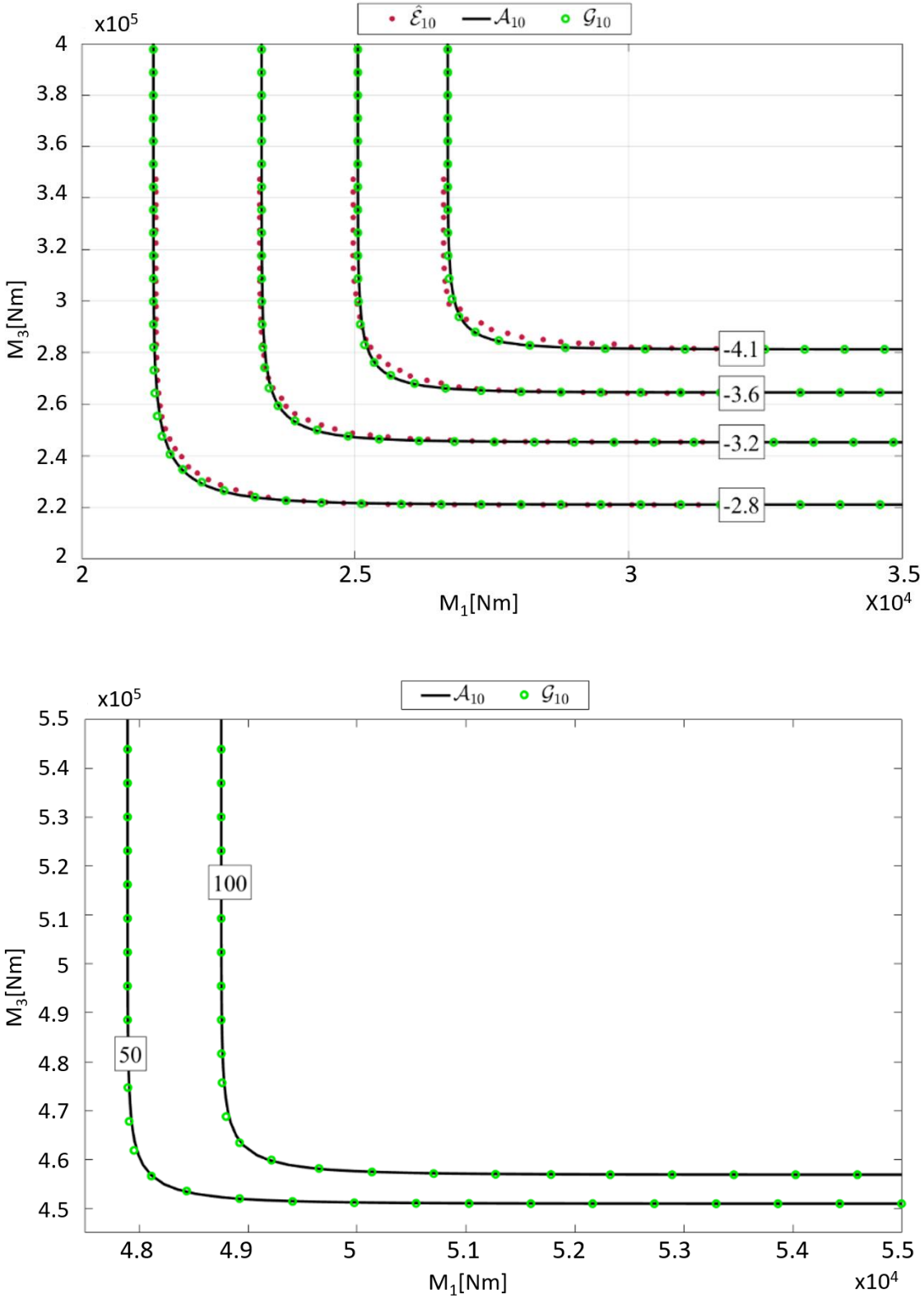

Figure 10 Top: ACER2D fit to empirical data; Bottom: predicted bivariate contours with return periods in years.

The lowest probabilities in **Figure 9** and **Figure 10** correspond to the value N^{-1} where N is the number of equidistant time points in the studied time series, see Eqs. (1) to (8). Figure 8 (bottom) presents the predicted bivariate contours with 50- and 100-years corresponding return periods. Note that the return period of a few years is quite long compared to the short duration of the analysed measured record. As seen from **Figure 10** (bottom), the fitted lines match the empirical data well, highlighting the accuracy of the ACER method. Further, the ACER method is efficient as it requires only 20 1-hour realisations to generate accurate results.

Figure 11 shows that the univariate design point lies outside the safe 50-year zone (dashed area) and is outside the 2D design zone. This means that the 1D method is not conservative.

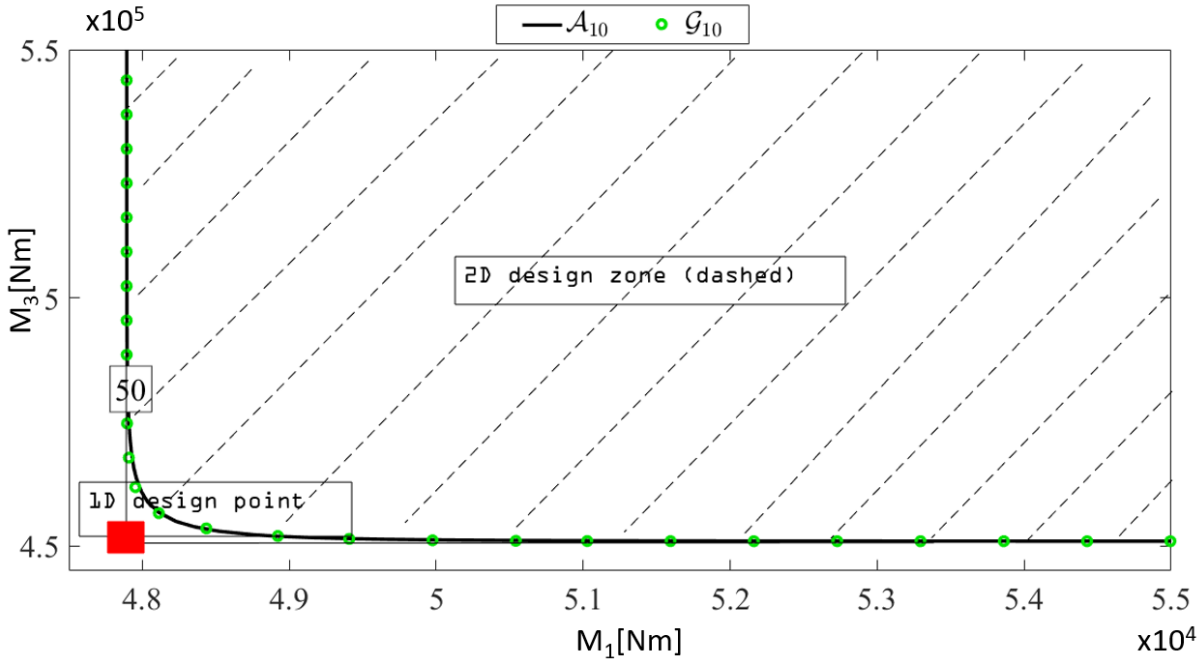

Figure 11 Design safe zone (dashed) due to bivariate analysis, versus univariate design point, based on **Figure 10**. Asymmetric logistic $\mathcal{A}_k(M_1, M_3)$ 50-year contour line.

Table *5* presents 50- and 100-year return period ACER1D response predictions in meters.

Table 5 50- and 100-year return period response ACER1D predictions

	50 yr	**100 yr**
M_1 (Nm)	4.8 x 10^4	4.9 x 10^4
M_3 (Nm)	4.5 x 10^5	4.6 x 10^5

5. Conclusions

A novel approach that is based on a 2D design point instead of the traditional 1D characteristic design values has been introduced. The proposed methodology provides an accurate bivariate extreme value prediction, utilizing all available data efficiently. Based on the overall performance of the proposed method, it was concluded that the ACER2D method could

incorporate environmental input and provide a more robust and accurate bivariate prediction based on proper numerical simulations. The method uses only a relatively small amount of data to provide reasonable predictions with long return periods.

The FWT blade root and tower bottom bending moments due to environmental wind and wave loads were studied for three operating conditions of mean wind speeds of 8, 12 and 16 m/s. The bivariate ACER2D method was briefly described and applied to account for the coupled load effects, namely dynamic moment and force simulated synchronously in time. Bivariate extreme value distribution low probabilities (or equivalently high quantiles) contours were estimated by adopting various bivariate copula models. Potential outliers present in the data set are also well managed by being neglected in the distribution tail through the proposed extrapolation and copula fit technique.

Regarding the safety and reliability of FWT operations, the multivariate analysis is a more proper approach than the classic univariate approach. The presented technique has the following advantages:

- Unlike IFORM/ SORM, the ACER2D method does not simplify model nonlinearities.
- Various kinds of coupled data can be studied: measured or numerically simulated.
- Clustering effects can be accounted for.
- The univariate estimation of design values may not be conservative as indicated through the comparison to a bivariate analysis as presented in this paper.
- ACER2D method may provide an efficient way of identifying practical design appropriate bivariate copula models.

The described approach may be used at the design stage of a large FWT to provide the opportunity of defining FWT parameters that would minimize extreme loads and potential damages. It is also noted that the study is limited to the quality of the data itself. This limitation applies for any type of statistical method.

References

[1] International Energy Agency. (2020). World energy outlook 2020. OECD Publishing.

[2] Veers, P., Butterfield, S. (2001). Extreme load estimation for wind turbines-issues and opportunities for improved practice. In 20th 2001 ASME Wind Energy Symposium (p. 44).

[3] Igba, J., Alemzadeh, K., Durugbo, C., Henningsen, K. (2015). Performance assessment of wind turbine gearboxes using in-service data: Current approaches and future trends. Renewable and Sustainable Energy Reviews, 50, 144-159.

[4] Irena, I. R. E. A. (2012). Renewable energy technologies: Cost analysis series. Wind Power.

[5] Sheng, S. (2012). Wind turbine gearbox condition monitoring round robin study-vibration analysis (No. NREL/TP-5000-54530). National Renewable Energy Lab.(NREL), Golden, CO (United States).

[6] Veers, P. S., Winterstein, S. R. (1998). Application of measured loads to wind turbine fatigue and reliability analysis.

[7] Dimitrov, N. (2016). Comparative analysis of methods for modelling the short-term probability distribution of extreme wind turbine loads. Wind Energy, 19(4), 717-737.

[8] Madsen, P., Pierce, K., Buhl, M. (1999). Predicting ultimate loads for wind turbine design. In 37th Aerospace Sciences Meeting and Exhibit (p. 69).

[9] Ronold, K. O., Wedel-Heinen, J., Christensen, C. J. (1999). Reliability-based fatigue design of wind-turbine rotor blades. Engineering structures, 21(12), 1101-1114.
[10] Ronold, K. O., Larsen, G. C. (2000). Reliability-based design of wind-turbine rotor blades against failure in ultimate loading. Engineering structures, 22(6), 565-574.
[11] Manuel, L., Veers, P. S., Winterstein, S. R. (2001). Parametric models for estimating wind turbine fatigue loads for design. J. Sol. Energy Eng., 123(4), 346-355.
[12] Fitzwater, L. Cornell A.C. (2002). Predicting the long term distribution of extreme loads from limited duration data: comparing full integration and approximate methods. J. Sol. Energy Eng., 124(4), 378-386.
[13] Moriarty, P. J., Holley, W. E., Butterfield, S. (2002). Effect of turbulence variation on extreme loads prediction for wind turbines. J. Sol. Energy Eng., 124(4), 387-395.
[14] Agarwal, P., Manuel, L. (2008). Extreme loads for an offshore wind turbine using statistical extrapolation from limited field data. Wind Energy: An International Journal for Progress and Applications in Wind Power Conversion Technology, 11(6), 673-684.
[15] Barreto, D., Karimirad, M., Ortega, A. (2022). Effects of Simulation Length and Flexible Foundation on Long-Term Response Extrapolation of a Bottom-Fixed Offshore Wind Turbine. Journal of Offshore Mechanics and Arctic Engineering, 144(3).
[16] McCluskey, C. J., Guers, M. J., Conlon, S. C. (2021). Minimum sample size for extreme value statistics of flow-induced response. Marine Structures, 79, 103048.
[17] Fogle, J., Agarwal, P., Manuel, L. (2008). Towards an improved understanding of statistical extrapolation for wind turbine extreme loads. Wind Energy: An International Journal for Progress and Applications in Wind Power Conversion Technology, 11(6), 613-635.
[18] Ernst, B., Seume, J. R. (2012). Investigation of site-specific wind field parameters and their effect on loads of offshore wind turbines. Energies, 5(10), 3835-3855.
[19] Graf, P. A., Stewart, G., Lackner, M., Dykes, K., Veers, P. (2016). High-throughput computation and the applicability of Monte Carlo integration in fatigue load estimation of floating offshore wind turbines. Wind Energy, 19(5), 861-872.
[20] Fitzwater, L. M., Winterstein, S. R. (2001). Predicting design wind turbine loads from limited data: Comparing random process and random peak models. J. Sol. Energy Eng., 123(4), 364-371.
[21] Moriarty, P. J., Holley, W. E., Butterfield, S. P. (2004). Extrapolation of extreme and fatigue loads using probabilistic methods (No. NREL/TP-500-34421). National Renewable Energy Lab., Golden, CO (US).
[22] Freudenreich, K., Argyriadis, K. (2007, July). The load level of modern wind turbines according to IEC 61400-1. In Journal of Physics: Conference Series (Vol. 75, No. 1, p. 012075). IOP Publishing.
[23] Ragan, P., Manuel, L. (2008). Statistical extrapolation methods for estimating wind turbine extreme loads. Journal of Solar Energy Engineering, 130(3).
[24] Peeringa, J. M. (2009). Comparison of extreme load extrapolations using measured and calculated loads of a MW wind turbine. Petten: ECN.
[25] Abdallah, I. (2015). Assessment of extreme design loads for modern wind turbines using the probabilistic approach. DTU Wind Energy. DTU Wind Energy PhD No. 0048(EN).
[26] Stewart, G. M., Lackner, M. A., Arwade, S. R., Hallowell, S., Myers, A. T. (2015). Statistical Estimation of Extreme Loads for the Design of Offshore Wind Turbines During Non-Operational Conditions. Wind Engineering, 39(6), 629-640.
[27] Zhang, J., Gaidai, O., Wang, K., Xu, J., Ye, R., Xu, X. (2019). A stochastic method for the prediction of icebreaker bow extreme stresses. Applied Ocean Research, 87, 95-101.

[28] Gaidai, O., Cheng, Y., Xu, X., Su, Y. (2018). Long-term offshore Bohai bay Jacket strength assessment based on satellite wave data. Ships and Offshore Structures, 13(6), 657-665.
[29] Gaidai, O., Storhaug, G., Naess, A. (2016). Extreme value statistics of large container ship roll. Journal of Ship Research, 60(2), 92-100.
[30] Naess, A., Gaidai, O. (2008). Monte Carlo methods for estimating the extreme response of dynamical systems. Journal of Engineering Mechanics, 134(8), 628-636.
[31] Næss, A., Gaidai, O. (2009). Estimation of extreme values from sampled time series. Structural Safety, 31(4), 325-334.
[32] Naess, A., Gaidai, O., Batsevych, O. (2010). Prediction of extreme response statistics of narrow-band random vibrations. Journal of Engineering Mechanics, 136(3), 290-298.
[33] Naess, A., Moan, T. (2013). Stochastic dynamics of marine structures. Cambridge University Press.
[34] Karpa, O., Naess, A. (2013). Extreme value statistics of wind speed data by the ACER method. Journal Of Wind Engineering And Industrial Aerodynamics, 112, 1-10. doi: 10.1016/j.jweia.2012.10.001
[35] Xu, S., Ji, C. Y., Soares, C. G. (2021). Short-term extreme mooring tension and uncertainty analysis by a modified ACER method with adaptive Markov Chain Monte Carlo simulations. Ocean Engineering, 236, 109445.
[36] Xu, K., Zhang, M., Shao, Y., Gao, Z., Moan, T. (2019). Effect of wave nonlinearity on fatigue damage and extreme responses of a semi-submersible floating wind turbine. Applied Ocean Research, 91, 101879. doi: 10.1016/j.apor.2019.101879
[37] Yu, W., Müller, K., Lemmer, F., Bredmose, H., Borg, M., Sanchez, G., Landbo, T. (2017). Public Definition of the Two LIFES50+ 10MW Floater Concepts.". *LIFES50+ Deliverable*, *4*.
[38] Bak, C., Zahle, F., Bitsche, R., Kim, T., Yde, A., Henriksen, L., Hansen, M.H., Blasques, J.P.A.A., Gaunaa, M.A., Natarajan, M. H. (2013). The DTU 10-MW reference wind turbine, Danish wind power Research 2013.
[39] Muggiasca, S., Taruffi, F., Fontanella, A., Di Carlo, S., Giberti, H., Facchinetti, A., Belloli, M. (2021). Design of an aeroelastic physical model of the DTU 10MW wind turbine for a floating offshore multipurpose platform prototype. Ocean Engineering, 239, 109837. doi: 10.1016/j.oceaneng.2021.109837
[40] Yu, Z., Amdahl, J., Rypestøl, M., Cheng, Z. (2022). Numerical modelling and dynamic response analysis of a 10 MW semi-submersible floating offshore wind turbine subjected to ship collision loads. Renewable Energy, 184, 677-699.
[41] Wang, S., Moan, T., Jiang, Z. (2022). Influence of variability and uncertainty of wind and waves on fatigue damage of a floating wind turbine drivetrain. Renewable Energy, 181, 870-897.
[42] Hu, R., Le, C., Gao, Z., Ding, H., Zhang, P. (2021). Implementation and evaluation of control strategies based on an open controller for a 10 MW floating wind turbine. Renewable Energy, 179, 1751-1766.
[43] Yu, W., Müller, K., Lemmer, F., Schlipf, D., Bredmose, H., Borg, M., Landbø, T., Andersen, H. (2018). LIFES50+ D4. 2: Public definition of the two LIFES50+ 10 MW floater concepts. University of Stuttgart.
[44] Moriarty, P. J., Hansen, A. C. (2005). *AeroDyn theory manual* (No. NREL/TP-500-36881). National Renewable Energy Lab., Golden, CO (US).
[45] Jonkman, J. M., Robertson, A. N., Hayman, G. J. (2014). HydroDyn user's guide and theory manual. *National Renewable Energy Laboratory*.
[46] Hall M. MoorDyn user's guide. Orono, ME: Department of Mechanical Engineering, University of Maine, 2015.

[47] Jonkman, J., Musial, W. (2010). Offshore code comparison collaboration (OC3) for IEA Wind Task 23 offshore wind technology and deployment (No. NREL/TP-5000-48191). National Renewable Energy Lab.(NREL), Golden, CO (United States).
[48] Robertson, A., Jonkman, J., Musial, W., Popko, W., Vorpahl, F. (2014). IEA Wind Task 30 Offshore Code Comparison Collaboration Continued.
[49] Coulling, Alexander Goupee, Andrew Robertson, Amy Jonkman, Jason Dagher, Habib. (2013). Validation of a FAST semi-submersible floating wind turbine numerical model with DeepCwind test data. Journal of Renewable and Sustainable Energy. 5. 10.1063/1.4796197.
[50] Lee, C. H., Newman, J. N. (2006). Wamit user manual. WAMIT, Inc, 42.
[51] Faltinsen, O. (1993). Sea loads on ships and offshore structures (Vol. 1). Cambridge university press.
[52] Kane, T. R., Levinson, D. A. (1983). The use of Kane's dynamical equations in robotics. The International Journal of Robotics Research, 2(3), 3-21.
[53] Cheng, Z., Madsen, H. A., Chai, W., Gao, Z., Moan, T. (2017). A comparison of extreme structural responses and fatigue damage of semi-submersible type floating horizontal and vertical axis wind turbines. Renewable Energy, 108, 207-219.
[54] Naess, A., Gaidai, O., Batsevych, O. (2010). Prediction of extreme response statistics of narrow-band random vibrations. Journal of engineering mechanics, 136(3), 290-298.
[55] Naess, A., Gaidai, O. (2008). Monte Carlo methods for estimating the extreme response of dynamical systems. Journal of Engineering Mechanics, 134(8), 628-636.
[56] Xu, X. S., Gaidai, O., Karpa, O., Wang, J. L., Ye, R. C., Cheng, Y. (2021). Wind Farm Support Vessel Extreme Roll Assessment While Docking in the Bohai Sea. China Ocean Engineering, 35(2), 308-316.
[57] Zhao, Y., Liao, Z., Dong, S. (2021). Estimation of characteristic extreme response for mooring system in a complex ocean environment. Ocean Engineering, 225, 108809.
[58] Galambos, J., Marci, N. (1999). Classical extreme value model and prediction of extreme winds. Journal of Structural Engineering, 125(7), 792-794.
[59] Naess, A., Moan, T. (2013). Stochastic dynamics of marine structures. Cambridge University Press.
[60] Naess, A., Stansberg, C. T., Gaidai, O., Baarholm, R. J. (2009). Statistics of extreme events in airgap measurements. Journal of offshore mechanics and Arctic engineering, 131(4).
[61] Naess, A, Karpa, O. (2015), "Statistics of bivariate extreme wind speeds by the ACER2D method", J. Wind Eng. and Ind. Aerodyn. Vol 139, pp.82–88.
[62] Karpa, O., and Naess, A. (2015), "Statistics of Extreme Wind Speeds and Wave Heights by the Bivariate ACER2D Method", Journal of Offshore Mechanics and Arctic Engineering, Vol 137(2).
[63] Gaidai, O, and Storhaug, G, and Naess, A. (2016) "Extreme large cargo ship panel stresses by bivariate ACER2D method", Ocean Engineering, Vol. 127, pp. 368-386.
[64] Jian, Z, Gaidai, O, Gao, J. (2018), "Bivariate Extreme Value Statistics of Offshore Jacket Support Stresses in Bohai Bay", Journal of Offshore Mechanics and Arctic Engineering, Vol 140 (4).
[65] Li, L., Gao, Z., Moan, T. (2013). Joint environmental data at five European offshore sites for design of combined wind and wave energy concepts. In 32nd International Conference on Ocean, Offshore, and Arctic Engineering, no. OMAE2013-10156.
[66] IEC 61400-3-2 (2019). Part 3-2: Design requirements for floating offshore wind turbines.
[67] Jonkman, B. J. (2009). TurbSim user's guide: Version 1.50 (No. NREL/TP-500-46198). National Renewable Energy Lab.(NREL), Golden, CO (United States).

[68] Gaidai, O., Ji, C., Kalogeri, C., Gao, J. (2017). SEM-REV energy site extreme wave prediction, Renewable Energy, Vol 101, pp. 894-899.
[69] X. Xu, O. Gaidai, O. Karpa, J. Wang, R. Ye, Y. Cheng, (2021), Wind Farm Support Vessel Extreme Roll Assessment While Docking in the Bohai Sea, China Ocean Engineering, Vol 35 (2), pp. 308-316.
[70] Xu, X., Gaidai, O., Naess, A., Sahoo, P., (2020), Extreme loads analysis of a site-specific semi-submersible type wind turbine, Ships and Offshore structures, DOI: 10.1080/17445302.2020.1733315.
[71] Bak, C., Zahle, F., Bitsche, R., Kim, T., Yde, A., Henriksen, L.C., Hansen, M.H., Blasques, J.P.A.A., Gaunaa, M. and Natarajan, A., 2013. The DTU 10-MW reference wind turbine. In Danish Wind Power Research 2013.
[72] Naess, A, Karpa, O. (2015), "Statistics of bivariate extreme wind speeds by the ACER2D method", J. Wind Eng. and Ind. Aerodyn. Vol 139, pp.82–88.
[73] Karpa, O., and Naess, A. (2015), "Statistics of Extreme Wind Speeds and Wave Heights by the Bivariate ACER2D Method", Journal of Offshore Mechanics and Arctic Engineering, Vol 137(2).
[74] Gaidai, O, and Storhaug, G, and Naess, A. (2016) "Extreme large cargo ship panel stresses by bivariate ACER2D method", Ocean Engineering, Vol. 127, pp. 368-386.
[75] Jian, Z, Gaidai, O, Gao, J. (2018), "Bivariate Extreme Value Statistics of Offshore Jacket Support Stresses in Bohai Bay", Journal of Offshore Mechanics and Arctic Engineering, Vol 140 (4).
[76] Jonkman, J. M., & Buhl, M. L. (2005). FAST users guide NREL/EL-500-38230. National Renewable Energy Laboratory, Tech. Rep.

Characterisation of extreme load responses of a 10-MW floating semi-submersible type wind turbine

Yihan Xing[1], Shuaishuai Wang[2,*], Anuraj Karuvathil[1], Rajiv Balakrishna[1], Oleg Gaidai[3]

[1]Department of Mechanical and Structural Engineering and Materials Science, University of Stavanger, Norway

[2]Norwegian University of Science and Technology, Trondheim, Norway

[3]Shanghai Engineering Research Centre of Marine Renewable Energy, College of Engineering Science and Technology, Shanghai Ocean University, Shanghai, China

[*]Corresponding author: shuaishuai.wang@ntnu.no

Abstract

Offshore wind turbines have been steadily increasing in size, with the global average size increasing from 1.5 MW to 6 MW from 2000 to 2020. With this backdrop, the research community has recently looked at very large offshore wind turbines (OWTs) in the 10 to 15 MW class. The larger rotor, nacelle structure and tower have larger structural flexibility. The larger structural flexibility, controller dynamics, aero, hydrodynamics, and various environmental conditions result in complex structural responses. The structural load effects of a very large OWT could be more severe than that of the lower MW classes. Accurate quantification of the extreme dynamic responses of OWT systems is essential in the Ultimate Limit State (ULS) based design due to the fully-coupled interaction between the OWT system and environmental conditions. Motivated by this, this paper uses the average conditional exceedance rate (ACER) and Gumbel methods to predict the extreme responses of the 10 MW semi-submersible type floating OWT under the operating conditions of 8, 12, and 16 m/s mean wind speed, representing the below-rated, rated and above-rated regions, respectively. The aim is to guide future research on very large OWTs by indicating the ULS loads expected.

Keywords: Floating wind turbine, FAST, Extreme value analysis, ACER method, Gumbel method

1. Introduction

Offshore wind has been developing quickly from the past decade. From the global wind report 2021 [1] issued by the global wind energy council, it is seen that the cumulative offshore installations have grown on average by 22 % annually in the past decade. The cumulative installed wind energy was 35 GW in 2020, 14 times higher than a decade ago. Further, it is estimated that there will be over 235 GW new installations over the next decade, which demonstrates a great prospect.

One observation over the years in the technological development of wind turbines is that wind turbine capacities have consistently increased. This is particularly true of offshore wind turbines (OWTs). Larger wind turbine sizes enable the same power output with fewer turbines, foundations, converters, and cables and lower maintenance costs, thus reducing the overall cost of energy. The global average offshore wind turbine size has increased from 1.5-MW in 2000 to 6.0-MW in 2020 [1]. The trend continues with the research community recently starting conceptual studies for 15-20 MW-class offshore turbines, such as the IEA 15-MW offshore reference wind turbine [2].

Accurate quantification of the extreme dynamic responses of OWT systems is essential in the Ultimate Limit State (ULS) based design. Due to the fully-coupled interaction between the OWT system and environmental conditions, the responses are strongly nonlinear and highly dynamic. A robust set of design requirements must ensure that the extreme load effects over the entire design lifetime are correctly assessed with corresponding structural capacities designed in the OWT. Estimating these extreme load effects can be challenging. Direct calculation of extreme structural responses could obtain accurate results, but this method needs many dynamic simulations and substantial computational costs. A statistical extrapolation method, as proposed in IEC 61400-3 [3], for ultimate strength analysis makes it possible to evaluate the extreme load effects of OWTs by using a much smaller amount of data, thereby saving a great deal of computational time.

Many studies have evaluated the effectiveness of various statistical extrapolation methods when used for the extreme load and load effect analysis for OWTs. Saha et al. [4] studied the extreme short-term responses of a jacket foundation of a 5 MW OWT. The authors studied the sensitivity of the extreme responses to sample sizes. Three extreme value analysis methods were investigated: the mean up crossing rate method, the Weibull tail method, and the global maxima method. It was found that the up crossing rate method performs better for both Gaussian and non-Gaussian responses than the other two methods. Dimitrov [5] compared three different methods for extracting independent responses peaks of wind turbine loads. Low-speed shaft torsion moment, tower base side-side bending moment, and flapwise blade root bending moment were compared. The results showed that the statistical load extrapolation method could reasonably estimate the statistical distribution of extreme loads under normal operating conditions. In contrast, uncertainties in the extrapolation approach exist in other conditions such as emergency stops, faults, grid drops, storms. Further, the behaviour is influenced by the turbine controller strategy. Using measurement data, Lott and Cheng [6] presented different methods to perform statistical extrapolations of extreme loads at wind turbine tower base and blade root. It was shown that the choices of the distribution function and the fitting method, and the database selection are important in determining the extrapolated extreme loads. Cao et al. [7] proposed a stochastic programming formulation based on statistical extrapolation techniques to mitigate long-term extreme loads in wind turbines. It is found that significant improvements in power extraction can be obtained while within the extreme mechanical loads. Cheng et al. [8] compared the extreme structural response and fatigue damage of a 5 MW horizontal axis floating wind turbine and a 5 MW vertical type. Li et al. [9] estimated the extreme values of the tower base fore-aft bending moments and mooring line tension forces of an integrated wind, wave and tidal energy system based on an extrapolated up-crossing rate method. Xu et al. [10] investigated the effect of wave nonlinearity on the fatigue damage and extreme responses of a 5MW semi-submersible floating wind turbine. Gumbel fitting and average conditional exceedance rate (ACER) methods were used to estimate the extreme responses of the tower base bending moments and mooring line tensions in extreme conditions.

Most studies on extreme structural response were performed on small-scale or medium-scale OWTs. Minimal effort has been devoted to very large (10-15 MW) floating OWTs. Very large floating OWT has longer blades, larger swept areas, and taller tower heights, leading to larger aerodynamic loads. In addition, it has a heavier rotor-nacelle-assembly (RNA) system and a larger support structure which leads to larger inertial loads. Further, studies performed by Wang et al. [11]-[12] indicated that larger wind turbines could be at risk of resonance. The larger rotor, nacelle structure and tower could be sufficiently flexible so their natural frequencies can be close to the low-frequency wind and wave excitations. The generally larger load effects mean that the structural load effects of a very large OWT could be more severe than that of the lower

MW classes. This highlights the importance of accurately quantifying the dynamic load effects of these very large OWTs, which is paramount in their ULS design.

Motivated by the above, the present work will characterise the extreme structural responses of a 10-MW floating semi-submersible OWT using the widely used Gumbel fitting and ACER methods. The paper will investigate the critical locations at the blades-hub, rotor-main shaft, and the tower base-floating platform interfaces. Representative operating conditions at below-rated, rated, and above-rated wind speeds are studied. The aim is to guide future research on very large OWTs by indicating the ULS loads expected.

2. System description

A 10-MW floating wind turbine (FWT) system [13] which is illustrated in Figure 1, is used in this work. The FWT system will be expounded in two parts in the following sections. Firstly, the reference wind turbine will be described, then the properties of the semi-submersible floater and the mooring system will be introduced.

Figure 1 The 10-MW OO-Star floating wind turbine [13].

2.1. DTU 10-MW Reference Wind Turbine

The DTU 10-MW reference wind turbine (RWT) [14] is used in this paper. The wind turbine was designed following International Electrotechnical Commission (IEC) Class 1A wind regime. It is a traditional three-bladed, clockwise rotation-upwind turbine and uses a variable speed and collective pitch control system. The DTU 10-MW RWT numerical model has been developed and studied by many researchers such as Muggiasca et al. [15], Yu et al. [16], Wang et al. [17], and Hu et al. [18]. The summary of the DTU 10-MW RWT is presented in Table 1.

Table 1 Key parameters of the DTU 10-MW reference wind turbine [14].

Parameter	**Value**
Rating	10-MW
Type	Upwind/3 blades
Control	Variable speed, collective pitch
Drivetrain	Medium-speed, multiple stage gearbox
Cut-in, rated and cut-out wind speed (m/s)	4, 11.4, 25
Minimum and maximum rotor speed (rpm)	6.0, 9.6
Maximum generator speed (rpm)	480
Rotor diameter (m)	178.3
Hub height (m)	119.0
Rotor mass (kg)	227962
Nacelle mass (kg)	446036
Tower mass (kg)	1.257×10^6

2.2. OO-Star Semi-submersible Wind Floater and mooring system

This paper considers the 10-MW RWT mounted on the semi-submersible developed by Dr.techn. Olav Olsen AS [13]-[14] in the LIFES 50+ project [13]. The floater is constructed using post-tensioned concrete. It has a central main column and three outer columns located radially outwards. The four columns are mounted on a star-shaped pontoon through a slab attached at the bottom. Three catenary mooring lines are used for station keeping. Clumped masses are attached at the middle of each mooring line for increased mooring tension. More details of the OO-Star Wind Floater and its mooring system are shown in Table 2 and Table 3, respectively.

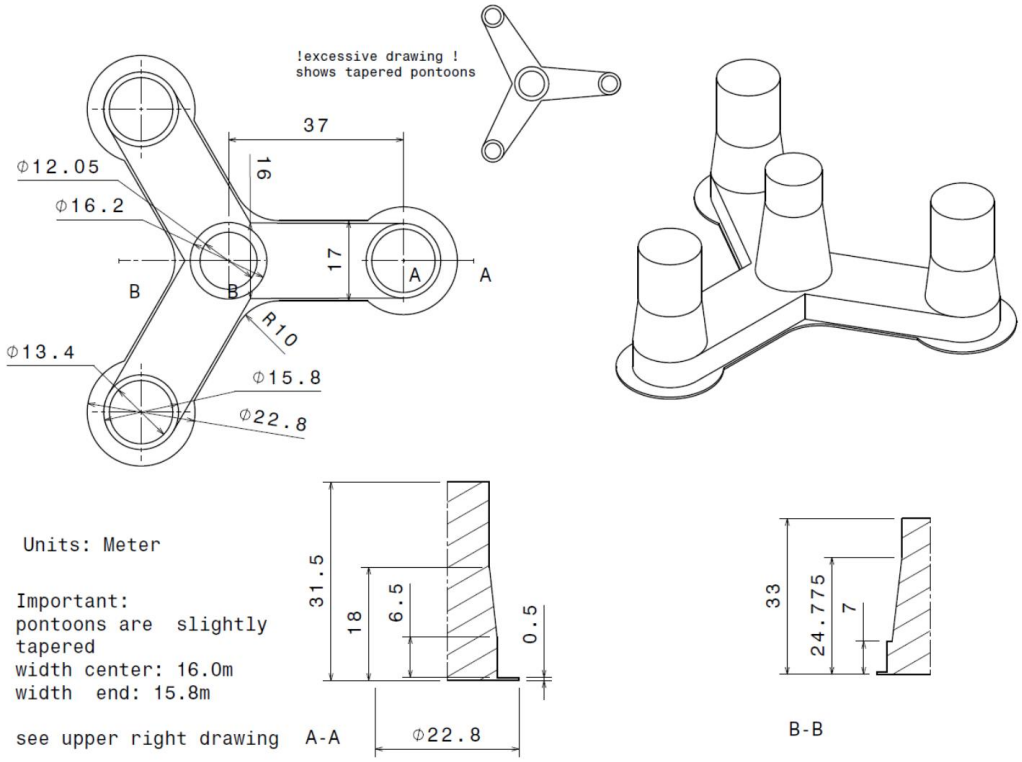

Figure 2 Main dimensions of the OO-Star floater of the 10-MW wind turbine [19].

Table 2 The main properties for the 10-MW OO-Star wind floater.

Parameter	**Value**
Water depth (m)	130
Draft (m)	22
Tower-base interface above mean sea level (m)	11
Displacement (kg)	24158
Overall gravity, including ballast (kg)	21709
Roll and pitch inertia about center of gravity (kg·m^2)	1.4462 x 10^{10}
Yaw inertia about center of gravity (kg·m^2)	1.63 x 10^{10}
Center of gravity height below mean sea level (m)	15.23
Center of buoyancy height below mean sea level (m)	14.236

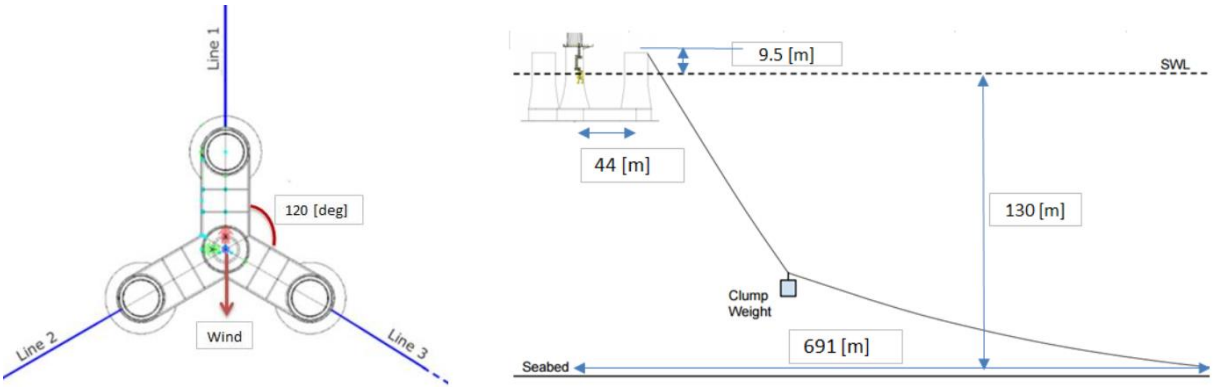

Figure 3 Sketch of the mooring system in the 10-MW FWT (left: top view; right: side view) [19].

Table 3 The main properties for the mooring system of the 10-MW FWT.

Parameter	**Value**
Radius to anchors from platform centerline (m)	691
Anchor position below MSL (m)	130
Initial vertical position of clump mass below MSL (m)	90.45
Initial radius to clump mass from centerline (m)	148.6
Length of clump mass upper segment (kg)	118
Length of clump mass lower segment (kg)	585
Equivalent weight per length in water (N/m)	3200.6
Extentional stiffness (N/m)	1.506×10^9

3. Methodology

3.1. Aero-hydro-elastic-servo dynamic analysis of the 10-MW FWT

The simulation tool used to simulate a wind turbine is an open-source code called FAST (v8.16.00a-bjj) developed by the National Renewable Energy Laboratory (NREL). FAST is an acronym for Fatigue, Aerodynamics, Structures and Turbulence. As its name suggests, it is a coupled aero-hydro-elastic-servo tool that has been used to execute the dynamic analysis of the 10-MW FWT. The five codes are implemented via MATLAB, and they work concurrently together to produce the aerodynamic and hydrodynamic loads, and control, structural and mooring system dynamics are commonly known as AeroDyn [20], HydroDyn [21], ServoDyn, and MoorDyn [22]. Furthermore, FAST can accept and analyse time-varying stochastic wind as an input for its time-domain simulations. FAST has been successfully used to execute various projects such as the OC3: Offshore Code Comparison Collaboration [23] and OC4: IEA (International Energy Agency) Task Wind 30 [24], with its modelling capability verified in the Netherlands [25].

Aerodynamics

In a wind turbine, the blades aerodynamic loads are measured using the quasi-steady Blade Element Momentum (BEM) theory, where the momentum and blade element theory are used together. The BEM method includes various corrections such as tip loss, hub loss, skewed

inflow, and dynamic stall corrections in its calculation. While the Pitt and Peters' model minimises the error by correcting the skewed inflow, the Boddoes-Leishman model helps correct the dynamic stall. Similarly, the Prandtl corrections and Glauert correction account for the blade's hub, tip losses, and induction factors. The AeroDyn theory manual can be used as a reference to understand the calculation of the aerodynamic load executed by the FAST code [20].

Hydrodynamics

The drag term from Morison's equation and potential flow theory are used together to calculate the hydrodynamic loads present in the semi-submersible floater. The wave pressures and viscous loads are accounted for in this method. Next, the panel code, WAMIT [26], as per the potential flow theory, is used to estimate the hydrodynamic coefficient and first-order wave excitation load transfer function. The hydrodynamic coefficient is made up of the added mass and damping coefficients. After that, the convolution technique is initiated to transform the hydrodynamic coefficients to obtain the solutions in the time domain [27].

Structural dynamics

To ensure that the structural dynamics of the FWT is accounted for in the FAST code uses the combined multi-body and modal structural approach. The blades, tower, and driveshaft are designed as flexible bodies in this approach. In contrast, the nacelle, hub, and floater are designed as rigid bodies. A coupled dynamics equation from Kane's approach is used to calculate the structural dynamic responses for the time-domain [28]. At the same time, the Rayleigh damping coefficient is used in design for the blade's inherent structural damping in both the blades and tower.

Control system dynamics

The 10-MW FWT's control system functions differently according to its operational modes. These modes are primarily called the below-rated or full-rated regions. In the below-rated region, speeds that are lower than the FWT's rated speed, the generator torque-speed curve controls the rotational speed of the rotor according to the optimal tip speed ratio, allowing the turbine to reach its maximum power. While at the full-rated region, speeds higher than the FWT's rated speed, the blade pitch is adjusted using a proportional-integral (PI) algorithm to control the rotational speed of the rotor to maintain the rated power generation. The PI parameters used in the FWTs differ from those used in land-based RWT since it is vital to avoid the negative damping effects that can significantly affect the FWTs.

3.2. Extreme value prediction

In any stochastic process $X(t)$ taken across a time period (T), the extreme value is classified as the largest maxima extracted from a group of individual maxima.

$$X_e = \boldsymbol{max}\{X_{m1}, X_{m2}, X_{m3}, \dots, X_{mn}\}\ , \qquad i = 1, \dots, n \tag{1}$$

where X_e describes the largest maximum value and X_{mi} describes the individual maxima. Therefore, from this assumption, it is observed that the individual maxima are independently and identically distributed across the common distribution function $F_{Xm}(x)$. Therefore, from the equation below, the distribution of X_e is labelled as:

$$F(x) = \boldsymbol{Prob}\{X_e \le x\} = [F_{Xm}(x)]^n , \qquad i = 1, \dots, n \tag{2}$$

Various statistical methods have been used to approximate an extreme value distribution. Examples of the extreme value methods used in the study of wind turbines includes an estimation of extreme structural responses in a floating vertical axis wind turbines by Cheng et al. [29] and extreme responses due to wave nonlinearity on a semi-submersible floating wind turbine by Xu et al. [30]. The two methods used in this paper are the ACER method (Section 3.3) and the Gumbel method (Section 3.4).

3.3. ACER (Average Conditional Exceedance Rate)

This paper uses the ACER method to estimate extreme structural responses. The method was proposed by Naess and Gaidai [31], and it is derived for a discretely sampled response process. The cascade of conditional approximation is the basis for calculating the exceedance probability for extreme value estimation. The primary purpose of the ACER method is to accurately determine the distribution function of the extreme value, which is denoted as $M_N = max\{X_j;\ j = 1,\ \cdots,\ N\}$. Let $P_\eta = Prob(M_N \le \eta)$ denotes the probability of the occurrence of the extreme value η and it follows:

$$P_\eta = Prob(M_N \le \eta) = Prob(X_1 \le \eta,\ \cdots,\ X_N \le \eta) \tag{3}$$

To solve this equation efficiently, a cascade of conditional approximation $P_k(\eta)$ is used, where $P_k(\eta)$ tends to close to P_η as k increases. For $N \gg 1$ and $k = 1,2,\cdots$, $P_k(\eta)$ is represented as:

$$P_k(\eta) \approx exp(-\sum_{j=k}^{N} \alpha_{kj}(\eta)) \tag{4}$$

where $\alpha_{kj}(\eta) = Prob\big(X_1 > \eta | X_{j-1} \ll \eta,\ \cdots,\ X_{j-k+1} \le \eta\big)$, and it represents the exceedance probability conditional on $k-1$ previous non-exceedances.

Equation (4) will be calculated based on the ACER, which is defined as:

$$\varepsilon_k(\eta) = \frac{1}{N-k+1}\sum_{j=k}^{N} \alpha_{kj}(\eta)\,, k = 1,2,\cdots \tag{5}$$

For $k \ge 2$, $\tilde{\varepsilon}_k(\eta)$ is used instead of $\varepsilon_k(\eta)$ because it is easier to use for nonstationary or long-term statistics, and it is defined as:

$$\tilde{\varepsilon}_k(\eta) = \lim_{N\to\infty} \frac{\sum_{j=k}^{N} a_{kj}(\eta)}{N-k+1} \quad (6)$$

where $a_{kj}(\eta)$ is the realised values for the observed time series, and $\lim_{N\to\infty} \frac{\tilde{\varepsilon}_k(\eta)}{\varepsilon_k(\eta)} = 1$.

For both stationary and nonstationary time series, the sample estimate of the ACER can be denoted as:

$$\hat{\varepsilon}_k(\eta) = \frac{1}{R}\sum_{r=1}^{R} \hat{\varepsilon}_k{}^{(r)}(\eta) \quad (7)$$

where *R* is the number of samples, and

$$\hat{\varepsilon}_k{}^{(r)}(\eta) = \frac{\sum_{j=k}^{N} a_{kj}{}^{(r)}(\eta)}{N-k+1} \quad (8)$$

where *r* denotes the realisation number.

When the realisations are sufficiently numerous and assumed to be independent, then the 95 % confidence interval (CI) for the ACER can be estimated as:

$$CI(\eta) = \hat{\varepsilon}_k(\eta) \pm 1.96 \,\hat{s}_k(\eta)\Big/\sqrt{R} \quad (9)$$

where $\hat{s}_k(\eta)$ refers to the standard deviation of samples and can be estimated by:

$$\hat{s}_k(\eta)^2 = \frac{1}{R-1}\sum_{r=1}^{R} (\hat{\varepsilon}_k{}^{(r)}(\eta) - \hat{\varepsilon}_k(\eta))^2 \quad (10)$$

The above equations for estimation of average exceedance rate are based on direct numerical simulations. In contrast, an extrapolation technique can reduce the computational time.

Assuming the mean exceedance rate in the tail behaves similarly to $exp\{-a(\eta-b)^c\}(\eta \geq \eta_0 \geq b)$, where *a*, *b* and *c* are suitable constants. The ACER will therefore be assumed by:

$$\varepsilon_k(\eta) \approx q_k(\eta) exp\{-a_k(\eta-b_k)^{c_k}\}, \eta \geq \eta_0 \quad (11)$$

where the function $q_k(\eta)$ varies slowly compared to the exponential function $exp\{-a_k(\eta-b_k)^{c_k}\}$ in the tail region, thus it can be replaced by a constant for a suitable choice of the tail marker η_0.

Finally, the Levenberg-Marquardt least-squares optimisation method can be used to determine the constants *a*, *b*, *c* and *q*. Based on this, the probability of the occurrence of the extreme value can be obtained by the ACER method. In the studies of Naess et al. [32] and Chai et al.[33] it is shown that the extrapolation technique can achieve a satisfactory estimation of the extreme values but saves significant simulation time. Detailed descriptions of the ACER method can be found in the reference [34].

3.4. Gumbel fitting method

Extreme value distribution Eq. (2) has been proven on numerous occasions to converge to the Gumbel, Fréchet or Weibull distribution if the sample size (*n*) is large enough. Therefore, these distributions are also recognised as the Type I, II and III extreme value distributions, respectively and are a family of cumulative distribution probability that combines the generalised extreme value (GEV) distribution.

$$F_{X_e}(x) = exp\left(-\left(1+\gamma\left(\frac{x-\mu}{\beta}\right)\right)^{-\frac{1}{\gamma}}\right) \quad \textbf{(12)}$$

where β describes the scale parameter, γ describes the shape parameter, and μ describes the location parameter. The limiting of γ→0 allows the approximation to fit the Gumbel distribution, commonly used as a recommendation when modelling marine structures [35].

$$F_{X_e}(x) = exp\left(-exp\left(-\frac{x-\mu}{\beta}\right)\right) \quad \textbf{(13)}$$

Eq. (13) can be rewritten by using logarithm on the equation, allowing it to become a linear function.

$$-ln\left(ln\left(F_{X_e}(x)\right)\right) = \frac{x}{\beta} - \frac{\mu}{\beta} \quad \textbf{(14)}$$

The parameters β and μ can be approximated from the original data using the least-square fitting method from the cumulative distribution probability, i.e., a straight line on a probability paper [36].

3.5. Load cases and environmental conditions

In this paper, the wind and wave data were generated using the hindcast data obtained from the North Sea from 2001 to 2010. The long-term joint wind and wave distribution consisted of 1-hour mean wind speed located 10 m above the sea level (U_{10}), wave spectral peak period (T_p) and significant wave height (H_s) [37]. The long-term joint wind and wave distribution are described below:

$$f_{U_{10},H_s,T_p}(u,h,t) = f_{U_{10}}(u) \cdot f_{H_s|U_{10}}(h|u) \cdot f_{T_p|U_{10},H_s}(t|u,h) \quad \textbf{(15)}$$

where the marginal distribution of U_{10} is described by $f_{U_{10}}(u)$, $f_{H_s|U_{10}}(h|u)$ and $f_{T_p|U_{10},H_s}(t|u,h)$, the conditional distribution of H_s for given U_{10} and the conditional distribution of T_p for given U_{10} and H_s. Figure 4 shows a scattered diagram for the in situ values of H_s and T_p that are used to assign probabilities for the individual sea states.

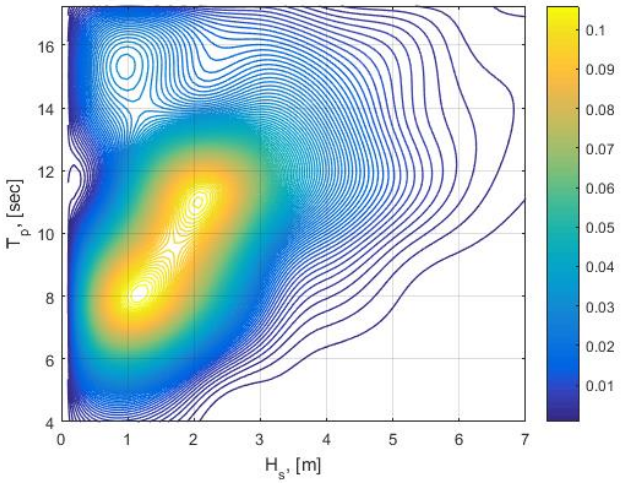

Figure 4 Scattered diagram: In situ values of H_s *and* T_p *used to assign* probabilities for the individual sea states.

Table 4 Load cases for numerical simulations.

Load cases	U_w **(m/s)**	T_I	H_s **(m)**	T_p **(s)**	**Samples**	**Simulation length (s)**
LC1	8	0.1740	1.9	9.7	20	4000
LC2	12	0.1460	2.5	10.1	20	4000
LC3	16	0.1320	3.2	10.7	20	4000

To replicate a highly probabilistic normal operational condition experienced by the turbine, three closely related load cases were selected, shown in Table 4. The wind speed used varied according to the turbine operating ranges, cut-in, rated and cut-out zones. The three-speed increased in blocks of 4 m/s. Each speed had its significant wave height and spectra peak period, and these values were measured using the joint distribution described in Eq. (15). In comparison, the turbulent wind and irregular waves used for all three cases were directionally aligned. Wind turbine Class C is used with normal turbulence and normal wind profiles. The wind speed profile is modelled using the wind power-law formulation described in Eq. (16).

$$U_w(z) = U_{hub}\,(\frac{\mathrm{Z}}{Z_{hub}})^{\alpha} \quad \textbf{(16)}$$

where $U_w(z)$ is the mean wind speed taken from height z above the still water level, u_{hub} is the mean wind speed w.r.t hub height, z_{hub} is the hub height w.r.t the still water level (119 m for the selected 10-MW FWT). α (power-law exponent) is equal to 0.14. These recommendations are from IEC 61400-3-2, see [38], used for offshore locations.

The 3-D wind turbulent fields generated using Turbsim is derived from the Kaimal's turbulence model [39]. At the same time, the JONSWAP (Joint North Sea Wave Project) spectrum allowed the modelling of the time-varying irregular waves with the respective H_s and T_p values.

Every simulation was conducted for a period of 4000s. The initial 400s of these simulations were disregarded to account for the transient effect often present during a turbine's start-up. Consequently, only 3600s of data is used to analyse the extreme value. Accordingly, each environmental condition had sea states with 20 random wind and wave conditions samples.

4. Response variables

The loads at the three measurement points presented in Figure 5 are considered. These are the blade 1 root flapwise bending moment (RootMyb1), main shaft tip up-down bending moment (LSSTipMys) and tower bottom fore-aft bending moment (TwrBsMyt).

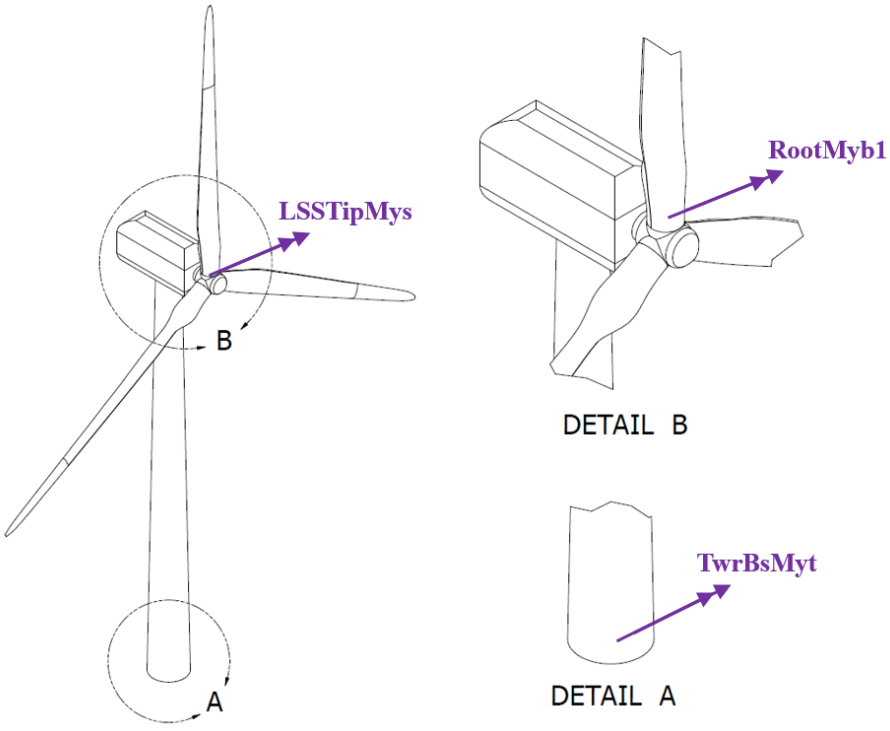

Figure 5 Location of points where bending moments are measured.

5. Results and discussions

This paper presents the methodology for estimating the 10 MW DTU WT-OO-Star's extreme loads during operating conditions. The empirical data is based on accurate numerical simulations using a FAST model as presented in Section 3.1. The Gumbel and ACER methods presented in Sections 3.3 and 3.4 are used.

5.1. Time-domain responses, PSD, and maximum values

The time-domain responses for one portion of a realisation, the power spectral distributions (PSDs) for a full realisation and the maximum values of each realisation are presented in Figure 6, Figure 7, and Figure 8, respectively. These results of each load case, i.e., LC1, LC2 and LC3 are taken from one of the 20 realisations calculated. The wind and wave elevation time series and PSDs are also plotted for reference.

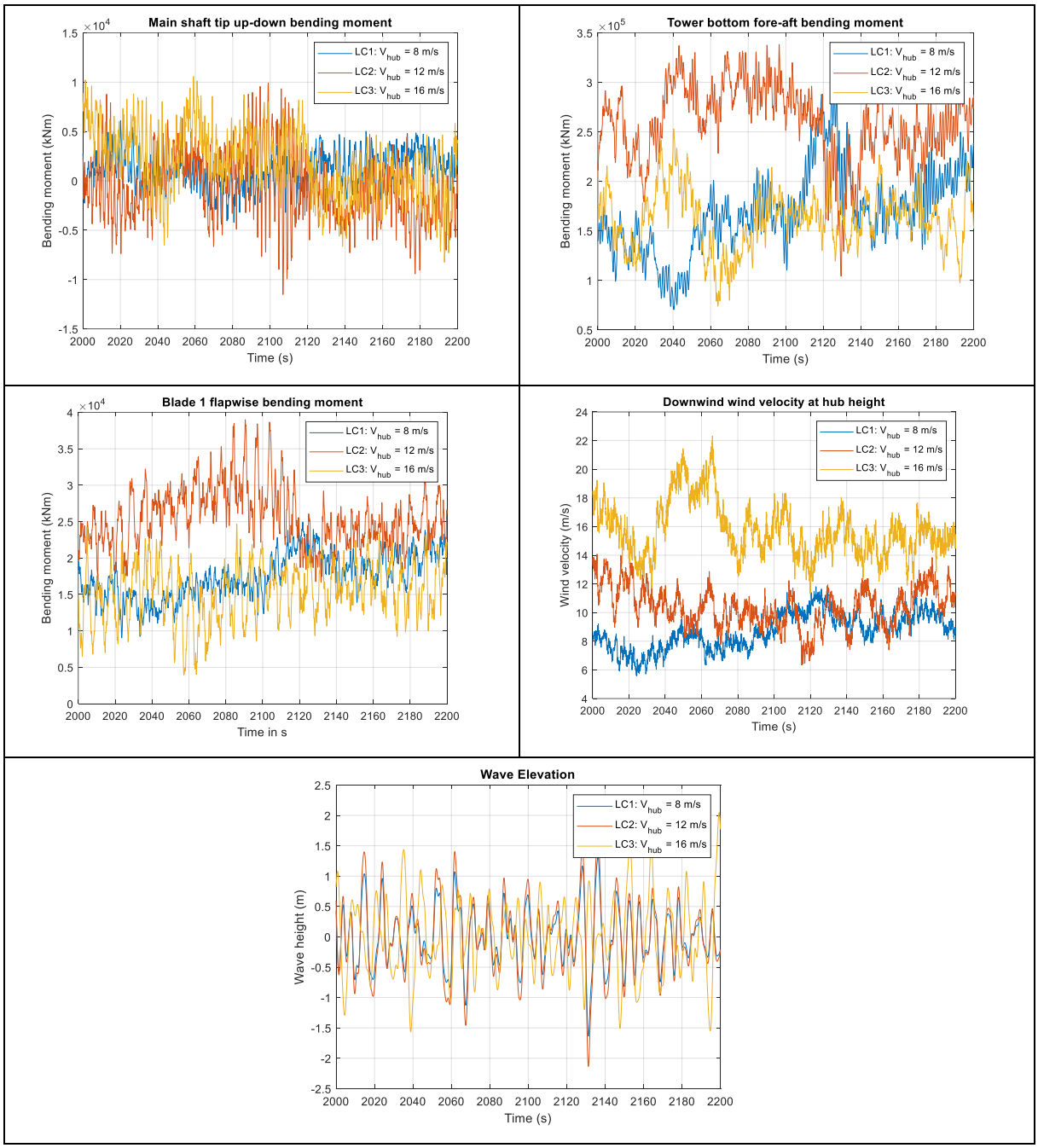

Figure 6 Example time domain results. Top-left: Main shaft tip up-down bending moment (LSSTipMys); Top-right: Tower bottom fore-aft bending moment (TwrBsMyt); Centre-left: Blade 1 root flapwise bending moment (RootMyb); Centre-right: Downwind wind velocity at hub height; Bottom: Wave elevation

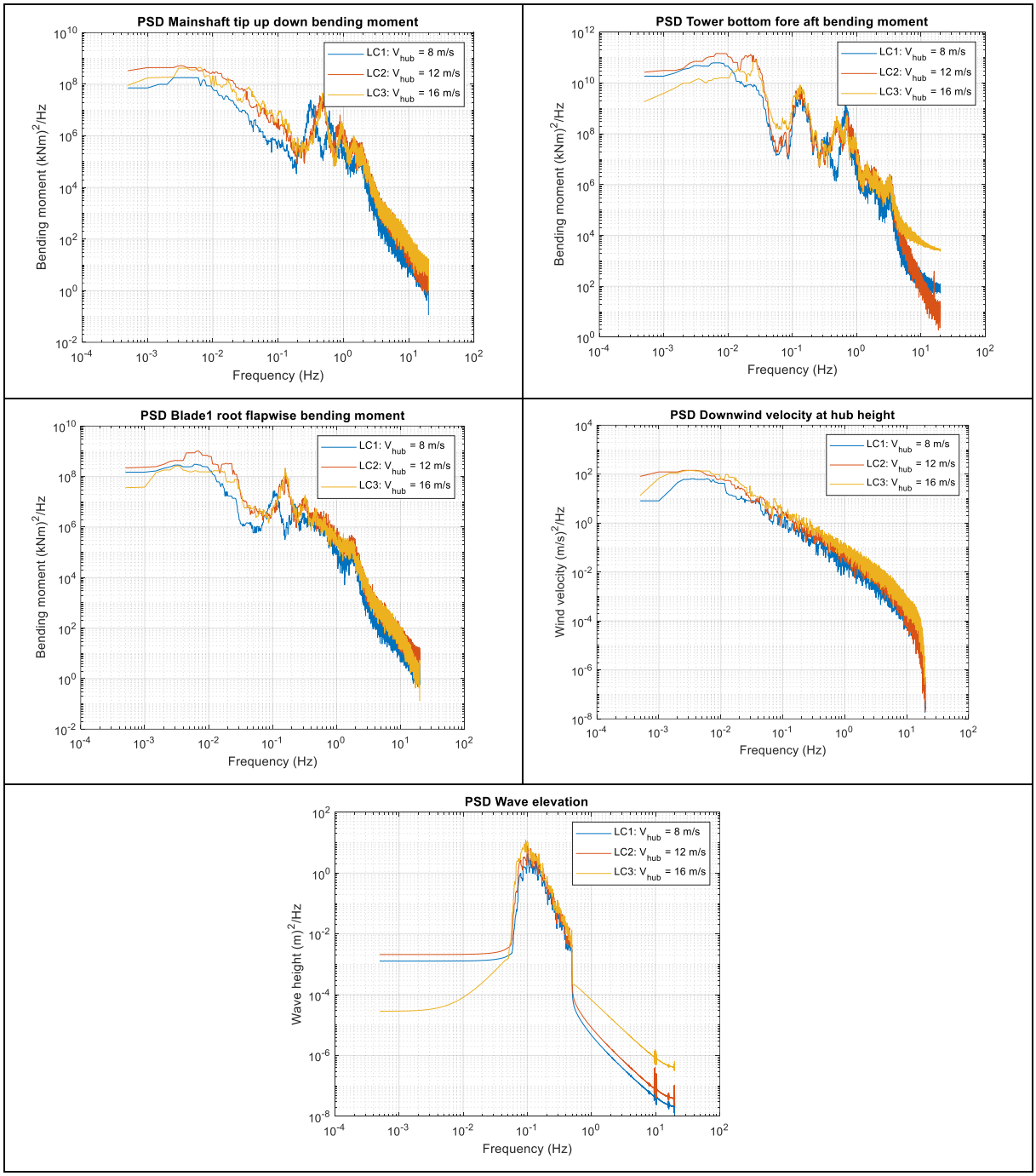

Figure 7 Power spectral distributions. Top-left: Main shaft tip up-down bending moment (LSSTipMys); Top-right: Tower bottom fore-aft bending moment (TwrBsMyt); Centre-left: Blade 1 root flapwise bending moment (RootMyb); Centre-right: Downwind wind velocity at hub height; Bottom: Wave elevation

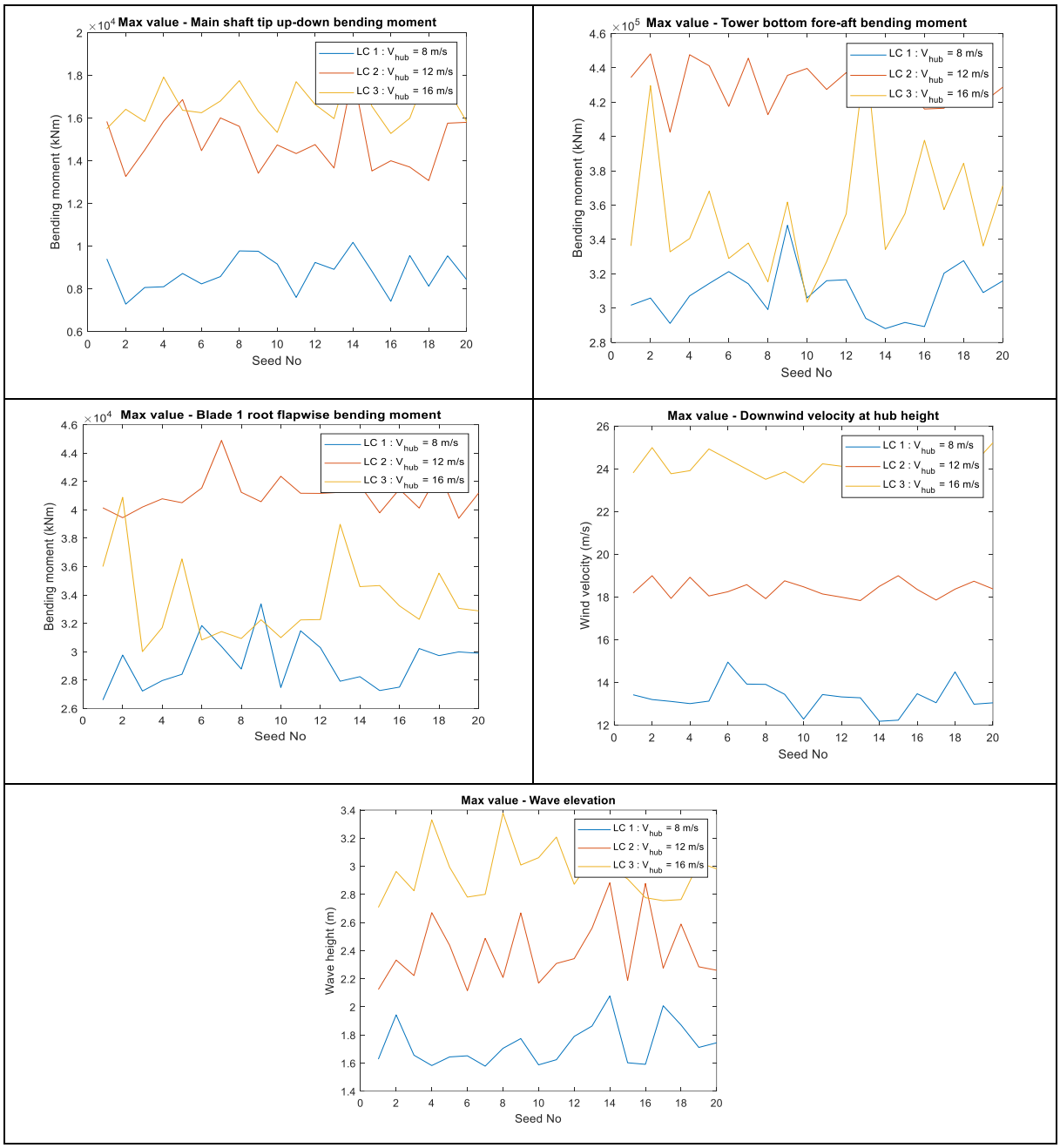

Figure 8 Maximum value in each realisation. Top-left: Main shaft tip up-down bending moment (LSSTipMys); Top-right: Tower bottom fore-aft bending moment (TwrBsMyt); Centre-left: Blade 1 root flapwise bending moment (RootMyb); Centre-right: Downwind wind velocity at hub height; Bottom: Wave elevation

5.2. Extreme load responses using ACER and Gumbel methods

This section presents the extreme load responses using the ACER and Gumbel methods for the three operating conditions (LC1 – LC3) presented in Table 4. k = 6 is used. For illustration, example plots of the ACER extrapolation and Gumbel fitting are presented in Figure 9 and Figure 10, respectively.

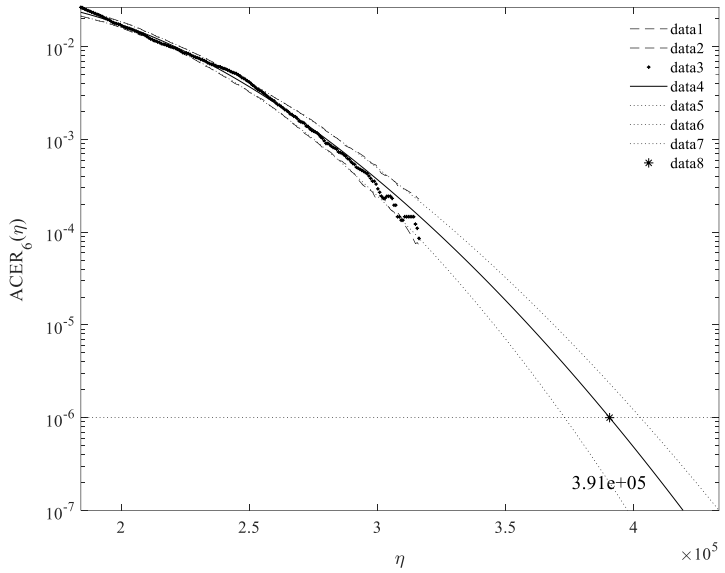

Figure 9 Example plot of ACER extrapolation,TwrBsMyt, LC1 – V_{hub} =8 m/s, Realisation #1

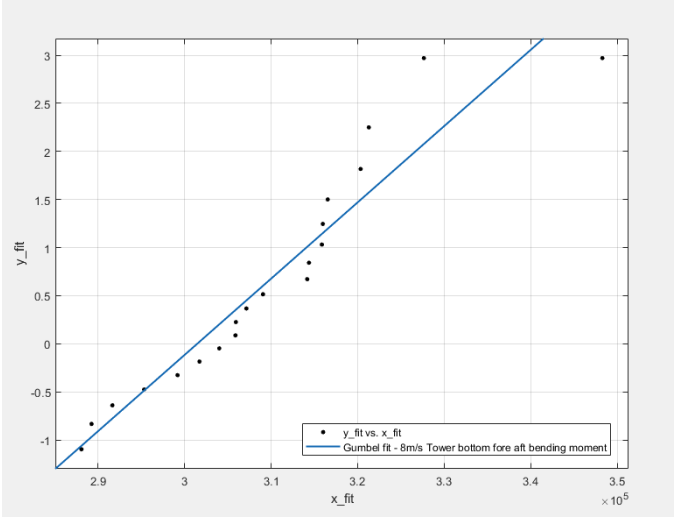

Figure 10 Example plot of Gumbel fitting, TwrBsMyt, LC1 – V_{hub} = 8 m/s, Realisation #1

As illustrated by the significantly smaller confidence intervals, the ACER method can lead to more accurate results as it does not assume a distribution. The ACER method does not assume any extreme value distribution. Instead, it follows the exact shape of the data points as presented in Figure 9. On the other hand, from Figure 10, it is observed that the Gumbel distribution does fit the upper-end tail well. The data points tend to curve up towards the left for increasing response values and are above the Gumbel line. This means the Gumbel distribution will tend to overpredict the extreme value responses. This example shows the advantages of the ACER method.

The extreme load responses together with the 95 % CIs from both ACER and Gumbel methods are then plotted in Figure 11, Figure 12 and Figure 13 for RootMyb, LSSTipMys and TwrBsMyt, respectively. The numerical values of the results are also presented in Table 6 and

Table *7* of the Appendix for extreme values calculated by the ACER and Gumbel methods, respectively.

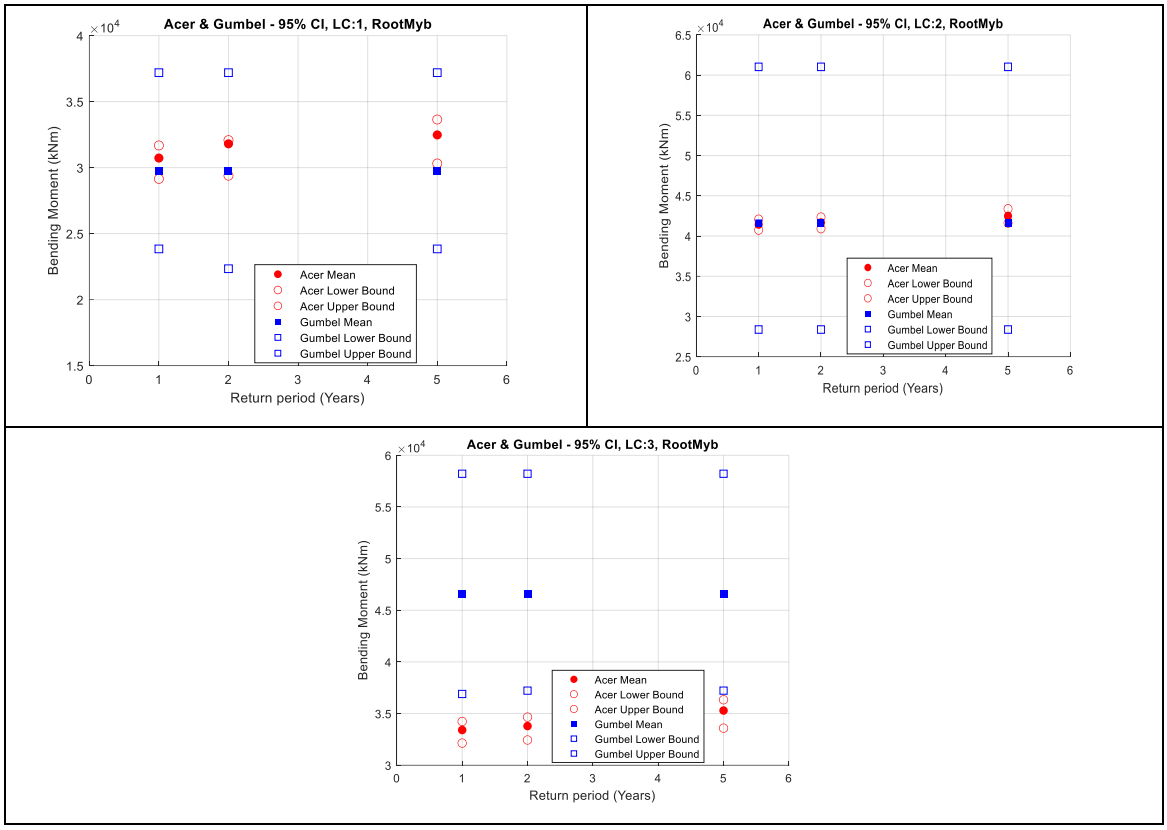

Figure 11 Blade 1 root flapwise bending moment. ACER and Gumbel with 95 % CI; Top-left: LC1, V_{hub} = 8 m/s; Top-right: LC2, V_{hub} = 12 m/s; Bottom: LC3, V_{hub} = 16 m/s.

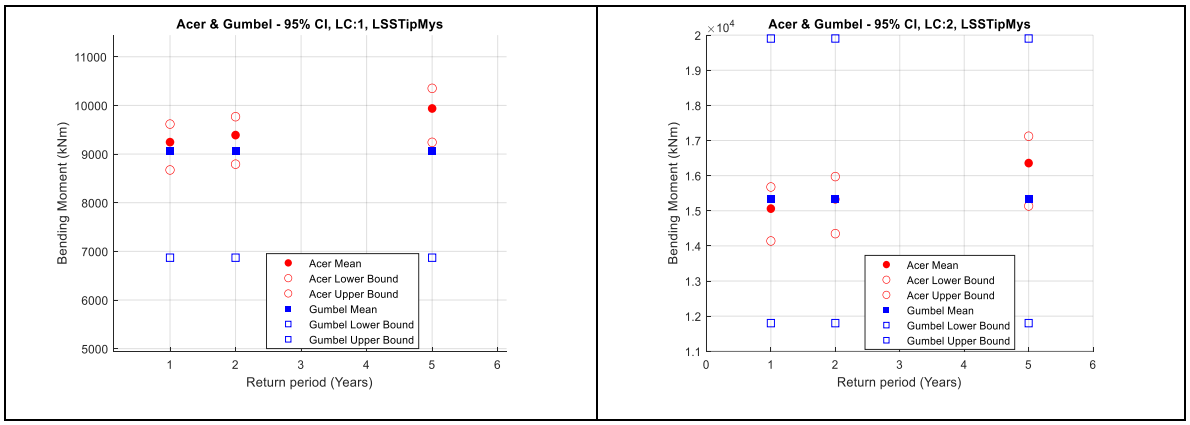

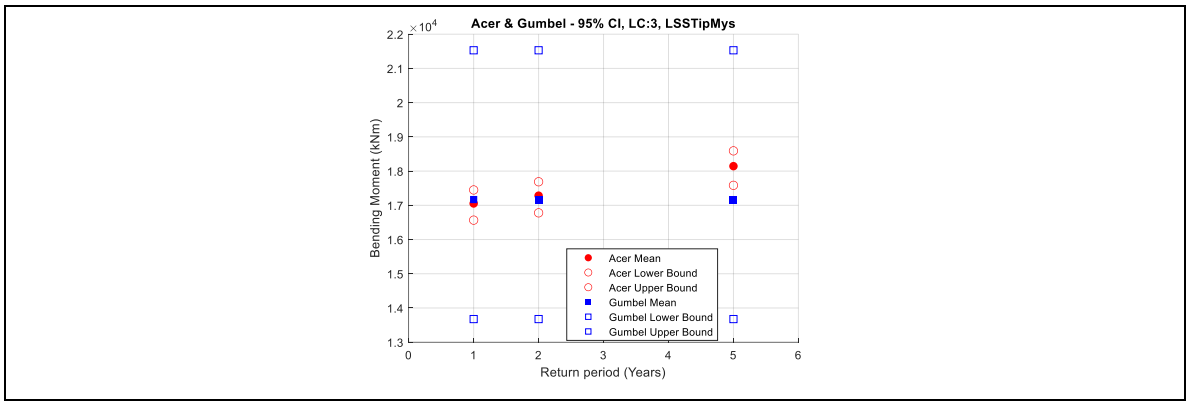

393 **Figure 12** Main shaft tip up-down bending moment. ACER and Gumbel with 95 % CI; Top-
394 left: LC1, V_{hub} = 8 m/s; Top-right: LC2, V_{hub} = 12 m/s; Bottom: LC3, V_{hub} = 16 m/s.

395

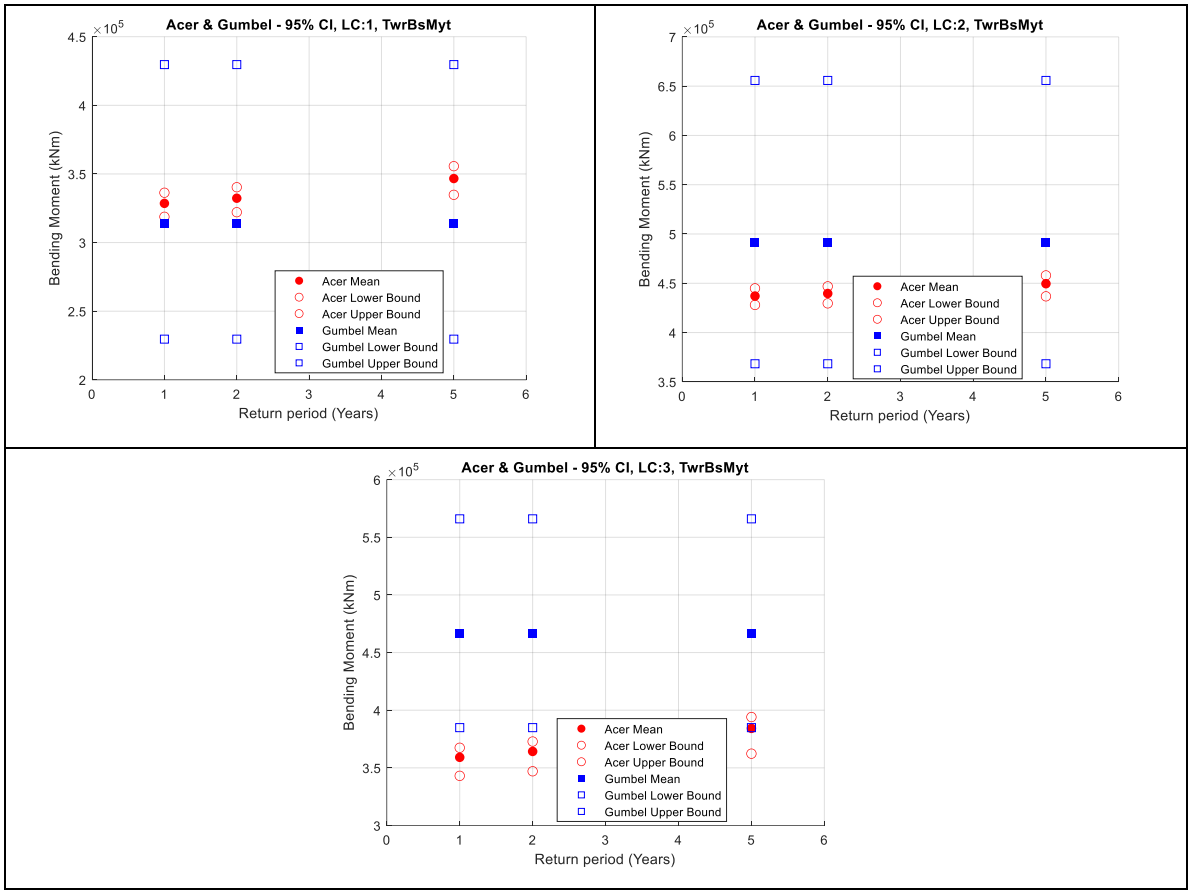

396 **Figure 13** Tower bottom fore-aft bending moment. ACER and Gumbel with 95 % CI; Top-
397 left: LC1, V_{hub} = 8 m/s; Top-right: LC2, V_{hub} = 12 m/s; Bottom: LC3, V_{hub} = 16 m/s.

398

399 The following observations are made:

400 • The 1, 2 and 5-year extreme values are generally 1.1-1.3 times larger than the
401 maximums of single 1-hour realisations. The relatively large range of values (about 20
402 %) indicates the importance of using extrapolation methods that are accurate in
403 predicting extreme values that can be used to define appropriate design values that can
404 be utilised in deterministic engineering design.

- The 95 % CIs of the results calculated using the ACER method are significantly smaller than those of the Gumbel method. This highlights the benefits of the ACER in not assuming a distribution in the extrapolation of extreme values.
- The 95 % Cis of the results calculated using the Gumbel method are larger. This indicates that the Gumbel distribution does not fit the extreme value responses very well.
- Further, the 1, 2, and 5-year extreme values calculated using the Gumbel method are relatively similar. This is due to the inaccurate fit of the probability distribution at the upper tail end. The fitted Gumbel probability density distribution slope is too steep at the upper tail end. This leads to very small changes in the response values for a unit change in probability.

5.3. Choice of *k* value in ACER method

It is recommended to perform sensitivity analyses of the *k* values used when studying new responses [31]. Therefore, the choice of *k* value is investigated in this section for a *q* value of 10^{-6}. The results for *k* = 2, 4 and 6 are presented in Table 5. The ACER function plots for *k* = 1 to 6 are presented in Figure 14.

Table 5 Extreme values calculated from the ACER method considering different values of *k*.

Load Case	***q* value**	**10^{-6}**		
	***k* value**	**2**	**4**	**6**
LC1, V_{hub} = 8 m/s	RootMyb (kNm)	36103	36441	37018
	LSSTipMys (kNm)	11509	11580	11592
	TwrBsMyt (kNm)	380076	368822	390514
LC2, V_{hub} = 12 m/s	RootMyb (kNm)	44536	44626	44951
	LSSTipMys (kNm)	19511	19228	19607
	TwrBsMyt (kNm)	476606	479938	480159
LC3 , V_{hub} = 16 m/s	RootMyb (kNm)	38980	40385	40214
	LSSTipMys (kNm)	20747	20803	20670
	TwrBsMyt (kNm)	450802	447620	450217

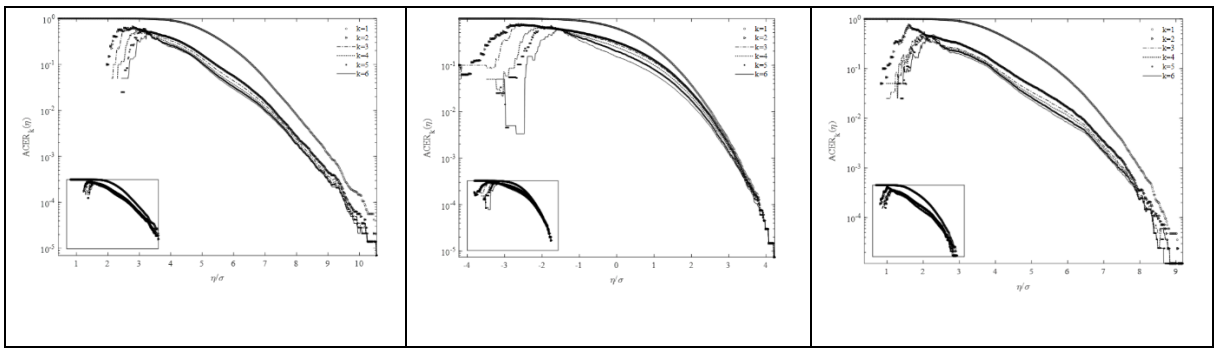

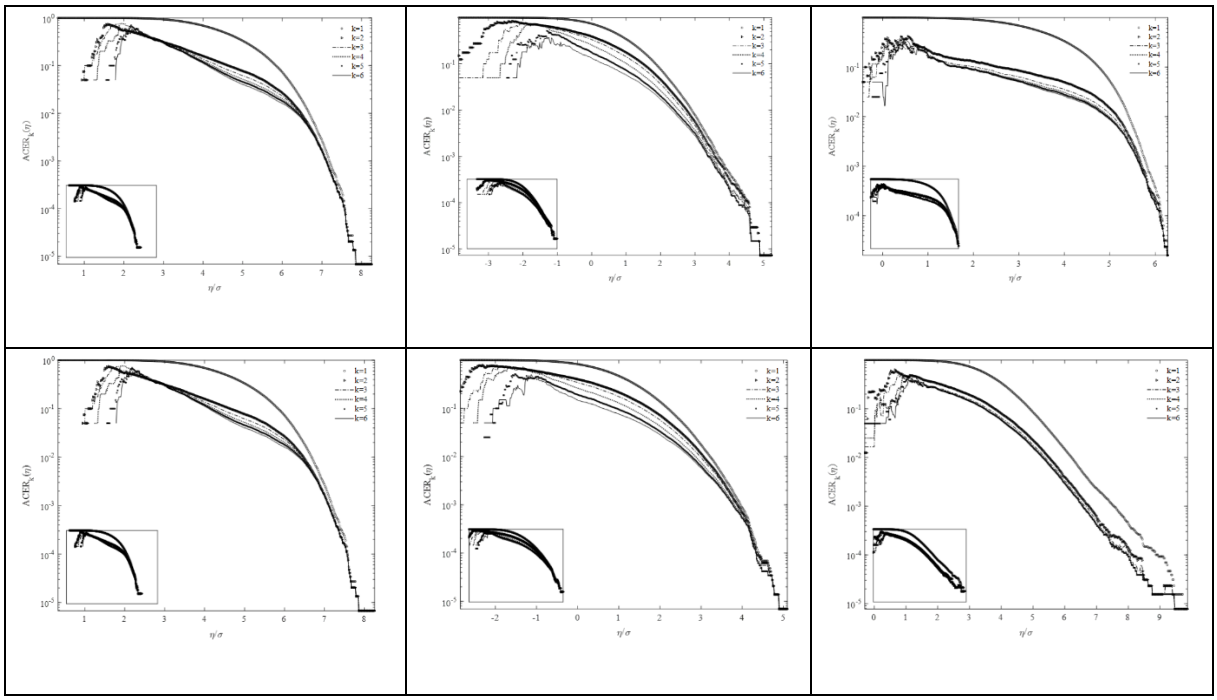

Figure 14 ACER functions for various k values. Top: LC1, V_{hub} = 8 m/s; Centre: LC2, V_{hub} = 12 m/s; Bottom: LC3, V_{hub} = 16 m/s; Left: Blade 1 root flapwise bending moment (RootMyb); Centre: Mainshaft tip up-down bending moment (LSSTipMys); Right: Tower bottom fore-aft bending moment (TwrBsMyt).

In general, the extreme values calculated do not vary significantly with the value of *k* used. A *k* value of 1 was found to lead to incorrect results. The extreme values estimated also increase for increasing values of *k* used. It was observed that the responses converged for $k > 2$. Therefore, it was decided to use $k = 6$ for the analyses in this paper.

6. Conclusions

This paper investigated the extreme responses for a 10 MW semi-submersible type FWT using ACER and Gumbel methods. The responses are based on fully coupled nonlinear numerical analysis, including structural flexibility, aero, hydrodynamics, control dynamics, interaction with combined turbulent wind and stochastic waves. The following conclusions are made:

- The 1, 2 and 5-year responses of the FWT were in general 1.1-1.3 times larger than the maximums of single 1-hour realisations. This reinforces the importance of using extrapolation methods to determine extreme loads to be used as ULS loads.
- The ACER results have a smaller 95 % CI than the Gumbel results. This means the ACER method is more accurate than the Gumbel method.
- The 1, 2 and 5-year responses predicted by the Gumbel method are quite similar. This is due to poor Gumbel fitting of the data at the upper tail. On the other hand, the ACER does not assume any distributions and therefore does not have the same poor fit issue at the tail end.
- The better performance of the ACER method is because, in contrast to Gumbel, it does not assume that the extreme responses follow a designated probability distribution.¨
- Lastly, it was found that $k = 1$ would lead to incorrect results and cannot be used, but otherwise, the choice of the *k* values does not affect the ACER results. When new

responses are studied, it is also recommended to perform sensitivity studies on the k values.

References

[1] Murdock, H. E., Gibb, D., Andre, T., Sawin, J. L., Brown, A., Ranalder, L., ... & Brumer, L. (2021). Renewables 2021-Global status report.

[2] Bak, C., Zahle, F., Bitsche, R., Kim, T., Yde, A., Henriksen, L. C., ... & Natarajan, A. (2013). The DTU 10-MW reference wind turbine. In Danish wind power research 2013.

[3] Turbines—Part, W. (2009). 3: design requirements for offshore wind turbines. Proceedings of the IEC, 61400-3.

[4] Saha, N., Gao, Z., Moan, T., & Naess, A. (2014). Short-term extreme response analysis of a jacket supporting an offshore wind turbine. Wind Energy, 17(1), 87-104.

[5] Dimitrov, N. (2016). Comparative analysis of methods for modelling the short-term probability distribution of extreme wind turbine loads. Wind Energy, 19(4), 717-737.

[6] Lott, S., & Cheng, P. W. (2016, September). Load extrapolations based on measurements from an offshore wind turbine at alpha ventus. In Journal of Physics: Conference Series (Vol. 753, No. 7, p. 072004). IOP Publishing.

[7] Cao, Y., Zavala, V. M., & D'Amato, F. (2018). Using stochastic programming and statistical extrapolation to mitigate long-term extreme loads in wind turbines. Applied energy, 230, 1230-1241.

[8] Cheng, Z., Madsen, H. A., Chai, W., Gao, Z., & Moan, T. (2017). A comparison of extreme structural responses and fatigue damage of semi-submersible type floating horizontal and vertical axis wind turbines. Renewable Energy, 108, 207-219.

[9] Li, L., Cheng, Z., Yuan, Z., & Gao, Y. (2018). Short-term extreme response and fatigue damage of an integrated offshore renewable energy system. Renewable Energy, 126, 617-629.

[10] Xu, K., Zhang, M., Shao, Y., Gao, Z., & Moan, T. (2019). Effect of wave nonlinearity on fatigue damage and extreme responses of a semi-submersible floating wind turbine. Applied Ocean Research, 91, 101879.

[11] Wang, S., Nejad, A. R., Bachynski, E. E., & Moan, T. (2020). Effects of bedplate flexibility on drivetrain dynamics: Case study of a 10 MW spar type floating wind turbine. Renewable Energy, 161, 808-824.

[12] Wang, S., Moan, T., & Nejad, A. R. (2021). A comparative study of fully coupled and de-coupled methods on dynamic behaviour of floating wind turbine drivetrains. Renewable Energy, 179, 1618-1635.

[13] Yu, W., Müller, K., Lemmer, F., Bredmose, H., Borg, M., Sanchez, G., & Landbo, T. (2017). Public definition of the two LIFES50+ 10MW floater concepts. LIFES50+ Deliverable, 4.

[14] Bak, C., Zahle, F., Bitsche, R., Kim, T., Yde, A., Henriksen, L. C., ... & Natarajan, A. (2013). The DTU 10-MW reference wind turbine. In Danish wind power research 2013.

[15] Muggiasca, S., Taruffi, F., Fontanella, A., Di Carlo, S., Giberti, H., Facchinetti, A., & Belloli, M. (2021). Design of an aeroelastic physical model of the DTU 10MW wind turbine for a floating offshore multipurpose platform prototype. Ocean Engineering, 239, 109837.

[16] Yu, Z., Amdahl, J., Rypestøl, M., & Cheng, Z. (2022). Numerical modelling and dynamic response analysis of a 10 MW semi-submersible floating offshore wind turbine subjected to ship collision loads. Renewable Energy, 184, 677-699.
[17] Wang, S., Moan, T., & Jiang, Z. (2022). Influence of variability and uncertainty of wind and waves on fatigue damage of a floating wind turbine drivetrain. Renewable Energy, 181, 870-897.
[18] Hu, R., Le, C., Gao, Z., Ding, H., & Zhang, P. (2021). Implementation and evaluation of control strategies based on an open controller for a 10 MW floating wind turbine. Renewable Energy, 179, 1751-1766.
[19] Yu, W., Müller, K., Lemmer, F., Schlipf, D., Bredmose, H., Borg, M., ... & Andersen, H. (2018). LIFES50+ D4. 2: Public definition of the two LIFES50+ 10 MW floater concepts. University of Stuttgart.
[20] Moriarty, P. J., & Hansen, A. C. (2005). AeroDyn theory manual (No. NREL/TP-500-36881). National Renewable Energy Lab., Golden, CO (US).
[21] Damiani, R., Jonkman, J., & Hayman, G. (2015). SubDyn user's guide and theory manual (No. NREL/TP-5000-63062). National Renewable Energy Lab.(NREL), Golden, CO (United States
[22] Wendt, F. F., Andersen, M. T., Robertson, A. N., & Jonkman, J. M. (2016, June). Verification and validation of the new dynamic mooring modules available in FAST v8. In The 26th International Ocean and Polar Engineering Conference. OnePetro.
[23] Jonkman, J., & Musial, W. (2010). Offshore code comparison collaboration (OC3) for IEA Wind Task 23 offshore wind technology and deployment (No. NREL/TP-5000-48191). National Renewable Energy Lab.(NREL), Golden, CO (United States).
[24] Robertson, A., Jonkman, J., Musial, W., Popko, W., & Vorpahl, F. (2014). IEA Wind Task 30 Offshore Code Comparison Collaboration Continued.
[25] Coulling, A. J., Goupee, A. J., Robertson, A. N., Jonkman, J. M., & Dagher, H. J. (2013). Validation of a FAST semi-submersible floating wind turbine numerical model with DeepCwind test data. Journal of Renewable and Sustainable Energy, 5(2), 023116.
[26] Wamit I. Wamit user manual. WAMIT Inc.: Chestnut Hill, MA, USA, 2006.
[27] Faltinsen O. Sea loads on ships and offshore structures[M]. Cambridge university press, 1993.
[28] Kane, T. R., & Levinson, D. A. (1983). The use of Kane's dynamical equations in robotics. The International Journal of Robotics Research, 2(3), 3-21.
[29] Cheng, Z., Madsen, H. A., Chai, W., Gao, Z., & Moan, T. (2017). A comparison of extreme structural responses and fatigue damage of semi-submersible type floating horizontal and vertical axis wind turbines. Renewable Energy, 108, 207-219.
[30] Xu, K., Zhang, M., Shao, Y., Gao, Z., & Moan, T. (2019). Effect of wave nonlinearity on fatigue damage and extreme responses of a semi-submersible floating wind turbine. Applied Ocean Research, 91, 101879.
[31] Næss A, Gaidai O. Estimation of extreme values from sampled time series[J]. Structural safety, 2009, 31(4): 325-334.
[32] Naess A, Gaidai O, Teigen P S. Extreme response prediction for nonlinear floating offshore structures by Monte Carlo simulation. Applied Ocean Research, 2007, 29(4): 221-230.
[33] Chai W, Naess A, Leira B J, et al. Efficient Monte Carlo simulation and Grim effective wave model for predicting the extreme response of a vessel rolling in random head seas. Ocean Engineering, 2016, 123: 191-203.
[34] Naess, A., & Moan, T. (2013). Stochastic dynamics of marine structures. Cambridge University Press.
[35] Peeringa, J. M. (2009). Comparison of extreme load extrapolations using measured and calculated loads of a MW wind turbine. Petten: ECN.

[36] Lott, S., & Cheng, P. W. (2016, September). Load extrapolations based on measurements from an offshore wind turbine at alpha ventus. In Journal of Physics: Conference Series (Vol. 753, No. 7, p. 072004). IOP Publishing.
[37] Li, L., Gao, Z., & Moan, T. (2013, June). Joint environmental data at five european offshore sites for design of combined wind and wave energy devices. In International Conference on Offshore Mechanics and Arctic Engineering (Vol. 55423, p. V008T09A006). American Society of Mechanical Engineers.
[38] Turbines-Part, W. (2009). 3: design requirements for offshore wind turbines. Proceedings of the IEC, 61400-3.
[39] Jonkman, B. J. (2009). TurbSim user's guide: Version 1.50 (No. NREL/TP-500-46198). National Renewable Energy Lab.(NREL), Golden, CO (United States).

559 **Appendix**

560

561 **Table 6** Extreme value responses using ACER method for various return periods; 95 %
562 confidence interval in paratheses.

Load Case	**Return period**	**1 yr**	**2 yr**	**5 yr**
	Exceedance probability, q	**7.19×10^{-5}**	**5.71×10^{-5}**	**2.28×10^{-5}**
LC1 V_{hub} = 8 m/s	RootMyb (kNm)	30726 (29149, 31682)	31084 (29393, 32082)	32479 (30315, 33645)
	LSSTipMys (kNm)	9245 (8673, 9616)	9390 (8792, 9768)	9937 (9241, 10351)
	TwrBsMyt (kNm)	328555 (318797, 336312)	332314 (322130, 340328)	346662 (334792, 355663)
LC2 V_{hub} = 12 m/s	RootMyb (kNm)	41445 (40752, 42073)	41662 (40934, 42338)	42485 (41615, 43372)
	LSSTipMys (kNm)	15061 (14140, 15677)	15327 (14349, 15973)	16357 (15136, 17122)
	TwrBsMyt (kNm)	437049 (428032, 444853)	439643 (429627, 446865)	449561 (436751, 457982)
LC3 V_{hub} = 16 m/s	RootMyb (kNm)	33406 (32141, 34231)	33790 (32440, 34657)	35293 (33587, 36335)
	LSSTipMys (kNm)	17054 (16567, 17449)	17282 (16780, 17688)	18144 (17584, 18591)
	TwrBsMyt (kNm)	359140 (343069, 367411)	364244 (347041, 372826)	384245 (362296, 394070)

563

564

Table 7 Extreme value responses using Gumbel method for various return periods; 95 % confidence interval in paratheses.

Load Case	**Return period**	**1 yr**	**2 yr**	**5 yr**
	Exceedance probablity, q	**7.19×10^{-5}**	**5.71×10^{-5}**	**2.28×10^{-5}**
LC1, V_{hub} = 8 m/s	RootMyb (kNm)	29772 (23844, 37194)	29772 (22344, 37194)	29772 (23844, 37195)
	LSSTipMys (kNm)	9061 (6870, 11953)	9061 (6870, 11953)	9061 (6870, 11953)
	TwrBsMyt (kNm)	314083 (229636, 429680)	314083 (229636, 429680)	314084 (229636, 429681)
LC2, V_{hub} = 12 m/s	RootMyb (kNm)	41593 (28380, 61026)	41593 (28380, 61026)	41593 (28380, 61026)
	LSSTipMys (kNm)	15321 (11801, 19903)	15321 (11801, 19904)	15321 (11801, 19904)
	TwrBsMyt (kNm)	491364 (368347, 655777)	491364 (368347, 655778)	491365 (368348, 655779)
LC3, V_{hub} = 16 m/s	RootMyb (kNm)	46542 (36896, 58215)	46542 (37218, 58215)	46542 (37218, 58215)
	LSSTipMys (kNm)	17168 (13676, 21530)	17168 (13676, 21530)	17168 (13676, 21530)
	TwrBsMyt (kNm)	466508 (384880, 566002)	466510 (384880, 566003)	466510 (384882, 566004)